# University of Southampton

Faculty of Engineering and Physical Sciences
School of Chemistry


# Targeting the IRES structure of mRNA for modulating gene translation


by

Albert Ferriol Monjo

ORCID ID 0000-0003-0754-4716


Thesis for the degree of Doctor of Philosophy

May 2025

**University of Southampton**

## Abstract

Faculty of Engineering and Physical Sciences
School of Chemistry

Thesis for the degree of Doctor of Philosophy

# Targeting the IRES structure of mRNA for modulating gene translation

by
Albert Ferriol Monjo

The c-Myc oncoprotein is a critically important cancer driver across a wide range of tumour types. Recent studies demonstrated that the translation of the *c-myc* mRNA could work as a potential Achilles' heel for cancer treatment. These studies suggest that *c-myc* is a promising, although challenging, target for cancer therapy.

The *c-myc* mRNA internal ribosomal entry site (IRES) was initially targeted. IRESs are found in mRNAs encoding a number of different oncoproteins and allow mRNA translation to initiate independently of the canonical 5'-CAP and have been proposed as therapeutic targets. Activity of the *c-myc* IRES is increased in malignant cells compared to the healthy cells, providing a potential window for cancer selective *c-myc* inhibition.

It was proposed to use the base-pairing capacity of nucleic acids for highly selective targeting of the *c-myc* mRNA, thereby avoiding potential confounding effects of broader translational inhibition obtained with eIF4A blockade. The hypothesis is that antisense oligonucleotides (ASOs), specific for parts of the *c-myc* IRES, will lead to inhibition of *c-myc* translation. Importantly, the *c-myc* IRES structure has been derivatised using footprinting. This mapping of the *c-myc* IRES sequence has revealed a minimal 50-base sequence that was responsible for the bulk of the IRES activity. Within this element, two 14-nt segments were responsible for ribosome recruitment. This mapping provides the basis for our rational design of targeting ASOs. The designed oligonucleotides (ODNs) will contain modifiers for increased nuclease resistance and increased RNA-DNA duplex formation (e.g. LNA, phosphorothioate). The combination of these modifications is introduced as a key for modulating gene translation as the target RNA must not be degraded. To introduce these target sequences into human cells a suitable AuNPs@PEG@ssDNA has to be designed.

# Table of Contents

# Table of Tables

# Table of Figures

# Research Thesis: Declaration of Authorship

Print name: Albert Ferriol Monjo

Title of thesis: Targeting the IRES structure of mRNA for modulating gene translation

I declare that this thesis and the work presented in it are my own and has been generated by me as the result of my own original research.

I confirm that:

1. This work was done wholly or mainly while in candidature for a research degree at this University; 2. Where any part of this thesis has previously been submitted for a degree or any other qualification at this University or any other institution, this has been clearly stated;

3. Where I have consulted the published work of others, this is always clearly attributed;

4. Where I have quoted from the work of others, the source is always given. With the exception of such quotations, this thesis is entirely my own work;

5. I have acknowledged all main sources of help;

6. Where the thesis is based on work done by myself jointly with others, I have made clear exactly what was done by others and what I have contributed myself;

7. None of this work has been published before submission

Signature: Date: 24.05.2024

# Acknowledgements

I would like to start by thanking Prof. Eugen Stulz for giving me the opportunity to perform this project and for being a mentor during these three years. It was a privilege to have a supervisor who was incredibly patient with all my questions and who was always available to offer advice or simply listen, no matter the issue. I would also like to thank Prof. Tilman Sanchez for his support and for being always a close person, showing patience during challenging moments and celebrating all the achievements over these three years.

Additionally, I would like to express my gratitude to Dr. Chloe Howells, Dr. Teresa Laurea, Dr. Elena Vodorova, and Dr. Gabriel Barbeta for their help and guidance in the lab, especially in areas and fields which I was not familiar with. A special thanks also goes to Tina and the rest of the OLIGOMED team for your support, advice, positive energy, and constant encouragement.

Als meus amics de tota la vida, és una sort poder anar complint etapes amb vosaltres desde petits i que triem cada dia seguir compartint tristeses i alegries junts. Mirar el mòbil i veure un missatge vostre és sinònim d'alegria, i cada vegada que he necessitat tornar, m'heu carregat les piles.

A la meva família, i en especial al meu pare, la meva mare i el meu germà, gràcies per ser sempre allà quan ho he necessitat. No puc imaginar com a pare com de dur deu ser veure marxar un fill lluny de casa per poder complir el seu somni de dedicar-se al que el fa feliç. Gràcies per fer-me sentir sempre important i estimat, sigui on sigui i faci el que faci. Sou un gran exemple.

A Laura, por haber compartido este viaje conmigo y por, a pesar de la dificultad de la situación, haber decidido quedarte. Demuestras una fe en mis cualidades que me ayuda a ser mejor persona y a superarme cuando las situaciones parecen imposibles.

I, finalment, volia agrair a la meva padrina per ser el major exemple de superació que he trobat a la vida. Pensar en tu ha estat l'empenta que necessitava en els moments difícils per donar sempre una mica més de mi. Gràcies per estimar-me com ho vas fer i per ajudar-me en tot el que podies i més. Aquesta tesi també és teva. T'estim.

# Definitions and Abbreviations

| | |
|---|---|
| **2'-MOE** | 2'-O-methoxyethyl |
| **2'-OME** | 2'-O-methyl |
| **6-FAM** | 6-Carboxyfluorescein |
| **ACN** | Acetonitrile |
| **aa-tRNA** | Aminoacyl transfer RNAs |
| **AgNP** | Silver nanoparticle |
| **AHP** | Acute hepatic porphyria |
| **ALAS1** | Aminolevulinate synthase 1 |
| **ApoB-100** | apolipoprotein B-100 |
| **ATP** | Adenosine triphosphate |
| **ASO** | Antisense oligonucleotide |
| **AuNP** | Gold nanoparticle |
| **AuNPs@Cit** | Citrate capped gold nanoparticles |
| **AuNPs@PEG** | Gold nanoparticles functionalized with polyethlene glycol |
| **AuNPs@PEG@DNA** | Gold nanoparticles functionalized with polyethlene glycol bioconjugated to DNA |
| **ARE** | AU-rich element |
| **bHLH-LZ** | Basic helix loop helix leucine zipper |
| **BME** | β-mercaptoethanol |
| **BSA** | Bovine serum albumin |
| **CDK** | Cyclin-dependent kinases |
| **cDNA** | Complementary DNA |

| | |
|---|---|
| **CNT** | Carbon nanotube |
| **CMV** | Cytomegalovirus |
| **CPG** | Controlled pore glass |
| **CPSF** | Cleavage and Polyadenylation Specificity Factor |
| **Ct** | Cycle threshold |
| **DDTT** | [(Dimethylaminomethylene)amino]-3H-1,2,4-dithiazole-5-thione |
| **DLS** | Dynamic light scattering |
| **DMD** | Duchenne muscular dystrophy |
| **DMEM** | Dulbecco's modified eagle medium |
| **DMSO** | Dimethyl sulfoxide |
| **DNA** | Deoxyribonucleic acid |
| **E-Box** | Enhancer Boxes |
| **EDITH** | 3-ethoxy-1,2,4-dithiazoline-5-one |
| **FDA** | U.S. Food and Drug Administration |
| **FSC** | Forward scatter |
| **eIF4F** | Eukaryotic initiation factor 4F |
| **ER** | Endoplasmic reticulum |
| **EIF** | Eukaryotic initiation factors |
| **FBS** | Fetal bovine serum |
| **GalNAc** | N-acetylgalactosamine |
| **hATTR** | Hereditary transthyretin amyloidosis |
| **HFIP** | Hexafluoro-2-propanol |
| **HOFH** | Homozygous familial hypercholesterolemia |

| | |
|---|---|
| **HPLC** | High performance liquid chromatography |
| **IF** | Immunofluorescence |
| **ITAF** | Internal initiation trans-acting factor |
| **IRES** | Internal ribosome entry site |
| **LDH** | Lactate dehydrogenase |
| **LNA** | Locked nucleic acid |
| **LSPR** | Localized surface plasmon resonance |
| **m5C** | 5-methylcytosine |
| **m7G** | 7-methylguanosine |
| **Met-tRNAi** | Methionine-charged initiator tRNA |
| **mRNA** | Messenger RNA |
| **mRNP** | Messenger ribonucleoprotein |
| **MWCO** | Molecular weight cutoff |
| **NHS** | N-Hydroxysuccinimide |
| **ON** | Oligonucleotides |
| **PABP** | Poly(A)-binding protein |
| **PBS** | Phosphate buffer saline |
| **PdI** | Polydispersity index |
| **PEG** | Polyethylene glycol |
| **PFA** | Paraformaldehyde |
| **PH1** | Primary hyperoxaluria type 1 |
| **PIC** | Pre-initiation complex |
| **PMO** | Phosphorodiamidate morpholino oligomer |

| | |
|---|---|
| **PNA** | Peptide nucleic acid |
| **PS** | Phosphorothioates |
| **PV** | Poliovirus |
| **qPCR** | Quantitative Polymerase Chain Reaction |
| **RES** | Reticuloendothelial system |
| **ROS** | Reactive Oxygen Species |
| **RNA** | Ribonucleic acid |
| **RNAi** | RNA interference |
| **rRNA** | Ribosomal RNA |
| **RT** | Reverse transcription |
| **SECIS** | Selenocysteine insertion sequence |
| **SMA** | Spinal muscular atrophy |
| **SNP** | Single nucleotide polymorphism |
| **snRNA** | Small nuclear RNAs |
| **snRNP** | Small nuclear ribonucleoprotein |
| **SPR** | Surface plasmon eesonance |
| **SSC** | Side scatter |
| **TAD** | Transactivation domain |
| **TEA** | Triethanolamine |
| **TC** | Ternary complex |
| **TCA** | Trichloroacetic acid |
| **TEM** | Transmission electron microscopy |
| **TFA** | Trifluoroacetic acid |

| | |
|---|---|
| **Tm** | Melting temperature |
| **tRNA** | Transference RNA |
| **TTR** | Transthyretin |
| **uORFs** | Open reading frames |
| **UTR** | Untranslated region |
| **UV-Vis** | Ultraviolet visible spectrophotometry |
| **WB** | Western Blot |
| **WGA** | Wheat germ agglutinin |

# Chapter 1 Introduction

## 1.1 Overview

Modified oligonucleotides designed to regulate gene expression have emerged as a promising therapeutic strategy for cancers that are resistant to conventional treatment approaches. The first chapter of this thesis provides an introduction to the fundamentals of gene expression, including the structure of nucleic acids and the processes of eukaryotic transcription and translation. It also compares IRES-mediated translation with canonical cap-dependent translation.

The chapter further explores the *c-myc* gene, which contains an internal ribosome entry site (IRES), discussing its structure and its critical roles in cell growth, apoptosis, and metabolism, as well as its involvement in a wide range of tumour types. Following this, antisense therapy is reviewed, highlighting the evolution of oligonucleotide-based treatments across different generations.

Finally, the chapter concludes by introducing nanoparticles as a promising platform for sensing and delivering oligonucleotide systems. Their unique nanoscale properties and core-based materials make them highly suitable for such applications.

## 1.2 Central dogma of molecular biology

The central dogma of molecular biology explains the flow of genetic information from DNA to RNA, ultimately resulting in the production of a functional protein. This concept was formally defined by Francis Crick in 1970[1], although it was first introduced during a public lecture by Crick in 1957.

Another fundamental concept in molecular biology is gene expression, which refers to the process by which the instructions encoded in DNA are converted into a functional product. Gene expression involves two key steps: transcription and translation. These processes are essential for the conversion of nucleic acids into proteins (**Figure 1.1**) and will be discussed in greater detail in subsequent chapters.

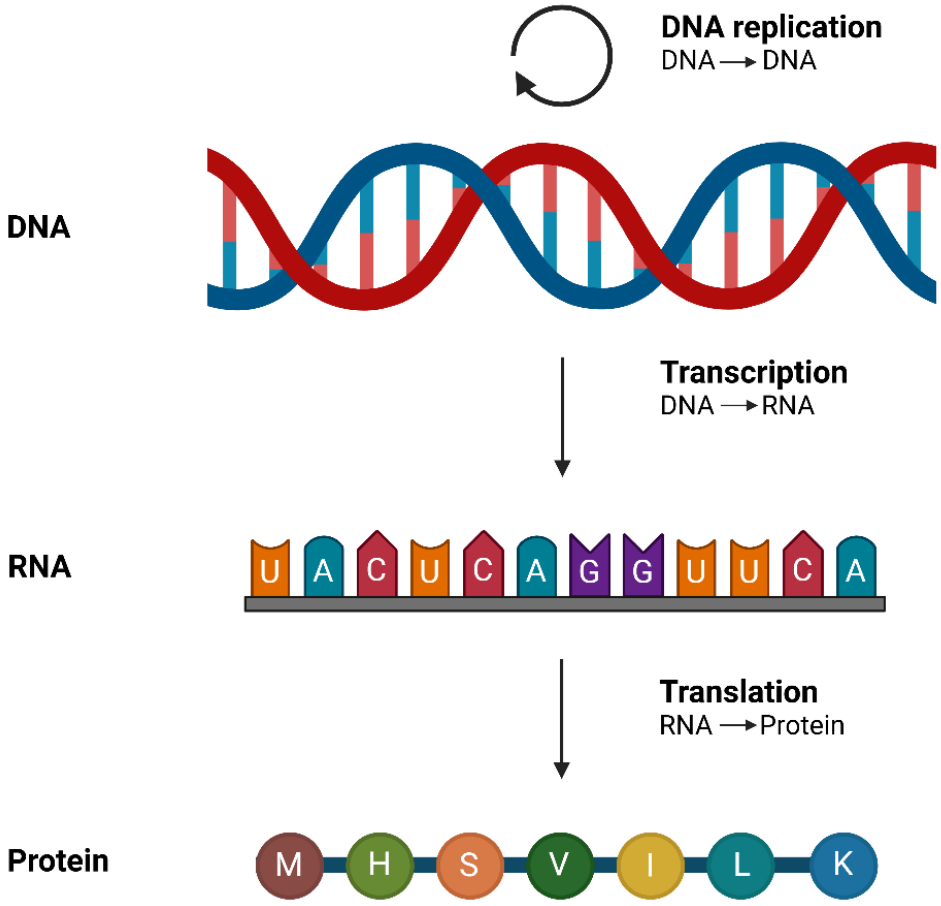


**Figure 1.1**: **The central dogma of molecular biology.** Image credit: Created with BioRender.com.

## 1.3 Nucleic Acids

Nucleic acids are a vital class of macromolecules that serve as the primary information-carrying molecules in cells. They were first discovered in 1869 by Friedrich Miescher, who isolated them from the nucleus of cells[2]. The primary functions of nucleic acids include the storage of genetic information and the regulation of protein synthesis. Beyond these roles, nucleotides, the building blocks of nucleic acids, also serve as energy sources in the form of adenosine triphosphate (ATP), physiological signaling mediators, secondary messengers, and allosteric enzyme effectors[3].

The two main classes of nucleic acids are deoxyribonucleic acid (DNA) and ribonucleic acid (RNA). Nucleic acids are composed of long chain-like molecules formed by nearly identical monomers called nucleotides, which combine to create polynucleotides. Each nucleotide consists of three components: a five-carbon ribose sugar (pentose), a phosphate group, and a nitrogenous base (**Figure 1.2**).

There are five canonical nitrogenous bases found in nucleic acids: adenine (A), cytosine (C), guanine (G), thymine (T), and uracil (U). Additionally, nucleic acids may contain non-canonical nitrogenous bases that are modified after the formation of the nucleic acid chain. In DNA, the most common modification is 5-methylcytosine (m5C). In RNA, numerous modified bases exist, including pseudouridine (Ψ), dihydrouridine (D), inosine (I), and 7-methylguanosine (m7G). These modifications play important roles in regulating nucleic acid function[4].

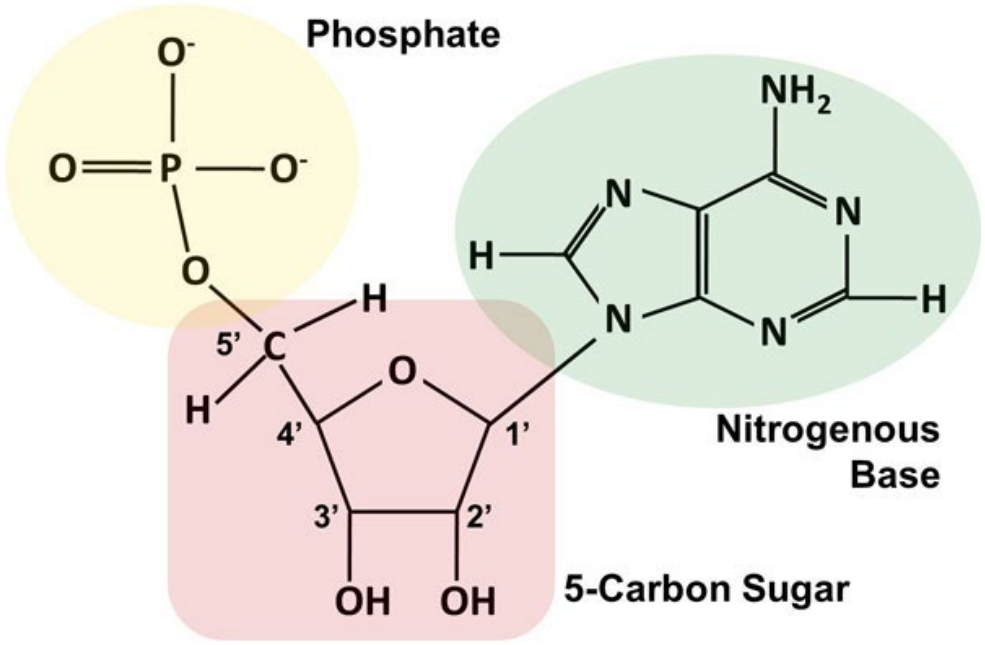


**Figure 1.2**: **Structure of a nucleotide consisting of a five-carbon sugar, a nitrogenous base, and a phosphate group.**

Adenine and guanine are classified as purine bases, characterized by a double-ring structure consisting of a six-membered aromatic ring fused to a five-membered aromatic ring, with each ring containing two nitrogen atoms. In contrast, cytosine, thymine, and uracil are classified as pyrimidine bases, which are defined by a single six-membered aromatic ring containing two nitrogen atoms as their primary structure.

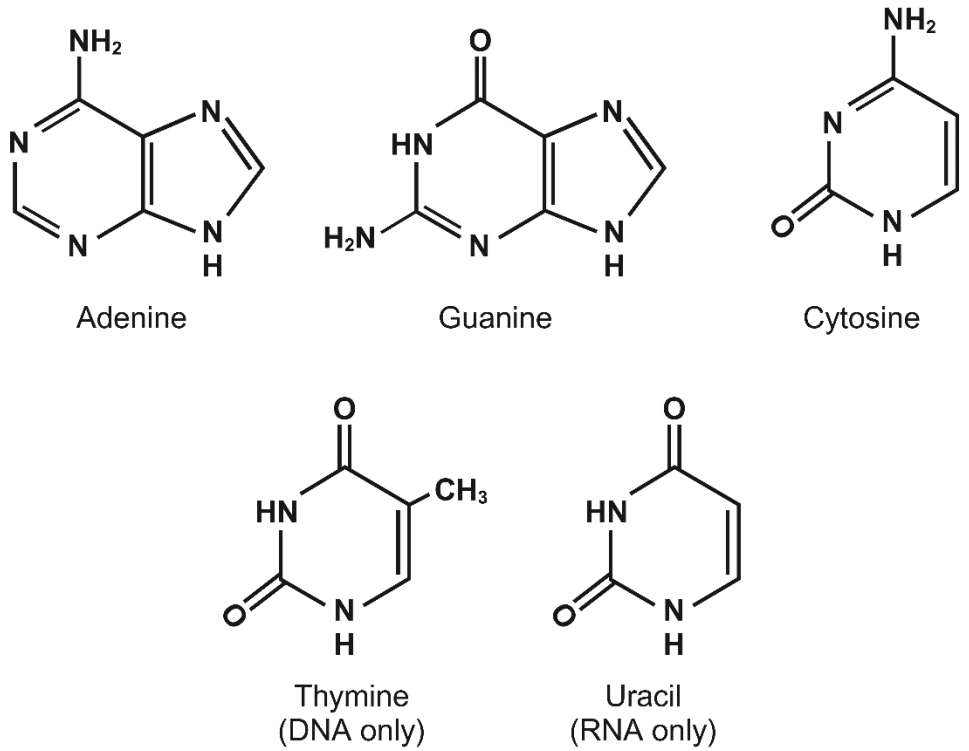


**Figure 1.3**: **Structures of Nitrogenous Bases in DNA and RNA**

There are notable differences between the various classes of nucleic acids. Nucleosides consist of a nitrogenous base, typically a purine or pyrimidine, attached to a five-carbon carbohydrate (ribose). In contrast, a nucleotide contains an additional phosphate group. Polynucleotides that include ribose as the carbohydrate are referred to as ribonucleotides or RNA.

There are five types of nucleosides and nucleotides: adenosine, guanosine, cytidine, thymidine, and uridine. Each nucleotide in DNA contains one of four nitrogenous bases: adenine (A), guanine (G), cytosine (C), or thymine (T). In RNA, however, uracil (U) replaces thymine as one of the bases (**Figure 1.3**). Another key difference lies in the pentose sugar: DNA contains 2’-deoxyribose, while RNA contains ribose. The distinction between these sugars is the presence of a hydroxyl (-OH) group on the 2'-carbon of ribose, which is absent in deoxyribose.

In the sugar molecule, each carbon atom is numbered as 1’, 2’, 3’, 4’, and 5’ (e.g., "1 prime"). For the heterocyclic nitrogenous bases, the atoms are numbered 1 through 9 for purines and 1 through 6 for pyrimidines. The nitrogen at position 9 in purines or

position 1 in pyrimidines forms a covalent bond with the 1' carbon of the pentose sugar. This bond is referred to as an N-glycosidic linkage (**Figure 1.4A**).

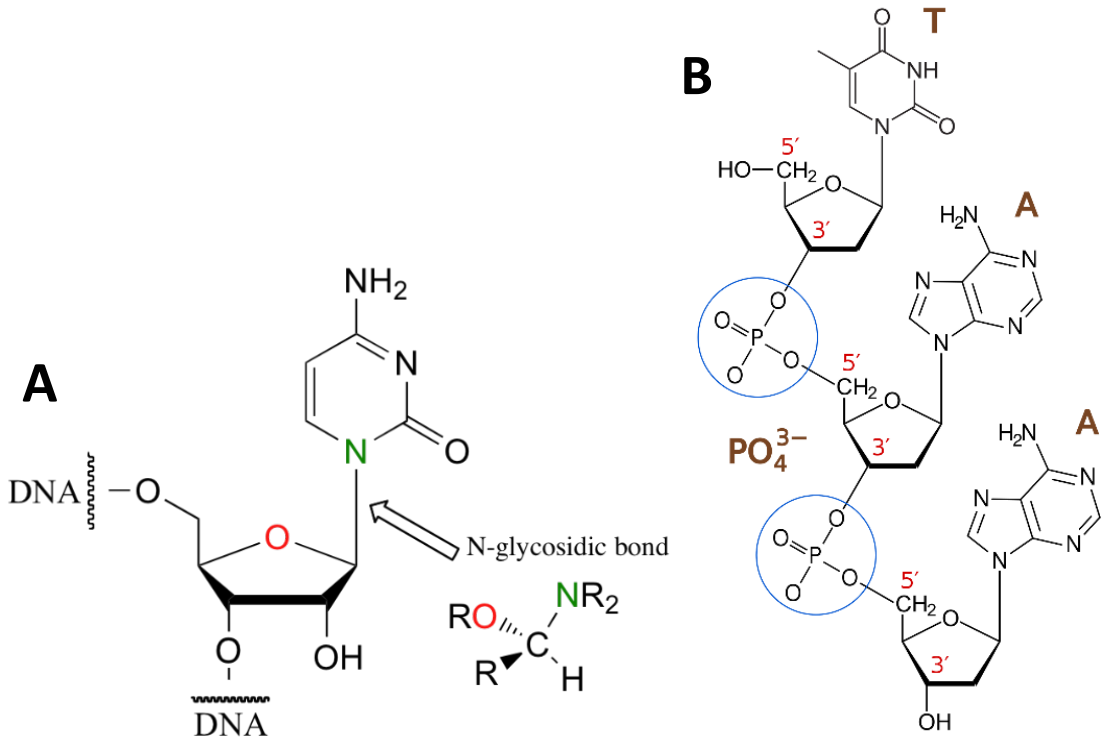


**Figure 1.4: Structure of DNA: Nucleotide composition and phosphodiester bonding.** (A) N-Glycosidic linkage between 1' nitrogen of pyrimidine bases and the 1' carbon of the pentose sugar. (B) Diagram of phosphodiester bonds (PO43−) between three nucleotides.

In DNA and RNA, the phosphate group serves as a linker, enabling the formation of oligonucleotide polymers through the combination of phosphodiester bonds and sugar molecules. The phosphate group connects the hydroxyl group of the 5’ carbon of one sugar to the hydroxyl group of the 3’ carbon of the sugar in an adjacent nucleotide, creating a 5’ to 3’ phosphodiester linkage (**Figure 1.4B**).

The ribose and deoxyribose sugars in nucleic acids are inherently non-planar and adopt a three-dimensional structure. This non-planarity is referred to as "puckering." The conformation of DNA or RNA molecules is influenced by non-bonded interactions between substituents on the four ring carbon atoms. Sugars with atoms puckered above the reference plane adopt the endo conformation, while those with atoms puckered below the plane adopt the exo conformation[5].

The C3'-endo conformation (also known as the N-type or A-form) is predominantly found in RNA and A-DNA, while the C2'-endo conformation (also referred to as the S-type or B-form) is characteristic of duplexes with a B-DNA helical structure (**Figure 1.5**).

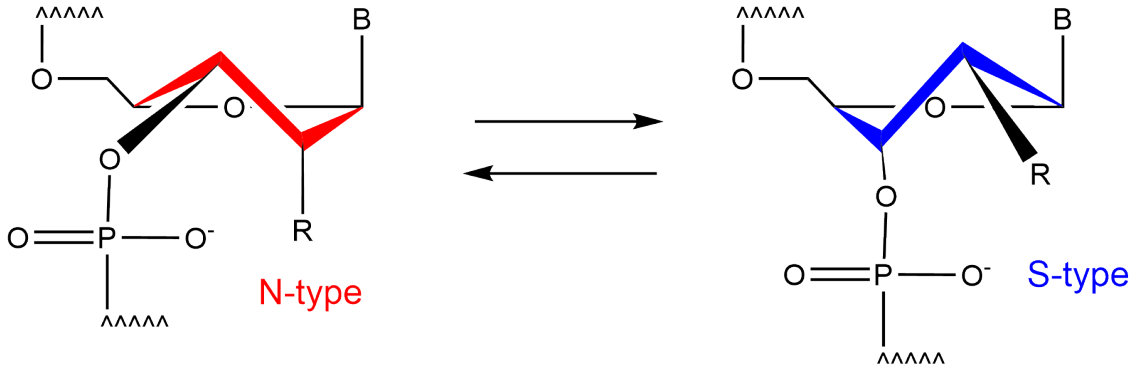


**Figure 1.5**: **Typical DNA sugar puckering conformations**. Sugars with atoms puckered above the reference plane are classified as endo-form, while those with puckered atoms located below the plane are classified as exo-form. Figure adapted from[6].

## 1.4 Deoxyribonucleic Acid (DNA)

DNA serves as the fundamental blueprint for life, constituting the genetic material in all free-living organisms and most viruses. In 1951, Maurice Wilkins and Rosalind Franklin utilized X-ray diffraction to capture images of DNA fibers. These images provided critical insights that enabled James Watson and Francis Crick, in 1953, to discover key structural features of B-DNA.[7].

The DNA molecule is composed of two strands that coil around a common axis in a right-handed helical structure with a diameter of approximately 20 Å. These strands are arranged in an antiparallel orientation, meaning their 5' to 3' directions run opposite to each other, imparting polarity to the molecule.

### 1.4.1 Structure of the DNA

The sugar and phosphate groups are positioned on the exterior of the DNA helix, forming the sugar-phosphate backbone. In contrast, the nitrogenous bases are located on the interior of the helix, oriented perpendicularly to the helical axis. The distance between two adjacent bases is 3.4 Å, and each base is rotated 36 degrees relative to

the one below it. The helical structure completes a full turn every 34 Å, corresponding to approximately 10.5 bases per turn.[8].

The secondary structure of DNA features two distinct grooves: the major groove, where the backbones are farther apart, and the minor groove, where the backbones are closer together. The major groove is 12 Å wide and slightly deeper (8 Å) than the minor groove, which is 6 Å wide and 7.5 Å deep [9] **(Figure 1.6)**.

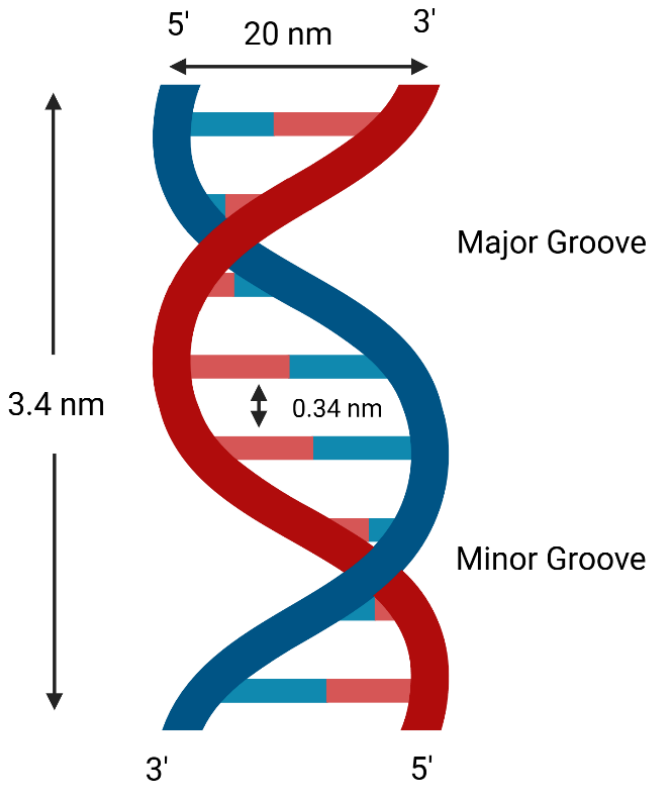


**Figure 1.6**: **Structure of the DNA Double Helix**. The illustration shows the major and minor grooves, as well as nucleotide base pairing within the DNA molecule. Notably, DNA can adopt various structural conformations under different conditions. Image credit: Created with BioRender.com.

Under physiological conditions, the predominant secondary structure of DNA is B-DNA. This conformation is a right-handed helix in which the base pairs are positioned along the helix axis, resulting in major and minor grooves of similar depth. However, DNA can adopt alternative conformations under specific environmental conditions.

One of these conformations is **A-DNA**, a right-handed, antiparallel double helix with a cylindrical structure approximately 24 Å in diameter. A-DNA typically forms under conditions of low humidity and high salt concentrations and is the predominant

structure in RNA-RNA and RNA-DNA hybrids[10]. Another possible conformation is Z-DNA, a left-handed, antiparallel double helix that commonly occurs in sequences with alternating purine-pyrimidine bases (e.g., dCGCGCG). Z-DNA is characterized by a pronounced zig-zag pattern in its phosphodiester backbone[11].

The formation of DNA relies on Watson–Crick base pairing, which is the dominant mode of base pairing in nucleic acids. In double-stranded DNA, adenine (A) pairs with thymine (T) via two hydrogen bonds, while guanine (G) pairs with cytosine (C) via three hydrogen bonds. This base pairing adheres to Chargaff's rule, which states that there is a 1:1 stoichiometric ratio of purines to pyrimidines in any DNA molecule[12].

An alternative form of base pairing, known as Hoogsteen pairing, can also occur. In Hoogsteen base pairs, two nucleobases from different nucleic strands or from distant regions of the same strand are held together by hydrogen bonds (**Figure 1.7**).

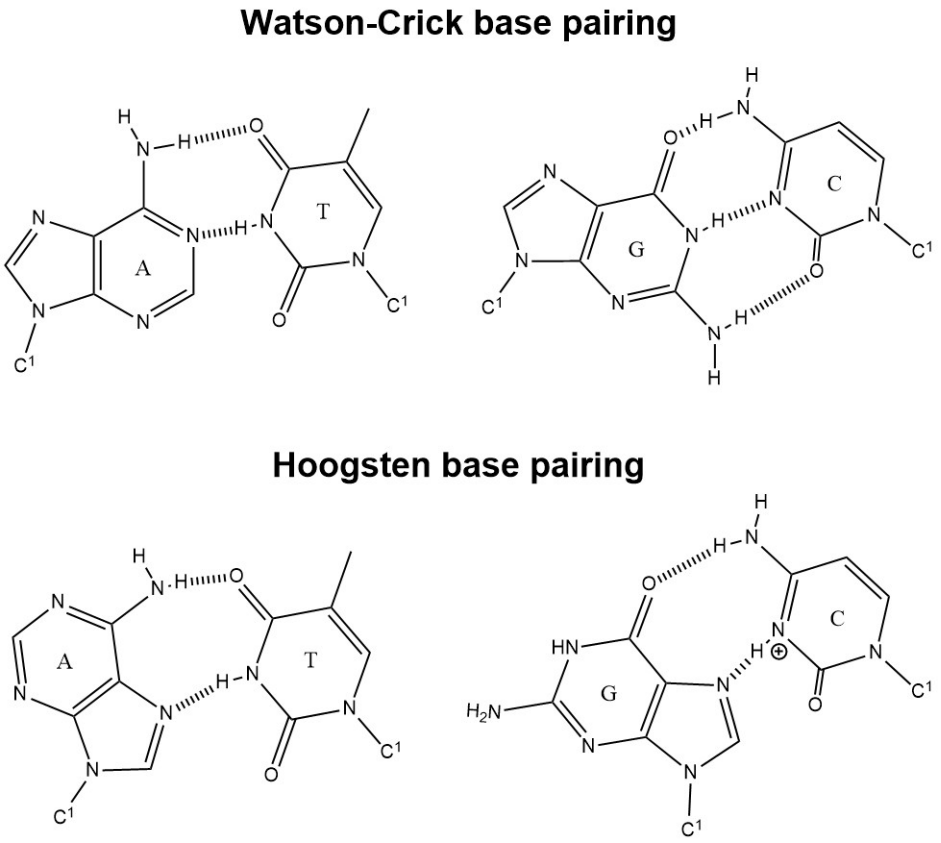


**Figure 1.7**: **Structural Representation of Watson–Crick and Hoogsteen Base Pairing in DNA.** Figure adapted from[13].

### 1.4.2 Transcription

Transcription is the first step in gene expression, during which the genetic information encoded in DNA is transcribed into messenger RNA (mRNA) within the nucleus of cells. This process is facilitated by various transcription factors and the enzyme RNA polymerase, which synthesizes a complementary RNA strand using a single-stranded DNA template. Nucleotides are added exclusively to the 3' end of the growing RNA strand, resulting in synthesis that proceeds in the 5' to 3' direction.

The transcription process consists of three main stages **(Figure 1.8):**

- Initiation: During this stage, RNA polymerase scans the DNA molecule until it recognizes a specific sequence known as the promoter. Each gene contains its own promoter, which indicates the starting point for transcription. Upon binding to the promoter, RNA polymerase unwinds the DNA strands, exposing the single-stranded template required for transcription[14]. The rate of transcription is regulated by transcription factors.

- Elongation: This stage involves the addition of nucleotides to form the growing mRNA strand. RNA polymerase reads the separated DNA strands and synthesizes the mRNA molecule in a 5' to 3' direction using complementary base pairing (A pairs with U, T pairs with A, C pairs with G, and G pairs with C). In this process, ribose is incorporated into the mRNA instead of deoxyribose[15].

- Termination: Transcription concludes when RNA polymerase encounters a stop (termination) sequence on the DNA strand. At this point, transcription ceases, and the newly synthesized RNA strand, now referred to as pre-mRNA, is released and detached from the RNA polymerase complex[16].

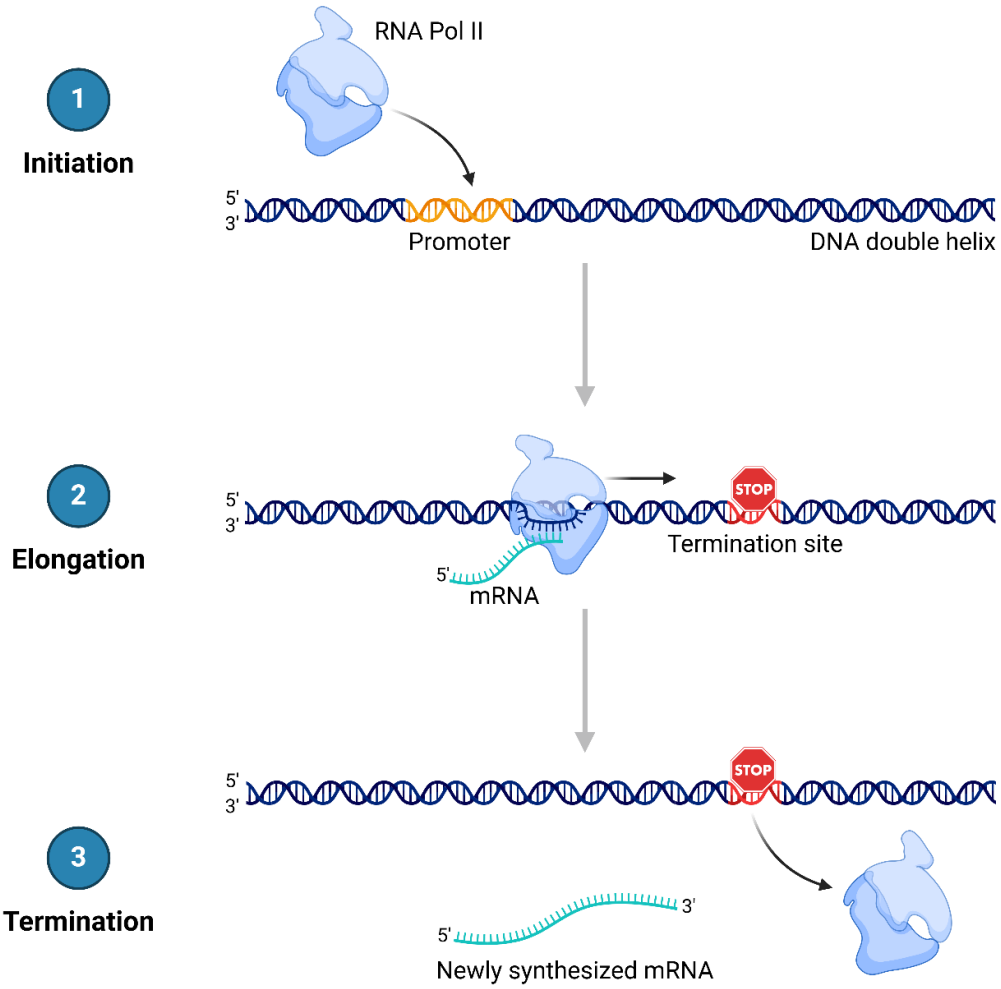


**Figure 1.8**: **The Transcription Process.** RNA polymerase unwinds the double-stranded DNA and initiates transcription at the transcription start site, continuing until it reaches the transcription end site. Upon completion, the pre-mRNA is cleaved and released. Image credit: Created with BioRender.com.

The processing of eukaryotic pre-mRNA to generate mature mRNA occurs after transcription and, in some cases, even during transcription. These processes include the addition of a 5' cap, splicing out introns, and the addition of a poly-A tail to the 3' end[16] (**Figure 1.9**).

The 5' end of eukaryotic mRNA is capped by the attachment of a 7-methylguanosine (7mG) cap. This guanine residue is added to the RNA by the enzyme guanylate transferase via an unusual 5'-5' triphosphate linkage, rather than the typical 3'-5' phosphate bond found between other nucleotides in the RNA molecule. Subsequently, the guanosine is methylated at the 7th position of the purine ring by the enzyme methyltransferase, producing 7-methylguanosine[17].

The cap structure protects the transcript from degradation by 5′ exonucleases, which would otherwise recognize a free 5′ end and degrade the RNA in the 5′ to 3′ direction. Additionally, the cap facilitates the recognition and export of RNA from the nucleus to the cytoplasm while preventing detection by cellular sensors that differentiate between self and non-self RNA.

Once transcription is complete and the pre-mRNA has been fully synthesized, its 3′ end is protected through polyadenylation[14]. The pre-mRNA contains a polyadenylation site flanked by two signal sequences: an upstream AAUAAA sequence and a downstream region rich in G and U residue[18]. These sequences are recognized by a set of factors, including CPSF (Cleavage and Polyadenylation Specificity Factor), which binds to the RNA and cleaves it.

Following cleavage, poly(A) polymerase adds over 250 adenylate residues to form a poly(A) tail. This tail is coated with Poly-A Binding Proteins (PABPs), which protect eukaryotic mRNA from degradation by 3′ exonucleases, enhance mRNA translation, and facilitate transport of mRNA from the nucleus to the cytoplasm[17].

After both ends of the pre-mRNA are protected, splicing occurs to remove intron sequences and join exons together. Pre-mRNA molecules contain exons (coding sequences included in mature mRNA) and introns (non-coding sequences)[19]. Splicing is carried out by a complex called the spliceosome, which consists of five small nuclear RNAs (snRNAs) (U1, U2, U4, U5, and U6) and over 300 associated proteins.

The splicing process begins with the binding of the U1 small nuclear ribonucleoprotein (snRNP) to the 5′ splice site, while the U2 snRNP recognizes the branch point near the 3′ splice site[20]. Following the recognition of these splice sites, the spliceosome undergoes conformational changes as U2, U4, U5, and U6 snRNPs assemble to form the active spliceosome.

Once assembled, the spliceosome cleaves the RNA at the 5′ splice site and subsequently at the 3′ end of the intron. The two exons are then ligated together, completing the splicing reaction. The excised intron is released in a lariat structure and is subsequently degraded in the nucleus by nucleases[17].

Alternative splicing allows a single gene to produce multiple protein isoforms by selectively including or excluding specific exons during splicing. This process significantly increases proteome complexity and enables functional diversity within cells.

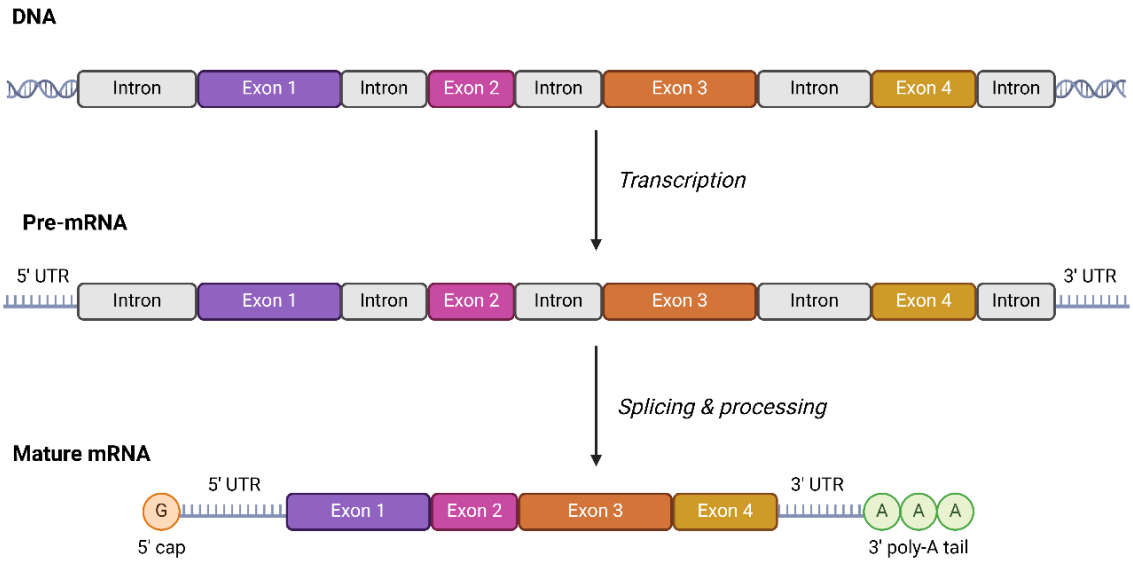


**Figure 1.9**: **mRNA Maturation Process.** The maturation of pre-mRNA involves both co-transcriptional and post-transcriptional processing steps, including the addition of an m7G cap to the 5′ end and a poly(A) tail to the 3′ terminus. This is followed by splicing, during which introns are removed, and exons are joined together. Image credit: Created with BioRender.com.

## 1.5 Ribonucleic acid (RNA)

RNA serves as the genetic material in certain viruses and plays crucial roles in all living cells, including coding, decoding, regulation, and gene expression. Although RNA is typically a single-stranded molecule, it requires proper three-dimensional folding to perform its specific biological functions.

The secondary structures of RNA were first observed in 1956 when Alexander Rich and David Davies, using X-ray crystallography, discovered that single strands of RNA can hybridize to form double-stranded molecules[21]. Later, in 1960, the discovery of a hybrid double helix formed by an RNA and a DNA molecule provided the first experimental evidence of information transfer from DNA to RNA[22].

The two-dimensional (2D) structure of RNA is defined as the sum of all base-base pairs within the molecule, including long-range base pairs involved in tertiary folds[23]. RNA

exhibits greater structural versatility than DNA, allowing for the coexistence of multiple conformations with distinct structures and functions[24]. The three main types of RNA directly involved in protein synthesis are messenger RNA (mRNA), ribosomal RNA (rRNA), and transfer RNA (tRNA).

Additionally, RNA can fold into complex three-dimensional (3D) structures that regulate various cellular processes such as translation, gene silencing, RNA splicing, and protein trafficking[24]. Understanding the 3D structure of RNA is essential for elucidating its interactions with other molecules and its functional mechanisms[23]. Techniques such as nuclear magnetic resonance (NMR) spectroscopy, X-ray crystallography, cryo-electron microscopy, and virtual modeling are valuable tools for studying and characterizing the 3D structures of RNA molecules[25].

### 1.5.1 Structure of eukaryotic mRNA

Following transcription, pre-mRNAs must undergo processing to become functional mRNAs. This processing involves the removal of introns, the addition of a m7G cap structure at the 5′ end of the first exon, and the addition of a poly(A) tail, consisting of 100–250 adenine residues, at the 3′ end of the last exon[26]. The resulting mature eukaryotic mRNA comprises three main regions: a 5′ untranslated region (5′ UTR), a coding region, and a 3′ untranslated region (3′ UTR) **(Figure 1.10).**

The 5′ UTR begins at the 5′ terminal end (m7G cap) and extends to the start codon. On average, the length of the 5′ UTR is approximately 200 nucleotides, which is relatively consistent across eukaryotes[26]. The GC content in this region is typically around 60%[27]. Although untranslated, the 5′ UTR can form secondary structures that influence mRNA translation, localization, and stability[28].

Post-transcriptional regulation of ribosome scanning and initiation codon selection is mediated by cis-acting elements located within the 5′ UTR. These elements include upstream open reading frames (uORFs)[29], hairpins or stem-loops[30], internal ribosome entry sites (IRESs)[28] and G-quadruplexes[31]. These structural features play critical roles in modulating mRNA function and gene expression.

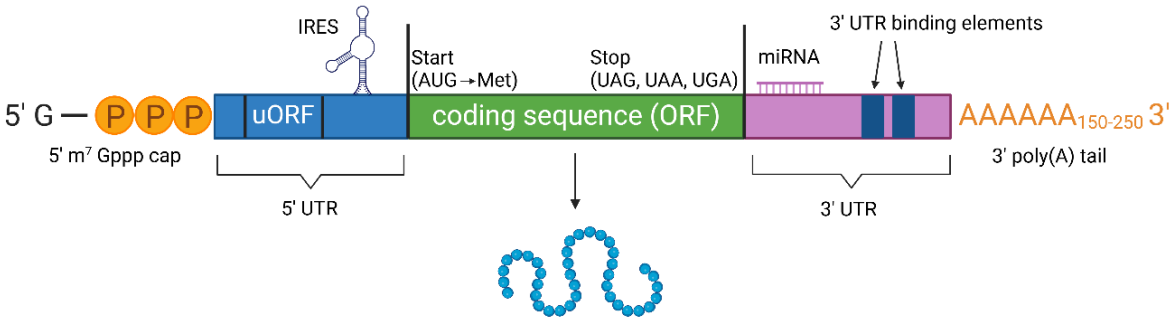


**Figure 1.10**: **Structure of a Eukaryotic mRNA.** A mature mRNA consists of three main regions: the 5′ untranslated region (5′ UTR), which is bounded by the 5′ m7G cap and the start codon and may contain structural elements such as hairpins, upstream open reading frames (uORFs), and internal ribosome entry sites (IRESs); the coding sequence, defined by the start and stop codons; and the 3′ untranslated region (3′ UTR), which is bounded by the stop codon and the poly(A) tail. Image credit: Created with BioRender.com.

The coding region of a mature mRNA is the sequence located between the start codon (typically AUG) and one of the stop codons (UGA, UAA, or UAG). This region is composed of triplets of nucleotides, known as codons, which are arranged in a continuous reading frame. Each codon encodes a specific amino acid, thereby determining the precise amino acid sequence of the protein it codes for[32].

The 3′ untranslated region (3′ UTR) is defined as the sequence between the stop codon and the poly(A) tail in an mRNA molecule. Compared to the 5′ UTR, the 3′ UTR is generally longer, with its length varying across taxonomic groups: approximately 200 nucleotides in plants and fungi and up to 800 nucleotides in humans and other vertebrates[26]. The average GC content of the 3′ UTR is around 45%, which is lower than that of the 5′ UTR[27].

The 3′ UTR contains numerous cis-acting regulatory elements that play essential roles in post-transcriptional gene regulation[33]. Among these elements, AU-rich elements (AREs) are the most common and are involved in regulating mRNA stability, translational efficiency, and alternative pre-mRNA processing[34]. Other examples of regulatory elements include GU-rich elements[35], CA-rich elements[36], iron responsive elements[37] , and the selenocysteine insertion sequence (SECIS) element[38], each contributing to specific regulatory functions within the mRNA molecule.

### 1.5.2 Translation in eukaryotes

Translation is the process by which proteins are synthesized using mRNA as a template. This process involves three key components: the mRNA, which serves as the genetic template; the ribosome, which functions as the assembly machinery; and aminoacyl transfer RNAs (aa-tRNAs), which deliver specific amino acids to the growing polypeptide chain[39]. Translation is one of the most energy-intensive cellular processes, consuming approximately 20% of the cell's ATP[40].

Protein synthesis is a highly intricate process that occurs in three distinct stages: initiation, elongation, and termination[41]. In eukaryotic cells, translation can be initiated through different mechanisms. The two most common modes are canonical cap-dependent initiation and internal initiation. It is estimated that cap-dependent initiation, which requires all canonical initiation factors, accounts for approximately 95–97% of all translation initiation events in eukaryotic cells. In contrast, internal initiation, which relies on a reduced subset of initiation factors, represents about 3–5% of translation initiation events[42].

### 1.5.2.1 Cap canonical translation

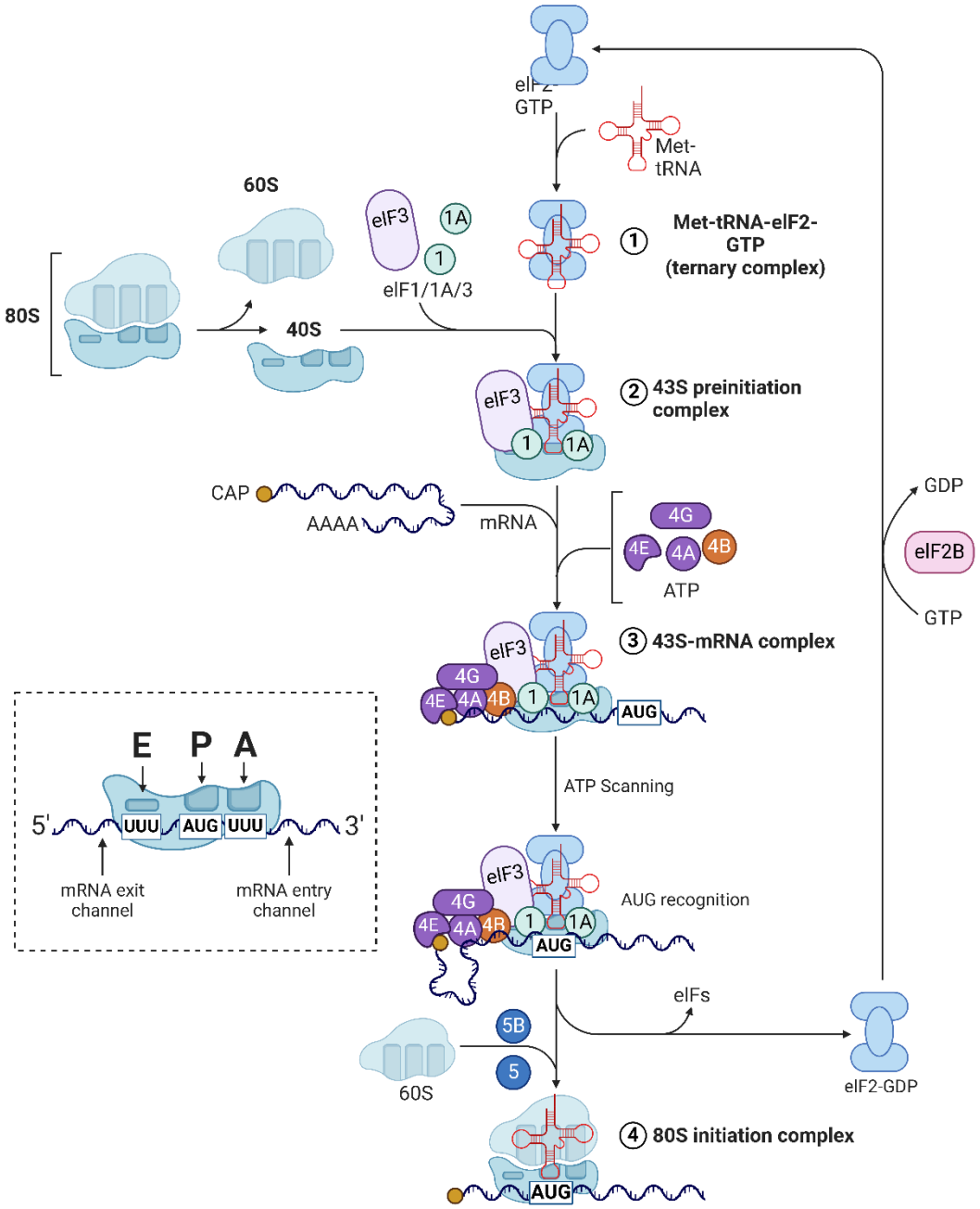


**Figure 1.11**: **Scheme of the Cap-dependent translation mechanism.** In the diagram, each coloured bubble represents a specific component involved in eukaryotic translation initiation. The purple bubbles (eIF4E, eIF4G, eIF4A, eIF4B) indicate the eIF4F complex and associated factors responsible for recognizing the mRNA 5' cap and unwinding secondary structures to facilitate ribosome binding and scanning. Green bubbles (eIF1, eIF1A) mark initiation factors that play a crucial role in scanning the mRNA for the start codon and ensuring accurate start site selection. The light blue bubbles denote the eIF3 complex, which stabilizes the preinitiation complex and recruits other initiation factors and the 40S ribosomal subunit. The pink bubble highlights eIF2B, a guanine nucleotide exchange factor essential for

recycling eIF2 by exchanging GDP for GTP. Orange bubbles specifically represent eIF4B, which assists eIF4A in unwinding mRNA. The blue ribosomal subunits (40S and 60S) illustrate the assembly of the functional 80S ribosome, and the red structure shows the initiator methionyl-tRNA (Met-tRNA), emphasizing its central role in initiating translation. Figure adapted from[43].

For most eukaryotic mRNAs, the canonical mode of translation initiation begins with the binding of the mRNA 5′ m7G cap structure to a protein complex known as eukaryotic initiation factor 4F (eIF4F) (**Figure 1.11**). This cap-binding complex consists of three proteins: (i) eIF4E, the cap-binding protein; (ii) eIF4G, a scaffolding protein that bridges the mRNA and the 40S ribosome by interacting with 40S-bound eIF3; and (iii) eIF4A, an ATP-dependent helicase that unwinds secondary structures in the 5′-UTR of the mRNA[44].

Following the binding of eIF4F to the mRNA, the 40S ribosomal subunit and its associated initiation factors are recruited, forming the 43S pre-initiation complex (PIC). This complex is is composed of (i) the 40S ribosomal subunit, (ii) a ternary complex (TC) consisting of eIF2, methionine-charged initiator tRNA (Met-tRNAi), and GTP, (iii) the multi-subunit initiation factor eIF3, which bridges the 40S ribosome and mRNA-bound eIF4G, and (iv) initiation factors eIF1 and eIF1A, which facilitate start codon recognition[45].

Additionally, eIF4G at the 5′ end interacts with the PABPs bound to the 3′ end of the mRNA, forming a circular messenger ribonucleoprotein (mRNP)[46]. When eIF4G interacts with eIF3, a protein bridge is established between the mRNA and the PIC, promoting attachment of the 40S ribosome to the mRNA. After ribosome assembly at the 5′ end, the 43S PIC scans the single-stranded 5′-UTR, unwound by eIF4A, in search of the start codon[47].

The most common start codon is AUG[48], but alternative codons such as CUG, GUG, or UUG can also initiate translation, as discovered by Marilyn Kozak in 1997[49]. Upon recognition of the start codon, base pairing occurs between the start codon and the anticodon of Met-tRNAi, halting scanning by the PIC. At this point, eIF5 and eIF5B promote GTP hydrolysis on eIF2, resulting in displacement of initiation factors and binding of the 60S ribosomal subunit to form the functional 80S ribosome[50].

Once the 80S ribosome is assembled, elongation begins, synthesizing polypeptide chains in an N-terminal to C-terminal direction. The interface between the large and small ribosomal subunits creates three tRNA binding sites: the acceptor (A) binds incoming aminoacyl tRNAs, peptidyl (P) binds tRNAs carrying the growing polypeptide chain, and exit (E) sites releases dissociated tRNAs.

During elongation, Met-tRNAi is initially bound to the P site while an aminoacyl-tRNA complementary to the next codon binds to the A site. Protein synthesis proceeds through a process called translocation, where tRNAs and mRNA are moved relative to ribosomal binding sites in a GTP-dependent manner. As tRNAs exit from the P site, the ribosome translocates along the mRNA to position a new codon in the A site for subsequent aminoacyl-tRNA binding[51].

Translation terminates when the ribosome encounters one of three stop codons (UAG, UAA, or UGA) on the mRNA. Since no tRNAs have anticodons complementary to stop codons, no tRNAs enter the A site at this stage. Instead, termination factors facilitate hydrolysis of the bond between the polypeptide chain and tRNA in the P site, releasing the newly synthesized polypeptide into the cytoplasm. Finally, the small and large ribosomal subunits dissociate from both each other and from the mRNA, making them available for subsequent rounds of translation[52].

### 1.5.2.2 IRES-mediated translation initiation

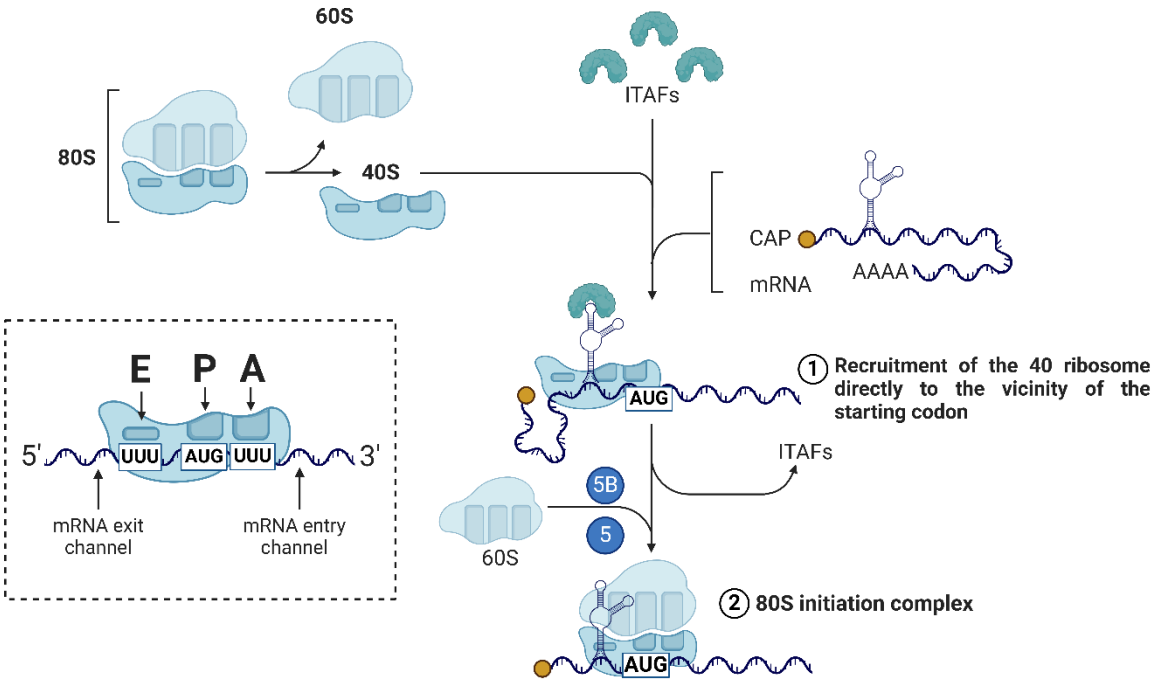


**Figure 1.12**: **Scheme of the IRES-mediated translation mechanism.** In this diagram, the light blue bubbles represent the ribosomal subunits (40S and 60S) that assemble to form the functional 80S ribosome during translation initiation. The yellow bubble marks the 5' cap structure on the mRNA, which is essential for ribosome recruitment. Green bubbles indicate ITAFs (IRES trans-acting factors), which assist in guiding the 40S ribosomal subunit directly to the vicinity of the start codon (AUG) on the mRNA. The process is depicted in two main steps: first, the recruitment of the 40S ribosomal subunit to the start codon region, facilitated by ITAFs and the 5' cap; and second, the joining of the 60S subunit to form the 80S initiation complex. The inset highlights the ribosomal E, P, and A sites, showing the mRNA entry and exit channels as the ribosome reads the coding sequence. Figure adapted from[43].

The internal initiation of translation is mediated by Internal Ribosome Entry Site (IRES) sequences (**Figure 1.12**). IRESs are specific regulatory elements, often containing stem-loops and pseudoknots, located within the 5’ untranslated regions (5’ UTRs) immediately upstream of the initiation codon of the mRNA[44]. These sequences enable the direct recruitment and binding of the 40S ribosomal subunit near the initiation codon, bypassing the need for the canonical mechanisms and transcription factors required for cap-dependent translation of 5’ m7G-capped mRNA transcripts[53].

Cellular IRESs are thought to perform two major physiological functions: (i) Supporting low levels of translation in mRNAs with highly structured 5’ UTRs under normal

physiological conditions when cap-dependent translation is fully active and (ii) facilitating translation of cellular mRNAs when cap-dependent translation is compromised due to various physiological stresses[54].

IRES structures were first identified in the late 1980s in viruses from the *Picornaviridae* family, such as poliovirus (PV) and encephalomyocarditis virus, through bicistronic assays[55]. These studies demonstrated an alternative mode of translation initiation that operates under conditions where cap-dependent initiation is severely impaired. Since this discovery, IRESs have been identified in many other viral families and in cellular mRNAs[56–58].

Despite extensive research, the precise cellular mechanisms underlying IRES-mediated translation initiation remain unclear. It is believed that IRES-mediated translation utilizes some components of canonical cap-dependent translation, such as eukaryotic initiation factors (eIFs) and the 40S ribosomal subunit[59]. However, how the 40S ribosomal subunit interacts with the IRES and the specific roles of eIFs in this process are not yet fully understood. Some studies suggest that these interactions enable proper positioning of the initiation codon at the ribosomal P-site without requiring prior scanning of the 5' UTR[60].

A key factor in regulating IRES-mediated translation is the involvement of Internal Initiation Trans-Acting Factors (ITAFs). These proteins, which belong to a group of heterogeneous nuclear ribonucleoproteins, shuttle between IRESs and components of the translational machinery. Their primary role is to bind to mRNA and act as RNA chaperones, maintaining the appropriate three-dimensional structure of the IRES to facilitate successful assembly of the 40S ribosomal complex[61].

IRES-driven translation initiation is preferentially utilized under conditions where cap-dependent initiation is compromised, such as during endoplasmic reticulum (ER) stress, hypoxia, nutrient deprivation, mitosis, or cellular differentiation[54,62]. Since many of these conditions are commonly observed in tumours, it is believed that IRES activity is elevated in tumour cells, contributing to their survival and adaptation under stress conditions.

## 1.6 *c-myc* gene

The *c-myc* gene is a well-known proto-oncogene that plays a central role in regulating cell growth, proliferation, metabolism, and apoptosis. It was first identified in 1979 by Bishop and Varmus during their study of the avian myelocytomatosis virus (MC29), a retrovirus that induces myeloid leukemia in chickens[63]. Their research revealed that a cellular gene, later named *c-myc*, acted as an oncogene capable of transforming normal cells into cancerous cells.

In humans, the *c-myc* gene is located on chromosome 8 (8q24.21) and spans approximately 7 kilobases (kb). It encodes a 62 kDa oncoprotein composed of 439 amino acids, which belongs to the basic helix-loop-helix leucine zipper (bHLH-LZ) family of transcription factors. This protein contains functional domains that regulate a cascade of downstream targets, influencing processes such as cell proliferation, transformation, and apoptosis[64]. Studies suggest that c-Myc is overexpressed in approximately 70% of human cancers[65,64].

The c-Myc protein consists of two different functional domains. At the N-terminus, the transactivation domain (TAD) interacts with coactivators and other transcription factors to activate gene expression. At the C-terminus, the helix-loop-helix and leucine zipper domain facilitates dimerization with its partner protein MAX and enables binding to specific DNA motifs.

To fold and become transcriptionally active, c-Myc must heterodimerize with MAX, another transcription factor from the same protein family. This interaction forms the **c-**Myc/MAX complex, which is essential for its function[66]. Once active, the complex binds to specific DNA sequences known as Enhancer-boxes (E-boxes) (**Figure 1.13**). These palindromic sequences, typically represented by the canonical motif CACGTG, serve as protein-binding sites for transcription factors to initiate gene transcription.

Upon binding to chromatin, c-Myc regulates the transcription of both protein-coding and non-coding RNAs through RNA Polymerase I, RNA Polymerase II, and RNA Polymerase III. This broad regulatory activity underscores its critical role in cellular function and its frequent dysregulation in cancer[67].

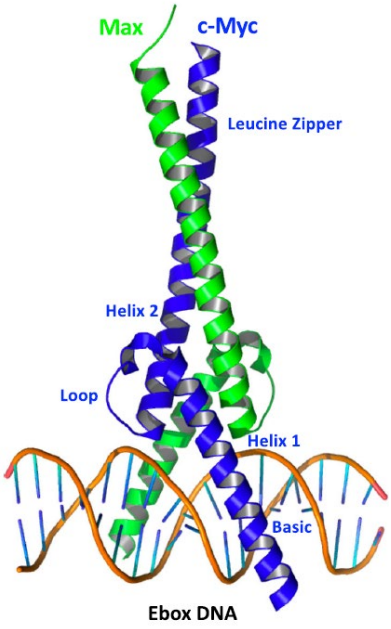


**Figure 1.13**: **Crystal structure of the c-Myc/MAX dimer bound to E-box DNA.** Figure adapted from[64].

In addition to its role in gene regulation, c-Myc plays a significant role in the regulation of key post-transcriptional mechanisms, both directly and indirectly. These functions include: (i) promoting mRNA capping, (ii) regulating the transcription of various splicing factors, (iii) indirectly influencing several pathways of RNA degradation, (iv) promoting translation and ribosome biogenesis, and (v) transcriptionally modulating microRNAs and long non-coding RNAs[67].

The c-Myc protein is also critically involved in cell proliferation by facilitating the transition from the G1 to the S phase of the cell cycle. This transition promotes DNA replication and mitosis. c-Myc achieves this by inducing the expression of cyclins (e.g., cyclin D1 and cyclin E), cyclin-dependent kinases (CDKs), and E2F transcription factors while repressing cyclin-dependent kinase inhibitors such as p21 and p27[68].

Despite its essential role in promoting cell growth and proliferation, c-Myc also has a pro-apoptotic function when its growth-promoting signals are not accompanied by survival signals. Under normal conditions, this apoptotic function is tightly regulated. However, overexpression of c-Myc sensitizes cells to apoptotic signals, potentially leading to uncontrolled cell death. This dual role underscores c-Myc's critical involvement in maintaining cellular homeostasis and highlights its dysregulation as a hallmark of cancer progression[69].

### 1.6.1 c-Myc Isoforms

The c-Myc protein exists in multiple isoforms, which arise from alternative splicing, alternative promoter usage, or post-translational modifications[70]. The most common isoform is the full-length c-Myc (also known as c-Myc1, p67/p64), which contains the two essential functional domains: the transactivation domain (TAD) and the basic helix-loop-helix leucine zipper domain (bHLH-LZ). This isoform plays dual roles in regulating cellular processes, exhibiting both pro-apoptotic and pro-proliferative activities depending on the cellular environment. Overexpression of the full-length c-Myc is a hallmark of various cancers, including breast cancer, colon cancer, lung cancer, lymphomas, and leukemia[71].

The short form of c-Myc, referred to as p64, is generated through alternative splicing. This isoform lacks a portion of the N-terminal transactivation domain, resulting in reduced pro-apoptotic activity while retaining its pro-proliferative role. In cancer, p64 supports tumour growth by promoting proliferation and increasing resistance to apoptosis[72].

ΔMyc (Delta Myc) is an isoform produced through alternative promoter usage or splicing and lacks significant portions of the N-terminal transactivation domain. This isoform competes with full-length c-Myc for binding to target E-boxes but is unable to activate transcription. As a result, ΔMyc may act as a natural dominant-negative regulator, modulating the activity of full-length c-Myc under specific conditions[73].

Finally, the c-Myc2 (p61) results from translation initiation at an alternative internal site on the MYC mRNA. This shorter isoform also lacks part of the N-terminal transactivation domain. Similar to p64, p61 retains the ability to bind DNA and interact with Max but exhibits reduced transcriptional activation capacity. Despite this limitation, p61 contributes to tumorigenesis by promoting cell proliferation while reducing susceptibility to apoptosis[74].

### 1.6.2 *c-myc* IRES

The IRES in the *c-myc* mRNA is a specific structural element located within the 5' UTR that facilitates direct ribosome binding and translation initiation, particularly under conditions where traditional cap-dependent translation is impaired[75,76].

The complex secondary structure of the *c-myc* IRES plays a critical role in this process and is composed of stem-loops and hairpin regions. These structural features are organized into functional domains that promote the recruitment of the small ribosomal subunit (40S) and facilitate translation initiation[76].

Using chemical probing data, Le Quesne et al. predicted the RNA structure of the *c-myc* IRES (**Figure 1.14**). Their findings suggest that the IRES can be divided into two distinct structural domains linked by a long unstructured region[77].

Domain 1 is located near the 5' end of the mRNA. this region contains a GNNRA apical loop and an overlapping double pseudoknot motif. This stem-loop is involved in the initial binding of internal initiation trans-acting factors (ITAFs) and serves as a landing site for the ribosome. Domain 2 is situated downstream and includes an apical AUUU loop that stabilizes the overall structure and ensures proper positioning of the ribosome for translation initiation[77,78].

The dynamic nature of the IRES allows it to adopt different conformations depending on the physiological state of the cell. For instance, during apoptosis or cellular stress, structural rearrangements make the IRES more accessible to the translational machinery, ensuring sustained production of c-Myc protein under these conditions. The predicted structure of the *c-myc* IRES is illustrated in.

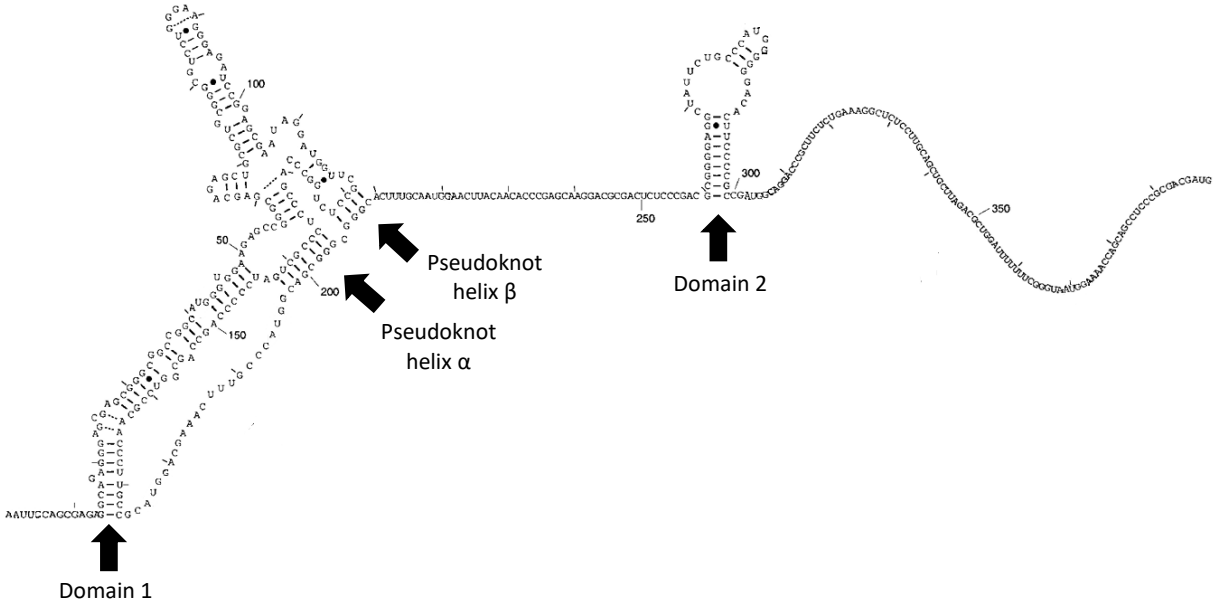


**Figure 1.14: Secondary structure of the human *c-myc* IRES.** The diagram highlights key structural and functional features: Domain 1 forms a large stem-loop at the 5' end; Pseudoknot helices α and β are indicated and are critical for tertiary structure and function; Domain 2 is a smaller stem-loop downstream of Domain 1**.** Figure adapted from[77].

### 1.6.3 *c-myc* and cancer

The oncoprotein c-Myc plays a pivotal role in the regulation of tumorigenesis across a wide range of human cancers. One of the most common characteristics of cancer cells is the aberrant activation of the c-Myc oncogene. This dysregulation can result from various genetic alterations, including gene amplification, chromosomal translocation, or increased transcriptional activation through upstream signalling pathways. Such alterations lead to uncontrolled cell proliferation, metabolic reprogramming, inhibition of differentiation, and evasion of apoptosis[67].

Overexpression of c-Myc enhances its interaction with lower-affinity E-boxes, driving excessive cell proliferation and growth that would not occur under normal physiological conditionsn[79,64]. Elevated levels of c-Myc protein are not only critical for tumour initiation and progression but are also essential for tumour maintenance[67].The deregulation of c-Myc is often associated with aggressive disease and resistance to therapy, underscoring the urgent need to develop therapeutic strategies targeting this pathway.

Recent studies have identified the translation of *c-myc* mRNA as a potential Achilles' heel for cancer treatment. Approaches to treating c-Myc-deregulated cancers can be categorized into five main strategies: (i) targeting *c-myc* transcription; (ii) targeting *c-myc* mRNA translation; (iii) targeting c-Myc protein stability; (iv) disrupting the c-Myc–MAX interaction; (v) blocking c-Myc accessibility to downstream target genes[80].

Evidence from mouse models has demonstrated that genetic elimination of c-Myc function can induce complete and irreversible tumour regression, highlighting its potential as a therapeutic target despite the challenges involved[66]. Furthermore, recent studies have shown that inhibition of the translation initiation factor eIF4A, a helicase required to unwind the 5' UTRs of highly structured mRNAs such as *c-myc*, resulted in long-term anti-tumour activity in a mouse model of APC-deficiency-driven colorectal cancer[81]. In contrast, inhibition of upstream signalling pathways driving *c-myc* expression proved less effective due to feedback mechanisms that bypassed drug effects.

These findings suggest that directly targeting *c-myc* translation or its associated machinery may offer a more effective therapeutic approach for treating cancers characterized by c-Myc dysregulation.

## 1.7 Antisense Oligonucleotides (ASOs)

An antisense oligonucleotide (ASO) is a short, single-stranded, chemically modified DNA-like molecule, typically 17–30 nucleotides in length, that selectively hybridizes to complementary sequences in target mRNA through Watson-Crick base pairing[73]. This approach was first demonstrated in 1978 by Zamecnik and Stephenson, who used an oligonucleotide complementary to the 3' end of the Rous sarcoma virus to inhibit viral expression in chicken fibroblasts[74].

The formation of an ASO–mRNA heteroduplex can lead to the redirection of splicing or inhibition of protein synthesis through various mechanisms. The first mechanism involves RNase H-mediated degradation of mRNA. In this process, DNA-based oligonucleotides hybridize with the target mRNA, forming an RNA-DNA heteroduplex. This hybrid activates RNase H, which cleaves the RNA strand within the duplex, leading

to degradation of the mRNA[82]. The second mechanism, known as steric block or steric hindrance, relies on the hybridization of ASOs with the target RNA to form an RNA-DNA heteroduplex. This duplex physically obstructs the translation machinery, preventing mRNA translation without degrading the RNA[83].

ASOs can also be designed to modulate splicing by binding to specific splice sites and either blocking or enhancing splice site recognition. This approach can promote exon skipping or exon inclusion[84].

In recent years, chemically modified ASOs have gained significant attention as potential therapeutics. Chemical modifications are employed to improve various drug-like properties, including enhanced in vivo stability, improved tissue distribution, increased RNA affinity, and greater bioavailability[85]. Based on these modifications, ASOs are classified into three generations:

In first-generation ASOs, the phosphate backbones were chemically modified to enhance the stability and bioavailability of the sequences. The most common modification in this generation is the phosphorothioate (PS) backbone, introduced by Fritz Eckstein[86]. In this modification, one of the non-bridging oxygen atoms in the phosphodiester bond is replaced with sulphur, creating PS[87] **(Figure 1.15)**.

Phosphorothioate modifications can be incorporated during solid phase phosphoramidite synthesis by substituting the oxidation step with a sulfurization step. Several sulfurization reagents, such as 3-ethoxy-1,2,4-dithiazoline-5-one (EDITH) or [(Dimethylaminomethylene)amino]-3H-1,2,4-dithiazole-5-thione (DDTT), are commercially available for this purpose.

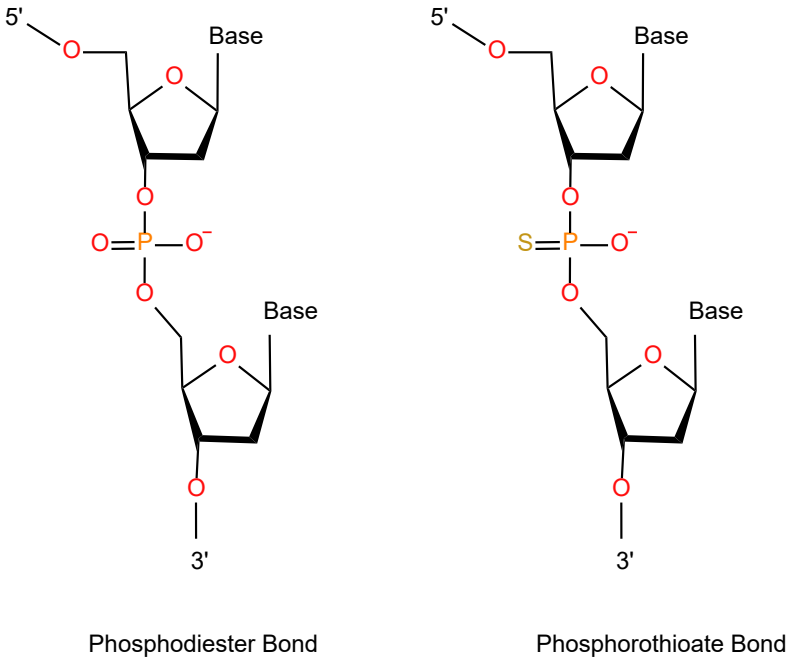


**Figure 1.15**: **Representation of phosphorothioate bond and a phosphodiester linkage.**

During the chemical synthesis of PS oligonucleotides, a random mixture of two diastereomers, Rp and Sp, is produced. This occurs because the substitution of one non-bridging oxygen atom in the phosphate group with a sulphur atom is non-specific, introducing a new stereocenter at each phosphorus atom[88]. These diastereomers differ in the positioning of the sulphur atom relative to the molecule: Rp indicates sulphur in the "pro-R" position, while Sp indicates sulphur in the "pro-S" position. The two conformations exhibit distinct biological properties: studies suggest that Rp enhances hybrid stability with RNA and increases RNase H activity, whereas Sp analogues demonstrate greater resistance to nuclease degradation[89].

The PS linkage increases the hydrophobicity of the ASO backbone, reducing nuclease binding and catalysis efficiency. This enhances resistance to nuclease digestion, improves cellular uptake, and prolongs the half-life of ASOs in biological systems[90]. The primary mechanism of action for PS ASOs involves RNase H-mediated degradation. Upon hybridization with complementary RNA, an RNA-DNA heteroduplex forms, activating RNase H to degrade the RNA target, thereby downregulating protein synthesis[91]. However, a significant limitation of PS-modified ASOs is their potential toxicity due to non-specific binding to proteins or unintended RNA sequences[92].

To address the limitations of first-generation PS ASOs, second-generation ASOs were developed with modifications at the 2′ position of the ribose sugar **(Figure 1.16)**. These modifications include replacing the hydrogen at the 2′ position with methoxyethyl or methyl groups, leading to 2′-O-methyl (2′-OME) and 2′-O-methoxyethyl (2′-MOE) modifications. These changes induce an RNA-like C3′-endo conformation in the oligonucleotide, increasing its binding affinity for complementary sequences[93].

Unlike first-generation ASOs, second-generation ASOs do not recruit RNase H due to their structural similarity to RNA. Instead, they function by sterically blocking translation or splicing without degrading the target RNA. However, by incorporating a gapmer design—where central DNA segments are flanked by modified ribose sugars—second-generation ASOs can retain RNase H-mediated degradation capability. These ASOs exhibit reduced toxicity compared to PS-modified ASOs and demonstrate slightly higher affinity for their targets[91].

The second generation of ASOs offers several advantages over the first generation. The 2′-O modifications significantly enhance stability and binding affinity, resulting in improved potency and reduced off-target effects. Additionally, these modifications contribute to better pharmacokinetics, including prolonged circulation times and improved tissue distribution[94].

Third-generation ASOs are more heterogeneous and include a variety of chemical modifications aimed at further improving specificity, stability, and therapeutic potential. The most common third-generation ASOs include Peptide Nucleic Acids (PNAs), Morpholinos, and Locked Nucleic Acids (LNAs) **(Figure 1.16)**:

- Peptide Nucleic Acid (PNA): PNAs are nucleic acid analogues in which the ribose-phosphate backbone is replaced by a neutral polyamide backbone composed of N-(2-aminoethyl) glycine units linked to nucleobases. The absence of electrostatic repulsion increases binding affinity to complementary DNA or RNA, resulting in highly stable duplexes. PNAs inhibit both transcription and translation[79] through steric hindrance rather than RNase H cleavage because PNA-DNA or PNA-RNA hybrids are not substrates for RNase H[95]. Advantages include resistance to enzymatic degradation and low toxicity, which extends

their half-life in biological systems[96]. However, PNAs face challenges such as poor cellular uptake and limited tissue distribution due to their neutral backbone charge[97].

- Morpholino: Morpholinos replace the natural sugar moiety of DNA or RNA with a morpholine ring and substitute the charged phosphodiester linkage with an uncharged phosphoramidate linkage. These modifications enhance resistance to nucleases and proteases while maintaining high specificity for molecular targets, minimizing off-target effects and demonstrating low toxicity in vivo[95]. Morpholinos have broad therapeutic potential for blocking viral replication, silencing disease-causing genes, and modulating splicing in genetic disorders[98]. However, their lack of charge complicates cellular transfection as they do not readily form complexes with conventional lipid-based delivery agents and exhibit limited interaction with cell surface proteins[99].

- Locked Nucleic Acids (LNA): LNAs feature a methylene bridge connecting the 2' oxygen and 4' carbon of ribose, locking the sugar into a rigid C3'-endo conformation that enhances binding affinity for complementary strands. This locked structure increases local organization within the phosphate backbone while reducing ribose flexibility, resulting in higher melting temperatures (Tm) for hybridized duplexes[100]. LNAs are resistant to nuclease degradation and do not recruit RNase H due to their structural similarity to RNA[101]. Their rigidity also minimizes secondary structure formation, reducing off-target effects[102].

  LNAs are widely used in antisense therapies for gene silencing via steric blocking[103] or target mRNA degradation when incorporated into gapmers[104]. Due to their high specificity and affinity, LNAs are also employed in diagnostic applications such as fluorescence in situ hybridization (FISH) and quantitative PCR (qPCR) for detecting specific DNA or RNA sequences, including single nucleotide polymorphisms (SNPs)[105]. Additionally, LNAs are used as antagomirs—oligonucleotides designed to bind and inhibit microRNAs implicated in diseases such as cancer or cardiovascular disorders[106].

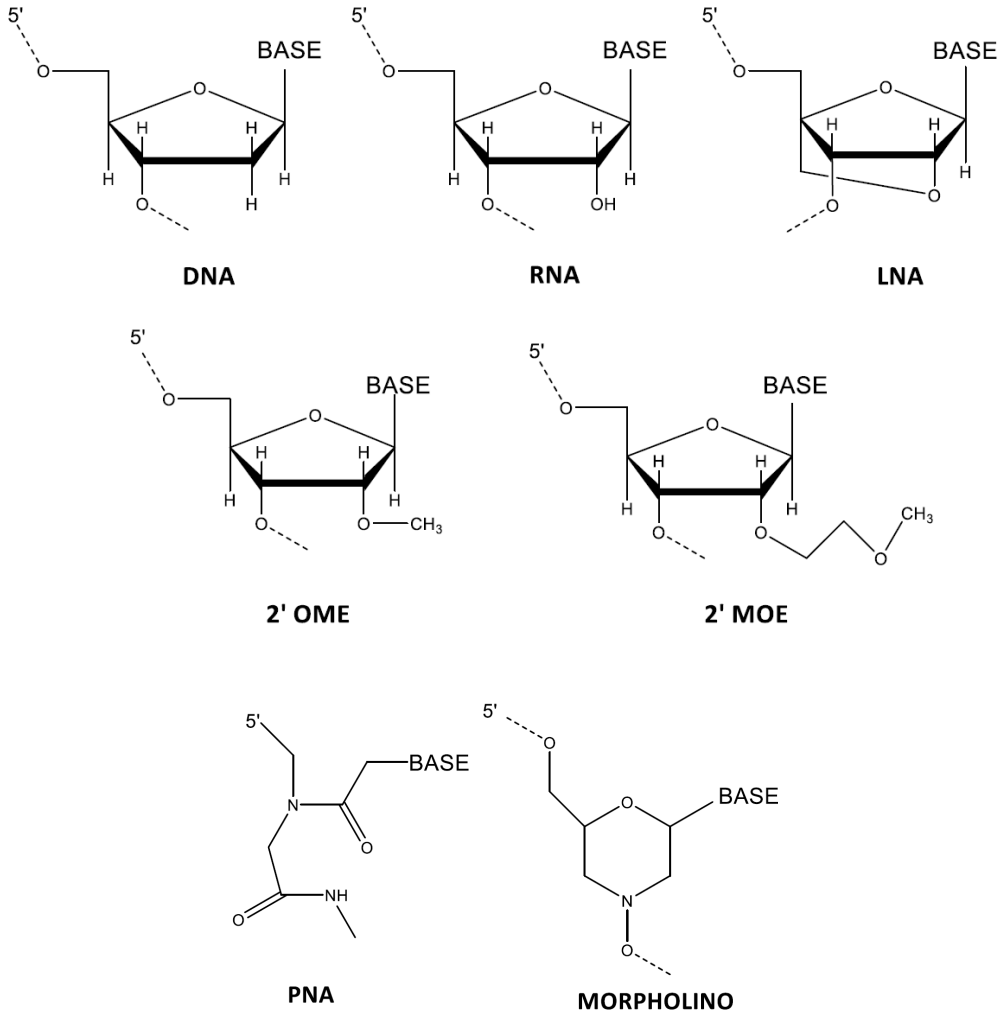


**Figure 1.16: Chemical structure of DNA, RNA, LNA 2'-OME, 2'-MOE, PNA and Morpholino nucleosides.**

## 1.7.1 Design of antisense oligonucleotides therapies

The design of ASOs is a multi-step process focused on maximizing efficacy, specificity, and safety for therapeutic applications.

The process begins with the identification of an RNA target, which may be a specific gene transcript or a non-coding RNA. Once the target is identified, the next step involves determining the specific region of the sequence to target, such as coding sequences, UTRs, or intron-exon junctions (for splicing modulation). The choice of the target region depends on the desired mechanism of action. For example, constructs

designed to modulate protein translation may target the start codon or sequences involved in ribosome recruitment (e.g., IRES or the m7G), while those aimed at altering RNA stability may focus on regions near cleavage and polyadenylation sites[107].

Computational tools are used to predict the secondary structure of the target RNA. ASOs are most effective when they bind to accessible regions, such as loops or single-stranded segments, which are more amenable to hybridization [108].

ASOs are typically designed to be 15–25 nucleotides in length. Shorter ASOs tend to have improved specificity and delivery properties, while longer ASOs may have higher binding affinity but increased risk of off-target effects and unwanted secondary structure formation. Bioinformatics tools (e.g., BLAST, RNAhybrid) are employed to ensure sequence specificity and minimize off-target hybridization[109].

Chemical modifications are introduced to enhance ASO stability and affinity. For example, PS linkages are used to modify the backbone, making ASOs resistant to nuclease degradation[110]. Additional modifications can be made to the sugar moiety, such as 2'-OME, 2'-MOE[111], or LNA[112] to improve binding affinity and nuclease resistance.

For ASOs intended to recruit RNase H, a gapmer structure is often used. This consists of a central DNA segment (typically 8–10 nucleotides) flanked by chemically modified nucleotides. The central gap enables RNase H-mediated degradation of the target RNA upon hybridization[113].

One of the main challenges in antisense therapy is efficient delivery of ASOs into cells to achieve therapeutic effects. Several strategies have been developed to improve cellular uptake: gold nanoparticles (AuNPs)[114], lipid nanoparticles (LNPs)[115] and conjugation with cell-penetrating peptides (CPPs)[116]. Additionally, ASOs can be conjugated with molecules that direct them to specific tissues or cell types. For instance, GalNAc-ASO conjugates efficiently deliver ASOs to hepatocytes in the liver[117].

By combining precise design strategies with advanced delivery methods, ASOs hold significant potential for treating a wide range of diseases through targeted gene regulation.

### 1.7.2 Toxicology of antisense oligonucleotides therapies

The toxicology of ASOs is a critical area of research, as their administration can lead to toxicity through various mechanisms, including immune system activation, off-target binding, and organ-specific toxicities. Proper ASO design, with careful consideration of key toxicological factors, is essential to minimize these adverse effects[118].

The majority of toxic effects associated with ASOs are related to their chemical modifications. For instance, PS linkages can result in nonspecific protein binding, which may lead to complement activation, platelet activation, and altered coagulation. These effects can manifest as thrombocytopenia and inflammation[119]. Similarly, sugar modifications such as 2'-OME and 2'-MOE have been linked to increased hepatotoxicity and nephrotoxicity. LNAs, due to their stronger binding affinities, are associated with higher toxicity[94].

Additionally, the use of gapmers can contribute to toxicity through off-target RNase H activation. This unintended degradation of non-target mRNA can induce cellular stress and apoptosis, further exacerbating toxicity[120].

ASOs are amphipathic molecules with hydrophobic nucleobases and hydrophilic phosphate groups that allow interactions with various serum and cell-surface proteins. These interactions can disrupt cellular pathways, resulting in unintended toxic effects. Additionally, off-target binding to RNA sequences may lead to unintended gene silencing or splicing modulation[121].

A common toxic effect associated with ASOs is the activation of the immune system. ASOs containing unmethylated CpG motifs can be recognized by toll-like receptors (TLRs), particularly TLR9, triggering the innate immune response. This activation can lead to B-cell proliferation and the release of pro-inflammatory cytokines, resulting in systemic inflammation, fever, and severe immune reactions[122].

Additionally, the incorporation of PS backbones can activate the complement system. This activation is characterized by an increase in inflammatory cytokine levels and, in severe cases, may lead to systemic immune responses or tissue damage[123].

From a clinical perspective, certain organs are particularly susceptible to toxicity induced by ASOs. The liver is a primary site of ASO clearance, and excessive accumulation can result in hepatotoxicity, characterized by oxidative stress, mitochondrial dysfunction, or apoptosis[124].

The kidneys also play a significant role in ASO clearance. Accumulation of ASOs in the proximal tubules of the kidneys can lead to glomerular damage, tubular necrosis, or proteinuria[125]. Nephrotoxicity and thrombocytopenia are commonly associated with ASOs containing PS linkages. Thrombocytopenia (low platelet count) occurs when ASOs interact with platelet surface proteins, forming immune complexes that promote platelet clearance[126].

In some cases, ASOs may also exhibit cardiotoxicity, particularly when targeting genes involved in cardiovascular function. This toxicity is often mediated through inflammation and immune activation[127].

ASO toxicity is generally dose-dependent and linked to long-term exposure. Higher doses or chronic administration can result in tissue and organ accumulation, leading to increased toxicity[128]. This phenomenon is especially pronounced with phosphorothioate-modified ASOs, which exhibit slow clearance from tissues due to their resistance to nuclease degradation[124].

To mitigate these toxic effects and enhance therapeutic outcomes, the development of ASOs requires rigorous evaluation through specific in vitro and in vivo toxicity studies as well as clinical monitoring during trials. Strategies include optimizing chemical modifications to improve specificity and reduce off-target effects while minimizing immune activation and organ-specific toxicity.

By addressing these challenges through improved design and comprehensive testing protocols, the therapeutic potential of ASOs can be maximized while minimizing adverse effects.

### 1.7.3 FDA and EMA approved ASO therapies

The U.S. Food and Drug Administration (FDA), a federal agency within the Department of Health and Human Services, and the European Medicines Agency (EMA) are

responsible for protecting public health by regulating and overseeing the safety, efficacy, and quality of various products. In 2024, FDA and EMA-approved ASOs therapies represent groundbreaking advancements in targeting rare genetic diseases[129].There are currently 15 approved ON therapeutics by the FDA and 12 by EMA, excluding 5 COVID-19 vaccines[130]. Below is an overview of these therapies[131]:

*Fomivirsen* (*Vitravene*) was the first ASO therapy approved by the FDA in 1998 and by the EMA in 1999. It is a 21-nucleotide phosphorothioate oligonucleotide with a CpG motif near the 5' end. This therapy is indicated for the treatment of cytomegalovirus (CMV) retinitis in immunocompromised patients. It works by binding to viral mRNA and inhibiting CMV replication[132].

*Mipomersen* (*Kynamro*) was FDA-approved in 2013. This sequence is a 20-nucleotide gapmer with 2'MOE modifications at positions 1–5 and 15–20. It treats homozygous familial hypercholesterolemia (HoFH) by targeting apolipoprotein B-100 (ApoB-100) mRNA, reducing its production and lowering LDL cholesterol levels[133].

*Eteplirsen* (*Exondys 51*) was FDA-approved in 2016. This drug is a 30-mer phosphorodiamidate morpholino oligomer (PMO) designed to promote exon 51 skipping in the dystrophin gene. This enables the synthesis of a truncated but partially functional dystrophin protein, making it an effective treatment for Duchenne muscular dystrophy (DMD) in patients with specific exon 51 skipping mutations[134].

*Nusinersen* (*Spinraza*) was FDA-approved in 2016 and by the EMA in 2017. This ASO is a 19-mer ASO with phosphorothioate linkages and 2'-O-methoxyethyl modifications. It modifies splicing of the SMN2 gene to increase functional SMN protein production, offering treatment for spinal muscular atrophy (SMA). This is one of the most commercially successful ASO therapies[135].

*Inotersen* (*Tegsedi*) was FDA and EMA-approved in 2018 . Inotersen is a 20-nucleotide ASO with phosphorothioate and 2'-MOE modifications, complementary to transthyretin (TTR) mRNA. It triggers RNase H1-mediated degradation of TTR mRNA, reducing wild-type and mutant TTR protein production in the liver to treat hereditary transthyretin amyloidosis (hATTR) and prevent amyloid deposits[136].

*Golodirsen* (*Vyondys 53*) was FDA-approved in 2019. This ASO is a 21-nucleotide PMO that induces exon 53 skipping in the dystrophin gene, enabling the production of a truncated but partially functional dystrophin protein for treating **DMD** in patients with specific exon 53 skipping mutations[137].

*Viltolarsen* (*Viltepso*) was FDA-approved in 2020. Viltolarsen is a 21-nucleotide PMO designed to promote exon 53 skipping, similar to Golodirsen, restoring partial dystrophin protein production for treating DMD in patients with exon 53 skipping mutations[138].

*Casimersen* (*Amondys 45*) was approved by the FDA in 2021. This drug is a 22-nucleotide PMO that induces exon 45 skipping to produce truncated but functional dystrophin protein, providing treatment for DMD in patients with exon 45 skipping mutations[139].

In addition to traditional ASOs, RNA interference (RNAi)-based therapies have emerged as highly specific and potent tools for reducing disease-causing gene expression:

*Givosiran* (*Givlaari*) was FDA-approved in 2019 and by the EMA in 2020. This drug is an RNAi therapeutic for treating acute hepatic porphyria (AHP). The siRNA sequence is chemically modified with 2'-OMe and 2'-fluoro (2'-F) groups to enhance stability and conjugated with N-acetylgalactosamine (GalNAc) for targeted delivery to hepatocytes[140]. It silences aminolevulinate synthase 1 (ALAS1) mRNA, reducing toxic porphyrin precursor accumulation that causes severe neurological and abdominal symptoms[141].

*Lumasiran* (*Oxlumo*) was approved by the FDA and the EMA in 2020. Lumasiran is a double-stranded siRNA chemically modified with 2'-OMe, 2'-F, and GalNAc for liver-specific delivery. It treats primary hyperoxaluria type 1 (PH1) by targeting HAO1 mRNA, which encodes glycolate oxidase, thereby reducing oxalate overproduction that leads to kidney damage[142].

These FDA-approved therapies illustrate significant advancements in leveraging antisense and RNAi technologies to target rare genetic diseases effectively while paving the way for future innovations in precision medicine. A summary of these therapies is provided in **Table 1.1**.

**Table 1.1: Overview of FDA and EMA-Approved ASO and RNAi Therapies for Rare Genetic Diseases as of 2024.** The table includes information on mechanisms, indications, and regulatory status.

| Therapy Name (Brand) | Approval Year (FDA/EMA) | Type/Structure | Target Disease/Indication | Mechanism of Action / Target mRNA |
|---|---|---|---|---|
| **Fomivirsen (Vitravene)** | 1998 / 1999 | 21-nt phosphorothioate ASO, CpG motif | CMV retinitis (immunocompromised patients) | Binds viral mRNA, inhibits CMV replication |
| **Mipomersen (Kynamro)** | 2013 / - | 20-nt gapmer, 2'MOE modifications | Homozygous familial hypercholesterolemia | Targets ApoB-100 mRNA, reduces LDL cholesterol |
| **Eteplirsen (Exondys 51)** | 2016 / - | 30-mer PMO | Duchenne muscular dystrophy (exon 51) | Exon 51 skipping in dystrophin gene |
| **Nusinersen (Spinraza)** | 2016 / 2017 | 19-mer ASO, phosphorothioate, 2'-O-methoxyethyl | Spinal muscular atrophy (SMA) | Modifies SMN2 splicing, ↑ SMN protein |
| **Inotersen (Tegsedi)** | 2018 / 2018 | 20-nt ASO, phosphorothioate, 2'-MOE | hATTR amyloidosis | RNase H1-mediated degradation of TTR mRNA |
| **Golodirsen (Vyondys 53)** | 2019 / - | 21-nt PMO | DMD (exon 53 skipping) | Exon 53 skipping in dystrophin gene |
| **Viltolarsen (Viltepso)** | 2020 / - | 21-nt PMO | DMD (exon 53 skipping) | Exon 53 skipping in dystrophin gene |
| **Casimersen (Amondys 45)** | 2021 / - | 22-nt PMO | DMD (exon 45 skipping) | Exon 45 skipping in dystrophin gene |
| **Givosiran (Givlaari)** | 2019 / 2020 | Chemically modified siRNA, GalNAc conjugate | Acute hepatic porphyria (AHP) | Silences ALAS1 mRNA |
| **Lumasiran (Oxlumo)** | 2020 / 2020 | Double-stranded siRNA, 2'-OMe, 2'-F, GalNAc | Primary hyperoxaluria type 1 (PH1) | Targets HAO1 mRNA |

## 1.8 Nanoparticles (NPs)

Nanoparticles (NPs) are the fundamental building blocks of nanotechnology and are generally defined as nanomaterials with diameters ranging from 1 to 100 nanometres. At the nanoscale, NPs exhibit unique and tuneable physical, chemical, and biological properties that distinguish them from their bulk counterparts at larger scales[143].

The size-dependent physicochemical characteristics of NPs, such as increased surface area, enhanced mechanical strength, optical activity, and heightened chemical reactivity, make them highly versatile and suitable for a wide range of applications across various scientific and technological fields[144].

### 1.8.1 Types of Nanoparticles

NPs are broadly categorized based on their morphology, size, and chemical properties. According to their physical and chemical characteristics, they are classified into six material-based categories[145]:

- Carbon based NPs: This category includes fullerenes, carbon nanotubes (CNTs), graphene, and carbon dots. These NPs have garnered significant commercial interest due to their exceptional electrical conductivity, high mechanical strength, unique structure, electron affinity, and versatility[146].
- Metal NPs: Metal nanoparticles are composed entirely of metal precursors. They exhibit unique optoelectrical properties due to localized surface plasmon resonance (LSPR) characteristics. The ability to control the size and shape of metal NPs makes them suitable for a wide range of biomedical applications, including anticancer therapies, radiotherapy enhancement, drug delivery, thermal ablation, antibacterial treatments, diagnostic assays, antifungal therapies, and gene delivery[147].
- Ceramic NPs: These nanoparticles are inorganic non-metallic solids composed of oxides, carbides, carbonates, or phosphates. They are synthesized through processes involving heat and subsequent cooling. Ceramic NPs are characterized by their high heat resistance and chemical inertness[148].

- Semi-conductor NPs: Semiconductor nanoparticles exhibit properties that lie between those of metals and nonmetals. Examples include GaN, GaP, InP, and InAs from group III-V; ZnO, ZnS, CdS, CdSe, and CdTe from group II-VI; as well as silicon and germanium from group IV[149].

- Polymeric NPs: These are organic-based nanoparticles that can take the form of nanocapsules or nanospheres depending on the synthesis method[150].

- Lipid NPs: Lipid nanoparticles are generally spherical in shape with a solid lipid core containing soluble lipophilic molecules. The external core is stabilized by surfactants or emulsifiers[151].

Among these categories, metal NPs are the most widely applied in engineering and material sciences. They can be synthesized using various techniques, including chemical, physical, or biological methods. The most common method for producing colloidal metal NPs is the chemical citrate reduction method, which involves reducing ionic metal species (in salt form) to their metallic state. This process consists of three essential steps: Reduction of metallic salts using reducing agents, stabilization of the ionic complexes, and size control through the use of capping agents[152]. The role of the capping agent is to prevent aggregation by maintaining separation between forming NPs.

Among metal NPs, gold (Au) and silver (Ag) NPs are the most widely utilized due to their unique properties:

- Gold Nanoparticles (Au NPs): Au NPs are non-toxic particles with large surface areas that can be easily functionalized with a wide range of organic molecules[153]. These characteristics make them highly versatile and suitable for numerous applications, including electrochemistry, drug delivery, diagnostics, and imaging.

- Silver Nanoparticles (Ag NPs): Ag NPs are of significant commercial interest due to their excellent conductivity, chemical stability, catalytic activity, and potent antimicrobial properties[154]. These attributes make them suitable for

applications similar to those of Au NPs, particularly in fields such as the food industry and biomedicine.

### 1.8.2 Localized Surface Plasmon Resonance (LSPR)

NPs exhibit the ability to interact with electromagnetic radiation, producing a valuable optical output through a phenomenon known as Localized Surface Plasmon Resonance (LSPR). This interaction results in the generation of a strong electric field near the surface of the NPs, which is maximized at the resonance frequency. The resonances associated with noble metal nanostructures produce sharp spectral absorption and scattering enhancements, making them widely applicable in sensing and biomedical fields[155].

LSPR occurs when light interacts with NPs that are significantly smaller than the incident wavelength. This interaction induces a localized plasmon, which oscillates around the nanoparticle at a specific frequency known as the LSPR frequency[156] (**Figure 1.17**). These are non-propagating excitations of conduction electrons in metallic NPs that are coupled to the electromagnetic field[157]. The LSPR condition is influenced by several factors, including the properties of the metal and its interface, the size and shape of the NPs, and the average distance between particles in a distribution.

For instance, spherical AuNPs with a diameter of 13 nm exhibit an LSPR peak around 520 nm, while AgNPs measuring 5–6 nm displays an LSPR peak near 400 nm. These size- and material-dependent properties make LSPR highly versatile for various applications in nanotechnology[158].

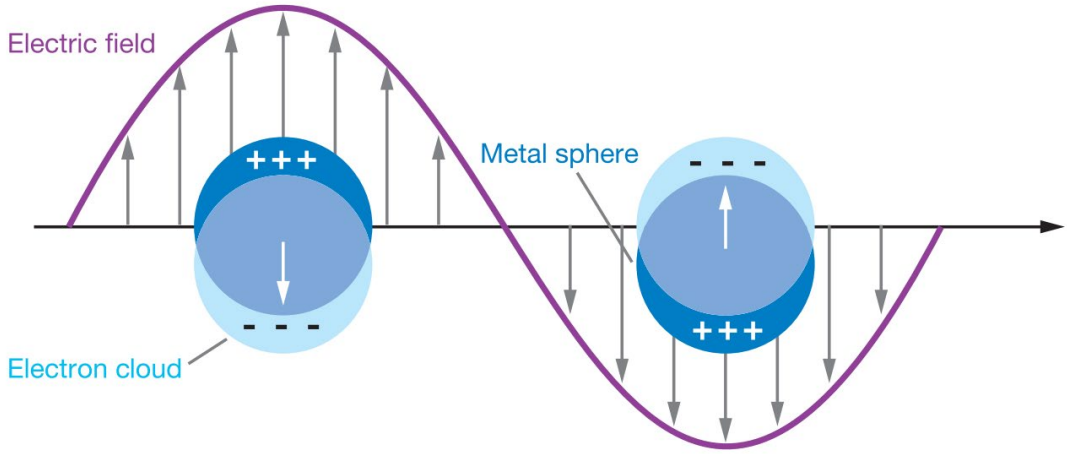


**Figure 1.17**: **Schematic diagram illustrating a localized surface plasmon**. When the oscillating electric field (purple wave) interacts with the metal sphere, it causes the electron cloud to shift relative to the positively charged ions, creating regions of positive and negative charge on opposite sides of the particle. This displacement induces collective oscillations of the electrons at a resonant frequency, which enhances the local electromagnetic field near the nanoparticle surface. Figure adapted from[156].

### 1.8.3 NPs as a Delivery Systems

Nanomedicine has emerged as a multidisciplinary field with applications in various areas of science, including medical imaging, tumour targeting, drug delivery, and biosensors[159]. The development of NPs as part of cancer therapeutics has given rise to a specialized area of research known as cancer nanomedicine. Compared to traditional anti-cancer drugs, NPs have been designed to overcome the limitations of free therapeutics by navigating biological barriers and minimizing undesirable side effects[160].

Cell-specific drug delivery is a critical aspect of nanoparticle-based drug delivery systems. This can be achieved through the functionalization of AuNPs with tumour-targeting ligands and therapeutic molecules[161]. Functionalization with biomolecules such as proteins, DNA, amino acids, and carboxylic acids has been widely employed in cancer therapy, providing an efficient platform for drug delivery[162].

One key feature influencing the efficiency of nanoparticle-based drug delivery is particle size. Studies have shown that reducing particle size from 50 nm to 15 nm decreases the accumulation of AuNPs in the liver and spleen. This size-dependent behaviour is linked to the reticuloendothelial system (RES), which preferentially

sequesters larger nanoparticles (>200 nm) in organs like the liver and spleen. Smaller nanoparticles (15 nm) exhibit reduced RES uptake, enabling prolonged recirculation and enhanced passive targeting of inflamed or malignant tissues through leaky vasculature[163].

Optimal recirculation and accumulation at inflamed or malignant sites are achieved with 15 nm AuNPs due to their ability to balance circulation time and tissue penetration. While very small nanoparticles (<10 nm) are rapidly excreted via renal clearance, 15 nm particles avoid both rapid elimination and excessive RES capture, allowing sufficient time for extravasation and retention in target tissues. This size also minimizes nonspecific organ accumulation, reducing potential toxicity in healthy tissues. The interplay between nanoparticle size, circulation half-life, and biodistribution highlights the importance of precise size control in designing effective drug delivery systems[161].

Moreover, the non-immunogenic and non-toxic nature of AuNPs, combined with their high permeability and enhanced retention effect, further supports their potential for effective accumulation and penetration at tumour sites, making them promising candidates for cancer therapy[164].

Despite their promising properties, non-functionalized AuNPs are unstable under normal physiological conditions. Research has shown that coating AuNPs with biopolymers significantly improves their stability and cellular uptake[165].

Polyethylene glycol (PEG), approved by the U.S. Food and Drug Administration (FDA), is one of the most commonly used agents for nanoparticle surface modification. PEGylation enhances nanoparticle stability due to its excellent hydrophilicity, biocompatibility, and non-fouling properties. By preventing aggregation and nonspecific protein adsorption in biological environments, PEGylation imparts "stealth" behaviour to NPs, reducing uptake by the reticuloendothelial system (RES) while enhancing circulation time[166–168].

PEGylation of AuNPs is typically achieved through covalent coating with thiolated PEG ligands. Thiols bind strongly to the gold surface via chemisorption, creating a stable PEG layer that improves nanoparticle performance under physiological conditions[169].

## 1.9 Objective and aims

The goal of this project is to develop novel approaches for antisense therapy to specifically modulate *c-myc* mRNA translation. The objective is to create a stable DNA/RNA hybrid at the targeted gene that can act as a molecular switch to either upregulate or downregulate *c-myc* expression. If successful, this strategy could provide a powerful tool for treating various cancers using a unified methodology, paving the way for personalized cancer therapy.

Personalized medicine in oncology is an emerging approach that tailors tumour treatment and prevention strategies based on inter- and intra-tumour variability in genetic profiles, tumour microenvironments (including immune factors), lifestyle factors, and comorbidities of individual patients[170].

The specific objectives of the project are:

- To design nanoparticle systems suitable for delivering ASOs sequences inside the cancerous cells allowing the hybridization with the molecular target.
- To develop modified antisense oligonucleotides targeting the *c-myc* IRES with the aim of either decreasing or increasing protein expression.
- To evaluate the effects of different oligonucleotide modifications on *c-myc* IRES activity *in vitro*, *in cellulo*, and *in vivo*.
- To establish an effective transfection protocol for delivering oligonucleotides into target cells.
- To assess the efficacy of the system in modulating other genes that utilize IRES elements for translation.

By achieving these objectives, this project aims to advance antisense therapy as a versatile and personalized approach for cancer treatment while exploring its broader applications in regulating other IRES-dependent genes.

# Chapter 2: Synthesis and characterization of the nano-delivery system

## 2.1 Synthesis of Nanoparticles

### 2.1.1 Design of Gold and Silver Nanoparticle-Based Drug Delivery Systems

The objective of achieving targeted delivery with controlled release of therapeutic agents will be addressed through the use of drug delivery systems. In this project, two distinct nanocarriers will be utilized: AgNPs and AuNPs. The aim is to synthesize multiple batches of NPs and evaluate how the unique properties of each material influence the overall performance of the delivery system.

AuNPs were synthesized using the Turkevich method, as described in **Section 5.2.2**, which is a well-established and reproducible technique known for producing uniform, spherical particles with diameters typically ranging from 10 to 30 nm[171]. In this method, sodium citrate functions not only as a reducing agent but also as a stabilizer and pH buffer. The citrate ions reduce gold ions ($Au^{3+}$) from chloroauric acid ($HAuCl_4$) to metallic gold ($Au^0$), initially through their own oxidation and subsequently via more potent reducing intermediates formed during the reaction. As the nanoparticles form, citrate molecules adsorb onto their surfaces via carboxylate groups, creating a negatively charged layer that stabilizes the colloidal suspension by electrostatic repulsion and prevents particle aggregation

According to the literature[163], AuNPs with a diameter of 15 nm exhibit optimal biodistribution, with enhanced recirculation and accumulation in organs such as the liver, spleen, lungs, and in pathological sites like inflamed or malignant tissues. Notably, accumulation in the liver and spleen diminishes as particle size increases beyond 15 nm. Based on these findings, 15 nm AuNPs were chosen as the primary candidate for our delivery system.

In addition to gold-based carriers, AgNPs were explored as a promising alternative due to their distinctive physicochemical properties, including high surface area, facile surface modification, and inherent antimicrobial activity[172]. The use of AgNPs as the core material offers a more cost-effective solution for the delivery of antisense oligonucleotides, leveraging their unique plasmonic characteristics for photoactivated release and their substantially lower synthesis costs compared to AuNPs[173]. AgNPs have demonstrated efficacy in a variety of biomedical applications, such as antimicrobial, anticancer, anti-inflammatory, and antiviral therapies[174]. Their versatility arises from their ability to interact with both hydrophilic and hydrophobic molecules, form stable conjugates with various ligands, and provide a high loading capacity for therapeutic agents[175]. Nonetheless, optimizing their performance requires careful control over parameters like particle size, shape, and colloidal stability, all of which can be finely tuned through synthetic protocols[176].

For AgNP synthesis, a modified Lee-Meisel method was employed as described in **Section 5.2.3**[177,178]. This method is recognized for its ability to produce stable, size-controlled silver colloids using sodium borohydride ($NaBH_4$) as a potent reducing agent and sodium citrate ($Na_3Cit$) as a stabilizer. Freshly prepared $NaBH_4$ solutions were used to maintain reducing efficiency, as the compound is sensitive to degradation from air and moisture.

Following synthesis, surface passivation was performed to minimize nonspecific interactions between nanoparticles and proteins, thereby enhancing their stability and biocompatibility, as detailed in **Section 5.2.4**[179]**.** In this study, citrate-coated AgNPs and AuNPs were passivated following a literature protocol[180]. Functionalization was achieved using thiol-polyethylene glycol (SH-PEG) molecules with a molecular weight of 0.8 kDa, corresponding to an approximate chain length of 17–18 ethylene glycol units and an extended length of about 6–7 nm.

The passivation process relies on the strong affinity of thiol groups for metal surfaces, resulting in the formation of robust covalent bonds with the nanoparticles. This interaction effectively displaces the more weakly bound citrate ions, ensuring a stable PEG coating[181].The introduction of PEGylated thiols enhances nanoparticle stability by

reducing aggregation and imparting steric hindrance through the flexible PEG chains[182–184].

PEGylation not only stabilizes the nanoparticles but also improves their pharmacokinetic profile. Notably, studies have shown that 24 hours post-administration, 15 nm PEG-coated AuNPs exhibit the highest concentration of gold in the bloodstream[185]. This increased circulation time enhances the probability of nanoparticle accumulation in organs of the reticuloendothelial system (RES) as well as in inflamed or malignant tissues[163].

To achieve effective surface passivation and enable subsequent oligonucleotide conjugation, nanoparticles were functionalized with self-assembled monolayers composed of a mixture of Thiol-PEG-NHS and Thiol-PEG-methyl. The Thiol-PEG-NHS component allows for the covalent attachment of oligonucleotides via its NHS ester group. However, due to limited availability of both Thiol-PEG-NHS and oligonucleotides, Thiol-PEG-methyl was incorporated as a cost-effective alternative. This strategy ensured efficient surface passivation while minimizing the consumption of the more expensive Thiol-PEG-NHS-oligonucleotide conjugates.

The synthesis of AuNPs and AgNPs, as well as their subsequent functionalization with PEG, was systematically analysed and characterized using a combination of techniques. Ultraviolet-visible (UV-Vis) spectroscopy was employed to monitor nanoparticle formation and assess surface modifications. Transmission electron microscopy (TEM) was used to visualize nanoparticle morphology and size. Dynamic light scattering (DLS) provided information on hydrodynamic diameter and size distribution, while zeta potential measurements were conducted to evaluate surface charge and colloidal stability. Together, these complementary methods ensured comprehensive characterization of both the synthesized and PEGylated nanoparticles.

## 2.1.2 Results and discussion

The particle size and distribution of citrate-stabilized AuNPs were characterized using both TEM and DLS. TEM images (**Figures 2.1A-B**), taken at scales of 100 nm and 200 nm, show that the majority of AuNPs are spherical, well-separated, and fairly uniform in size, with some clustering likely due to high sample concentration and drying effects

on the TEM grid. Analysis of the size distribution (**Figure 2.1C**) indicates the formation of a monodisperse colloidal solution, with an average particle diameter of 14.17 ± 1.11 nm. Achieving a narrow size distribution is crucial for drug delivery applications, as it ensures a consistent biological response from each particle[181].

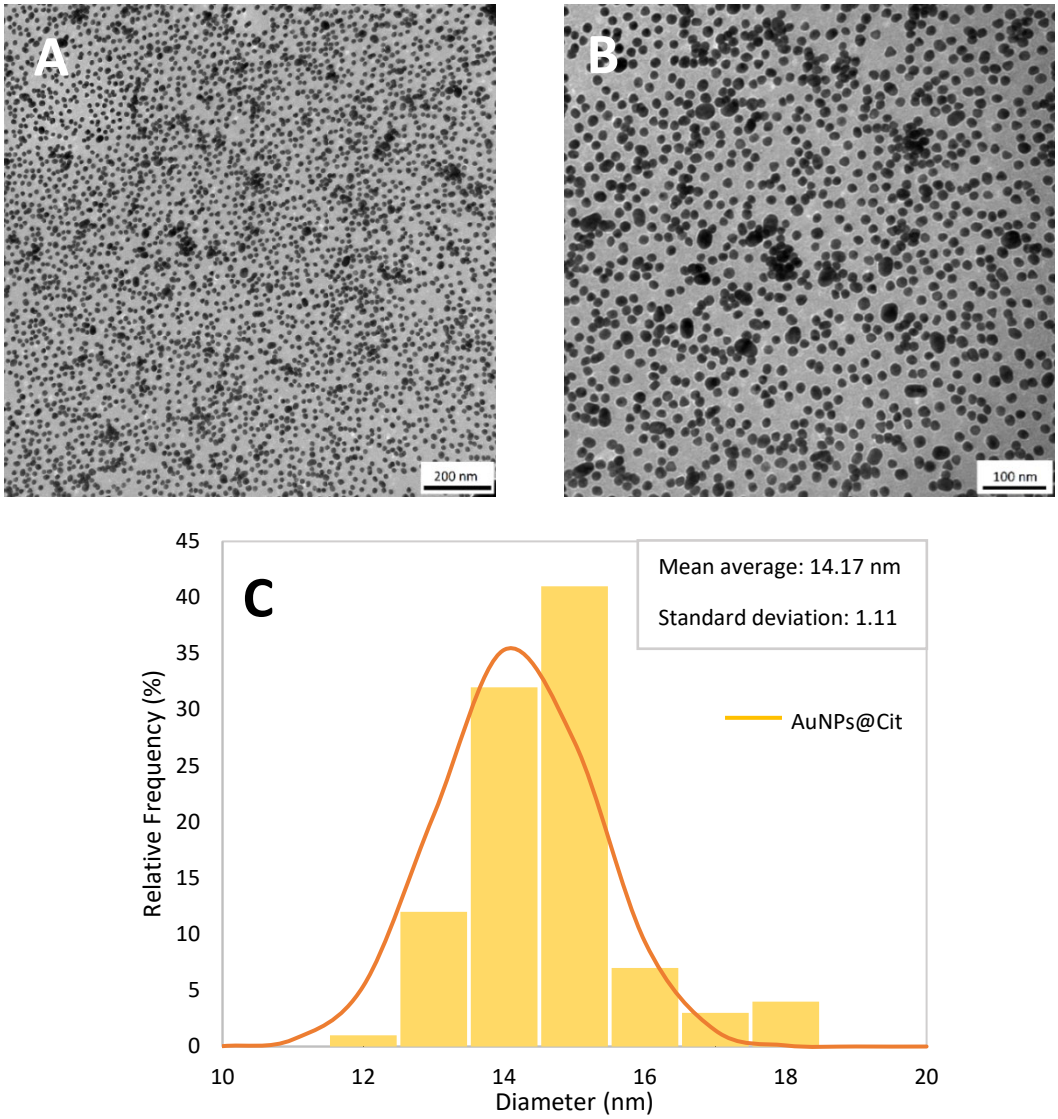


**Figure 2.1: Synthesis and Characterization of Gold Nanoparticles.** (A) A TEM image illustrating the spherical morphology and physical diameter of the citrate-functionalized AuNPs. (B) A magnified view that distinctly shows the consistent size distribution of the citrate-functionalized AuNPs. (C) A size distribution graph based on measurements from 100 particles in the sample.

Further assessment by DLS revealed a mean hydrodynamic diameter of 21.8 nm and a polydispersity index (PdI) of 0.185 (**Figure 2.2A**), confirming the narrow distribution observed by TEM. DLS measures the hydrodynamic radius, which reflects not only the nanoparticle core but also the surrounding layer of adsorbed citrate and water

molecules. Therefore, DLS-derived sizes are typically larger than those observed by TEM.

The UV-Vis absorption spectrum (**Figure 2.2B**) of the AuNPs exhibited a prominent peak at 520 nm, characteristic of 14 nm gold nanoparticles due to their LSPR. The sharp, well-defined peak further supports the absence of aggregation in the colloidal solution.

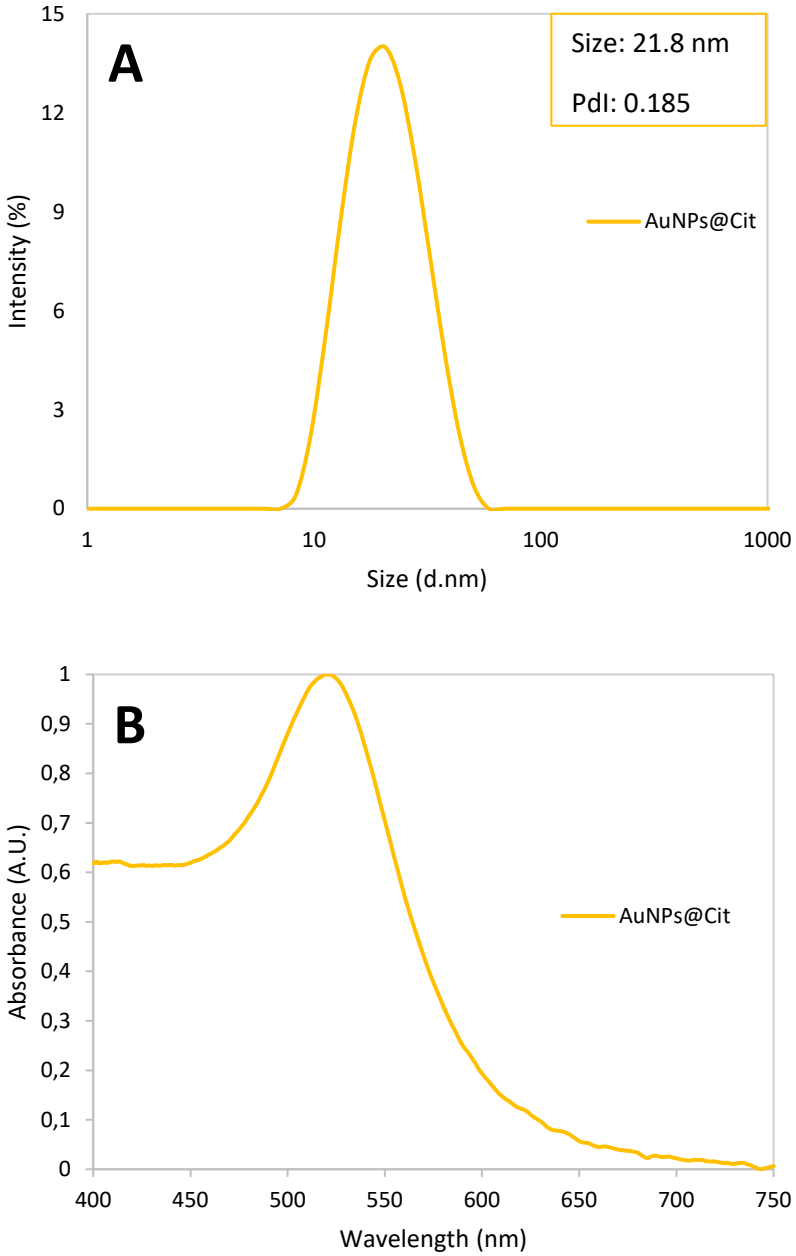


**Figure 2.2: DLS and UV-Vis analysis of AuNPs.** (A) DLS measurements of stabilized citrate-functionalized with an average size of 15 nm. (B) UV-Vis spectrum of 15 nm citrate-functionalized AuNPs synthesized via the citrate reduction method.

Citrate-stabilized AgNPs were also characterized following synthesis. TEM images (**Figures 2.3A-B**) show that the AgNP colloid consists of monodisperse particles with an average diameter of 7.55 ± 1.88 nm. However, the broader range of values in the size distribution graph (**Figure 2.3C**) indicates a more polydisperse solution compared to the AuNPs.

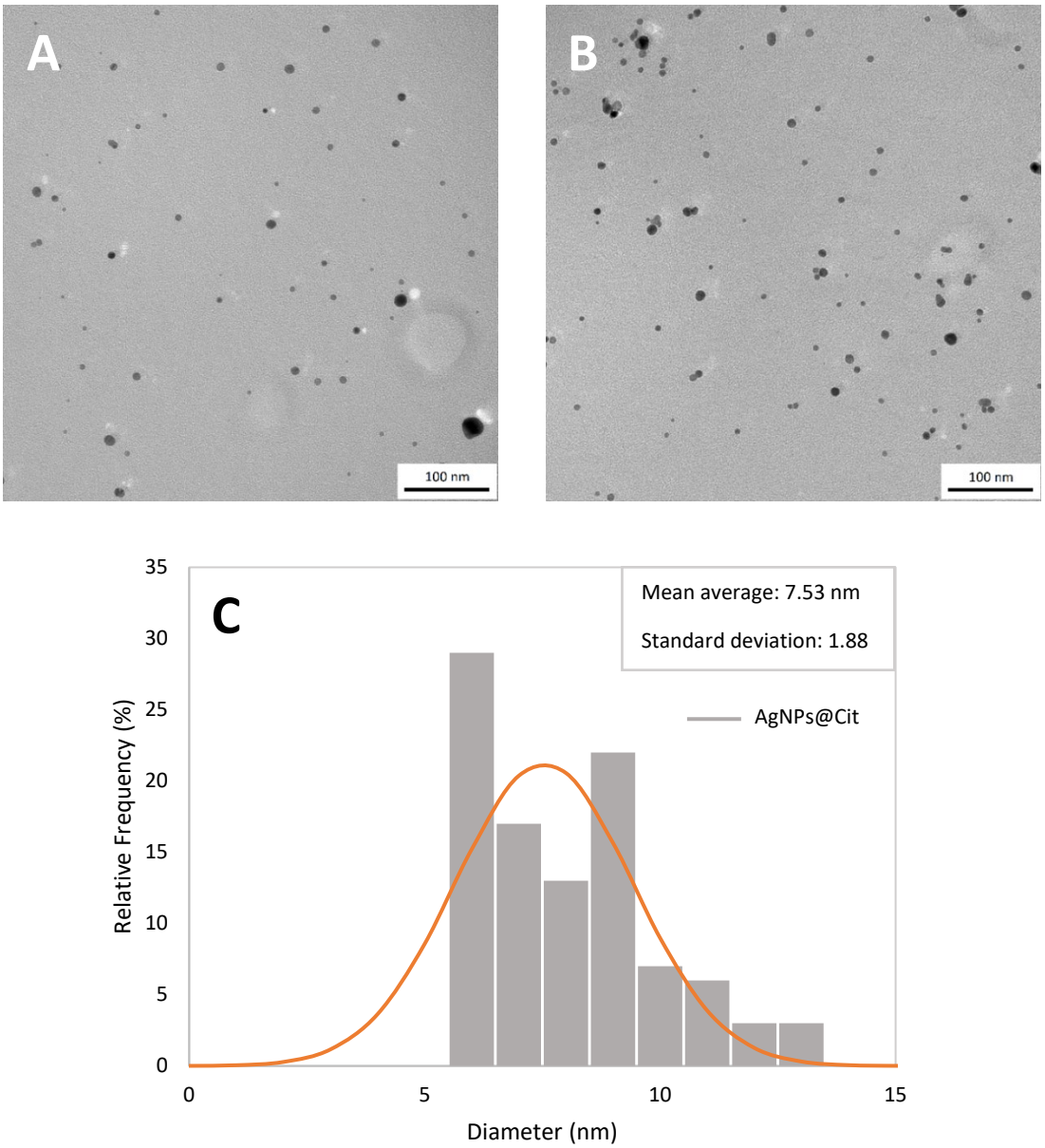


**Figure 2.3: Silver nanoparticles synthesis and characterization.** (A) A TEM image showing spherical morphology and physical diameter of citrate-functionalized AgNPs. (B) A 100 nm view clearly revealing the larger size distribution of the citrate-functionalized AgNPs (C) Size distribution graph made by taking 100 particles of the sample.

DLS analysis (**Figure 2.4A**) revealed two distinct populations, with peaks at 31.2 nm and 3.99 nm, and a low PdI, indicating a relatively homogeneous stock solution. The UV-Vis spectrum (**Figure 2.4B**) displayed a prominent absorbance peak at 400 nm, consistent with AgNPs of approximately 7 nm in size. The differences in peak slope and shape compared to AuNPs reflect the distinct SPR properties of silver, while the narrow peak confirms the absence of aggregation.

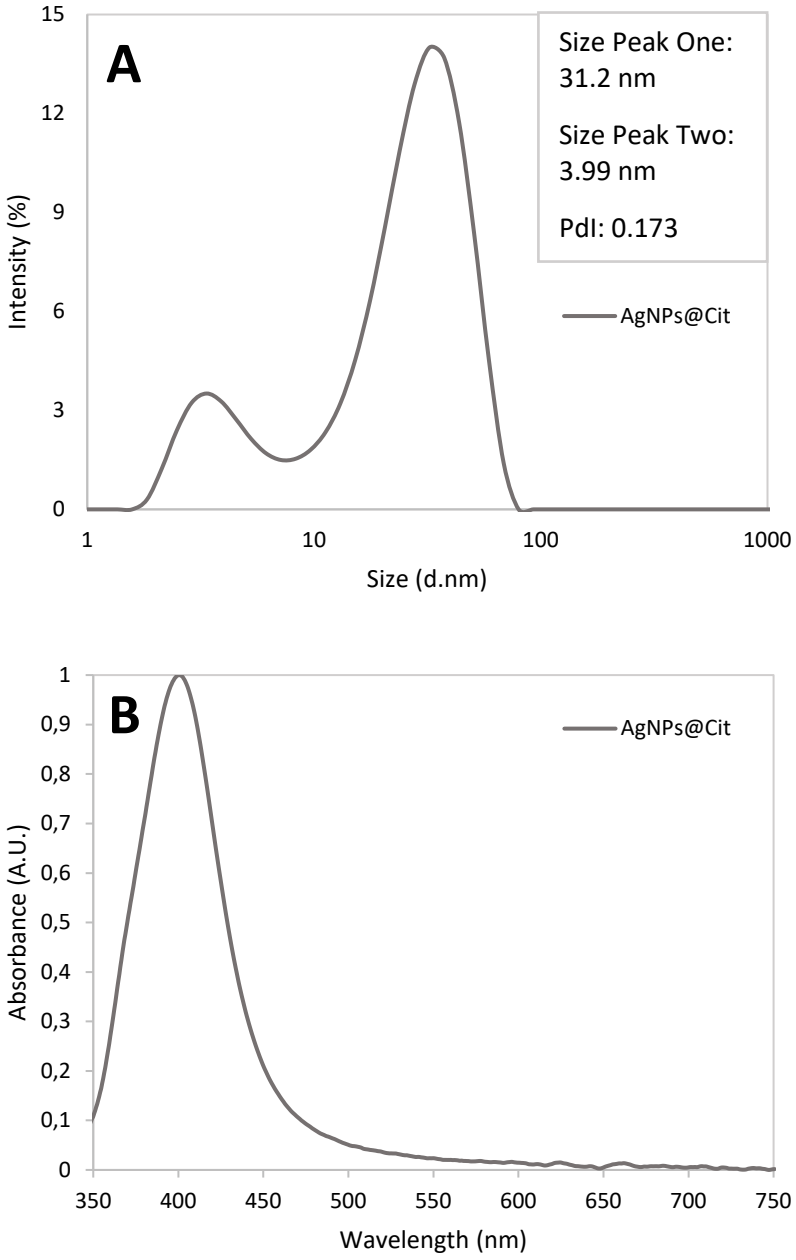


**Figure 2.4: DLS and UV-Vis analysis of AgNPs.** (A) DLS measurements of a stabilized batch of citrate-functionalized AgNPs. (B) UV-Vis spectrum of citrate-functionalized AgNPs with an average size of 9.22 nm, synthesized via the citrate reduction method.

To enhance the suitability of both AuNPs and AgNPs for drug delivery, surface functionalization with PEG was performed. This modification leads to an increase in the hydrodynamic diameter, as measured by DLS, though the core size remains unchanged in TEM images (**Figures 2.5A-B**).

To confirm the uniformity and distinct size profiles of the nanoparticles after PEGylation, size distribution analyses were performed using the TEM images (**Figures 2.6A-B**). The analysis showed that PEGylated AgNPs (**Figure 2.6A**) had a mean diameter of 8.50 nm with a standard deviation of ±3.04 nm. In comparison, the PEG-functionalized AuNPs (**Figure 2.6B**) formed a monodisperse solution with an average core size of 14.20 nm and a standard deviation of ±1.38 nm.

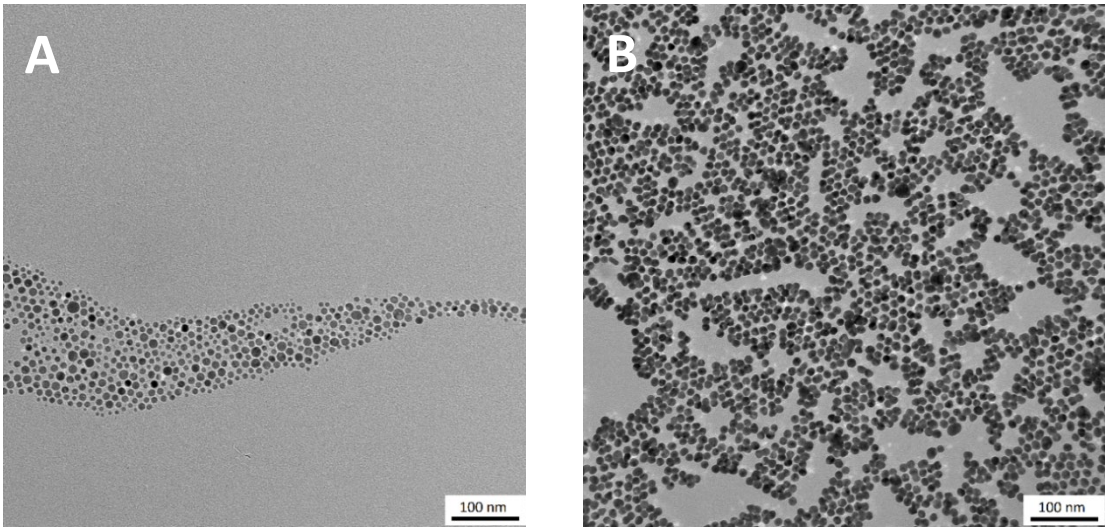


**Figure 2.5: TEM analysis of PEG passivated NPs.** (A) TEM image illustrating the spherical morphology and physical diameter of PEG-functionalized AgNPs. (B) TEM image showing a 100 nm view of the arrangement of spherical PEGylated AuNPs.

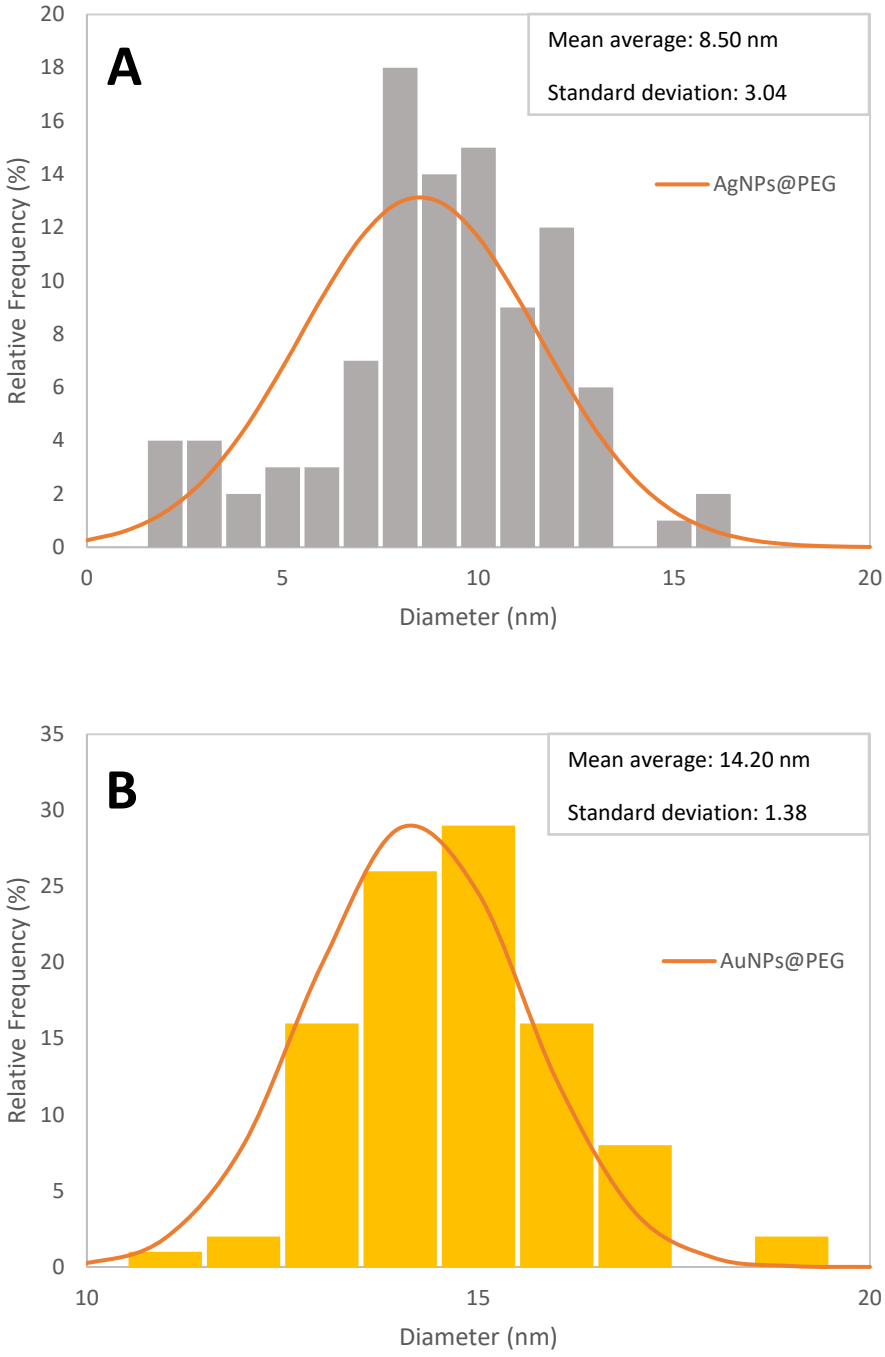


**Figure 2.6: Size distribution analysis of PEG passivated NPs.** (A) Size distribution graph made by taking 100 particles of the PEG-functionalized AgNPs sample. (B) Size distribution graph made by taking 100 particles of the PEG-functionalized AuNPs sample.

The efficiency of PEG passivation was further confirmed by DLS (**Figures 2.7A-B**), which showed an increase in hydrodynamic diameter for both types of nanoparticles after PEGylation. For AgNPs, the primary peak shifted from 31.20 nm to 36.40 nm and the secondary peak from 3.99 nm to 6.43 nm, with a decrease in PdI from 0.173 to 0.108.

For AuNPs, the hydrodynamic diameter increased from 21.80 nm to 26.10 nm, accompanied by a reduction in PdI from 0.185 to 0.154. The decrease in PdI for both samples indicates improved uniformity and homogeneity following PEGylation.

UV-Vis spectra of PEGylated nanoparticles (**Figures 2.8A-B**) revealed further differences: AuNPs showed a shift in the slope of the absorbance peak, while AgNPs exhibited a broader spectrum. In both cases, the absence of aggregation was indicated by the maintenance of consistent peak slopes, and the unchanged LSPR confirmed that the nanoparticle shape and core structure were preserved after functionalization.

A comparison of the data obtained from UV-Vis, TEM, and DLS analyses of both citrate-capped and PEGylated nanoparticles demonstrates that PEG passivation was successful, as evidenced by increased hydrodynamic diameters, shifts in LSPR peaks, and consistent core conformations in TEM images.

It is important to note that the smaller size (7 nm) and greater polydispersity of AgNPs present challenges for drug delivery applications compared to the monodisperse 15 nm AuNPs. Smaller AgNPs are associated with increased cytotoxicity due to higher reactive oxygen species (ROS) production and silver ion release, and their polydispersity can lead to inconsistent biodistribution, unpredictable protein corona formation, and variable dosing, which undermine therapeutic precision[186]. Additionally, AgNPs below approximately 8 nm are rapidly cleared by the kidneys, reducing circulation time and limiting their ability to accumulate in target tissues via the enhanced permeability and retention effect[187]. In contrast, AuNPs offer greater biocompatibility, longer circulation times, and multifunctional utility, including imaging and photothermal therapy. For these reasons, monodisperse AuNPs were selected for subsequent experiments to ensure safer, more predictable, and versatile drug delivery performance[188].

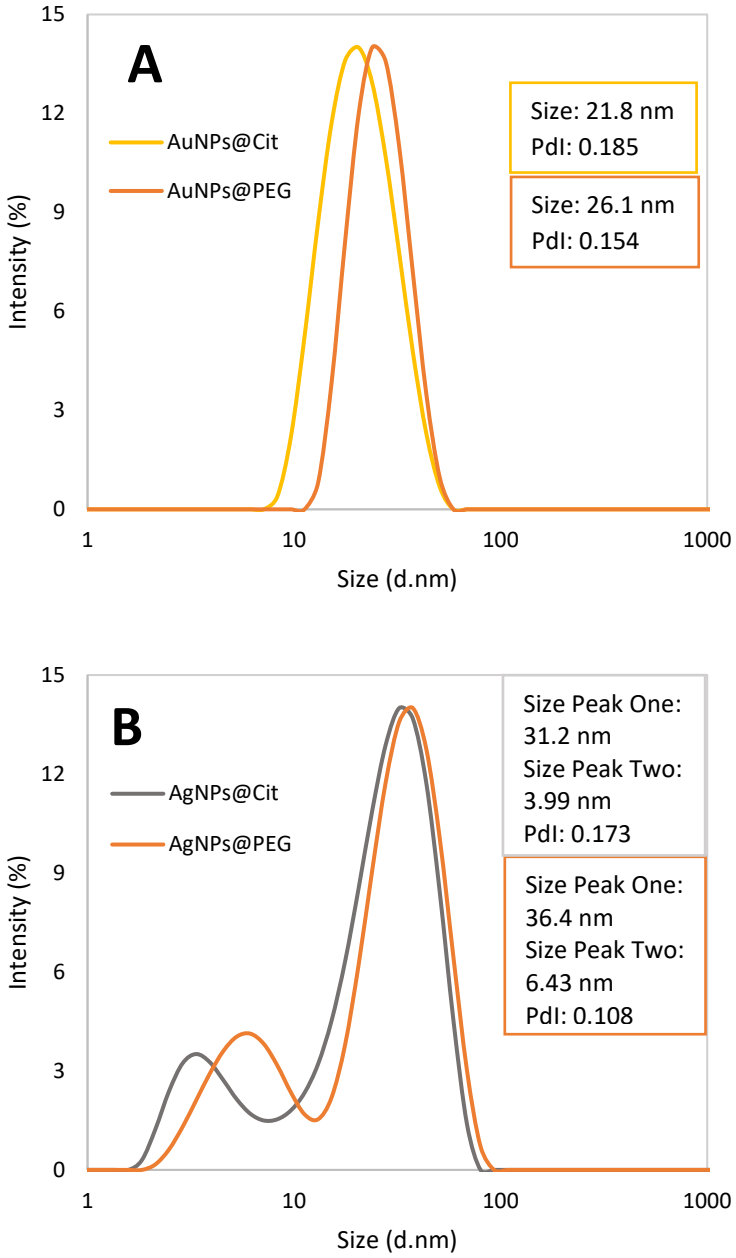


**Figure 2.7: Comparison of DLS Analysis for Gold and Silver Nanoparticles Post-Passivation.** (A ) DLS spectrum of PEG-passivated AuNPs compared to citrate-coated nanoparticles. (B) DLS spectrum of PEG-passivated AgNPs compared to citrate-coated nanoparticles.

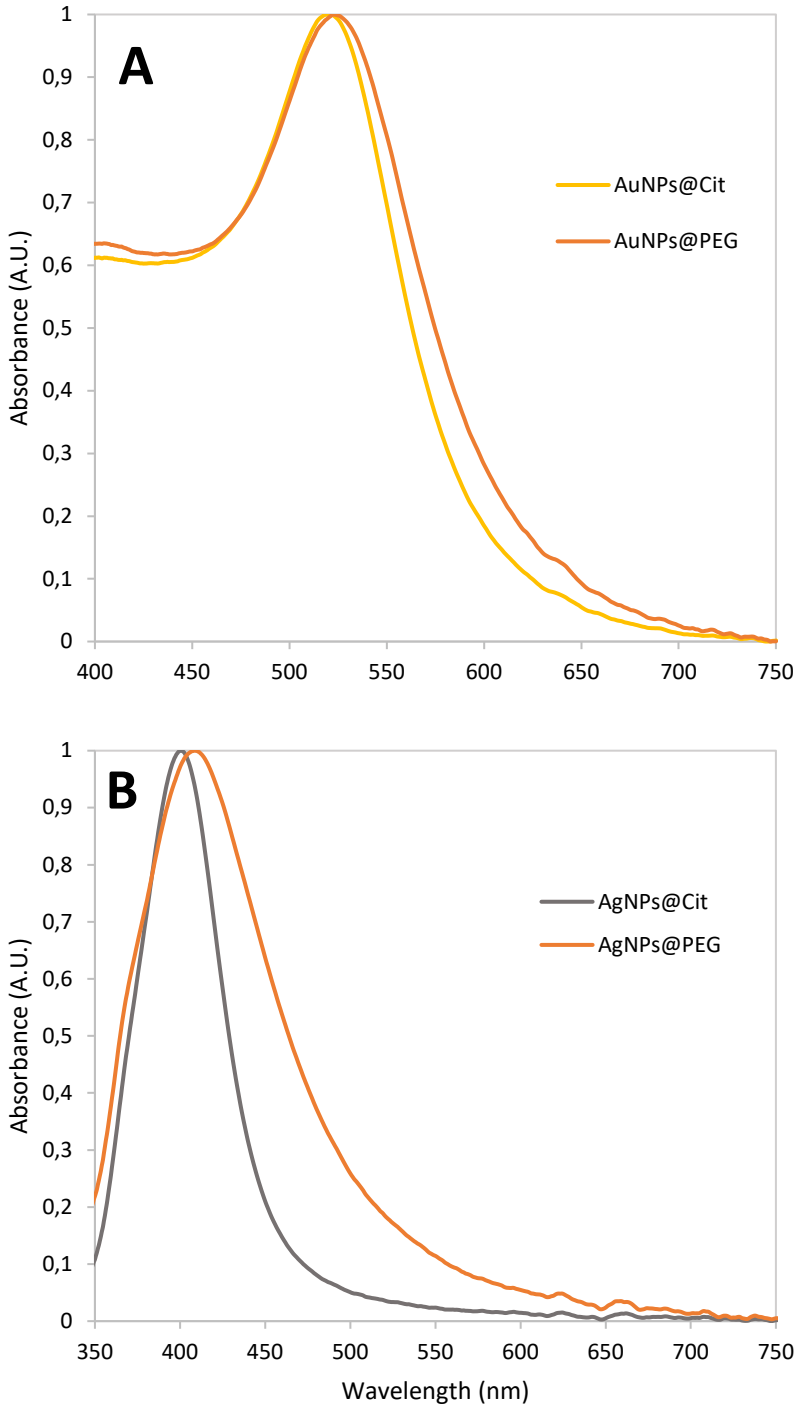


**Figure 2.8: Comparison of UV-Vis Analysis for Gold and Silver Nanoparticles Post-Passivation.** (A) Optical characterization of PEG-passivated AuNPs compared to citrate-coated nanoparticles. (B) Optical characterization of PEG-passivated AgNPs compared to citrate-coated nanoparticles.

## 2.2 Synthesis of Oligonucleotides

### 2.2.1 Design of Antisense Oligonucleotides Targeting the *c-myc* IRES

The project aimed to modulate *c-myc* mRNA translation by targeting its Internal Ribosome Entry Site (IRES) region. Based on predicted structural models, five antisense oligonucleotides (ONs) of approximately 28 nucleotides were strategically designed to target specific regions within Domain 1, which is the location of the Ribosome Entry Site (**Figure 2.9**).

The secondary structure of the *c-myc* IRES, as predicted in the literature [77], served as a template for designing the ONs. Each ON was positioned to target distinct structural elements within Domain 1 to systematically evaluate how hybridization to these different regions affects IRES function. The five targeting sites were selected to provide comprehensive coverage of Domain 1's key structural features, including pseudoknot helices and apical loop regions.

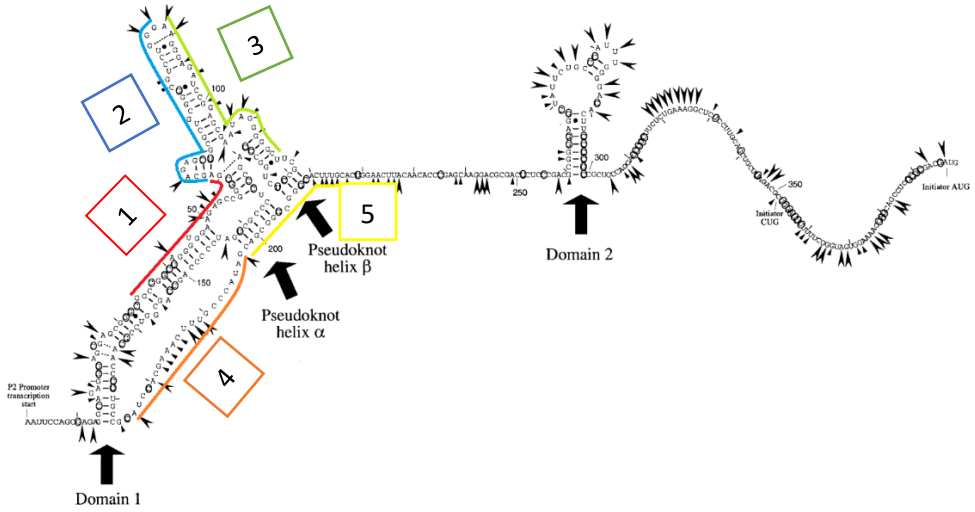


**Figure 2.9**: **Secondary Structure of the Human *c-myc* IRES**. The selected sequences for synthesis are underlined in different colours and labelled numerically from 1 to 5. Image credit: Figure adapted from[77].

Notably, ON4 was specifically designed to target a sequence lacking secondary structures, which is hypothesized to directly interact with the ribosome during translation initiation. This unstructured region represents a particularly promising

target as it likely remains accessible for ON binding and may play a critical role in ribosome recruitment.

The five different DNA sequences were synthesized along with a scramble sequence used as a control in cell assays (**Table 2.1**). This scramble sequence is an oligonucleotide with chemical properties identical to those of the other synthesized sequences but does not hybridize with any region of the human genome. The Gggenome software was employed to ensure that the scramble sequence does not target any gene.

**Table 2.1**: **Theoretical Properties of the six Selected Sequences for Synthesis**. Each strand incorporates Locked Nucleic Acid (LNA) (+), Phosphorothioate (*) modifications, and a 5' amino (/5AmMC6/) modification. These properties were calculated using the OligoAnalyzer Tool from IDT Technologies.

| Number of Sequence | Sequence | Length (nt) | GC Content (%) | Molecular Weight (g/mole) | Extinction Coefficient (L/(mole·cm)) |
|---|---|---|---|---|---|
| Scramble | 5'- /5AmMC6/G*C*C* +T*T*C* +G*C*C* A*G*C* C*+G*C* T*A*C* +T*C*C* T*C*A* +T*T*C*T -3' | 28 | 60,70 | 9140,3 | 236200 |
| 1 | 5'- /5AmMC6/T*C*+G* C*C*C* +G*G*C* T*C*T* +T*C*C* A*C*C* C*+T*A* G*C*C* G*+G*C*C -3' | 28 | 75.00 | 8972.1 | 233400 |
| 2 | 5'- /5AmMC6/C*C*C* A*+G*G* A*C*G* C*C*C* +G*C*A* G*C*G* C*A*+G* C*T*C* +T*G*C*T -3' | 28 | 75.00 | 9042.2 | 245600 |
| 3 | 5'- /5AmMC6/A*+G*C* C*C*C* C*+T*A* T*T*C* +G*C*T* C*C*G* G*A*+T* C*T*C* C*C*+T*T -3' | 28 | 60.71 | 8961.2 | 239500 |
| 4 | 5'- /5AmMC6/C*+T*A* T*G*G* +G*C*A* A*A*G* +T*T*T* C*G*T* G*+G*A* T -3' | 22 | 45.45 | 7254.8 | 214100 |
| 5 | 5'- /5AmMC6/ A*G*+T* T*C*C* A*G*+T* G*C*A* A*A*+G* T*G*C* C*C*+G* C*C*C* G*C*+T*G -3' | 28 | 64.29 | 9124.3 | 257200 |

All oligonucleotide sequences were analysed using the OligoAnalyzer Tool from IDT Technologies, which provides theoretical properties for each strand. This data was

utilized to calculate the concentration and nanomoles obtained after purification of each strand.

As previously discussed, the synthesized strands were designed to attach to the surface of PEGylated NPs, forming a delivery system capable of binding to the target through complementary base pairing. In order to do so, several aspects needed to be considered, such as considering modifications to improve the stability of the DNA-RNA heteroduplex and enhance the pharmacological properties of the delivery system, which could impact its performance.

To enhance nuclease resistance and prolong the elimination half-life of ASOs in tissues, a full phosphorothioate backbone was introduced. Additionally, LNAs were strategically incorporated during synthesis using LNA analogues of T and G phosphoramidites. This modification improves RNA-DNA duplex stability and further bolsters enzymatic degradation resistance.

The LNAs were spaced throughout the oligonucleotide sequence to retain their benefits while avoiding unintended RNase H activation. RNase H activity requires a 7–10 nucleotide DNA gap, which was intentionally omitted to prevent premature cleavage of the target RNA.

The next step involved virtual modelling using mFold software to evaluate whether secondary structures could form in the proposed sequences, as such structures might hinder heteroduplex formation with the mRNA target. Previous statistical studies on phosphorothioate-modified oligonucleotides revealed that oligo-probes forming stable RNA duplexes ($\Delta G^0_{37}$ < -30 kcal/mol) with minimal self-interaction potential are more likely to be active. Optimal thresholds for self-interaction are ($\Delta G^0_{37}$) > -8 kcal/mol for inter-oligonucleotide pairing and ($\Delta G^0_{37}$) > -1.1 kcal/mol for intra-molecular pairing[189]. Appendix A provides the conformations of the strands, all of which exhibit free energy values within the threshold for stable hybridization. Initially, sequences ON1 and ON2 were excluded due to their higher GC content; however, they were later tested to assess whether their free energy value of -6 kcal/mol a value exceeding the -1.1 kcal/mol threshold-to empirically assess hybridization interference.

To enable bioconjugation with the previously synthesized nanoparticle system, an additional modification was introduced: a 5'-amino group was added to the end of each sequence. This modification allows reaction with the NHS group on the PEG coating of the NPs, forming a covalent amide bond that securely attaches ASO strands to the nanoparticle surface (**Figure 2.10**).

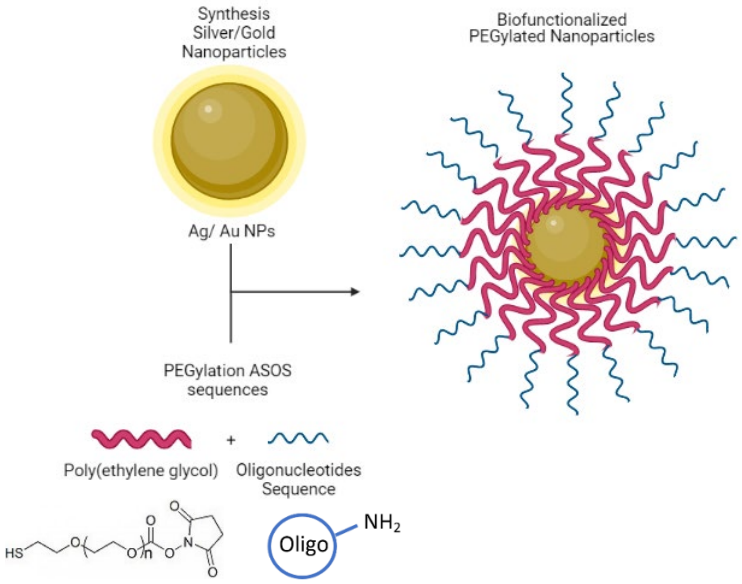


**Figure 2.10: Schematic Representation of the Synthesis and Design of the AuNPs@PEG@ssDNA for ASO Delivery.**

## 2.2.2 Results and discussion

The five ASOs sequences were synthesized via solid-phase synthesis using phosphoramidite chemistry on 1 µmol CPG (controlled pore glass) columns, as outlined in **Section 5.3.1**. To ensure reproducibility and adequate yield for downstream applications, multiple replicates of each strand were synthesized. Following synthesis, the oligonucleotides underwent deprotection and purification via reversed-phase HPLC, as detailed in **Section 5.3.2**.

Following purification, the concentration of each synthesized replicate was calculated using the absorbance readings and theoretical extinction coefficient values obtained from the OligoAnalyzer Tool by IDT Technologies, applying the Lambert-Beer law. From these concentrations, the number of nanomoles synthesized in each replicate was calculated (**Table 2.2**). The synthesis yield was determined, by comparing this value to the initial 1 µmol present in the column. Although these values were not considered

precise due to spectrophotometer limitations, they served as a qualitative reference for subsequent assays.

**Table 2.2**: **Calculated yield of the Synthesis Process for each Sequence replicate using 1 µmol CPG Columns.**

| Sequence | Replicates | Nanomols DNA (nmol) | Yield (%) |
|---|---|---|---|
| **Scramble** | Sc.1 | 344 | 34 |
| | Sc.2 | 352 | 35 |
| **ON1** | 1.1 | 236 | 24 |
| | 1.2 | 308 | 31 |
| **ON2** | 2.1 | 235 | 48 |
| | 2.2 | 149 | 44 |
| **ON3** | 3.1 | 479 | 48 |
| | 3.2 | 440 | 44 |
| **ON4** | 4.1 | 420 | 42 |
| | 4.2 | 459 | 46 |
| **ON5** | 5.1 | 469 | 47 |
| | 5.2 | 485 | 49 |

The sequences were qualitatively evaluated using mass spectrometry (**Appendix B**). This analysis involved comparing the expected mass of the oligonucleotides with the mass obtained from the spectrometry analysis. The ESI-MS systems used have a mass resolution of approximately 0.03%, which translates to ±3 Da for a 10 kDa oligonucleotide. Consequently, the comparison revealed that most strands have a mass similar to the theoretical value (**Table 2.3**).

**Table 2.3**: **Expected mass *vs* obtained mass of the ONs in the mass spectrometry analysis.**

| Sequence | Expected Mass (g/mole) | Measured Mass (g/mole) |
|---|---|---|
| **ON1** | 9151.3 | 9151.0 |
| **ON2** | 9221.4 | 9221.6 |
| **ON3** | 9140.3 | 9140.9 |
| **ON4** | 7433.9 | 7432.5 |
| **ON5** | 9303.4 | 9302.2 |

All samples exhibited a UV/Vis spectrum with a primary peak absorbing at 260 nm. Mass deconvolution of this main peak indicated the presence of two populations: sequences with the amino modifier coupled and sequences without the amino modification at the strand's end.

The purity of the oligonucleotides was confirmed by HPLC (**Appendix C**). All sample chromatograms displayed a clean peak, suggesting that these sequences are suitable for use in subsequent experiments.

## 2.3 Synthesis and Characterization of PEGylated ASOs Conjugates

### 2.3.1 Design and Optimization of PEGylated ASOs Conjugates

The aim of this experiment was to conjugate ASOs with PEG to enable subsequent coating of nanoparticle surfaces. In selecting an appropriate PEG molecule, it was essential that one end be functionalized with a thiol group to facilitate covalent attachment to the nanoparticles, as described previously in **Section 5.2.4**. The opposite end of the PEG chain needed a functional group capable of binding to the oligonucleotide sequence. SH-PEG-NHS was chosen as the optimal linker due to its

cost-effectiveness, commercial availability, and the presence of an NHS ester group, which allows efficient coupling with the amino group of the oligonucleotides.

To optimize the conjugation conditions, a commercial DNA sequence corresponding to ON4 was used as a control. This sequence, purchased from IDT, was synthesized without PS or LNA modifications to serve as a straightforward model for method development. The conjugation assay was analysed using HPLC, employing the same chromatographic conditions as those used for the characterization of synthesized strands (**Section 5.6.1**). The primary objective of this control assay was to establish a reliable protocol for identifying the peak corresponding to unconjugated DNA in the HPLC chromatogram, which is essential for monitoring and quantifying the efficiency of the bioconjugation process.

Following optimization using the unmodified ON4 control, the established protocol was applied to conjugate the remaining phosphorothioate- and LNA-modified ASO sequences with SH-PEG-NHS. Each conjugate was purified via reversed-phase HPLC under the same chromatographic conditions, ensuring removal of unreacted oligonucleotides and PEG reagents. Purified PEG-ASO conjugates were characterized by LCMS to confirm the successful conjugation of ssDNA to SH-PEG-NHS.

## 2.3.2 Results and Discussion

### 2.3.2.1 Optimization of conjugation Conditions Using a Control Sequence for Protocol Validation

The initial phase of the optimization process focused on determining the retention time and chromatographic profile of the unconjugated DNA under conditions that closely replicate those of the intended bioconjugation reaction. For this purpose, DNA samples were prepared at concentrations specified in the established protocol (**Section 5.4**) and analysed in the presence of the two solvents utilized in the subsequent bioconjugation steps: DMSO and 300 mM $NaHCO_3$.

By analysing the DNA samples in both solvents under identical HPLC conditions, the assay enabled direct comparison of the retention profiles. This comparison was crucial

for distinguishing any solvent-induced shifts in the DNA elution profile, thereby ensuring accurate localization of the peak corresponding to unconjugated DNA. Establishing these baseline retention times in both DMSO and $NaHCO_3$ was essential for the subsequent steps of the project, as it allowed for precise tracking of conjugation efficiency and clear differentiation between conjugated and unconjugated ssDNA during the bioconjugation reactions. This careful optimization addresses the analytical challenges posed by solvent effects, ultimately supporting robust and reliable monitoring of the bioconjugation process.

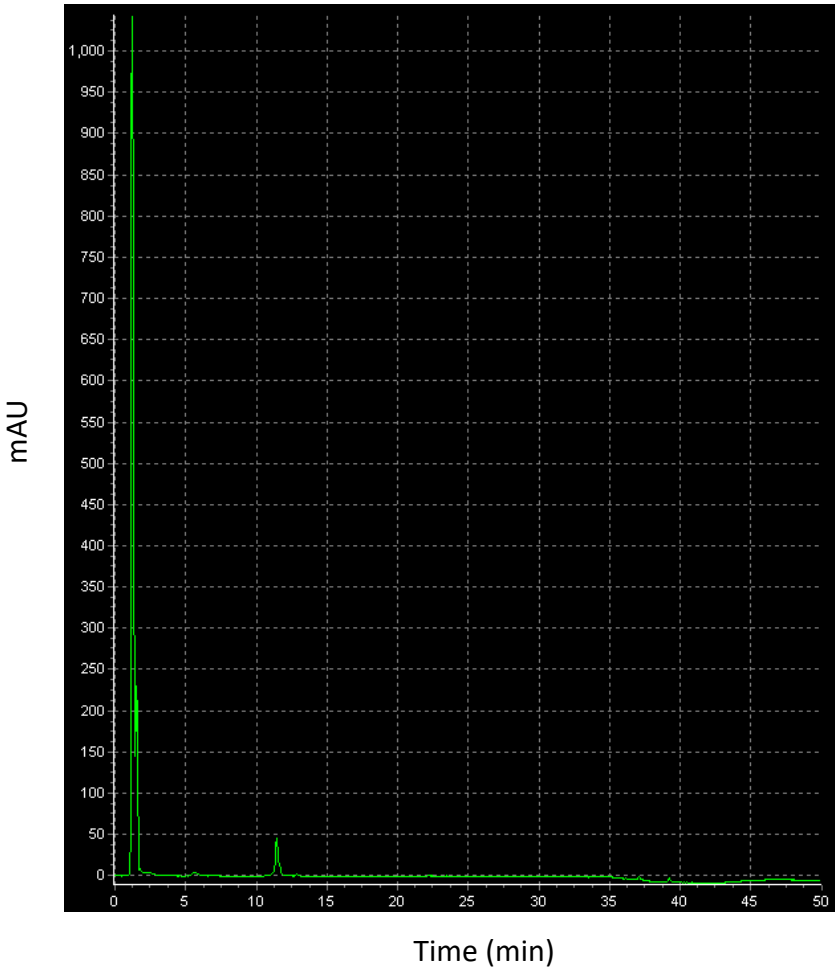


**Figure 2.11: HPLC elution profile of ssDNA in DMSO solvent:** The chromatogram displays a dominant, sharp peak at approximately 1 minute, corresponding to DMSO, followed by a smaller peak between 10 and 15 minutes, which represents DNA.

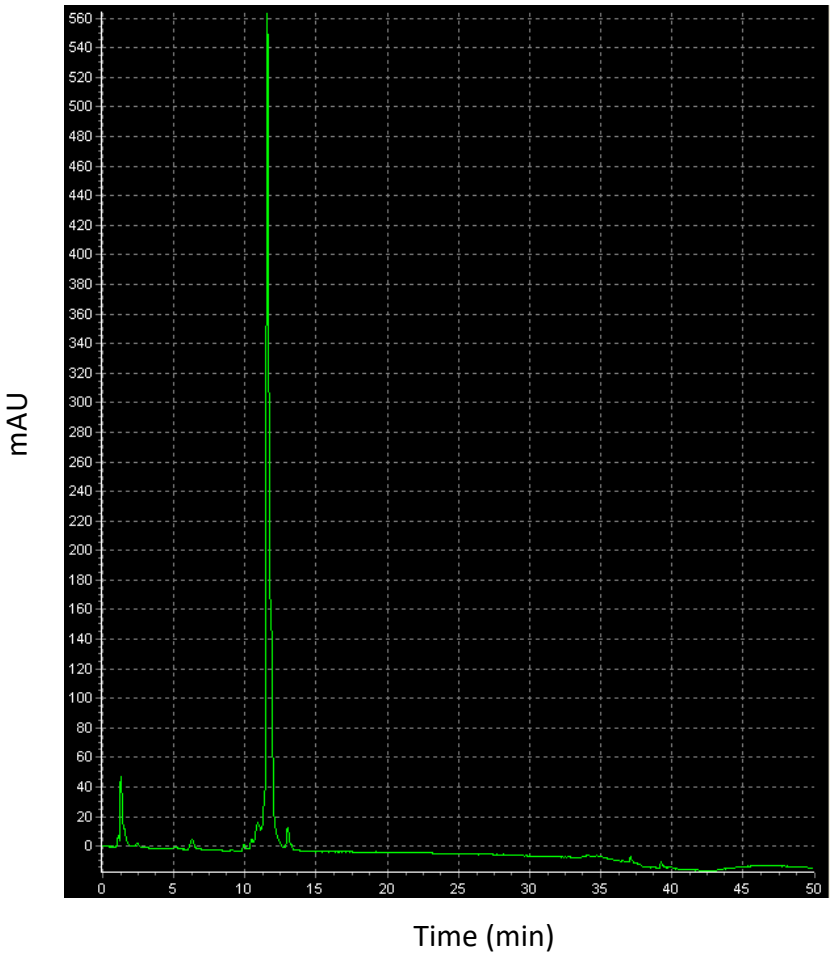


**Figure 2.12: HPLC elution profile of ASO in $NaHCO_3$ buffer.** The chromatogram displays a small peak at approximately 1 minute corresponding to the injection, followed by a dominant, sharp peak between 10 and 15 minutes, which represents DNA.

The ASO strands exhibited consistent retention behaviour across both solvent systems, eluting at approximately 12 minutes in all chromatograms. However, a notable solvent-dependent artifact emerged: when DMSO was employed, a prominent peak appeared at ~1 minute, coinciding with the solvent front (**Figure 2.11**).. This early eluting DMSO signal caused significant suppression of the DNA peak intensity at 12 minutes, despite identical DNA concentrations in both solvent systems. The reduced signal likely stems from DMSO's strong UV absorbance at the detection wavelength or column saturation effects during injection, which can distort later-eluting analyte peaks. In contrast, the $NaHCO_3$-based chromatograms lacked this interfering early peak, resulting in clearer resolution of the ASO signal (**Figure 2.12**). A minor peak at ~1 minute was also observed but attributed to routine injection artifacts (e.g., air bubbles or solvent front disturbances), with negligible impact on the ASO signal.

It was also essential to confirm that PEG does not exhibit absorbance at 260 nm, the wavelength used to detect the conjugated DNA product. To assess this, PEG was dissolved in DMSO and subsequently mixed with 300 mM $NaHCO_3$, following the same procedure outlined previously for the DNA samples. The resulting solution was then analysed under the same HPLC and UV detection conditions to ensure that any observed absorbance at 260 nm could be attributed solely to the DNA or its conjugates, and not to the presence of PEG (**Figure 2.13**). This verification step was crucial to rule out any potential interference from PEG in the detection and quantification of the bioconjugated product.

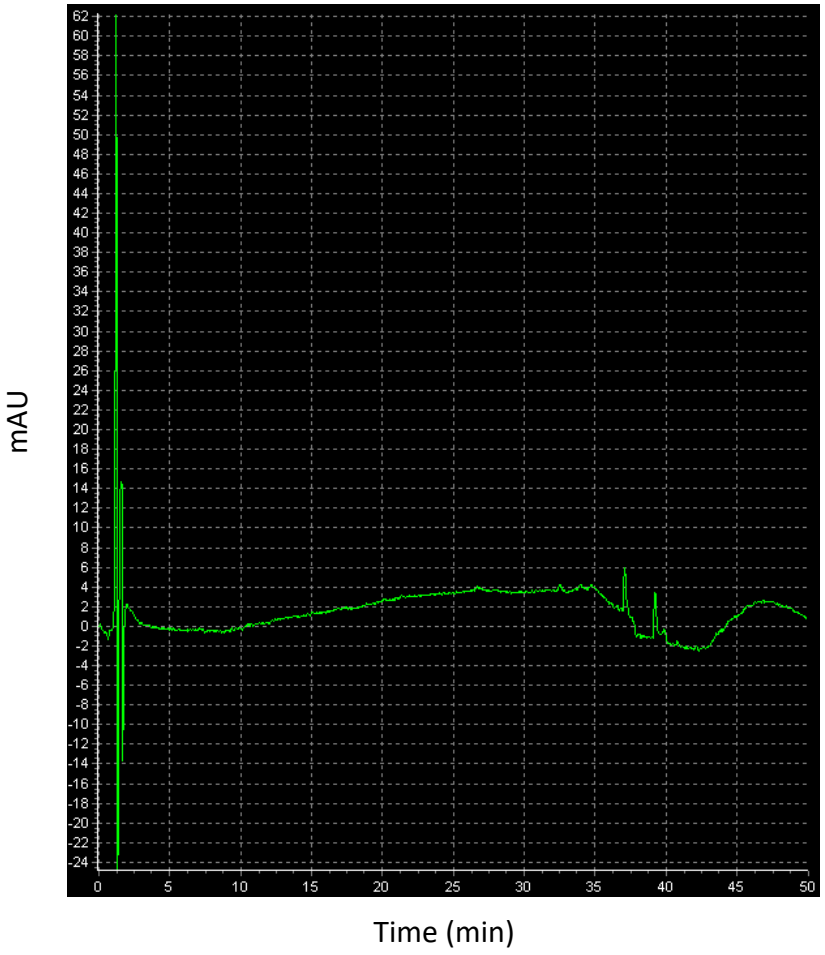


**Figure 2.13: HPLC Chromatogram of a Control Sample: PEG in DMSO Mixed with 300 mM $NaHCO_3$.** The first large peak at around 1 minute is associated with the injection solvent, which in this case is DMSO. The two small peaks that appear toward the end of the chromatogram are associated with the elution phase using 100% methanol, representing the baseline shift or minor impurities eluting during the solvent change.

The chromatogram demonstrates the absence of peaks in the region, specially between 10 and 15 minutes, which corresponds to the elution time of DNA (**Figure 2.12**). This confirms that PEG does not absorb at 260 nm. (**Figure 2.13**).

DMSO plays a crucial role in the bioconjugation process, particularly for dissolving thiol-PEG-NHS, which is essential for efficient coupling with DNA strands. Thanks to its excellent solvation properties, DMSO ensures that both the hydrophilic DNA and the hydrophobic PEG are uniformly dissolved, creating optimal conditions for the conjugation reaction. To assess how incubation time affects the efficiency of this process, aliquots were collected from each reaction mixture at 2, 24, and 72 hours and analysed by HPLC (**Figures 2.14-16**). The results showed that reactions carried out in DMSO produced well-defined product peaks, and a qualitative comparison of peak areas indicated that most of the DNA was successfully coupled to PEG, particularly after longer incubation periods.

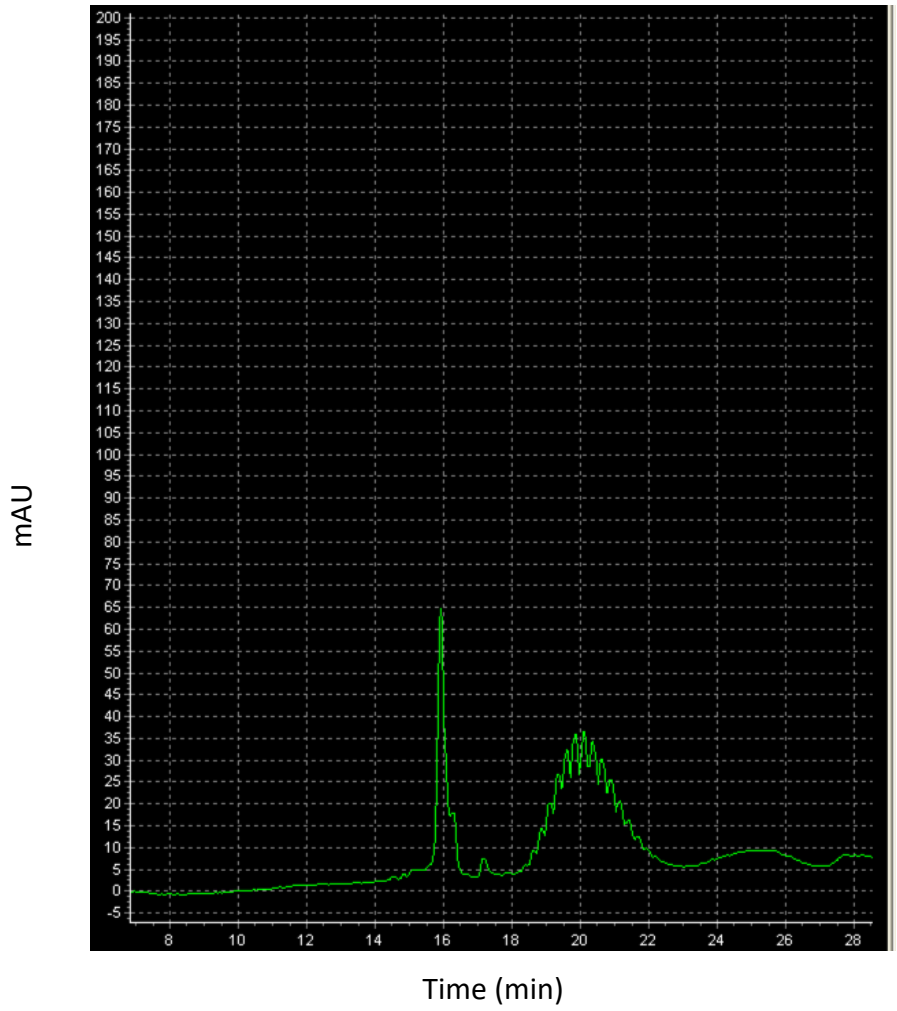


**Figure 2.14: HPLC elution profiles of DNA-PEG bioconjugation in DMSO at 2 hours.** At the 2-hour time point, the HPLC chromatogram for the reaction in DMSO shows a prominent peak at 16 minutes, corresponding to unconjugated DNA, with minor peaks appearing between 18 and 22 minutes, which represent initial formation of PEG-conjugated DNA species.

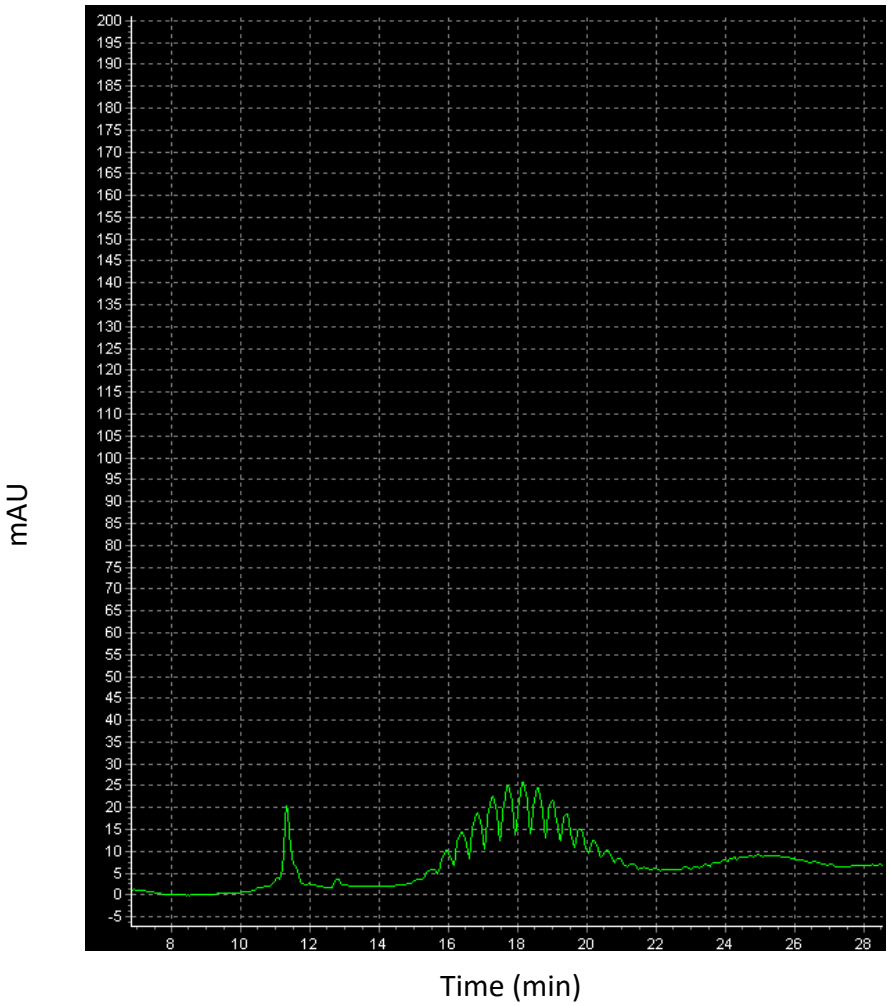


**Figure 2.15: HPLC elution profiles of DNA-PEG bioconjugation in DMSO at 24 hours.** At the 24-hour time point, the HPLC chromatogram for the reaction in DMSO shows a prominent peak at 11 minutes, corresponding to unconjugated DNA, with minor peaks appearing between 16 and 22 minutes, which represent initial formation of PEG-conjugated DNA species.

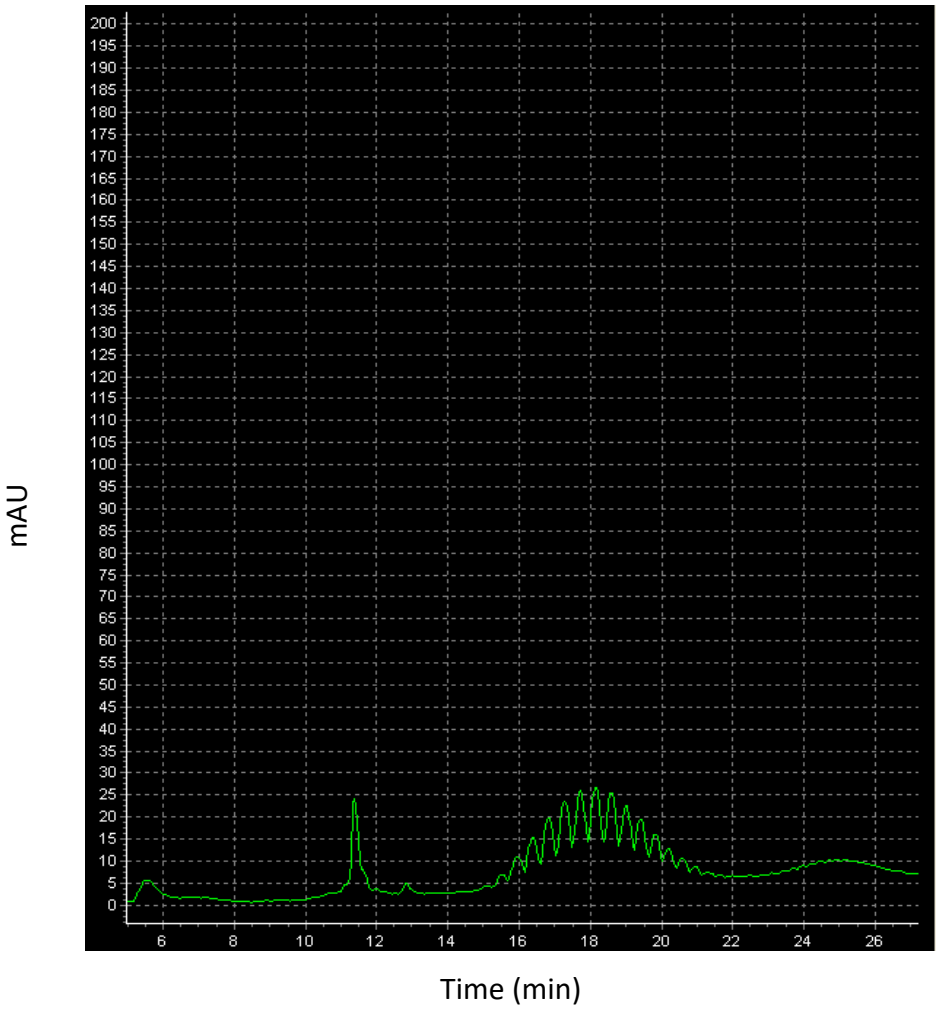


**Figure 2.16: HPLC elution profiles of DNA-PEG bioconjugation in DMSO at 72 hours.** At the 72-hour time point, the HPLC chromatogram for the reaction in DMSO shows a prominent peak at 11 minutes, corresponding to unconjugated DNA, with minor peaks appearing between 16 and 22 minutes, which represent initial formation of PEG-conjugated DNA species.

Furthermore, this test provided insights into the product's composition, which appears as a series of peaks, each representing a PEG molecule attached to a DNA strand. This occurs because the PEG used in this assay does not have a specific mass; instead, it is a solution with an average size of 0.8 kDa. Consequently, each peak corresponds to a DNA strand coupled with a PEG molecule of a particular size within this average.

Despite its effectiveness in promoting the bioconjugation reaction, DMSO poses challenges for the subsequent biofunctionalization of citrate-stabilized NPs. These NPs rely on electrostatic interactions for stability, and the high polarity of DMSO, along with its tendency to interact with surface ligands, can disrupt these interactions and

lead to NP aggregation. Moreover, DMSO is notoriously difficult to remove due to its low volatility, complicating the preparation of NP suspensions free of residual solvent.

To overcome these issues, dimethylformamide (DMF) was evaluated as an alternative solvent (**Figures 2.17-19**). DMF is easier to evaporate and could potentially simplify the removal process before NPs biofunctionalization. However, when comparing the two solvents, it became clear that DMF did not perform as well as DMSO. The HPLC chromatograms from DMF-based reactions showed less distinct product peaks and lower apparent conjugation efficiency. These findings suggest that while DMSO is more effective for the DNA-PEG conjugation, its removal is essential to maintain the stability of citrate-stabilized NPs in subsequent applications. Therefore, a balance must be struck between achieving high reaction yields and ensuring NP stability, possibly by optimizing solvent removal techniques when using DMSO.

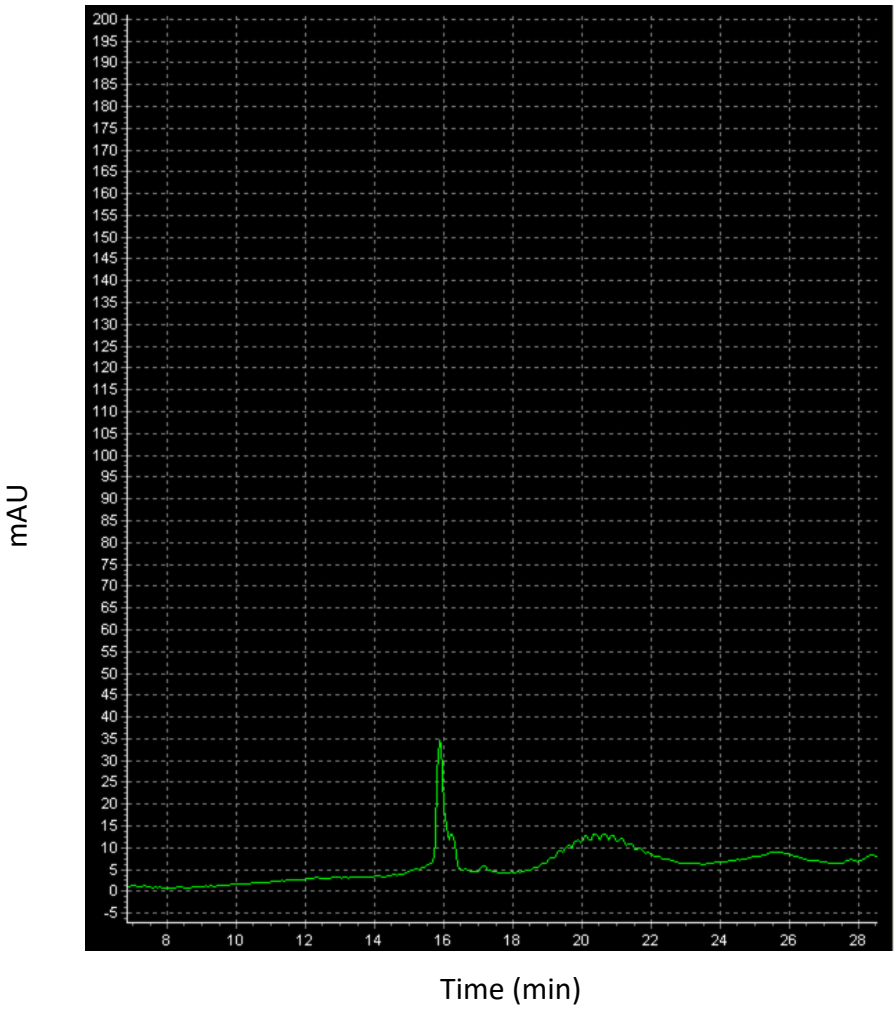


**Figure 2.17: HPLC elution profiles of DNA-PEG bioconjugation in DMF at 2 hours.** At the 2-hour time point, the HPLC chromatogram for the reaction in DMF shows a prominent peak at 16 minutes, corresponding to unconjugated DNA, with minor peaks appearing between 18 and 22 minutes, which represent initial formation of PEG-conjugated DNA species.

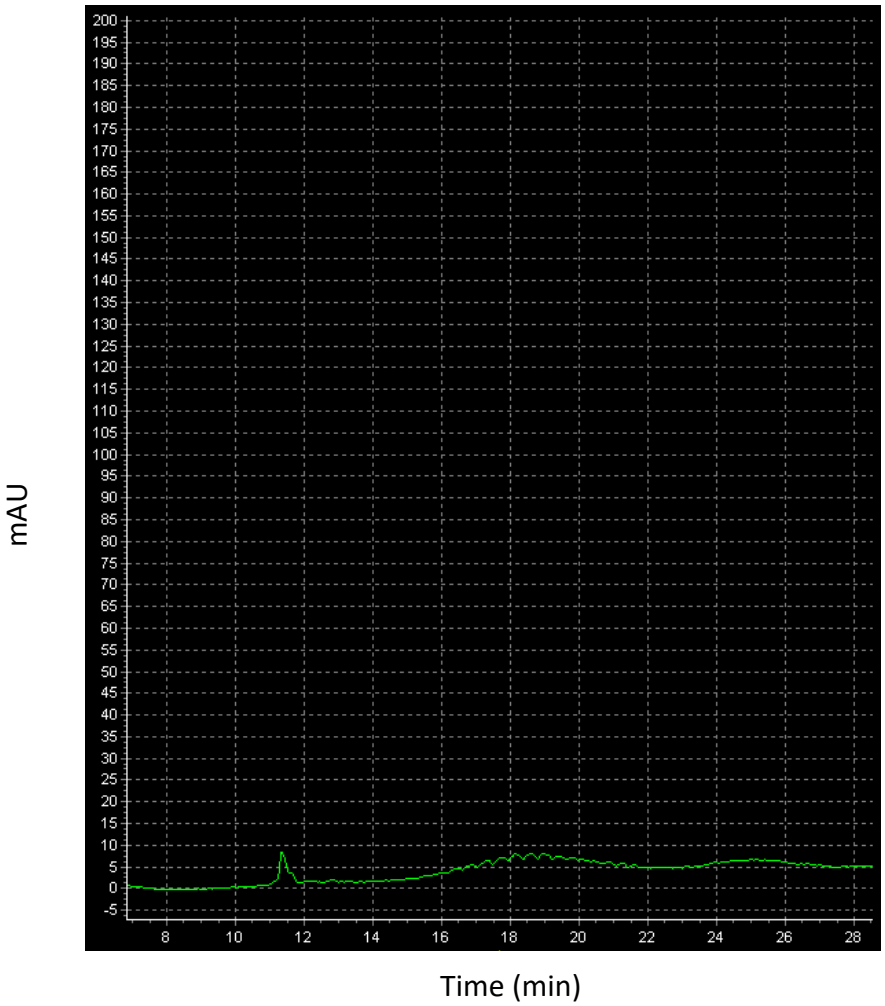


**Figure 2.18: HPLC elution profiles of DNA-PEG bioconjugation in DMF at 24 hours.** At the 24-hour time point, the HPLC chromatogram for the reaction in DMF shows a prominent peak at 11 minutes, corresponding to unconjugated DNA, with minor peaks appearing between 16 and 22 minutes, which represent initial formation of PEG-conjugated DNA species.

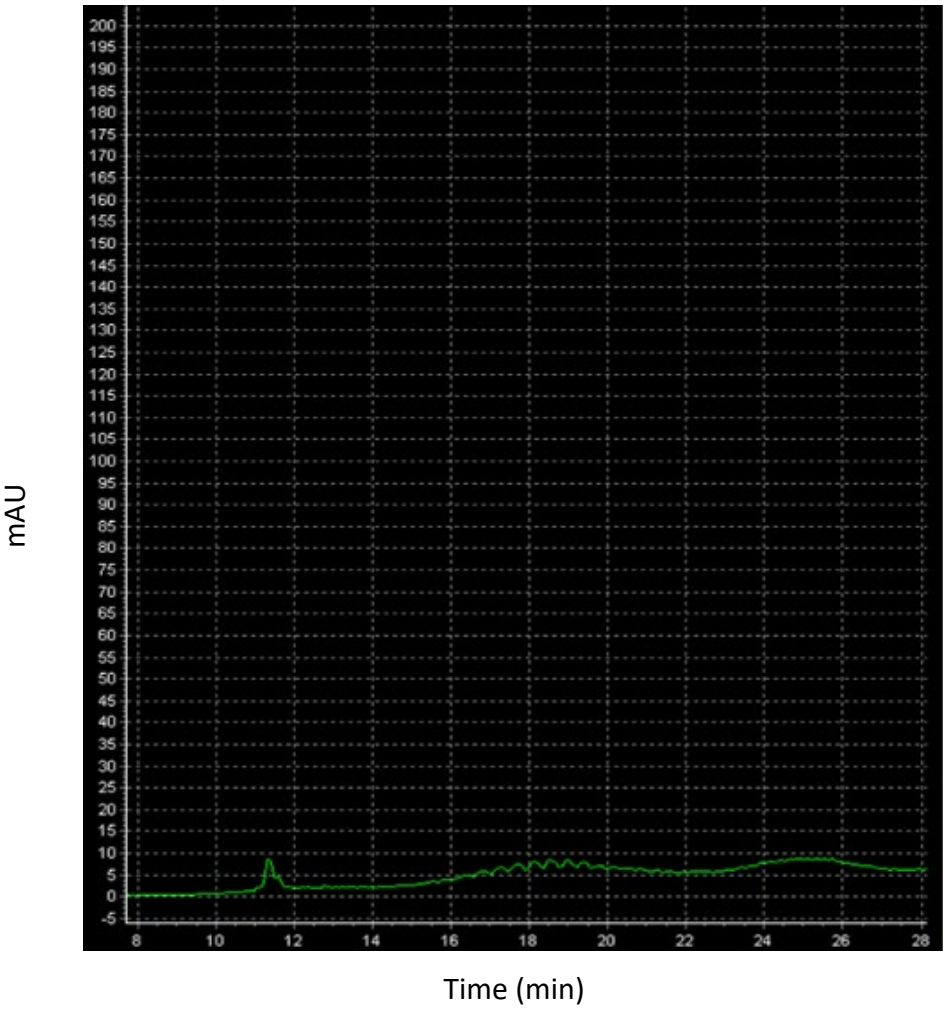


**Figure 2.19: HPLC elution profiles of DNA-PEG bioconjugation in DMF at 72 hours.** At the 72-hour time point, the HPLC chromatogram for the reaction in DMF shows a prominent peak at 11 minutes, corresponding to unconjugated DNA, with minor peaks appearing between 16 and 22 minutes, which represent initial formation of PEG-conjugated DNA species.

The efficiency of the reaction between NHS esters and amino groups is highly dependent on pH. At low pH values, the amino group becomes protonated, losing its nucleophilicity and thus its ability to attack the electrophilic carbonyl carbon of the NHS ester. As a result, conjugation does not occur under acidic conditions. On the other hand, if the pH is too high, the NHS ester becomes increasingly susceptible to hydrolysis, rapidly converting into a non-reactive carboxylic acid. This leads to a significant reduction in the yield of the desired modification, as the reactive NHS ester is depleted before it can participate in the conjugation reaction.

Optimal bioconjugation is achieved in a narrow pH window, specifically between pH 8.3 and 8.5, where the amino group remains deprotonated and nucleophilic, while the NHS ester retains sufficient stability to react efficiently (**Figure 2.20**). This pH range provides the best balance, ensuring that the reaction proceeds with high yield and minimal side reactions.

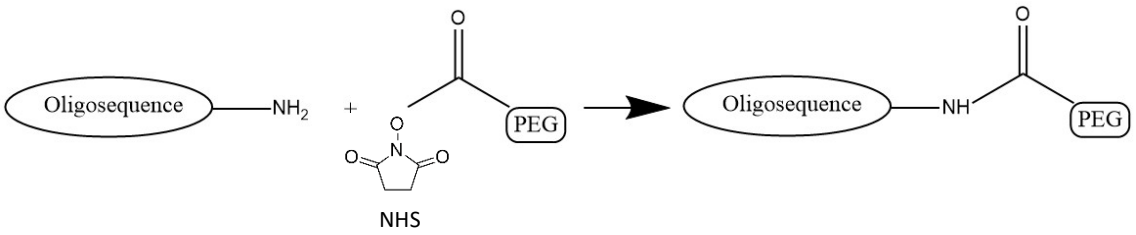


**Figure 2.20: Schematic representation of the bioconjugation reaction between the amino group of the oligonucleotide strand and the NHS ester of SH-NHS-PEG (0.8 kDa).**

To experimentally confirm the pH dependence of this reaction, the same bioconjugation protocol was tested at pH 5 and pH 9 (**Figure 2.21-22**). The HPLC chromatograms provide clear insights into the pH dependence of the bioconjugation protocol between NHS esters and amino-modified DNA.

When the reaction was performed at pH 5 (**Figure 2.21**), the chromatogram displayed a single, sharp peak eluting at approximately 11 minutes, corresponding exclusively to the unconjugated DNA. No additional peaks were observed at higher retention times, indicating the absence of PEG-conjugated DNA species. This result confirms that under acidic conditions, the amino groups on the DNA are fully protonated and thus unreactive toward the NHS ester, effectively preventing the conjugation reaction from occurring. The lack of product peaks is entirely consistent with the well-established

requirement for a deprotonated, nucleophilic amine in NHS ester–mediated coupling chemistry.

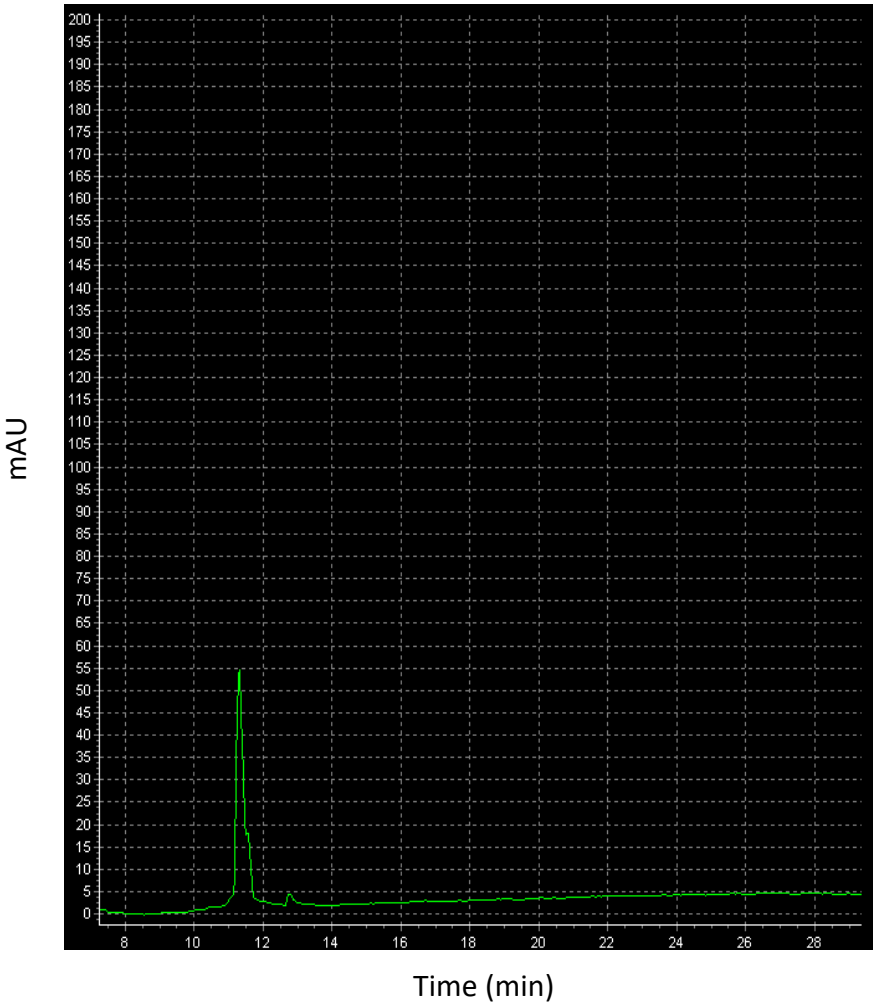


**Figure 2.21: HPLC Analysis of Bioconjugation Reaction at pH 5.** The chromatogram shows the result of the bioconjugation protocol performed at pH 5 using HPLC analysis. A single, sharp peak appears at approximately 11 minutes, corresponding to the unconjugated DNA. No additional peaks are observed at higher retention times, indicating the absence of PEG-conjugated DNA products.

In contrast, the chromatogram obtained from the bioconjugation protocol at pH 9 (**Figure 2.22**) reveals a distinctly different profile. Here, a sharp peak at approximately 11–12 minutes again marks the presence of residual unconjugated DNA. More importantly, a series of overlapping peaks appears between 16 and 20 minutes, each representing DNA strands successfully conjugated with one or more PEG molecules. The emergence of these product peaks demonstrates that bioconjugation does occur at pH 9. The simultaneous presence of both product and starting material peaks indicates partial conversion.

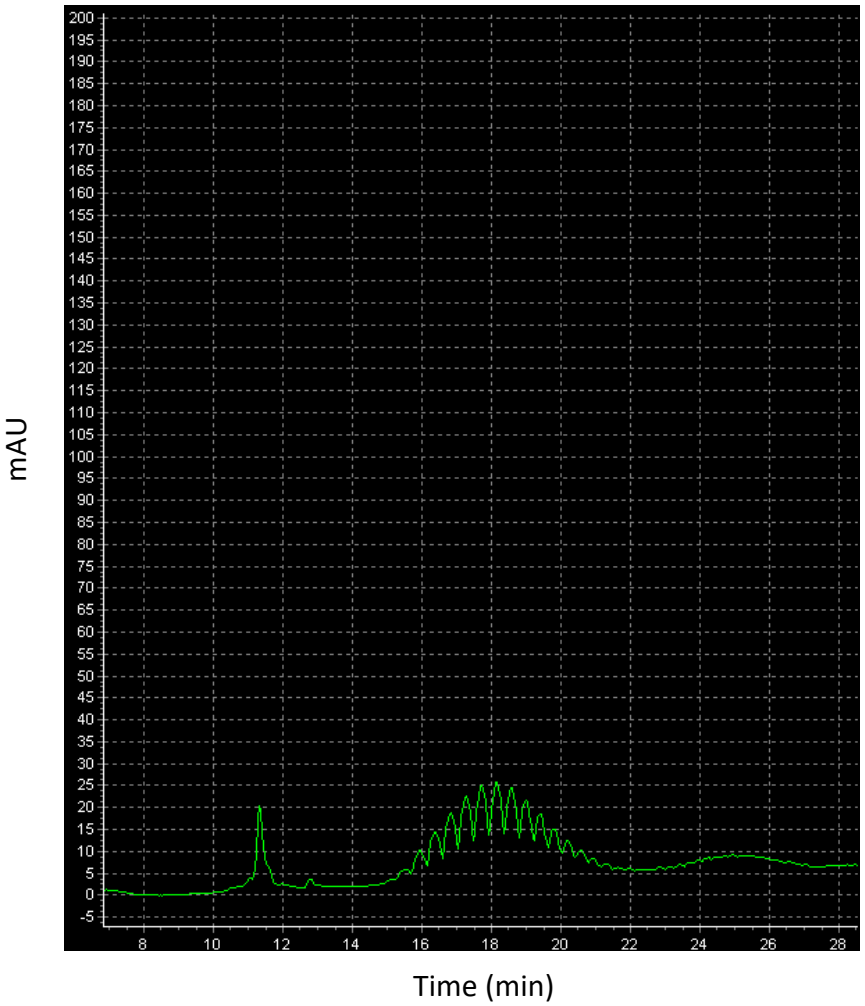


**Figure 2.22: HPLC Analysis of Bioconjugation Reaction at pH 9.** The chromatogram displays the outcome of the bioconjugation protocol at pH 9. A peak at 11–12 minutes corresponds to the remaining unconjugated DNA, while a series of overlapping peaks between 16 and 20 minutes indicate the presence of PEG-conjugated DNA species

### 2.3.2.2 Conjugation of Synthesized ONs with SH-PEG-NHS

The synthesized and characterized ONs sequences were subjected to conjugation with SH-PEG-NHS (0.8 kDa) following the protocol described in detail in **Section 5.4**. A major concern that was raised with the conditions required for the conjugation was that the DMSO used to dissolve the PEG can cause the nanoparticles to aggregate, preventing further functionalization. To overcome this, the samples were purified by HPLC under the conditions detailed in **Section 5.6.1.2**, effectively removing the DMSO and minimizing the risk of nanoparticle instability.

The chromatogram (**Figure 2.23**), acquired using a HPLC system with photodiode array (PDA) detection at 260 nm, presents the separation of analytes over a 20-minute retention time window (x-axis) with detector response measured in milli-absorbance units (mAU, y-axis). The chromatogram reveals several key features that provide insight into the composition of the reaction mixture.

The first notable feature is a doublet peak appearing at approximately 6 minutes, which corresponds to the DMSO solvent front. This early-eluting signal is characteristic of DMSO, known for its strong UV absorbance and rapid elution from the C18 column. The presence of this peak serves as a marker for the solvent used in the reaction and confirms proper sample injection and chromatographic conditions.

At 7.5 minutes, a sharp and well-defined peak is observed, representing the unconjugated DNA. The intensity of this peak provides a direct measure of the efficiency of the conjugation reaction, with lower intensity indicating more complete modification.

Between 8 and 10 minutes, the chromatogram reveals a series of broad, overlapping peaks that correspond to DNA strands modified with PEG. The diversity and width of these peaks indicate the presence of DNA conjugated to PEG molecules with different molecular weights, reflecting the inherent heterogeneity of the conjugation process. This region serves as the main indicator of successful bioconjugation, confirming the formation of the intended DNA-PEG products. Vertical black lines labelled “Fraction” along the x-axis indicate automated fraction collection during the run, targeting this region for downstream processing.  Post-collection, the fractions containing the product were combined and concentrated to dryness. Once dry, the product was resuspended, and the concentration was quantified.

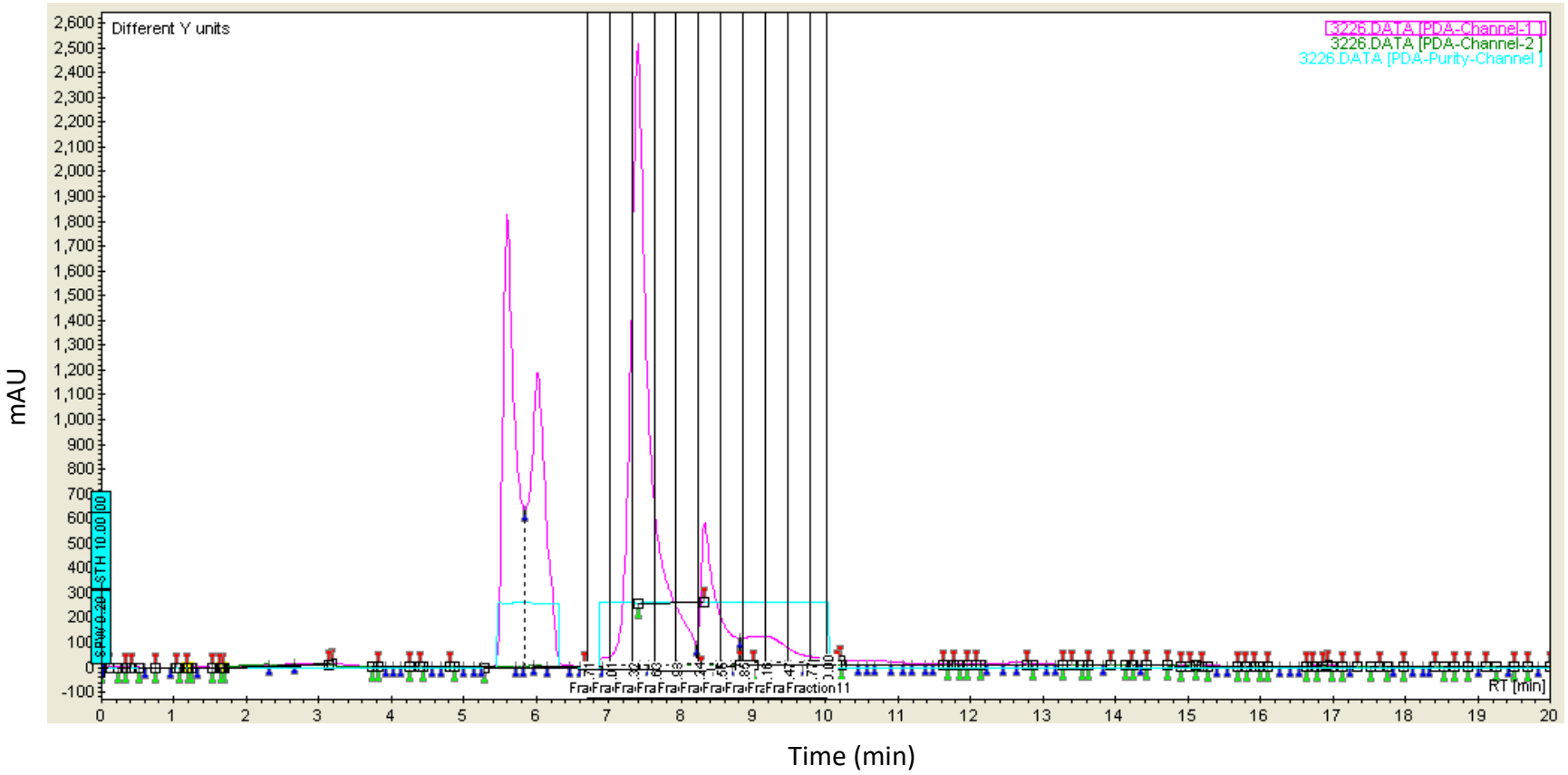


**Figure 2.23: HPLC chromatogram of the DNA-PEG conjugation reaction mixture, analysed using a HPLC system with photodiode array (PDA) detection at 260 nm.** The y-axis represents absorbance in milli-Absorbance Units (mAU) and the x-axis shows retention time in minutes. The magenta trace (PDA-Channel-1) displays the main separation profile, highlighting a doublet peak at approximately 6 minutes corresponding to DMSO, a sharp peak at 7.5 minutes for unconjugated DNA, and a series of broad, overlapping peaks between 8- and 10-minutes representing PEG-conjugated DNA species. A horizontal cyan line at approximately 250 mAU represents a threshold for peak detection. Vertical black lines labelled “Fraction” indicate points where sample fractions were collected

Mass spectrometry was employed to further characterize the samples and confirm the successful conjugation of DNA to SH-PEG-NHS. The LCMS UV trace of the collected fractions (**Figure 2.24**) revealed a distribution of DNA species conjugated to PEG molecules of varying lengths, reflecting the pattern previously observed in the HPLC chromatogram (**Figure 2.22**). A notable peak at 4.45 minutes corresponded to the unmodified DNA sequence ON3, which lacked the 5' amino modification necessary for PEG coupling (**Figure 2.25**). The theoretical mass for this unmodified ON3 was 8961.2 Da, and the measured mass obtained by MS was 8959 Da, confirming the identity of this residual unmodified DNA. This incomplete amino modification during synthesis resulted in a fraction of the DNA that could not react with the PEG molecules.

To improve the purification process, the different fractions collected from the HPLC were carefully analysed using LC-ESI-MS (**Figure 2.26**). The first chromatogram (**Figure 2.26-1)** displays the oligonucleotide prior to bioconjugation, while the subsequent chromatograms (**Figures 2.26-2 to 2.26-5**) show the analysis of fractions collected after bioconjugation and HPLC purification. This approach allowed for more precise selection of fractions containing the desired DNA-PEG conjugates and enabled effective separation from unreacted single-stranded DNA, as detailed in **Appendix D.** As a result, the final product was highly purified and well-suited for downstream applications, such as nanoparticle functionalization.

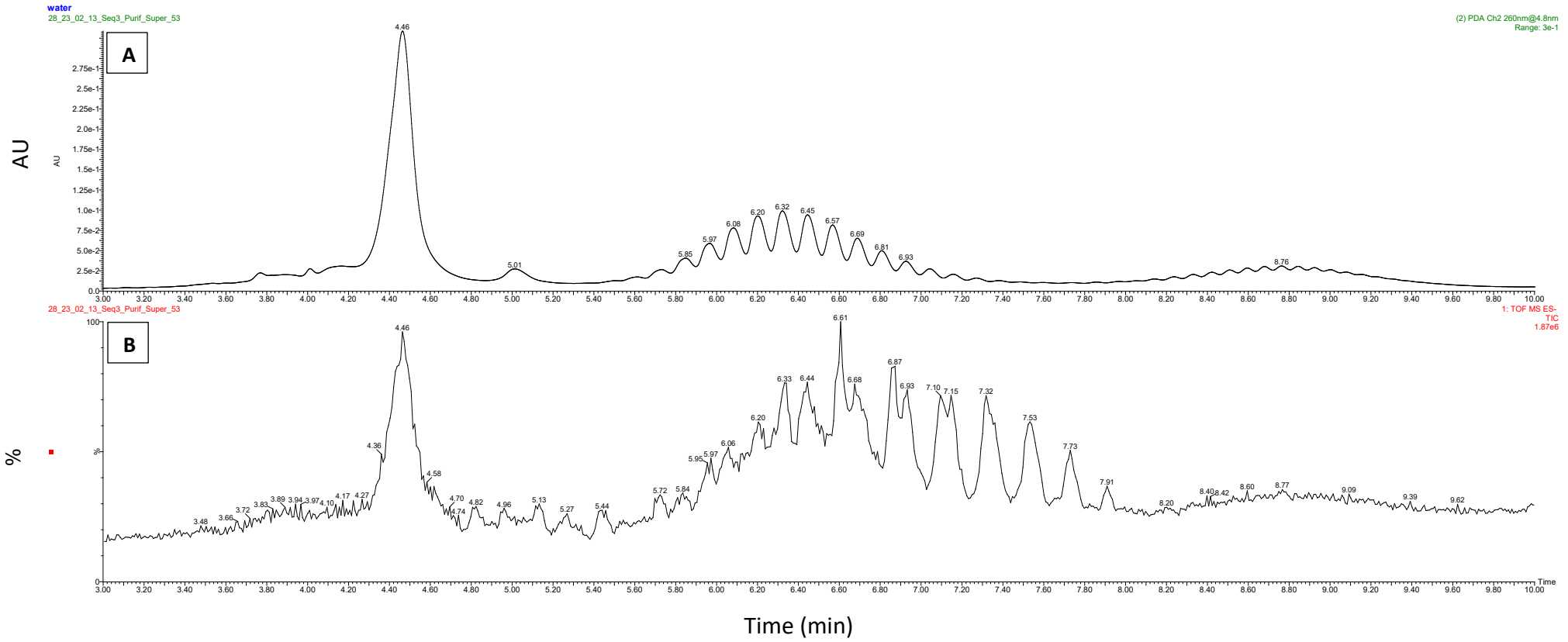


**Figure 2.24: LC-ESI-MS analysis of the purified bioconjugation product.** (A) UV Chromatogram (260 nm) of Purified DNA-PEG Conjugate Sample (B) Total Ion Chromatogram (TIC) from LC-MS Analysis of DNA-PEG Conjugate Sample**:** The prominent peak at 4.46 minutes in both traces corresponds to the unmodified DNA (ON3) lacking the amino modification. A series of broad, overlapping peaks between 5 and 8 minutes, visible in both the UV and TIC traces, represent DNA conjugated to PEG molecules of varying length.

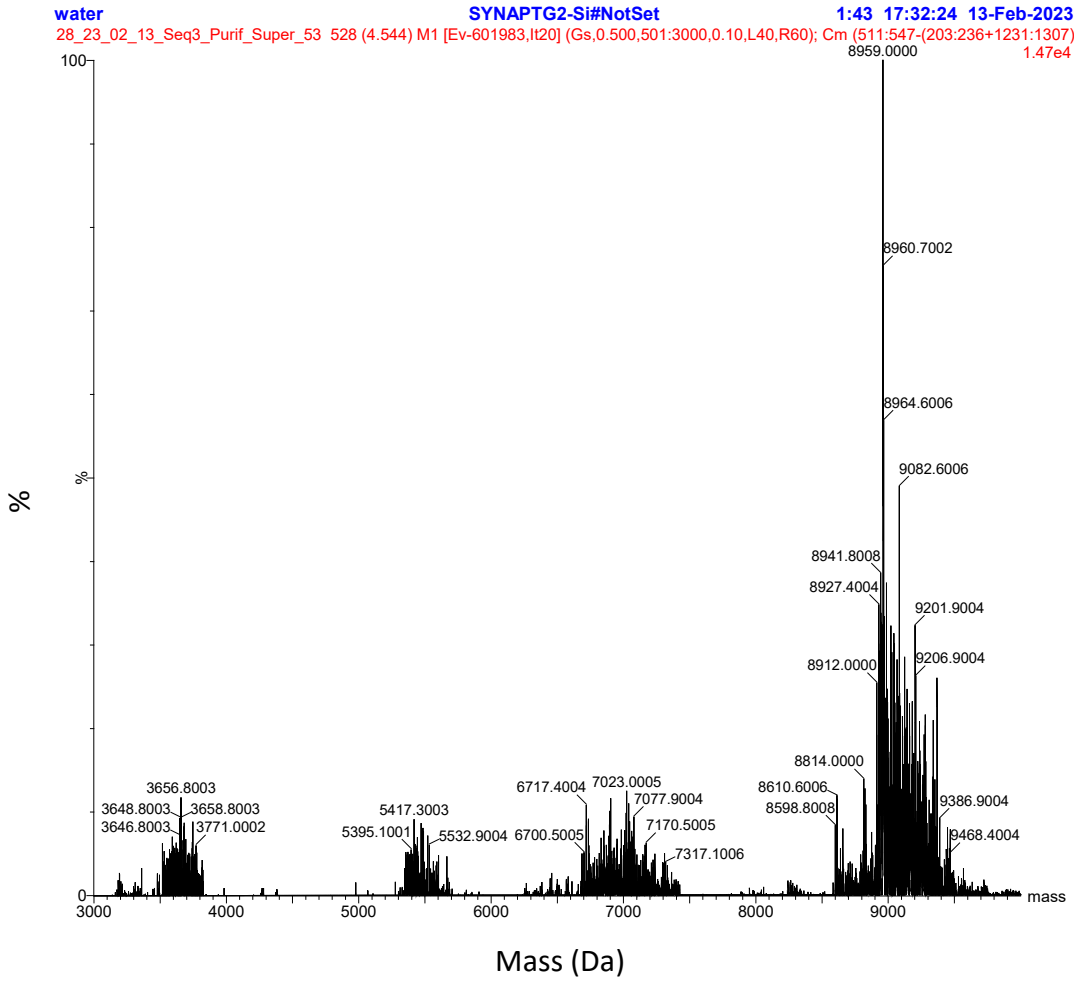


**Figure 2.25: Mass spectrum deconvolution of the purified bioconjugation product:** Mass spectrum deconvolution of the peak eluting at 4.46 minutes present in Figure 2.21, confirming the presence of unmodified ON3 DNA. The dominant peak at 8959.0 Da closely matches the theoretical mass of 8961.2 Da for unconjugated ON3 lacking the 5' amino modification. Additional peaks at lower intensities represent sodium adducts and fragments of the primary sequence. Data was acquired on a SYNAPT G2-S mass spectrometer using electrospray ionization in negative mode.

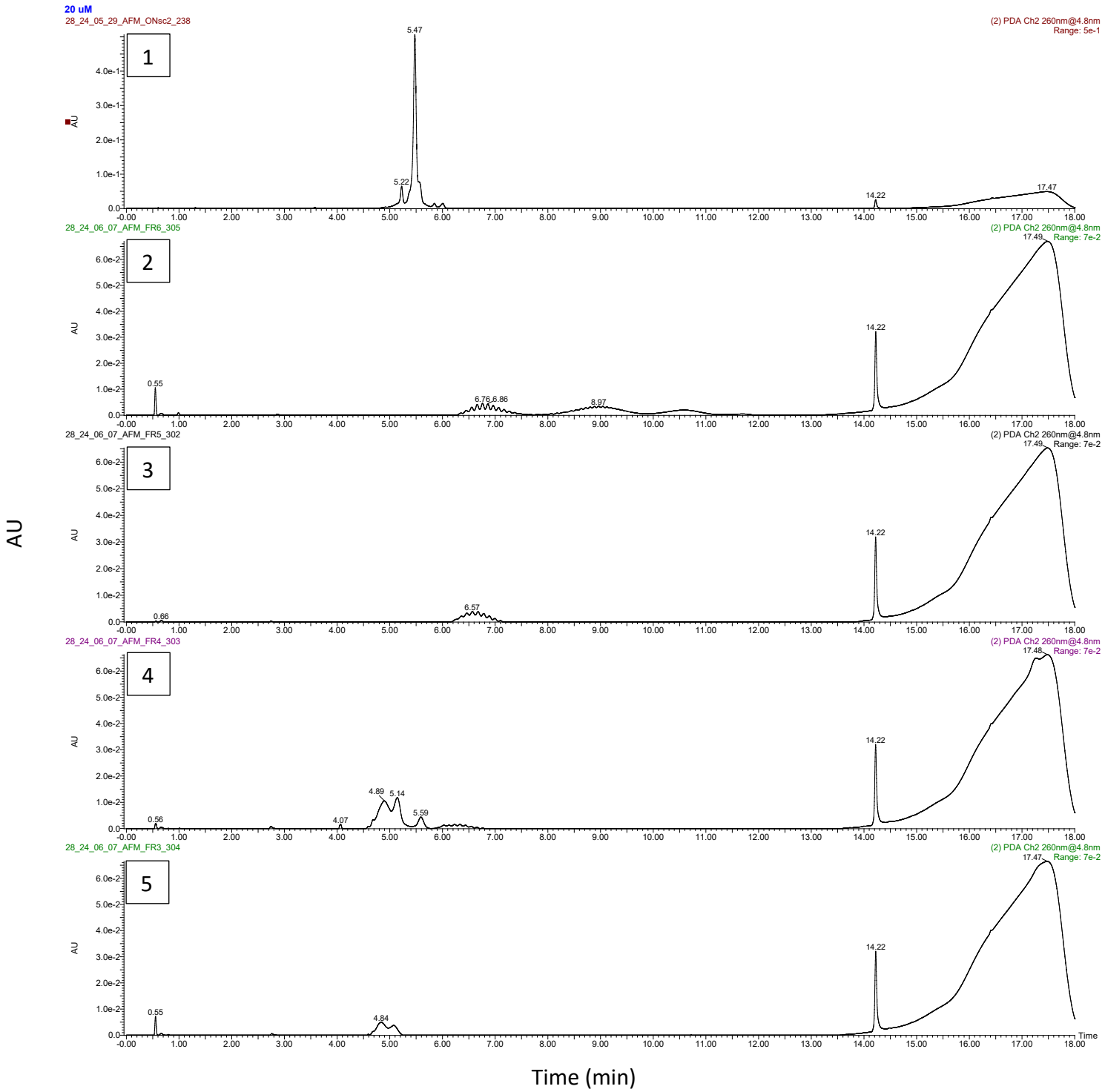


**Figure 2.26: Comparative UV chromatograms (260 nm) from LC-ESI-MS analysis of purified fractions of the bioconjugation product.** Chromatogram 1 (top) displays the unconjugated DNA, characterized by a sharp peak at 5.47 minutes. Chromatograms 2 and 3, which correspond to fractions collected after bioconjugation and HPLC purification, show a series of broad, overlapping peaks between 6 and 12 minutes, indicating the presence of DNA conjugated to PEG molecules of varying lengths. Chromatograms 4 and 5 reveal additional peaks between 4 and 6 minutes, likely corresponding to DNA fragments that were not conjugated to PEG or to degradation products. All analyses were performed using LC-ESI-MS with PDA detection at 260 nm, allowing for precise identification and selection of fractions enriched in the desired DNA-PEG conjugates for downstream nanoparticle functionalization applications.

## 2.4 Functionalization of the NPs with the PEGylated ASOs Conjugates

### 2.4.1 Design of PEG-ASO AuNPs Delivery Systems

The objective of this step in the project was to bioconjugate SH-PEG-ASO sequences to the surface of nanoparticles, thereby forming a nano-delivery system for subsequent cellular assays. AuNPs with a diameter of 15 nm were chosen for these experiments due to their superior homogeneity and reproducibility compared to AgNPs, as demonstrated in **Section 2.1.2**. The functionalization process involved coating the AuNPs with a self-assembled monolayer composed of a mixture of SH-PEG-ASO and SH-PEG-methyl, following the protocol described in **Section 5.5**.

The 0.8 kDa PEG linker was selected to balance nanoparticle stability with oligonucleotide accessibility. Shorter PEG chains minimize steric hindrance, enabling the conjugated ssDNA to interact effectively with its molecular target while still providing sufficient colloidal stabilization. Although longer PEG chains enhance stealth properties, they can shield the oligonucleotide and reduce hybridization efficiency. Recent studies have shown that PEG chain length significantly influences ligand accessibility, with shorter PEG spacers generally improving the ability of surface-tethered ligands, such as oligonucleotides, to interact with their targets[190]. This design consideration ensures that the ssDNA remains accessible for molecular recognition while maintaining the stability of the nanoparticle construct.

To thoroughly characterize the resulting nanoconstructs, several analytical techniques were employed. The AuNPs were analysed using UV-Vis spectroscopy, DLS, TEM both before and after the bioconjugation process.

## 2.4.2 Results and Discussion

### 2.4.2.1 Quantification of DNA Loading and Coupling Efficiency on Functionalized Gold Nanoparticles

First step was to quantify the amount of DNA attached to the NPs, to understand the efficiency of the reaction. 7 mL of the reaction mixture were filtered using a centrifugal filter unit. This process concentrated the NPs on top of the filter while allowing unreacted PEG and other excess materials to pass through. The filtration process was repeated multiple times until the NPs volume was reduced to 0.5 mL.

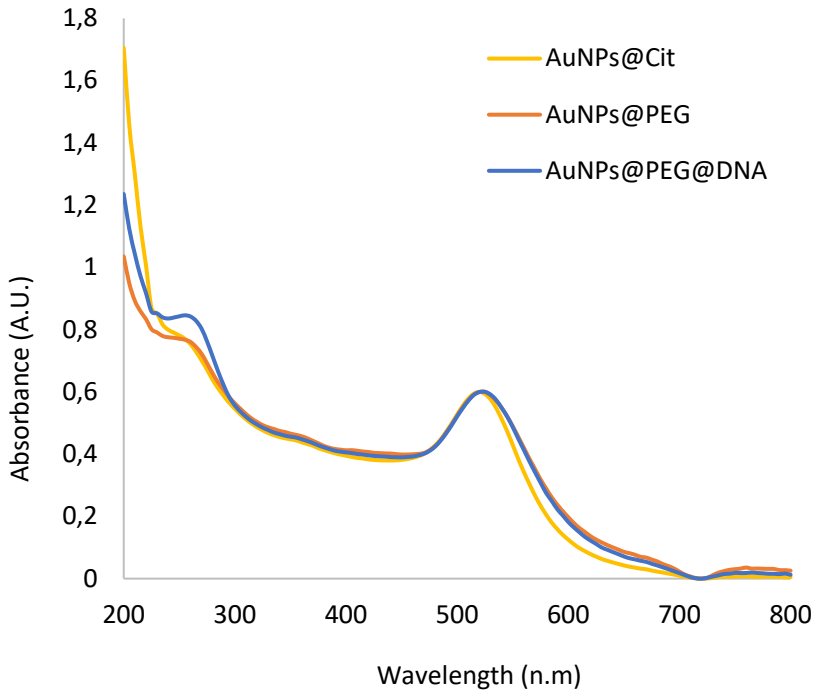


**Figure 2.27: Comparison UV-Vis analysis of Gold nanoparticles after Bioconjugation of SH-PEG-ON5 with AuNPs functionalized with citrate and PEG.**

UV-Vis spectroscopy was used to confirm and quantify the amount of ssDNA successfully biofunctionalized onto AuNPs via SH-PEG-NHS linkers (**Figure 2.27**). To ensure the measurement reflected only the DNA attached to the nanoparticles, the absorbance signal specific to DNA was isolated by subtracting the background signals from control samples: AuNPs@Cit and AuNPs@PEG.

The absorbance at 260 nm, characteristic of ssDNA, was measured for the AuNPs@PEG@DNA samples. To correct for any background interference from the nanoparticles themselves, the absorbance at 520 nm (the plasmon resonance peak of AuNPs) was also recorded. The DNA-specific absorbance was then determined by subtracting the 520 nm value from the 260 nm value, and further subtracting the absorbance measured for the control samples at 260 nm. This approach ensured that only the signal from the DNA conjugated to the nanoparticles was considered.

To quantify the amount of DNA, the corrected absorbance values were averaged across three independent measurements. The concentration of ssDNA was then calculated using the Lambert-Beer law, taking into account the DNA extinction coefficient and an optical path length of 1 cm. This allowed for the determination of the molar concentration of ssDNA present in the AuNPs@PEG@DNA colloid.

The total number of nanomoles of DNA attached to the nanoparticles was calculated based on this concentration and the total volume of the colloid. This value was compared to the initial amount of DNA added during the biofunctionalization reaction to determine the coupling efficiency, expressed as a percentage. The same procedure was applied to different DNA sequences to produce various batches of biofunctionalized nanoparticles for use in subsequent cell assays. It was observed that the coupling efficiency varied depending on the DNA sequence, likely due to differences in the purity of the DNA stock solutions.

LC-ESI-MS analysis of purified bioconjugation products revealed uncoupled DNA in stock solutions, as shown by comparative UV chromatograms (260 nm) in **Figure 2.26** (**panels 2-5**). These unbound DNA strands lack the critical thiol group required for attachment to the nanoparticles via PEG linkers. As a result, only a portion of the DNA in the stock solution can bind to the nanoparticles, directly reducing biofunctionalization efficiency.

**Table 2.4: Coupling efficiency and number of nanomols of SH-PEG-ASO attached to nanoparticles during the biofunctionalization processes conducted on 12/07/2024.**

| BIOFUNCIONALIZATION 12/07/24 | | | |
|---|---|---|---|
| **Sequence** | **Total DNA used for the Biofunctionalization (nanomols)** | **Total DNA in the NPs after the Biofunctionalization (nanomols)** | **% DNA attached in the NPs solution** |
| **SC** | 18.72 | 11.39 | 60.83 |
| **ON1** | 17.05 | 13.41 | 78.64 |
| **ON2** | 25.54 | 9.46 | 37.02 |
| **ON3** | 14.30 | 9.96 | 69.65 |
| **ON4** | 13.03 | 5.96 | 45.70 |
| **ON5** | 14 | 7.08 | 50.53 |

The number of oligonucleotide strands coupled onto the AuNPs can now be calculated using the number of moles of DNA. The calculation utilized the number of nanomoles previously determined for ON1 was used (**Table 2.4**). The first step involved converting the number of nanomoles of DNA into molecules to determine the number of sequences present in the solution.

$$13.41\ nmols \times \frac{1\ mol}{10^9\ nmol} \times \frac{6.022 \times 10^{23}}{1\ mol} = 8.08 \times 10^{15}\ sequences$$

The subsequent step involved calculating the number of AuNPs present in the colloid. This was achieved by multiplying the concentration of the stock solution ($5.52 \times 10^{12}$ NPs/mL) by the volume of AuNPs used in the reaction, which was 4.7 mL.

$$5.52 \times 10^{12}\ \frac{NPs}{mL} \times 4.7\ mL = 2.59 \times 10^{13}\ NPs$$

Finally, the number of sequences was divided by the number of NPs to estimate the average number of sequences that were attached per NPs:

$$\frac{8.08 \times 10^{15}\ DNA\ sequences}{2.59 \times 10^{13}\ NPs} = 311.80\ \frac{DNA\ sequences}{NPs}$$

In this assay, the number of sequences coupled per nanoparticle was estimated at 311.80. These calculations were then used to approximate the ratio in the different biofunctionalization for each sequence (**Table 2.5**).

**Table 2.5: Ratio of number of SH-PEG-ASO sequences attached per nanoparticle following the biofunctionalization processes conducted on 12/07/2024.**

| BIOFUNCIONALIZATION 12/07/24 | |
|---|---|
| **Sequence** | **Ratio sequence per Nanoparticle** |
| **SC** | 264.83 |
| **ON1** | 311.80 |
| **ON2** | 219.95 |
| **ON3** | 231.58 |
| **ON4** | 138.58 |
| **ON5** | 164.62 |

### 2.4.2.2 Post-Conjugation Characterization of AuNPs

The AuNPs were analysed using a UV-Vis spectroscopy, DLS, and TEM both before and after the conjugation process. The UV-Vis spectra (**Figure 2.28**) display that the DNA-bioconjugated AuNPs exhibit a spectrum similar to that of PEG-functionalized AuNPs. Both display a slight shift due to the PEG coating compared to citrate-covered AuNPs which presents an absorbance peak at 520 nm, as previously discussed in **Section 2.1.2**.

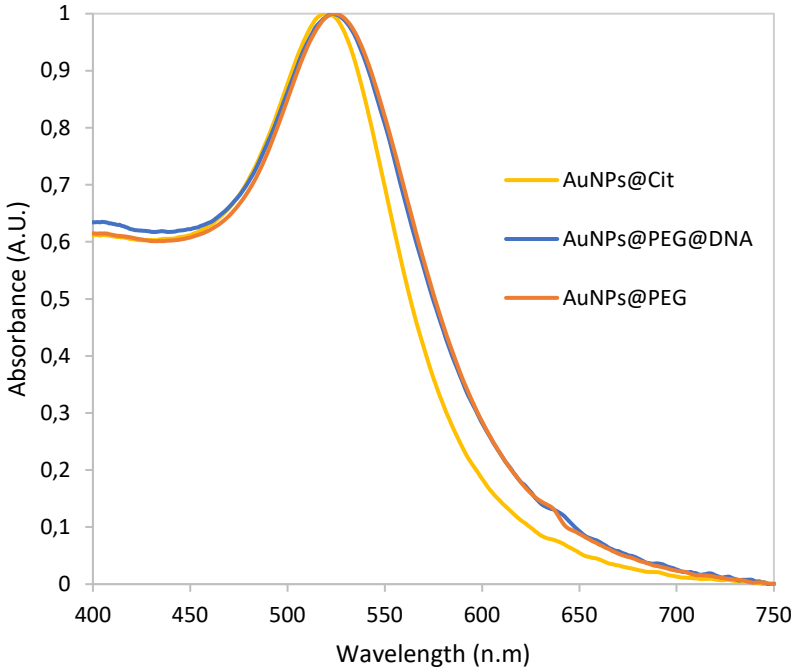


**Figure 2.28: Comparison UV-Vis analysis of Gold nanoparticles after Bioconjugation of the SH-PEG-ASO with the AuNPs functionalized with citrate and with PEG.**

Regarding the DLS analysis (**Figure 2.29**), functionalized NPs exhibit a comparable shift relative to the citrate-capped AuNPs, similar to the UV-Vis measurements. Specifically, the AuNPs@Cit (citrate-capped AuNPs) have a hydrodynamic diameter of 21.8 nm, whereas both AuNPs@PEG (PEG-functionalized AuNPs) and AuNPs@PEG@DNA (PEG-functionalized AuNPs bioconjugated with DNA) have a hydrodynamic diameter of 26.1 nm. In terms of polydispersity, the polydispersity index decreases from 0.185 for AuNPs@Cit to 0.154 for both PEG and PEG-DNA functionalized AuNPs, indicating that the final colloidal NPs exhibit a high degree of homogeneity.

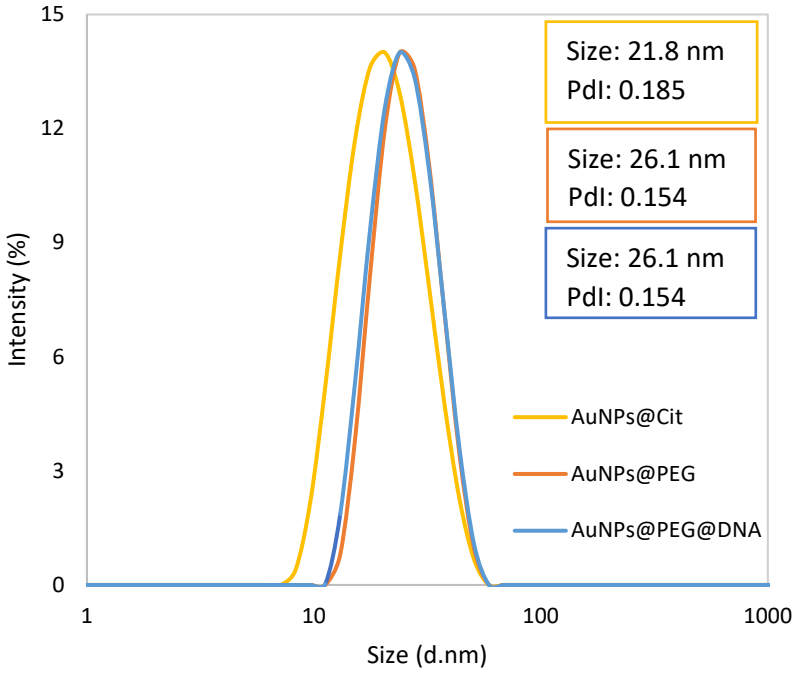


**Figure 2.29: Comparison of DLS analysis of AuNPs after bioconjugation of SH-PEG-ASO with AuNPs functionalized with citrate and PEG.**

TEM analysis revealed that the core size and shape of the NPs remain unchanged following bioconjugation with SH-PEG-ASO (**Figure 2.30**). However, the presence of PEG on the surface induces interactions between the molecules, resulting in the formation of a network that reorganizes the NPs, similar to what was observed during the functionalization of AuNPs with SH-PEG-methyl.

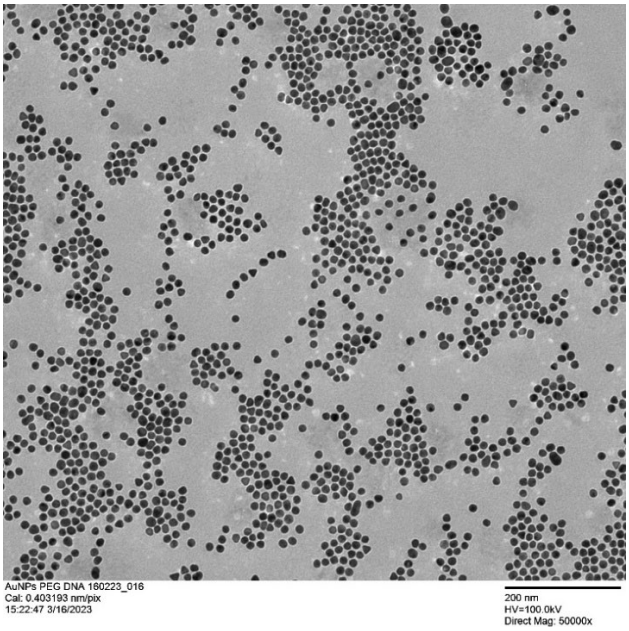


**Figure 2.30: TEM analysis of AuNPs after bioconjugation of the SH-PEG-ASO.**

To assess the colloidal stability of the nanoparticles and determine whether aggregation occurs over time, a 15-day assay was performed using UV-Vis spectroscopy (**Figure 2.31**). The nanoparticles were analysed at three key stages of functionalization: AuNPs@Cit (**Figure 2.31A**), AuNPs@PEG (**Figure 2.31B**) and AuNPs@PEG@ssDNA (**Figure 2.31C**). Aggregation of nanoparticles typically disrupts their LSPR, leading to reduced extinction cross-sections and increased light scattering. These changes are reflected in the UV-Vis spectrum as a flattened curve with diminished peak intensity and broader features.

Throughout the 15-day period, the absorbance at 520 nm was closely monitored. The high degree of spectral overlap observed among all three nanoparticle states indicates that no significant aggregation occurred, and the samples remained stable for more than two weeks. This stability is particularly important for ensuring reliable performance in downstream applications, as it confirms that both PEG and ssDNA coatings effectively preserve the colloidal integrity of the nanoparticles over time.

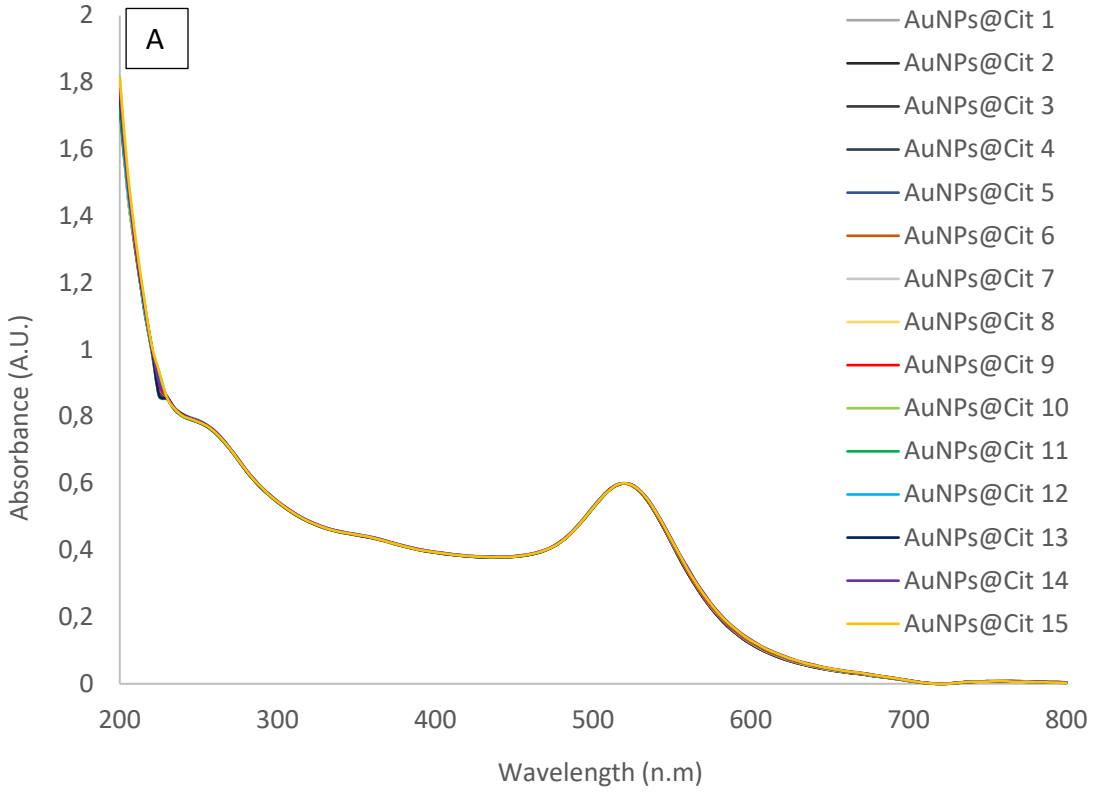

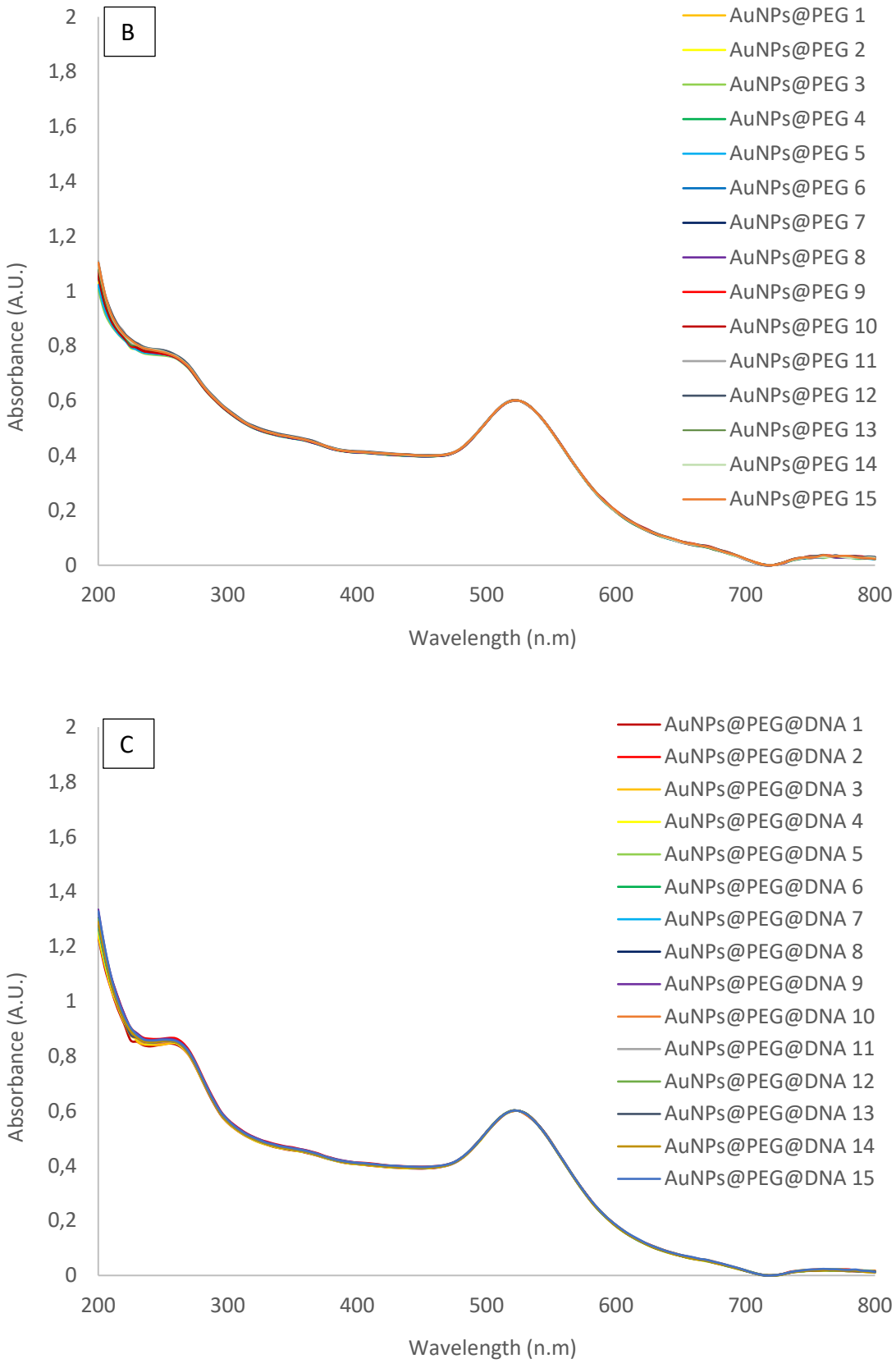


**Figure 2.31: UV-Vis spectra of AuNPs monitored over 15 days in three different functionalization states: (A) AuNPs@Cit, (B) AuNPs@PEG, and (C) AuNPs@PEG@ssDNA.**

# Chapter 3: In vitro testing of the nano-delivery systems

## 3.1 Introduction

The *c-myc* oncogene encodes a transcription factor that plays a pivotal role in cell proliferation, growth, and apoptosis[69]. Aberrant overexpression of *c-myc* is frequently observed in a wide range of cancers and is closely associated with uncontrolled cell division and tumour progression. Therefore, strategies aimed at reducing *c-myc* expression are of significant therapeutic interest, as downregulation of *c-myc* can inhibit tumour growth and promote cancer cell apoptosis[191].

In this chapter, the synthetic sequences described in **Chapter 2** were evaluated for their ability to hybridize with various regions of the IRES structure of *c-myc* mRNA, thereby potentially reducing its translation and overall expression. To establish the most effective and efficient transfection conditions, initial optimization was carried out using free, unconjugated ssDNA. The transfection protocol was optimized for time and cost efficiency by varying several parameters:

- Selection of Cell Lines for Oligonucleotide Transfection
- Optimal HeLa Cell Seeding Density
- Optimal Duration for Oligonucleotide Transfection Assays
- Evaluation of Transfection Reagents for Optimal Efficiency
- Determination of Oligonucleotide Concentration for Transfection
- Optimal Concentration of Transfection Reagent for Oligonucleotide Delivery

The results from these transfections served as a control to evaluate the impact of each sequence. Subsequently, the same methodology was applied to transfect sequences conjugated to synthesized gold nanoparticles (AuNPs@PEG@ssDNA), as detailed in **Chapter 2**, allowing for a direct comparison between the two delivery methods.

The AuNP-based delivery system offers several advantages over traditional methods, including enhanced cellular uptake, improved stability of the ONs, and potentially greater specificity and efficiency in targeting *c-myc* mRNA[192]. By facilitating more effective delivery of antisense sequences to the target cells, these nanoparticles may significantly improve the downregulation of *c-myc* expression, offering a promising approach for future therapeutic applications[193194].

To thoroughly characterize the effects of the different oligonucleotides and delivery strategies, various molecular biology assays and techniques were employed, including qPCR, Western Blot, Flow Cytometry, Microscopy analysis, and Cytotoxicity assays. The detailed experimental procedures for these techniques are outlined in **Chapter 5.7**.

# 3.2 Results and Discussion

## 3.2.1 Oligonucleotide Transfection Optimization

### 3.2.1.1 Lipofectamine transfection optimization

#### 3.2.1.1.1 Selection of Cell Lines for Oligonucleotide Transfection

When Stoneley et al. discovered the *c-myc* IRES in 1998[195], their experiments were conducted using both HepG2 and HeLa cells. Subsequently, Stoneley et al. investigated *c-myc* IRES activity across various cell lines. Their analysis demonstrated that HeLa cells exhibited the highest activity of *c-myc* IRES-mediated internal initiation among the cell lines tested, which included Cos-7, MCF7, Balb/c-3T3, MEL, MRC5, HK293, GM637, HeLa, and HepG2. Additionally, previous experience within the laboratory group had shown efficient transfection results in HEK293 and HeLa cells. Therefore, it was decided to initiate the study of oligonucleotide activity using HeLa cells.

#### 3.2.1.1.2 Optimization of HeLa Cell Seeding Density and the Optimal Duration for Oligonucleotide Transfection Assays

The number of HeLa cells seeded for the experiment was optimized because translation rates have been shown to decrease once cells reach confluency[196]. High levels of confluency increase cellular stress, leading to abnormal translation levels.

Therefore, assays should be conducted in plates where cells maintain 60% to 80% confluency.

To determine the optimal number of cells per well, 300,000; 500,000; 700,000; and 1,000,000 cells were seeded in a 6-well plate. Cells were transfected after 24 hours and monitored every 24 hours post-transfection. The confluency was measured by observing the cell culture under a light microscope and estimating the percentage of the surface area covered by cells compared to the total area of the well.

After 48 hours, wells with 700,000 and 1,000,000 cells were over 90% confluent. After 72 hours, only wells seeded with 300,000 cells maintained approximately 90% confluency, while the others reached full confluency.

Based on these results, it was concluded that the optimal seeding density for HeLa cells in a 6-well plate is 300,000 cells per well. This number was adjusted accordingly for assays conducted in plates with larger or smaller growth surface areas.

Since wells seeded with 300,000 cells reached approximately 90% confluency by 72 hours-the upper threshold for reliable transfection-subsequent analyses were focused on earlier time points, specifically 24- and 48-hours post-transfection. This approach was chosen to avoid the confounding effects associated with overconfluent cultures and to ensure optimal assay conditions.

#### 3.2.1.1.3 Comparative Evaluation of Transfection Reagents for Optimal Efficiency

For this assay, Lipofectamine™ 3000 Reagent was selected as the most efficient and cost-effective option compared to other transfection agents. Lipofectamine™ 3000 demonstrates high efficiency across a wide range of cell types, including hard-to-transfect cells. Alternative options available on the market include PEI, which offers moderate efficiency; jetPRIME, which is effective for plasmid DNA; and Lipofectamine™ 2000, which is comparable but slightly less efficient than Lipofectamine™ 3000.

Lipofectamine™ 3000 also exhibits relatively low cytotoxicity, particularly when compared to PEI and Lipofectamine™ 2000. While reagents such as Fugene and jetPRIME have lower cytotoxicity, they may be less effective in certain cell lines.

Furthermore, Lipofectamine™ 3000 is highly versatile, supporting the transfection of DNA, RNA, and co-transfections (e.g., DNA + siRNA) in both adherent and suspension cells. In contrast, PEI is primarily suited for DNA transfections, Fugene is focused on DNA delivery, and jetPRIME supports some co-transfections but lacks the broad applicability of Lipofectamine™ 3000.

The simple protocol and flexible DNA/reagent ratio of Lipofectamine™ 3000 make it suitable for both small- and large-scale transfections. In comparison, PEI requires optimization and preparation of "in-house" reagents, while Fugene and jetPRIME are user-friendly but less adaptable to optimization. Although all these reagents are scalable, they often require more protocol adjustments than Lipofectamine™ 3000.

Finally, while Lipofectamine™ 3000 is relatively expensive compared to reagents like PEI or Fugene, its high stability and ability to produce reproducible results make it the optimal choice for transfecting the various oligonucleotide sequences in this study.

#### 3.2.1.1.4 Determination of Oligonucleotide Concentration for Transfection

According to the commercial protocol provided by Invitrogen for Lipofectamine™ 3000 Reagent transfection, the recommended amount of DNA for a 6-well plate is 2,500 ng. Consequently, this value was selected as the optimal amount for the transfection assays conducted in this project. However, while the total amount of DNA remains constant, the concentration varies depending on the sequence, as it is directly influenced by the molecular mass of each oligonucleotide. The calculations for the concentration of the transfected sequences per well are detailed below:

**Scramble**

$$2500\ ng \times \frac{1\ g}{10^9\ ng} \times \frac{1\ mol}{9140.3\ g} \times \frac{10^9\ nmols}{1\ mol} = 0.27\ nmols$$

$$x = \frac{0.00027\ \mu mols}{0.00225\ L} = 0.12\ \mu M$$

**ON1**

$$2500\ ng \times \frac{1\ g}{10^9\ ng} \times \frac{1\ mol}{9151.3\ g} \times \frac{10^9\ nmols}{1\ mol} = 0.27\ nmols$$

$$x = \frac{0.00027\ \mu mols}{0.00225\ L} = 0.12\ \mu M$$

**ON2**

$$2500\ ng \times \frac{1\ g}{10^9\ ng} \times \frac{1\ mol}{9221.4\ g} \times \frac{10^9\ nmols}{1\ mol} = 0.27\ nmols$$

$$x = \frac{0.00027\ \mu mols}{0.00225\ L} = 0.12\ \mu M$$

**ON3**

$$2500\ ng \times \frac{1\ g}{10^9\ ng} \times \frac{1\ mol}{9140.3\ g} \times \frac{10^9\ nmols}{1\ mol} = 0.27\ nmols$$

$$x = \frac{0.00027\ \mu mols}{0.00225\ L} = 0.12\ \mu M$$

**ON4**

$$2500\ ng \times \frac{1\ g}{10^9\ ng} \times \frac{1\ mol}{7433.9\ g} \times \frac{10^9\ nmols}{1\ mol} = 0.34\ nmols$$

$$x = \frac{0.00034\ \mu mols}{0.00225\ L} = 0.15\ \mu M$$

**ON5**

$$2500\ ng \times \frac{1\ g}{10^9\ ng} \times \frac{1\ mol}{9303.4\ g} \times \frac{10^9\ nmols}{1\ mol} = 0.27\ nmols$$

$$x = \frac{0.00027\ \mu mols}{0.00225\ L} = 0.12\ \mu M$$

#### 3.2.1.1.5 Determining the Optimal Concentration of Transfection Reagent for Oligonucleotide Delivery

According to the commercial protocol from Invitrogen, the recommended volume of Lipofectamine™ 3000 Reagent per well in a 6-well plate ranges from 3.75 to 7.5 µL. To determine the optimal concentration for transfecting oligonucleotides, two assays were conducted: RT-qPCR and a cytotoxicity assay. In these experiments, three different volumes of the transfection agent were tested: 3.75, 5.63, and 7.5 µL.

Reverse transcription quantitative PCR (RT-qPCR) is considered the gold standard for quantifying mRNA levels in antisense ASO-treated cells or tissues. It is extensively utilized in research, diagnostics, and clinical applications due to its high sensitivity, specificity, and ability to quantitatively measure nucleic acids. In this context, RT-qPCR was employed to evaluate the effectiveness of oligonucleotides in modulating target mRNA levels compared to untreated controls. The specific experimental procedures are detailed in **Section 5.7.6**.

For the RT-qPCR assays, sequence ON5 was incubated with 300,000 HeLa cells for 24 hours in a 6-well plate using each of the three transfection volumes. To normalize the results, a scramble sequence was incubated in separate wells with the same cell density, using a different volume of the transfection agent in each well.

RNA was extracted and quantified, then used as a template to synthesize complementary DNA (cDNA) via reverse transcription (RT). Subsequently, qPCR was performed to measure *c-myc* RNA levels in each sample.

To calculate relative mRNA expression, the $2^{-\Delta Ct}$ method was employed. In this method, the expression of the target gene (*c-myc*) is normalized to a reference gene and expressed relative to a reference sample (scramble sequence). In this study, *GAPDH* was selected as the reference gene due to its stable and consistent expression across various tissues and experimental conditions.

The cycle threshold (Ct) values represent the number of cycles required for the fluorescent signal to exceed a defined threshold, set above background fluorescence, indicating the point at which the target nucleic acid is detectable. Lower Ct values suggest a higher initial amount of target nucleic acid, while higher Ct values indicate a lower initial quantity. In this assay, Ct values were calculated in triplicate for each sample. The differences between the average Ct values were used to determine the relative mRNA expressions for each condition.

The Ct values and the calculation procedures for determining relative mRNA expression after incubating HeLa cells with ON5, using three different volumes of the transfection agent (3.75 µL, 5.63 µL, and 7.5 µL), are presented in **Table 3.1**.

**Table 3.1: Ct values obtained from RT-qPCR used to compare the housekeeping gene (*GAPDH*) as a reference for measuring the relative expression of *c-myc* mRNA**. Ct (Cycle Threshold): Number of cycles required for the florescent signal of the amplified gene to exceed baseline; CtMean = ($Ct_1$+$Ct_2$+$Ct_3$) ÷3; $Ct_1$: Ct value of the first triplicate 1; $Ct_2$: $C_T$ value of second triplicate; $Ct_3$: Ct value of third triplicate; ΔCt = *c-myc* $Ct_{Mean}$ - Housekeeping gene (*GAPDH*) $Ct_{Mean}$; 2-ΔCt: Relative Expression of *c-myc* mRNA for *gadph* housekeeping gene.

| | ***GAPDH*** | | | | ***c-myc*** | | | | | | |
|---|---|---|---|---|---|---|---|---|---|---|---|
| | **$Ct_1$** | **$Ct_2$** | **$Ct_3$** | **$Ct_{Mean}$** | **$Ct_1$** | **$Ct_2$** | **$Ct_3$** | **$Ct_{Mean}$** | **ΔCt** | **$2^{-\Delta Ct}$** | **Rel.to Sc** |
| **Scramble Lipo 3.75** | 17,48 | 17,03 | 17,63 | 17,38 | 23,56 | 22,94 | 23.2 | 23,23 | 5,85 | 0,017 | 1 |
| **ON5 Lipo 3.75** | 16,67 | 17,01 | 17,38 | 17,02 | 23,85 | 23,31 | 23,49 | 23,35 | 6,33 | 0,016 | 0,63 |
| **Scramble Lipo 5.63** | 17,59 | 17,43 | 17,25 | 17,42 | 23,35 | 23,05 | 23,66 | 23,64 | 6,22 | 0,025 | 1 |
| **ON5 Lipo 5.63** | 17,08 | 17,1 | 17,08 | 17,09 | 23,64 | 23,57 | 23,90 | 23,55 | 6,46 | 0,011 | 0,62 |
| **Scramble Lipo 7.5** | 18,61 | 18,27 | 18,09 | 18,32 | 23,99 | 23,55 | 23,37 | 23,70 | 5,38 | 0,010 | 1 |
| **ON5 Lipo 7.5** | 17,07 | 16,83 | 17,25 | 17,05 | 22,2 | 22,24 | 22,4 | 22,28 | 5,23 | 0,027 | 1,06 |
| **Blank** | 17,39 | 17,28 | 17,29 | 17,32 | 22,94 | 23,04 | 23,08 | 23,02 | 5,7 | 0,019 | 1,11 |

These values represent the data from one replicate, with the assay repeated in five independent experiments. Subsequently, RT-qPCR data were analysed using a one-way ANOVA followed by Dunnett's multiple comparison test, comparing *c-myc* mRNA levels in oligonucleotide-transfected cells to those treated with the scramble sequence. (**Figure 3.1**).

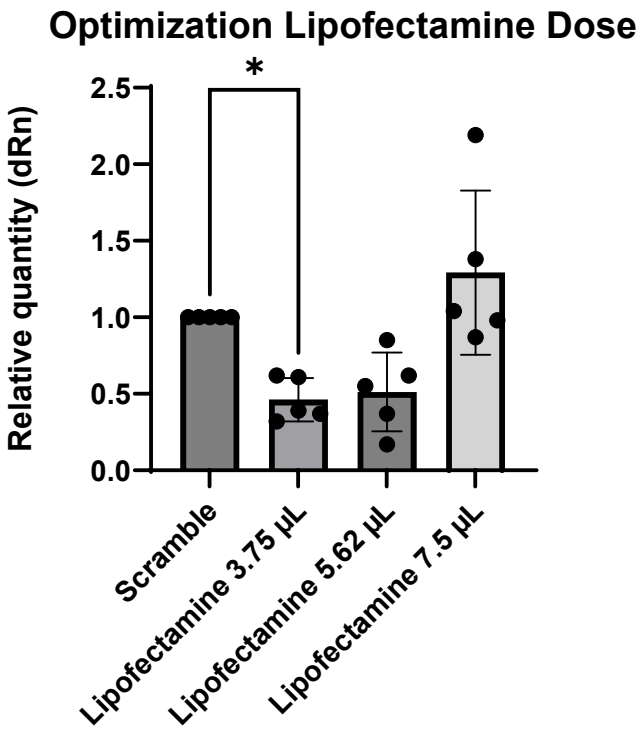


**Figure 3.1: Analysis of RT-qPCR of HeLa cells transfected with ON5 using 3.75, 5.62 and 7.5 µL of Lipofectamine™ 3000 Reagent for 24 hours transfection.** For each ON5 transfection condition, c-myc mRNA levels were normalized to GAPDH mRNA and compared to a scramble control transfected with the same Lipofectamine™ 3000 dose; each scramble control (for 3.75, 5.62, and 7.5 µL) was set to 1. Statistical analysis was performed by one-way ANOVA with Dunnett's multiple comparison test. Asterisks indicate the level of significance between groups: *P ≤ 0.05, **P ≤ 0.01, ***P ≤ 0.001, ****P ≤ 0.0001. Error bars represent ± SD.

The use of 7.5 µL Lipofectamine™ 3000 Reagent can be excluded due to greater variability in values compared to the other conditions and its higher cost. Additionally, only the transfection using 3.75 µL was statistically significant. The values obtained from the five replicates were consistent, indicating stable transfection and reproducible results. Although results with 5.63 µL Lipofectamine™ 3000 Reagent were similar, the higher standard deviation, lack of statistical significance, and use of 50% more reagent led to selecting 3.75 µL as the optimal volume for transfecting sequences.

An important aspect of this study was to evaluate the cytotoxicity induced by the Lipofectamine™ 3000 Reagent. To achieve this, the Invitrogen™ CyQUANT™ LDH Cytotoxicity Assay Kit was used to measure the potential for Lipofectamine™ 3000 to

cause cell damage or death. Although, as previously discussed in **Section 3.2.1.1.3**, Lipofectamine™ 3000 exhibits relatively low cytotoxicity compared to other transfection agents, it can become toxic at higher concentrations. Therefore, this assay aimed to test different volumes of the transfection reagent and correlate the results with the RT-qPCR data from earlier experiments to determine the optimal volume for transfection.

In this experiment, the scramble sequence was transfected into HeLa cells using the same three volumes of transfection reagent—3.75 µL, 5.63 µL, and 7.5 µL—tested in the RT-qPCR assay. The incubation periods were extended to 24 and 48 hours to provide a more comprehensive assessment of Lipofectamine™ 3000's impact. The assay was conducted in a 96-well plate format, with all reagents and cell numbers scaled down accordingly. Specifically, 12,000 cells were seeded per well, and volumes of 0.15 µL, 0.225 µL, and 0.3 µL of transfection reagent were used to transfect 100 ng of the scramble sequence into each well.

This experimental design allowed for a detailed evaluation of cytotoxicity across different reagent volumes while maintaining consistency with prior assays. By correlating these results with RT-qPCR data, it was possible to identify the most efficient and least cytotoxic volume of Lipofectamine™ 3000 for oligonucleotide transfection.

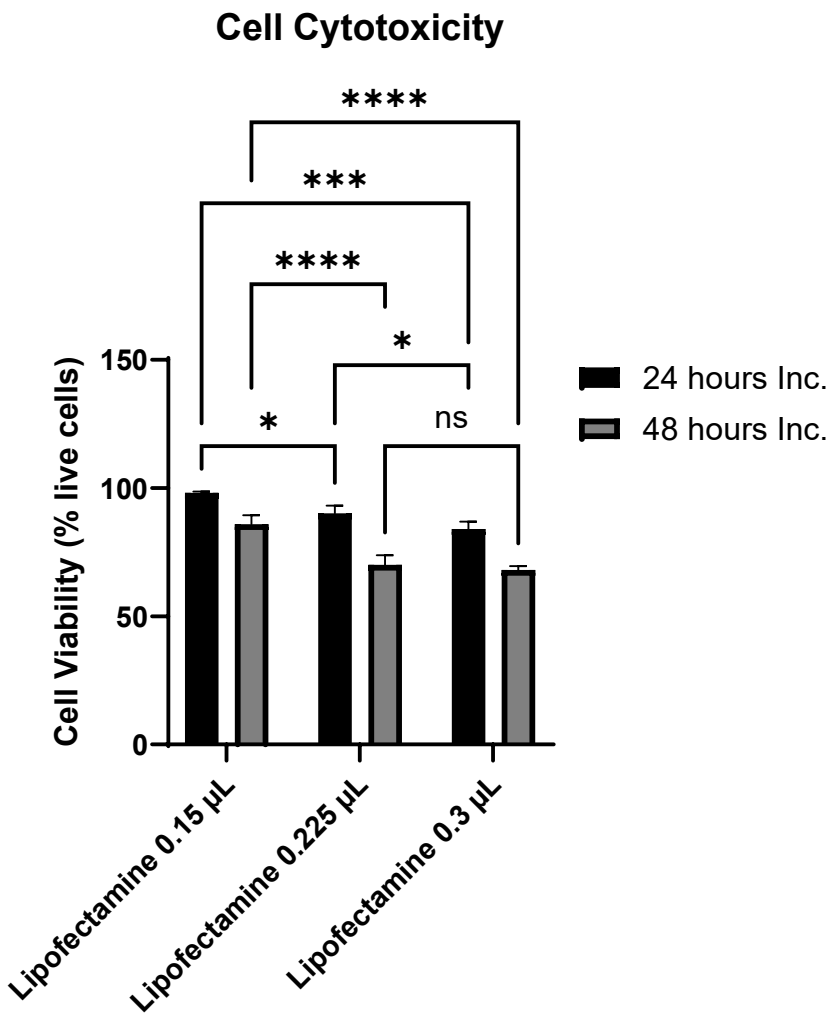


**Figure 3.2: Cell cytotoxicity analysis of HeLa cells transfected with scramble sequence using 0.15, 0.225 and 0.3 µL of Lipofectamine™ 3000 Reagent in a 96 well plate for 24/48 hours transfection.** Cell viability (% live cells) was measured after incubation with the indicated Lipofectamine™ 3000 concentrations for 24 hours (black bars) or 48 hours (gray bars). Statistical significance was assessed using two-way ANOVA followed by multiple comparisons. Asterisks indicate the level of significance between groups: *P ≤ 0.05, **P ≤ 0.01, ***P ≤ 0.001, ****P ≤ 0.0001, ns = not significant. The assay was performed in triplicate. Error bars represent ± SD.

The results demonstrate that both the concentration of Lipofectamine™ 3000 and the incubation time significantly influence HeLa cell viability (**Figure 3.2**). Two-way ANOVA revealed highly significant main effects for both factors (P<0.0001), with cell viability decreasing as Lipofectamine concentration increased and as incubation time extended from 24 to 48 hours. Multiple comparisons highlight these effects: significant reductions in viability were observed between 24 and 48 hours at both 0.15 µL and 0.225 µL Lipofectamine concentrations (P<0.05 and P<0.0001, respectively), while the

difference at 0.3 µL was not significant (ns). Comparisons across concentrations at each time point also revealed significant decreases in viability, particularly between 0.15 µL and higher concentrations (**P<0.001 and ***P<0.0001). These findings confirm that both higher doses of Lipofectamine and longer incubation times independently contribute to increased cytotoxicity in HeLa cells.

These observations are consistent with the RT-qPCR assay results, suggesting that increased Lipofectamine™ volumes may induce cellular stress, thereby affecting experimental reliability. Based on the combined outcomes of the RT-qPCR and cytotoxicity assays, 3.75 µL was identified as the optimal volume of Lipofectamine™ 3000 Reagent for transfecting the synthesized sequences in this study. This volume provided robust and reproducible RT-qPCR results while minimizing cytotoxicity. Furthermore, the lower reagent amount compared to other tested conditions highlights its efficiency and cost-effectiveness.

Lipofectamine™ 3000 Reagent, provided by Invitrogen as part of a kit, includes supplementary components such as P3000™ Reagent, which enhances sequence delivery into cells. To assess its suitability for this project, an additional assay was conducted.

Sequences ON3, ON4, and ON5 were transfected into HeLa cells alongside a scramble sequence. In this experiment, P3000™ Reagent was incorporated during the formation of ssDNA-Lipofectamine complexes. The sequences were incubated with cells for 24 and 48 hours. A blank control, consisting of cells treated with the same volume of cell culture medium as the transfection samples but without Lipofectamine™ 3000 or oligonucleotides, was included. After incubation, cells were harvested, and *c-myc* mRNA levels for each condition were analysed via RT-qPCR. This assay was repeated across four independent experiments, each performed in triplicate (mean ± SD; **Figure 3.3**). *c-myc* mRNA levels were normalized to *GAPDH* mRNA levels (used as an internal control) and to those of scramble-transfected cells. Statistical analysis was performed using one-way ANOVA followed by Dunnett's multiple comparison test.

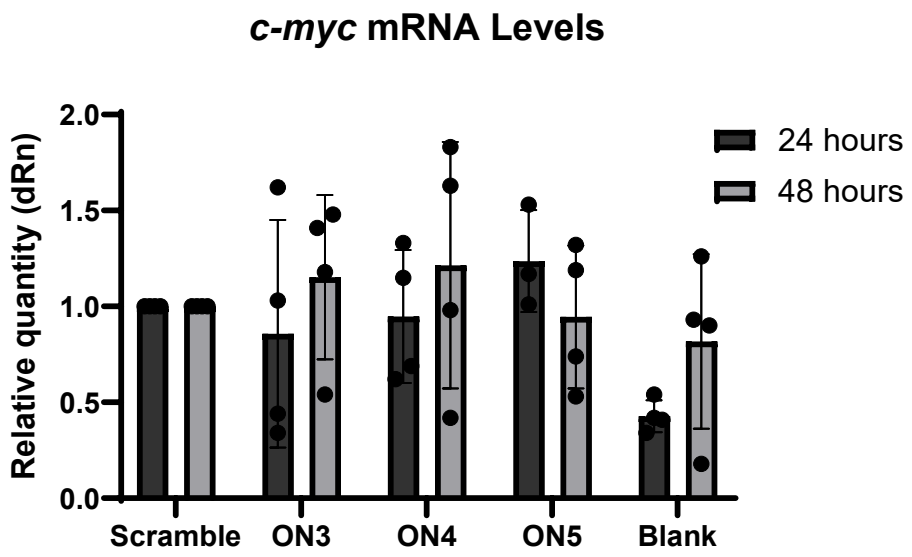


**Figure 3.3: Analysis of RT-qPCR of HeLa cells transfected with ON3, ON4 and ON5 using Lipofectamine™ 3000 and P3000™ reagent for 24/48 hours transfection.** *c-myc* mRNA levels were normalised to *GAPDH* mRNA levels and to scramble transfected cells. The "Blank" control represents cells exposed to the same volume of cell culture medium as the transfection samples, but without Lipofectamine™ 3000 or ONs. Statistical analysis done by one-way ANOVA with a Dunnet's multiple comparison test. Error bars show ± SD.

The results demonstrate a high degree of polydispersity across all conditions (**Figure 3.3**). Among the three sequences analysed, there appears to be a trend suggesting that mRNA levels are higher at 48 hours compared to 24 hours. However, statistical analysis did not reveal any significant differences for any condition. Additionally, the broad error bars indicate a lack of consistency in the results. To gain a deeper understanding of the P3000™ reagent's functions, the Invitrogen product specialist service was consulted. According to their explanation, the reagent facilitates and directs the internalization of the ssDNA complex into the nucleus of the cells. The primary objective of this project is the hybridization of the sequences with *c-myc* mRNAs, and these are in the cytosol and near the outer layer of the nucleus, it was decided not to use this reagent in subsequent assays.

### 3.2.1.2 AuNPs@PEG@ssDNA transfection optimization

Following the optimization of sequence transfection using Lipofectamine™ 3000, additional tests were conducted to evaluate whether the same conditions could be applied to the transfection of AuNPs@PEG@ssDNAs.

Preliminary assays were performed to adapt the protocol optimized for Lipofectamine™ 3000 to the specific requirements of the AuNPs@PEG@ssDNAs. In these experiments, HeLa cells were incubated with a solution of biofunctionalized NPs to assess the interactions between the NPs, the cells, and the cell culture medium.

Another important consideration was the calculation of the volume of the AuNPs@PEG@ssDNA stock solution required to achieve the optimal concentration of sequences for cell incubation. This involved determining the number of ssDNA molecules attached to the NPs and calculating the volume necessary to provide 2500 nanograms of ssDNA.

#### 3.2.1.2.1 Selecting the AuNPs@PEG@ssDNA optimal transfection protocol

The first assay involved the incubation of AuNPs@PEG@ASO with HeLa cells for 24 hours. In this experiment, a stock solution of NPs functionalized with the ON5 sequence was utilized. Calculations were performed to determine the specific volume of the stock solution required to correspond to 2500 ng of ssDNA.

Initially, 300,000 HeLa cells were seeded per well in a 6-well plate containing 2 mL of growth medium (Dulbecco's Modified Eagle Medium (DMEM)) supplemented with 10% FBS. After 24 hours, a solution of AuNPs@PEG@ssDNA was added to one of the wells. To assess the impact of ssDNA functionalization on the NPs, a solution containing only AuNPs@PEG (without ssDNA) was added to another well. Additionally, a solution containing the ON5 sequence without NPs was introduced into a separate well as a control for the sequence alone. Finally, an equivalent volume of water was added to one well as a control without NPs or sequences.

After 24 hours of incubation, brightfield microscopy was employed to visually examine the interactions between the NPs and HeLa cells. The analysis was performed using a Nikon Diaphot Inverted Phase Contrast Photomicroscope at 40x magnification. Images

were captured with a Nikon D3300 DSLR camera and subsequently analysed using the Fiji (ImageJ) processing software package[197].

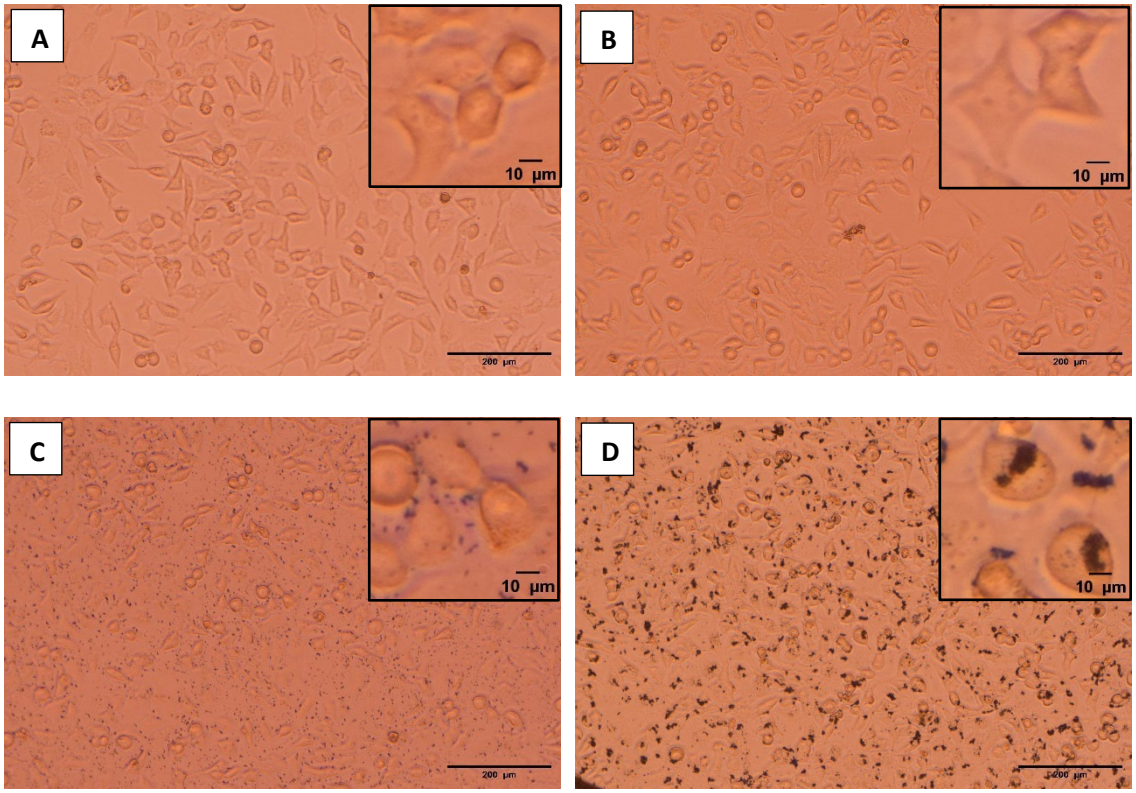


**Figure 3.4: Phase-contrast microscopy analysis of HeLa cells after 24-hour incubation with different treatments.** Representative images show HeLa cells incubated with: (A) Water (negative control), (B) ON5, (C) AuNPs@PEG, and (D) AuNPs@PEG@ON5. Insets display higher magnification views of cellular morphology for each condition. Images were acquired using a Nikon Diaphot Inverted Phase Contrast Photomicroscope equipped with a 40x (LWD) objective and an electronic 3-axis micromanipulator system. A Nikon D3300 DSLR camera was used for image capture. Scale bars: main images, 200 µm; insets, 10 µm. Image analysis was performed using Fiji (ImageJ) software

The incubation with water (**Figure 3.4A**) and the ON5 sequence (**Figure 3.4B**) does not appear to affect cell morphology. Since the ON5 sequence lacks a fluorescent or luminescent tag, further confocal microscopy assays, discussed in subsequent chapters, will be necessary to evaluate its internalization potential.

For the samples incubated with AuNPs@PEG (**Figure 3.4C**) and AuNPs@PEG@ON5 (**Figure 3.4D**), the NPs functionalized with the ON5 sequence seem to exhibit greater interaction with the cell membrane. Confocal microscopy analysis, detailed in later chapters, will provide additional insights into whether these NPs remain on the cell surface or are internalized.

When comparing the samples treated with AuNPs@PEG and AuNPs@PEG@ON5, it is evident that nanoparticle aggregation occurs in both cases. However, the aggregates in the AuNPs@PEG@ON5 sample appear larger than those in the AuNPs@PEG sample. This phenomenon may result from the presence of ON5 sequences on the nanoparticle surface, which could enhance interactions with fetal bovine serum (FBS) proteins or elevated glucose levels in the medium due to their charge[198]. To address this issue, it was decided to replace the serum-supplemented medium with Opti-MEM™, an optimized Minimal Essential Medium (MEM) that reduces FBS supplementation without affecting cell growth rate or morphology, at the time of AuNPs@PEG@ssDNA addition.

#### 3.2.1.2.2 Calculations for transfecting the AuNPs@PEG@ssDNAs into HeLa cells

Prior to the transfection of the AuNPs@PEG@ssDNAs, calculations were performed to determine whether the same transfection concentrations used in the optimized Lipofectamine™ 3000 protocol could be replicated.

After coupling the purified sequences, linked to PEG molecules, onto the NPs, the amount of ssDNA conjugated to the NPs was quantified using a NanoDrop 2000 UV-Vis spectrophotometer. However, the number of sequences coupled to the NPs varied across samples. This variability arises because the synthesized sequences are not entirely pure. Specifically, not all sequences possess the amino modifier at the 5’ end required for binding to PEG molecules.

The purification step aims to separate ssDNA molecules bound to PEG from those that remain unreacted, as described in **Section 5.6.1.2**. However, even after purification, some contamination by unreacted sequences persists. Consequently, when these samples are added to AuNPs, only sequences with PEG molecules—containing a thiol group—successfully bind to the NPs. Sequences lacking PEG molecules fail to attach due to the absence of this functional group.

Once the reaction is complete, the nanoparticle solutions are washed and purified to remove unreacted sequences and then resuspended in 0.5 mL of buffer. UV-Vis analysis of the purified samples revealed that the number of nanomoles present in the final solution is lower than the number initially introduced into the reaction. This

discrepancy is attributed to the removal of unreacted sequences during washing and purification steps.

**Table 3.2**: **The number of nanomoles present at various stages of the biofunctionalization process for different oligos attached to nanoparticles, as well as the percentage of nanomoles successfully attached at the conclusion of the process**. All these data were obtained from a NanoDrop 2000 UV-Vis spectrophotometer analysis.

| Sequence | Total nanomols of ssDNA after purification | Nanomols used for biofuncionalization | Nanomols attached onto the NPs after biofunctionalization | % of nanomols attached |
|---|---|---|---|---|
| **1** | 85,26 | 17,05 | 13,41 | 79 |
| **2** | 127,71 | 25,54 | 9,46 | 37 |
| **3** | 47,66 | 14,30 | 9,96 | 70 |
| **4** | 43,44 | 13,03 | 5,96 | 46 |
| **5** | 46,68 | 14 | 7,08 | 51 |

All the data from the coupling process of the different sequences to the AuNPs is displayed in a table (**Table 3.2**). The column labelled "Total Nanomoles of ssDNA After Purification" represents the number of nanomoles obtained following the isolation of PEG-ssDNA sequences. From this total, a portion of the nanomoles was utilized for biofunctionalization onto AuNPs The column "Nanomoles Attached to Nanoparticles After Biofunctionalization" reflects the number of nanomoles successfully conjugated to the AuNPs at the end of the biofunctionalization process. Lastly, based on the total number of nanomoles initially used in the reaction, the percentage of nanomoles attached to the AuNPs was calculated.

The objective was to calculate the volume of each stock solution required to transfect 2500 ng of ssDNA into the cells. To achieve this, the required mass of ssDNA was first converted to nanomoles, as detailed in **Section 3.2.1.4**. Using the calculated nanomole content of each sequence conjugated to the nanoparticles in a 0.5 mL stock solution (see **Table 3.2**), the precise volume required to deliver 2500 ng of ssDNA was then determined.

**Scramble**

$$x = \frac{0.027\ nmols \times 500\ \mu L}{11.39\ nmols} = 11.85\ \mu L$$

**ON1**

$$x = \frac{0.027\ nmols \times 500\ \mu L}{13.41\ nmols} = 10.07\ \mu L$$

**ON2**

$$x = \frac{0.027\ nmols \times 500\ \mu L}{9.46\ nmols} = 14.27\ \mu L$$

**ON3**

$$x = \frac{0.027\ nmols \times 500\ \mu L}{9.96\ nmols} = 13.55\ \mu L$$

**ON4**

$$x = \frac{0.027\ nmols \times 500\ \mu L}{5.96\ nmols} = 28.52\ \mu L$$

**ON5**

$$x = \frac{0.027\ nmols \times 500\ \mu L}{7.08\ nmols} = 19.07\ \mu L$$

These volumes were used in the following cell assays to transfect the different AuNPs@PEG@ssDNAs into the Hela Cells following the protocol described in **Section 5.7.1.3.2**.

## 3.3 Oligonucleotide Transfection Evaluation

The various sequences were transfected into HeLa cells following previously optimized protocols. Initially, Lipofectamine™ 3000 Reagent was used to assess the direct effects of the sequences on HeLa cells. Subsequently, the same sequences were biofunctionalized onto NPs and transfected to evaluate whether a similar effect could be achieved as with the transfection reagent.

A range of techniques was employed to analyse the impact of each sequence on HeLa cells and its modulation of *c-myc* after 24 or 48 hours of incubation. First, RT-qPCR was conducted to measure *c-myc* mRNA levels following incubation with each sequence. Western blot analysis was then performed to determine how the sequences influenced

c-Myc protein levels. Additionally, cytotoxicity assays were carried out to assess whether incubation with the sequences increased cell mortality. Finally, confocal microscopy was used to confirm the internalization of the sequences into the cells and to determine their intracellular localization post-transfection.

### 3.3.1 Sequence-Specific Modulation of *c-myc* mRNA Levels by Antisense Oligonucleotides

The endogenous *c-myc* mRNA levels in HeLa cells transfected with modified synthesized oligonucleotides were analysed using RT-qPCR. The experiments began with ON5 during the optimisation of transfecting reagent´s volume. Once optimised, the assays followed with sequences ON3 and ON4. The different replicates for these experiments can be found in **Appendix F**. As indicated in **Section 2.2.1**, sequences ON1 and ON2 were initially excluded due to their higher GC content, which results in a -6 kcal/mol free energy of structure, potentially complicating the hybridization process.

For this initial experiment, cells were seeded at a concentration of $3\times10^5$ cells per well and cultured for 24 hours in 6-well culture dishes. Following the incubation period, sequences ON3, ON4, and ON5 were transfected into the cells for an additional 24 hours using Lipofectamine™ 3000, in accordance with the previously described protocol. After transfection, the cells were harvested for further analysis.

Once completed, the results from the five independent replicates were plotted alongside the ON5 RT-qPCR results obtained during the protocol optimization assays (**Figure 3.5**). The graph illustrates the relative quantity of *c-myc* mRNA expression in HeLa cells following transfection with different sequences (Scramble, ON3, ON4, ON5) and a blank control. The "Blank" control represents cells exposed to the same volume of cell culture medium as the transfection samples, but without Lipofectamine™ 3000 or ONs. All results are relative to the Scramble sequence, which serves as a baseline for comparison.

Sequences ON3 and ON4 exhibit increased *c-myc* mRNA levels compared to the Scramble, with ON4 showing the most significant increase. The asterisks indicate statistical significance, suggesting that the differences in expression levels are

meaningful. However, the values obtained from the ON5 transfection display lower *c-myc mRNA* levels compared to Scramble, indicating a potential inhibitory effect.

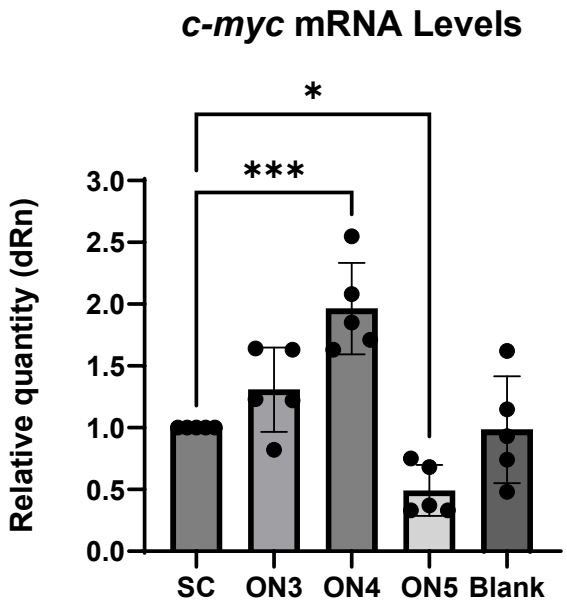


**Figure 3.5: RT-qPCR results of HeLa cells transfected, using Lipofectamine 3000™ Reagent with a Scramble sequence (SC), ON3, ON4 and ON5 for 24 hours**. The "Blank" control represents cells exposed to the same volume of cell culture medium as the transfection samples, but without Lipofectamine™ 3000 or ONs. The error bars represent variability within the samples. Statistical analysis was done using a one-way ANOVA with a Dunnett's multiple comparison test. Asterisks indicate the level of significance between groups: *P ≤ 0.05, **P ≤ 0.01, ***P ≤ 0.001, ****P ≤ 0.0001.

Based on these results, the observed upregulation of mRNA for sequences ON3 and ON4 was unexpected. This effect was particularly pronounced for ON4, which showed nearly a twofold increase in relative mRNA levels compared to the Scramble control. Since the oligonucleotides were designed to target specific mRNA sequences, it was anticipated that the predominant outcome would be downregulation, either through degradation of the target mRNA or inhibition of translation. These mechanisms likely explain the downregulation observed following transfection with ON5.

Initially, it was ensured that the procedure was consistent across both assays: the optimization of the transfection protocol using ON5 and the transfection assays of ON3 and ON4. The stocks of the various reagents used throughout the process remained unchanged; however, the number of cell passages differed. Consequently, it was opted to repeat the experiment using a fresh batch of cells (**Figure 3.6**)**.**

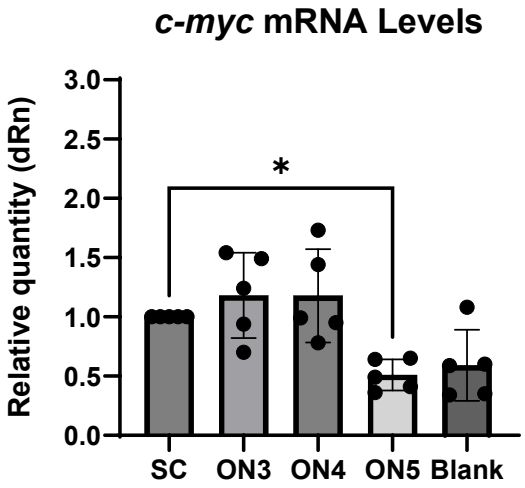


**Figure 3.6: RT-qPCR results from a fresh batch of HeLa cells transfected with Lipofectamine™ 3000 Reagent using a scramble sequence (SC), ON3, ON4, and ON5 for 24 hours**. The "Blank" control represents cells exposed to the same volume of cell culture medium as the transfection samples, but without Lipofectamine™ 3000 or ONs. The error bars represent variability within the samples. Statistical analysis was done using a one-way ANOVA with a Dunnett's multiple comparison test. Asterisks indicate the level of significance between groups: *P ≤ 0.05, **P ≤ 0.01, ***P ≤ 0.001, ****P ≤ 0.0001.

As observed, sequences ON3 and ON5 exhibit values comparable to those in the previous assay. In contrast, sequence ON4 shows a decrease in relative quantity, losing all significance observed in the experiment with the previous batch. Despite these changes, it is evident that sequences ON3 and ON4 induce some upregulation of *c-myc* mRNA levels. Therefore, a review of the literature was undertaken to identify the causes of this effect.

The increase in mRNA levels upstream after transfection with ASO sequences targeting the 5' UTR can be attributed to several factors:

ASOs targeting the 5' UTR can stabilize mRNA transcripts, leading to an increase in mRNA levels. This stabilization may occur by preventing degradation pathways that typically act on these regions, thereby increasing the overall abundance of the mRNA[199].

Also, the 5' UTR often contains secondary structures, such as G-quadruplexes and hairpins, which can inhibit translation. ASOs can disrupt these structures, enhancing the recruitment of translation initiation factors and potentially increasing mRNA stability as a secondary effect[200].

Given this context, it was decided to proceed with experiments involving sequences ON1 and ON2 (**Figure 3.7)**, which were initially excluded due to their higher GC content that could potentially cause hybridization issues. This approach allowed for a comprehensive screening of Domain 1 of the IRES structure of c-*myc*.

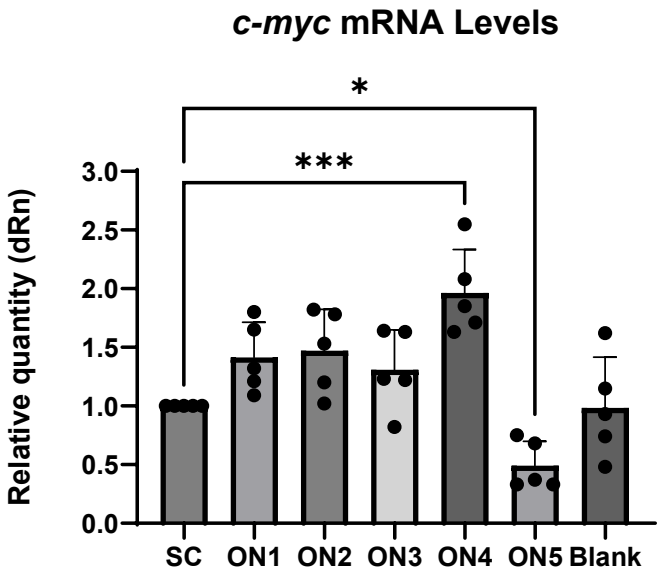


**Figure 3.7: RT-qPCR results of HeLa cells transfected with Lipofectamine 3000™ Reagent using a Scramble sequence (SC), ON1, ON2, ON3, ON4, and ON5 for 24 hours**. The "Blank" control represents cells exposed to the same volume of cell culture medium as the transfection samples, but without Lipofectamine™ 3000 or ONs**.** The error bars indicate the variability within the samples. Statistical analysis was conducted using a one-way ANOVA followed by Dunnett's multiple comparison test. Asterisks indicate the level of significance between groups: *P ≤ 0.05, **P ≤ 0.01, ***P ≤ 0.001, ****P ≤ 0.0001.

After 24 hours of transfection, ON1 and ON2 produced results similar to ON3, with all three sequences showing *c-myc* mRNA levels comparable to the scramble control **(Figure 3.7)**. In summary, the initial screening revealed three distinct effects: ON5 caused a significant downregulation of *c-myc* mRNA, ON4 led to an upregulation, and ON1, ON2, and ON3 had minimal impact, maintaining *c-myc* expression at levels close to the negative control.

Subsequent assays involved transfecting HeLa cells with the various sequences, adhering to the same protocol but extending the incubation period to 48 hours (**Figure 3.8**). The objective was to determine whether prolonged exposure between the cells

and the lipofectamine-ssDNA complex would induce a different effect on the modulation of *c-myc* mRNA levels.

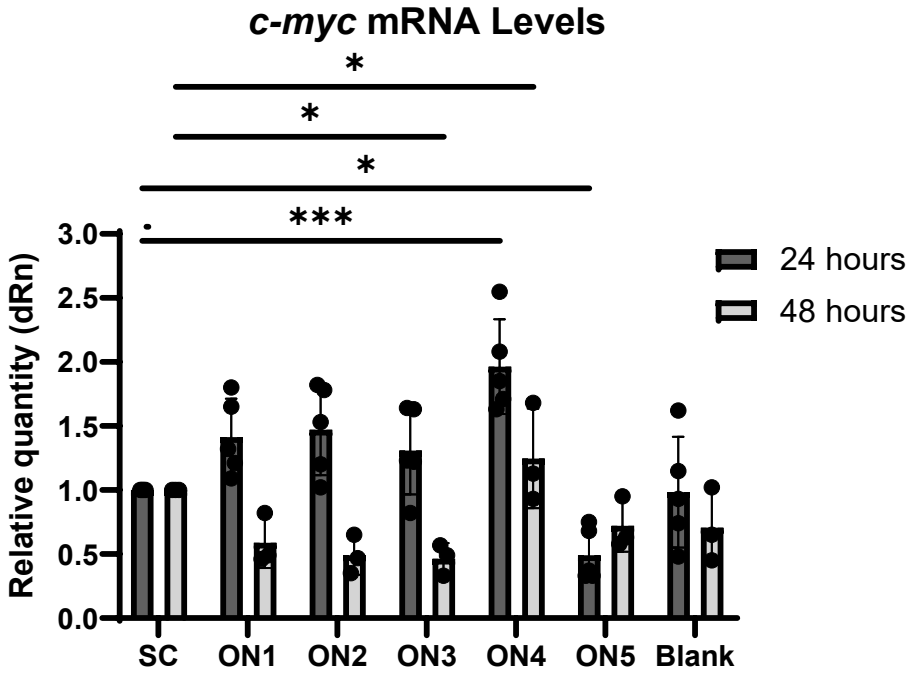


**Figure 3.8: RT-qPCR results of HeLa cells transfected with Lipofectamine 3000™ Reagent using a Scramble sequence (SC), ON1, ON2, ON3, ON4, and ON5 for 24 or 48 hours**. The "Blank" control represents cells exposed to the same volume of cell culture medium as the transfection samples, but without Lipofectamine™ 3000 or ONs. The error bars indicate the variability within the samples. Statistical analysis was conducted using a one-way ANOVA followed by Dunnett's multiple comparison test. Asterisks indicate the level of significance between groups: *P ≤ 0.05, **P ≤ 0.01, ***P ≤ 0.001, ****P ≤ 0.0001.

Upon examining the results, it is evident that after 48 hours, there is a decrease in the relative quantity of mRNA compared to the results obtained after 24 hours for all sequences except ON5. Two results show statistical significance (* for $p<0.05$): ON3, which has the lowest value, and ON4, which, despite a decrease compared to the 24-hour results, still exhibits the highest values. Notably, ON5 is the only sequence that shows an increase in mRNA levels.

The decrease in mRNA levels following transfection with ASO sequences targeting the 5' UTR can be attributed to several mechanisms:

ASOs can induce mRNA degradation through various decay pathways. For instance, they can trigger the no-go decay (NGD) pathway, which involves the recruitment of

specific proteins like PELO and HBS1L that interact with stalled ribosomes, leading to mRNA degradation. This mechanism is translation-dependent and does not rely on RNase H1[201].

Also, the downregulation of mRNA levels can be produced by the hybridized ASOs recruiting RNase H1, an enzyme that cleaves the RNA strand of RNA-DNA hybrids. This cleavage leads to the degradation of the target mRNA. Although this mechanism is more commonly associated with ASOs targeting coding regions, it can also occur when ASOs bind near the 5' UTR if the conditions allow for RNase H1 activity[202].

Finally, it is important to mention that by binding to the 5' UTR, ASOs can obstruct the binding of ribosomal subunits or other essential factors needed for translation initiation. This inhibition can lead to a decrease in translation efficiency and potentially trigger mRNA decay pathways that are sensitive to stalled translation processes[201,202].

After completing experiments characterizing the effects of sequences transfected with Lipofectamine 3000™ Reagent, the same oligonucleotides were transfected into HeLa cells biofunctionalized onto AuNPs (**Figure 3.9**). These assays followed the protocol outlined in **Section 5.7.1.3.2**. Additionally, a new condition was introduced compared to previous experiments: AuNPs fully covered by PEG molecules were used to assess the impact of different AuNPs@PEG@ssDNAs without sequences on HeLa cells.

Lipofectamine 3000™ Reagent is a well-studied commercial reagent; thus, it was assumed that these assays reflect the true effects of the oligonucleotides. The objective was to determine if similar results could be replicated using an alternative delivery system.

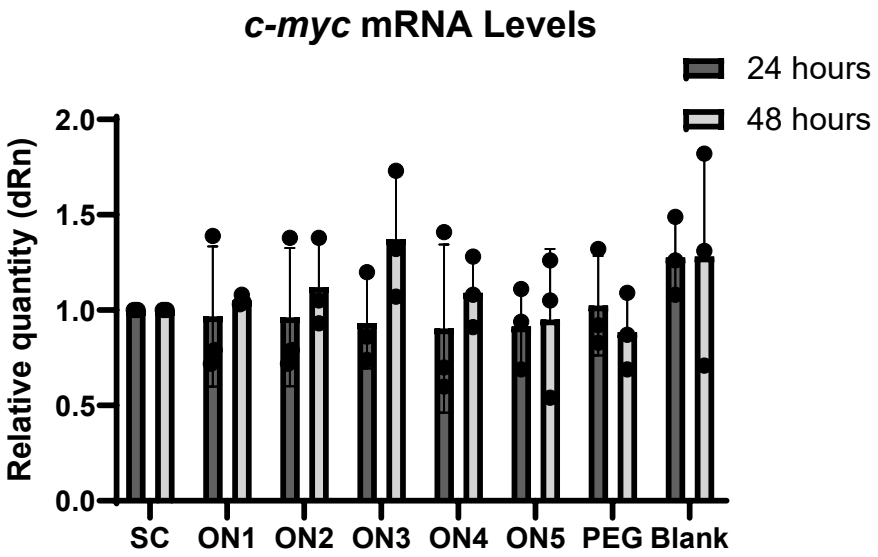


**Figure 3.9: RT-qPCR results of HeLa cells transfected with Scramble sequence (SC), ON1, ON2, ON3, ON4, and ON5 biofunctionalized onto AuNP, for 24 or 48 hours.** The "Blank" control represents cells exposed to the same volume of cell culture medium as the transfection samples, but without AuNPs or ONs. The error bars indicate the variability within the samples. Statistical analysis was conducted using a one-way ANOVA followed by Dunnett's multiple comparison test. Asterisks indicate the level of significance between groups: *P ≤ 0.05, **P ≤ 0.01, ***P ≤ 0.001, ****P ≤ 0.0001.

When comparing the results obtained at 24 and 48 hours, there is minimal difference between the samples. ON3 exhibits the most significant change between incubation times; however, this difference does not reach statistical significance. For the other sequences, all values are similar to those of the scramble control, with relative quantities close to 1. One hypothesis to explain these results is that the presence of the nanoparticle, covalently linked to the sequence, may impede the sequence's ability to hybridize with its molecular target. Nevertheless, further characterization techniques are necessary to fully understand these findings.

### 3.3.2 Sequence-Specific Modulation of c-Myc protein expression by Antisense Oligonucleotides

The modulation of c-Myc protein levels was analysed using Western blotting to assess the impact of different sequences on endogenous c-Myc protein levels following the transfection of each sequence. These assays were conducted in parallel with the RT-qPCR tests, maintaining a similar experimental design and procedural steps.

The Western blot technique is employed in ASO testing to assess their impact on protein expression levels. Transfected oligonucleotides function by targeting mRNA to modulate gene expression, with the ultimate objective of altering protein levels. Western blotting offers a direct and reliable approach for evaluating these changes. The specific experimental procedures are detailed in **Section 5.7.3**.

For all assays, cells were seeded at a concentration of $3\times10^5$ cells per well and cultured for 24 hours in 6-well culture dishes. Following this incubation period, sequences ON3, ON4, and ON5 were transfected into the cells for an additional 24 hours using Lipofectamine™ 3000, adhering to the previously described protocol. After transfection, proteins were extracted and quantified as outlined in **Section 5.7.2.** Using RIPA lysis buffer, which disrupts the cell membrane, proteins were released into the medium. These proteins were then quantified using a spectrophotometer set to 595 nm with the Bradford reagent. Finally, the proteins were loaded onto gels and subjected to Western blotting according to the protocol detailed in **Section 5.7.3**.

In Western Blot membranes, each lane corresponds to a different transfected sequence. A blank control, consisting of cells treated with the same volume of cell culture medium as the transfection samples but without Lipofectamine™ 3000 or oligonucleotides, was included. Each lane displays two distinct bands, representing the target gene (*c-myc*) and the housekeeping gene (*GAPDH*) (**Figure 3.10-1A**).

GAPDH was selected as the housekeeping protein because its molecular weight (approximately 36 kDa) differs from that of the target protein, c-Myc (approximately 55 kDa), thereby preventing overlapping bands on the blot. Additionally, GAPDH is abundantly expressed in most eukaryotic cells due to its central role in the glycolytic pathway. Its expression is also generally stable across various experimental conditions, making it a reliable loading control.

The Western blot results were analysed using Image Lab 6.1 software. This software extracts the intensity value of each band from the background signal of the blot. Once all values are extracted, they are compiled into a table (**Figure 3.10-1B**). The intensity values for GAPDH are used to normalize the c-Myc intensity values obtained from the same lane. Finally, these normalized values are expressed relative to the scramble

control to assess whether the transfection of specific sequences results in upregulation or downregulation of c-Myc protein production. The different replicates for these experiments can be found in **Appendix E**.

A

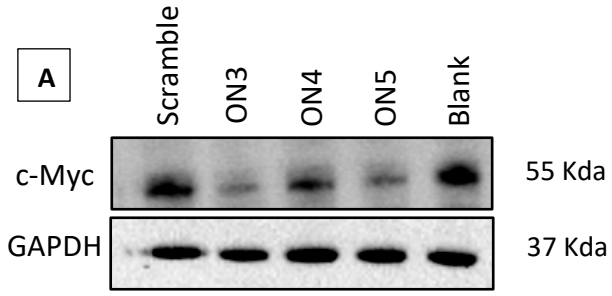


B

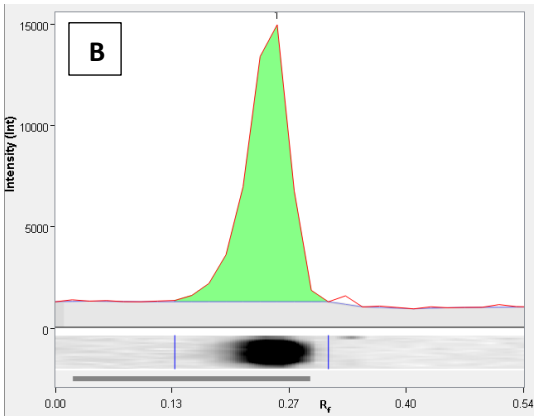


C

| | Lane | Band Label | Intensity | Adj. Intensity |
|---|---|---|---|---|
| Scramble | 1 | GADPH | 1491803 | 1147309 |
| ON3 | 2 | GADPH | 1245024 | 957924 |
| ON4 | 3 | GADPH | 1853570 | 1514205 |
| ON5 | 4 | GADPH | 1597617 | 1300131 |
| Blank | 5 | GADPH | 1626639 | 1290198 |
| Scramble | 1 | c-Myc | 4943252 | 1950262 |
| ON3 | 2 | c-Myc | 2980180 | 557800 |
| ON4 | 3 | c-Myc | 4426114 | 1326666 |
| ON5 | 4 | c-Myc | 3233475 | 750435 |
| Blank | 5 | c-Myc | 4969746 | 2285820 |

D

| | Intensity c-Myc /GAPDH | Rel. to Scramble |
|---|---|---|
| Scramble | 1,70 | 1 |
| ON3 | 0,58 | 0,34 |
| ON4 | 0,88 | 0,52 |
| ON5 | 0,58 | 0,34 |
| Blank | 1,77 | 1,04 |

**Figure 3.10: Analysis procedure of a Western Blot assay following the transfection of HeLa cells with the Scramble sequence, ON3, ON4, and ON5 using Lipofectamine 3000™ Reagent for 24 hours**.1A: Western Blot displaying bands corresponding to *c-myc* (target gene) and *GAPDH* (reference gene) for each transfected condition.1B: Blot processing using Image Lab 6.1 software.1C: Compilation table of intensity values for each condition.1D: Normalization of c-Myc intensity values to GAPDH and expression of these values relative to the Scramble sequence.

In the initial phase, transfection was performed using Lipofectamine™ 3000. Once these assays were completed, the same experimental design was applied to ONs conjugated to AuNPs, following the rationale outlined in **Section 3.3.1**. This parallel strategy maintained consistent conditions and enabled a direct comparison of the two delivery methods on protein expression.

The results shown represent one of the independent experiments in which ON3, ON4, and ON5 were transfected into HeLa cells with Lipofectamine™ 3000 (**Figure 3.10**). To

ensure the findings were robust and reproducible, each condition was tested in five independent replicates. Data analysis was performed using one-way ANOVA followed by Dunnett's multiple comparison test, comparing *c-myc* mRNA levels in ON-transfected cells to those treated with the scramble control sequence.

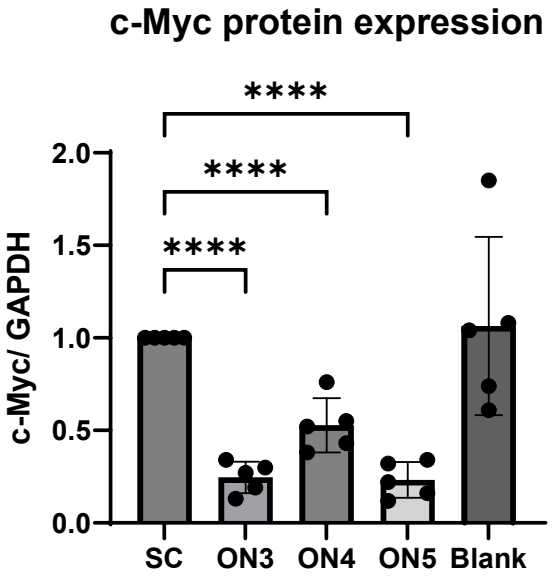


**Figure 3.11: Western Blot results of HeLa cells transfected, using Lipofectamine 3000™ Reagent with a Scramble sequence (SC), ON3, ON4 and ON5 for 24 hours.** The "Blank" control represents cells exposed to the same volume of cell culture medium as the transfection samples, but without Lipofectamine™ 3000 or ONs. The error bars represent variability within the samples. Statistical analysis was done using a one-way ANOVA with a Dunnett's multiple comparison test. Asterisks indicate the level of significance between groups: *P ≤ 0.05, **P ≤ 0.01, ***P ≤ 0.001, ****P ≤ 0.0001.

After 24 hours, all sequences significantly downregulate c-Myc protein levels, demonstrating a robust statistical difference (**** for $p<0.001$) for each condition **(Figure 3.11)**. Furthermore, when comparing all sequences, ON3 and ON5 exhibit similar values, whereas ON4 shows less pronounced downregulation, with values remaining around 0.5 relative to the Scramble. It is also noteworthy that the results obtained exhibit similar values for each condition, indicating a high degree of consistency and reproducibility.

When comparing these results to those obtained in the RT-qPCR assays for the same conditions (**Figure 3.6**), it is evident that sequence ON4, which exhibited the highest upregulation in mRNA levels, also shows the highest values in c-Myc protein expression despite overall downregulation. A similar effect is observed with sequence

ON5, which maintains the downregulation noted in the RT-qPCR assays in the Western Blot tests. Lastly, sequence ON3 exhibited a slight upregulation in the RT-qPCR assay that is not sustained in the Western Blot assays.

After completing the assays with sequences ON3, ON4, and ON5, the same conditions were utilized to perform assays with sequences ON1 and ON2 (**Figure 3.12**). This approach allowed for a comprehensive screening of the effects of these sequences on protein expression modulation, specifically targeting Domain 1 of the IRES structure.

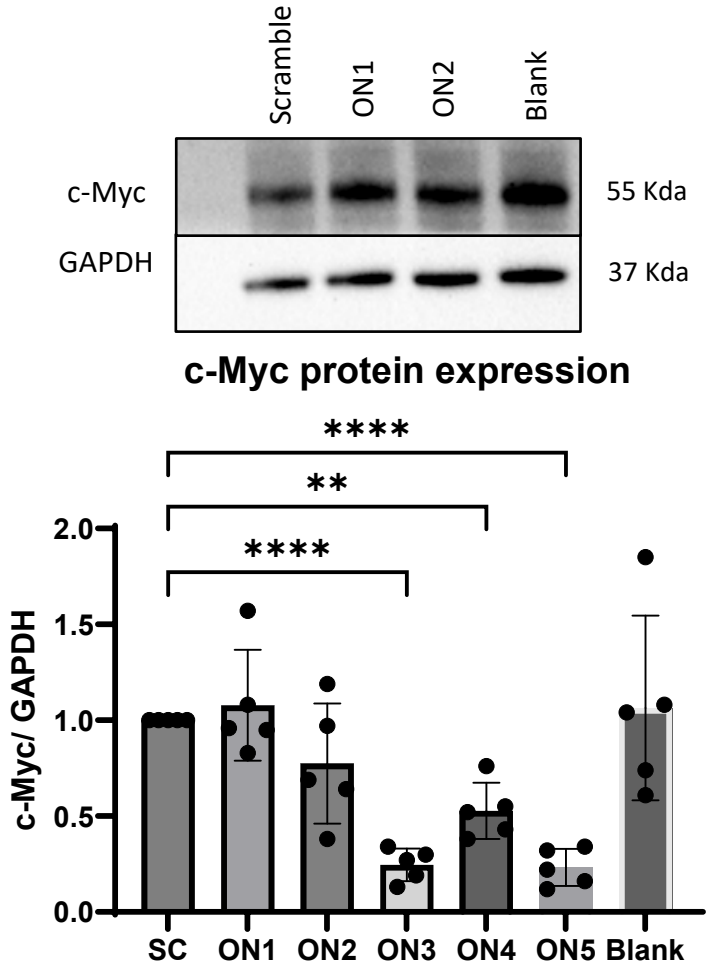


**Figure 3.12**: **Western Blot results of HeLa cells transfected, using Lipofectamine 3000™ Reagent with a Scramble sequence (SC), ON1, ON2, ON3, ON4 and ON5 for 24 hours.** The blot shows the results of one independent experiment. The "Blank" control represents cells exposed to the same volume of cell culture medium as the transfection samples, but without Lipofectamine™ 3000 or ONs. The error bars represent variability within the samples. Statistical analysis was done using a one-way ANOVA with a Dunnett's multiple comparison test. Asterisks indicate the level of significance between groups: *P ≤ 0.05, **P ≤ 0.01, ***P ≤ 0.001, ****P ≤ 0.0001.

Sequences ON1 and ON2 do not appear to significantly impact c-Myc protein modulation, as the levels of c-Myc protein following transfection with both sequences remain similar to those of the Scramble sequence (**Figure 3.12)**. Although sequence ON2 seems to cause a slight downregulation, the reduction in c-Myc protein levels is not substantial enough to achieve statistical significance. The initial hypothesis to explain these results was that the high GC content in each sequence adversely affects hybridization with the molecular target, thereby not influencing c-Myc protein levels. However, further testing of subsequent conditions will help clarify the actual effects of these sequences.

Comparing these findings with the RT-qPCR results, there is a slight upregulation in *c-myc* mRNA levels. Nevertheless, this upregulation is insufficient to reach statistical significance. Thus, considering these results after 24 hours, it appears that the transfection of these sequences does not significantly affect *c-myc* modulation.

As with the RT-qPCR assays, the next step involved transfecting HeLa cells with all the different sequences, following the same protocol but extending the incubation period to 48 hours. The results for the various sequences are summarized comparing the effects of transfection on c-Myc protein expression after 48 hours with those observed after 24 hours (**Figure 3.13**). It is important to note that the experiments conducted after 48 hours were repeated three times.

The values obtained from the experiments after a 48-hour incubation period are similar to those observed after 24 hours (**Figure 3.13)**. Specifically, sequence ON1 exhibits a slight decrease after 48 hours, with the protein expression levels remaining close to 1. Similarly, for sequence ON2, c-Myc levels increase slightly but also remain near 1 compared to the scramble control. Based on these results, it can be concluded that, in terms of protein expression modulation, transfections with sequences ON1 and ON2 do not appear to have any significant impact.

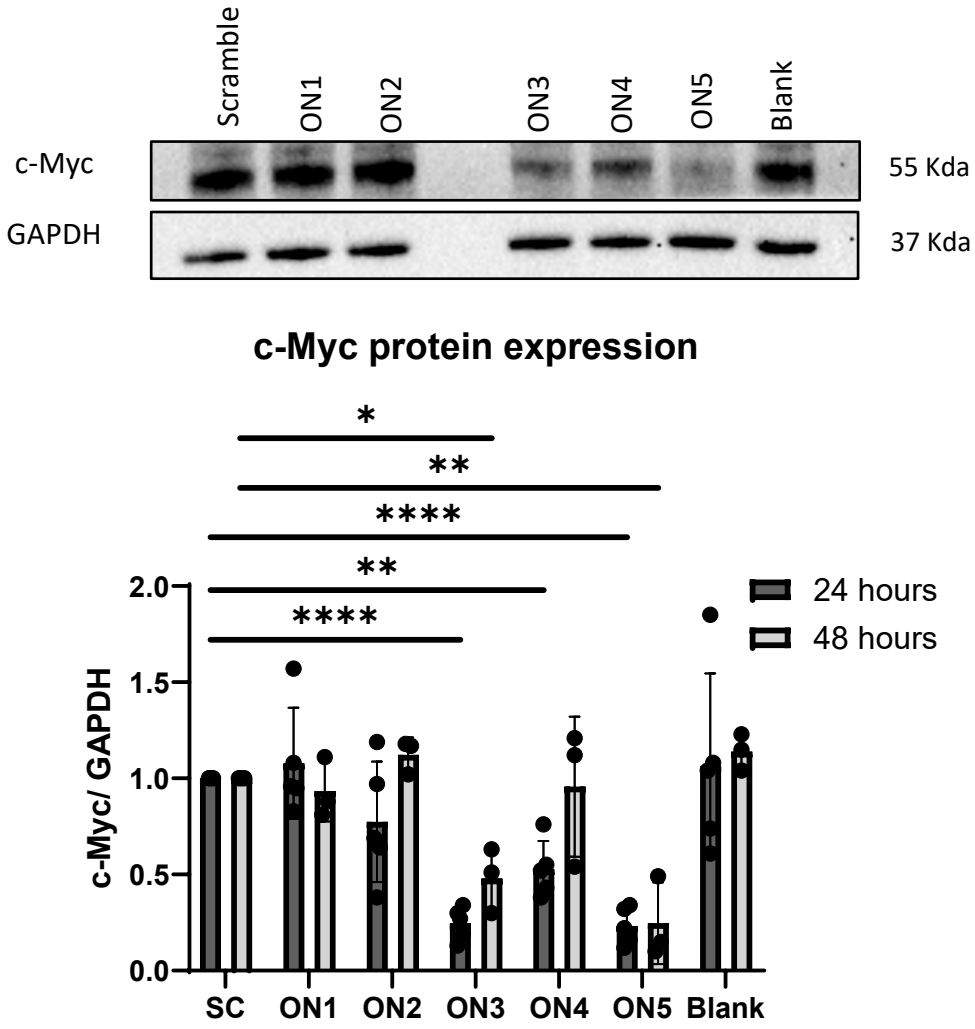


**Figure 3.13: Western Blot results of HeLa cells transfected, using Lipofectamine 3000™ Reagent with a Scramble sequence (SC), ON1, ON2, ON3, ON4 and ON5 for 24/48 hours**. The "Blank" control represents cells exposed to the same volume of cell culture medium as the transfection samples, but without Lipofectamine™ 3000 or ONs. The blot shows the results of one independent experiment. The error bars represent variability within the samples. Statistical analysis was done using a one-way ANOVA with a Dunnett's multiple comparison test. Asterisks indicate the level of significance between groups: *P ≤ 0.05, **P ≤ 0.01, ***P ≤ 0.001, ****P ≤ 0.0001.

For ON3, c-Myc protein levels are significantly reduced compared to the scramble control at 24 hours (****, P≤0.0001), but this effect diminishes at 48 hours, where the significance drops (**, P≤0.01), due to a partial recovery of c-Myc expression over time.

ON4 shows a similar pattern: at 24 hours, there is a significant decrease in c-Myc levels compared to the scramble (**, P≤0.01), but at 48 hours, the difference is no longer statistically significant, and c-Myc expression returns to levels similar to the scramble, ON1 and ON2.

ON5 maintains a consistent downregulation of c-Myc protein at both time points. The reduction is highly significant at 24 hours (****, P≤0.0001), but at 48 hours, the significance decreases (**, P≤0.01), reflecting a slight increase in c-Myc expression while remaining well below the scramble control.

The downregulation of the protein levels after transfection with sequences ON3, ON4 and ON5 can be attributed to several mechanisms:

First, is the downregulation of the mRNA levels via RNase H1 activation. ASOs can hybridize with target mRNAs, forming RNA-DNA hybrids that are recognized and cleaved by RNase H1. This cleavage results in the degradation of the target mRNA, leading to a reduction in protein synthesis since there is less mRNA available for translation. However, the design of the proposed ASOs should not activate RNase H1 activity, as the sequence modifications are arranged to ensure that no gapmers are present[202,203].

Also, as described in the RT-qPCR section, ASOs can induce mRNA degradation through the no-go decay pathway which is translated into a downregulation of the protein levels[199].

Finally, the ASOs can bind to the 5' UTR or other regions of the mRNA, obstructing the assembly of the translation initiation complex, by steric hindrance. This binding can interfere with the recruitment of ribosomes and other necessary factors, reducing translation efficiency and consequently decreasing protein levels[204].

When comparing these results with those obtained from the RT-qPCR assays, certain correlations can be observed. For instance, sequence ON4 is the most active in terms of upregulating both mRNA and protein levels. Conversely, sequence ON5 consistently downregulates both mRNA and protein levels. Regarding sequences ON1, ON2, and ON3, they exhibit similar behaviour in the RT-qPCR assays; however, sequence ON3 demonstrates strong downregulation activity by reducing C-MYC protein levels after both 24 and 48 hours. As previously described, ON1 and ON2 do not appear to modulate C-MYC protein levels after 24 and 48 hours and also do not affect mRNA levels after 24 hours. Nevertheless, the hypothesis that they do not show any effect

due to a lack of hybridization with the target cannot be concluded, as they show some downregulation of mRNA levels after 48 hours.

After completing the characterization of the impact of sequences transfected with Lipofectamine 3000™ Reagent, the oligonucleotides were delivered into HeLa cells using the previously synthesized AuNPs@PEG@ssDNAs. These assays were conducted in triplicate, adhering to the protocol outlined in **Section 5.7.1.3.2**. As with previous assays, the sequences tested included Scramble, ON1, ON2, ON3, ON4, and ON5. Additionally, AuNPs fully covered with PEG molecules were used as a control (**Figure 3.14)**.

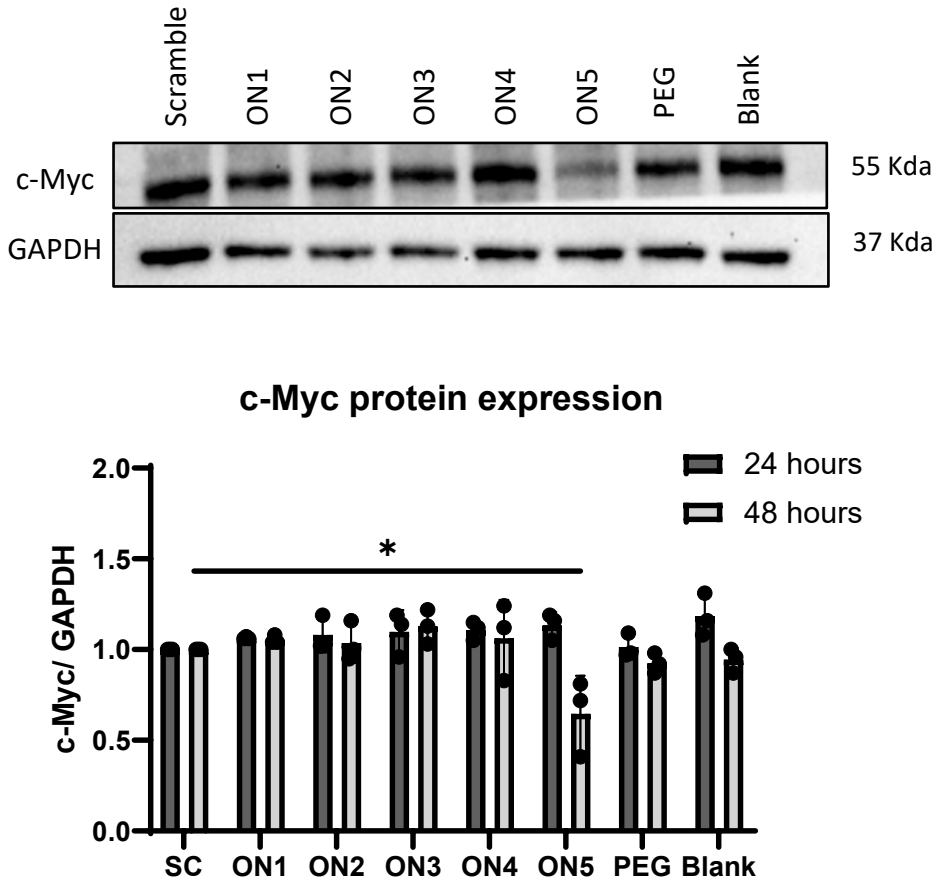


**Figure 3.14: Western Blot results of HeLa cells transfected using the biofunctionalized AuNPs with a Scramble sequence (SC), ON1, ON2, ON3, ON4 and ON5 for 24/48 hours**. The blot shows the results of one independent experiment. The "Blank" control represents cells exposed to the same volume of cell culture medium as the transfection samples, but without AuNPs or ONs. The error bars represent variability within the samples. Statistical analysis was done using a one-way ANOVA with a Dunnett's multiple comparison test. Asterisks indicate the level of significance between groups: *P ≤ 0.05, **P ≤ 0.01, ***P ≤ 0.001, ****P ≤ 0.0001.

Across all conditions, c-Myc protein levels remain similar to those of the Scramble control, except for the transfection with sequence ON5 after 48 hours of incubation, which exhibits a statistically significant decrease in protein levels (* for $p<0.05$) (**Figure 3.14**). This effect aligns with previous observations indicating that sequence ON5 is the most effective in downregulating c-Myc protein expression. Unlike the RT-qPCR results, these findings suggest that sequences biofunctionalized with AuNPs@PEG@ssDNAs may replicate the outcomes achieved with Lipofectamine transfection. Additional characterization techniques will be employed in subsequent sections to explore hypotheses explaining these results.

### 3.3.3 Impact of *c-myc* Targeting Oligonucleotides on HeLa Cell Viability

Following the completion of the RT-qPCR and Western Blot assays, the next step was to evaluate whether the modulation of *c-myc* activity induced by the transfection of the different sequences translated into increased cell mortality. To address this, various techniques and assays were conducted to assess the cytotoxicity and its impact on cell viability.

#### 3.3.3.1 Sequence-Dependent Effects on HeLa Cell Survival Assessed by Flow Cytometry

Flow cytometry was the primary technique employed to evaluate the impact of different sequences on the viability of HeLa cells. This method is highly versatile and precise, offering the ability to distinguish between cell populations and facilitate high-throughput analysis. Cell death or membrane compromise was assessed using viability dyes, which selectively stain cells with damaged membranes, providing a direct measure of cytotoxicity. The detailed protocol for this technique is described in **Section 5.7.7**.

For this assay, cells were stained using the Zombie Violet™ Fixable Viability Kit (BioLegend), an amine-reactive fluorescent dye that remains impermeable to live cells but readily penetrates cells with compromised membranes. This approach allowed for the quantification of dead cells as a proportion of the total cell population following the transfection of each sequence.

For this experiment, $3\times10^5$ cells were seeded per well and cultured for 24 hours in 6-well plates. After the incubation period, the scramble sequence, ON1, ON2, ON3, ON4, and ON5 were transfected into the cells for either 24 or 48 hours using Lipofectamine™ 3000 in DMEM cell medium. Importantly, in all experiments described in this section, ON transfection was performed exclusively with Lipofectamine™ 3000 and not with ON conjugated to AuNPs. Each condition was performed in triplicate across three wells. Following transfection, the cells were harvested and processed according to the protocol described in **Section 5.7.7**.

HeLa cells were stained with the Zombie Violet™ Fixable Viability Kit (BioLegend) and analysed by flow cytometry to assess cell viability. The analysis began with the establishment of a precise gating strategy to accurately identify viable cells. Singlet cells were first selected based on forward scatter height (FSC-H) versus area (FSC-A), which distinguishes single cells from aggregates. From this singlet population, cells were further characterized by size (FSC) and granularity (SSC). Viable cells were then identified by their lack of Zombie Violet™ staining, as only dead cells exhibit a positive signal for this dye.

To set the gating parameters, control samples were included: a live control consisting of untreated cells, and a dead control generated by incubating untreated cells at 60°C for 20 minutes to induce complete cell death. These controls were used to establish accurate gating parameters, ensuring reliable discrimination between viable and non-viable cells in all experimental samples. (**Figure 3.15**). Once the gating strategy was established, all experimental samples were analysed. The results show that, following ON1 transfection with Lipofectamine™ 3000, the majority of cells remained viable (99.0%), with only a small fraction identified as dead (0.97%). These findings confirm that ON1 does not induce significant cytotoxicity in HeLa cells under the conditions tested.

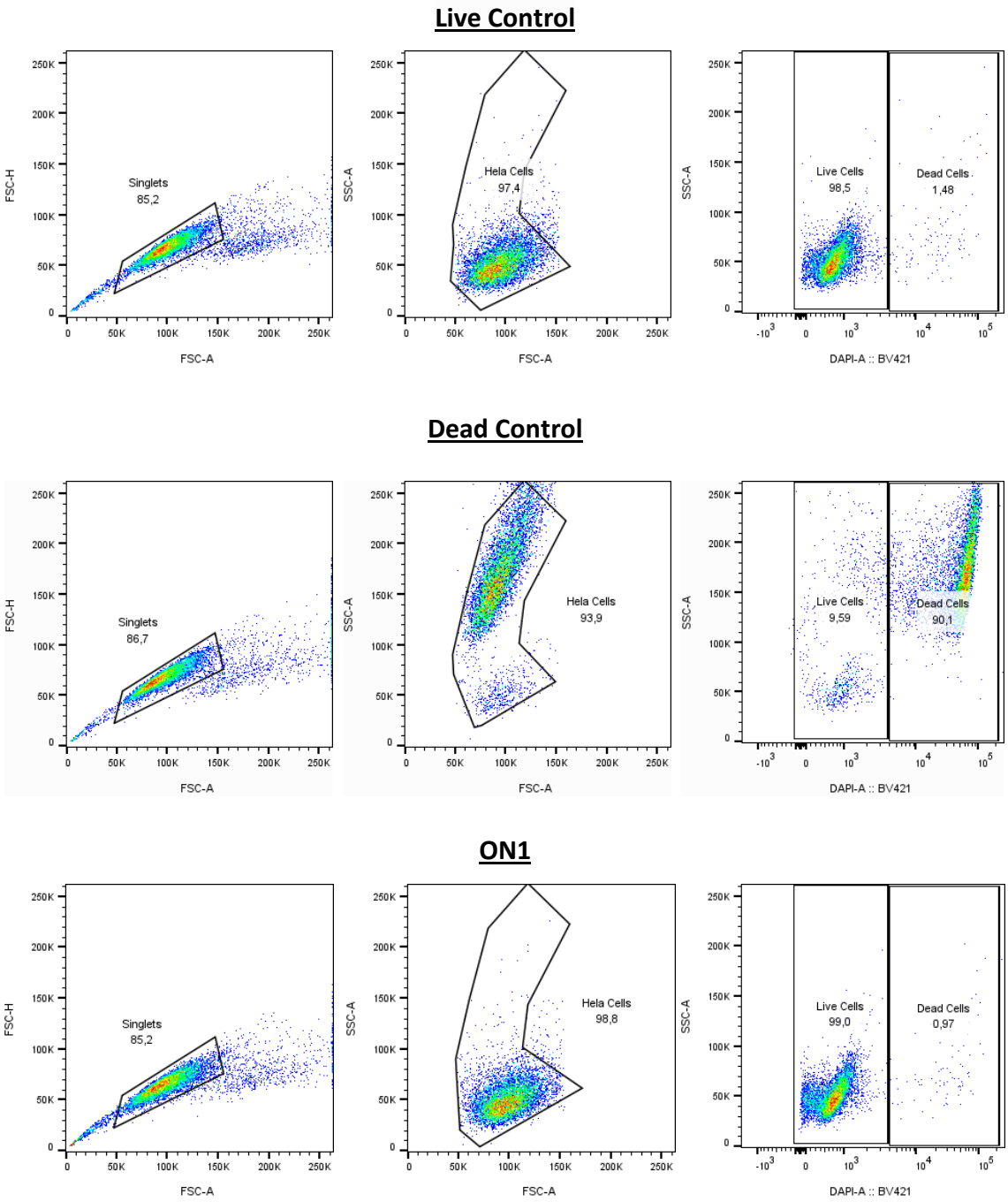


**Figure 3.15: Gating strategy for flow cytometric assessment of HeLa cell viability**. The figure illustrates the sequential gating approach used to analyze HeLa cells stained with Zombie Violet™ Fixable Viability Kit. Representative dot plots are shown for a live control, a dead control, and ON1-transfected cells. The first gate (FSC-A vs. FSC-H) identifies singlet cells, the second gate (FSC-A vs. SSC-A) isolates the main cell population, and the final gate (SSC-A vs. Zombie Violet) distinguishes live (negative staining) from dead (positive staining) cells.

Cell viability was evaluated for each oligonucleotide sequence transfected with Lipofectamine™ 3000 after 24 and 48 hours of incubation, with three replicates per condition (**Figure 3.16**). This standardized methodology enabled a direct comparison of

cytotoxicity across all experimental groups and ensured that any differences in cell viability were due to the specific oligonucleotide sequence rather than inconsistencies in the experimental procedure. The different replicates for these experiments can be found in **Appendix G**.

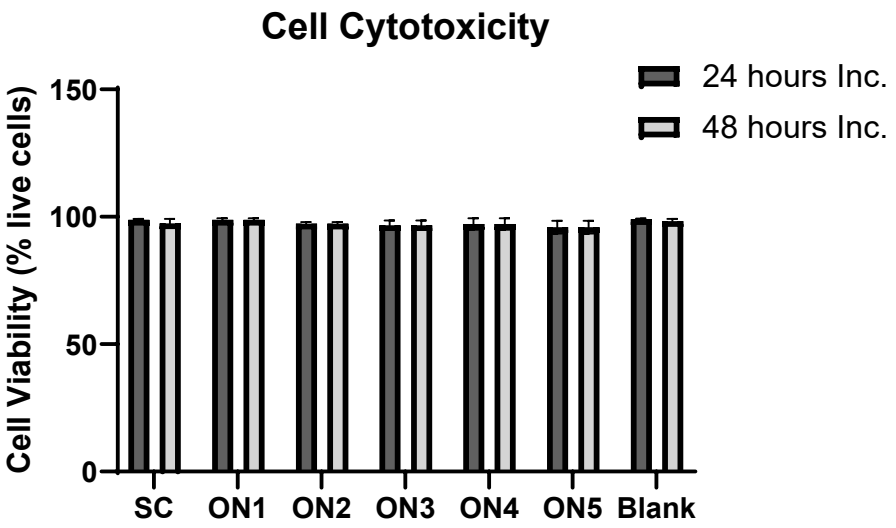


**Figure 3.16: Cell cytotoxicity analysis by Flow Cytometry of HeLa cells transfected with scramble sequence (SC), ON1, ON2, ON3, ON4, ON5 using Lipofectamine™ 3000 Reagent in a 6 well plate for 24/48 hours transfection.** The "Blank" control represents cells exposed to the same volume of cell culture medium as the transfection samples, but without Lipofectamine™ 3000 or ONs. The assay was done in triplicate. Error bars are represented by ± SD.

Across all conditions and time points, cell viability remained consistently high, with values close to 100% and only minimal variation observed between samples (**Figure 3.16**). No significant cytotoxicity was detected for any of the oligonucleotide sequences compared to the scramble control or the blank, indicating that transfection with these oligonucleotides using Lipofectamine™ 3000 does not adversely affect HeLa cell viability under the experimental conditions tested.

These results were unexpected, as it was anticipated that the modulation of c-Myc levels, depending on the sequence transfected, would impact cell cytotoxicity, particularly in cases where c-Myc protein levels were downregulated.

It was hypothesized that the washing steps performed during sample preparation for flow cytometry may have removed dead cells, thereby preventing their detection during the analysis.

Initially, this technique was employed because it allowed for the use of the same transfection protocol in 6-well plates as was used in the RT-qPCR and Western Blot assays. However, it was decided to transition to more standard cytotoxicity assays that are less invasive and permit analysis directly on the same plate. This approach ensures that no cells are lost or excluded during the experimental process. Consequently, all these experiments will need to be scaled down for execution in 96-well plates.

#### 3.3.3.2 Sequence-Dependent Effects on HeLa Cell Survival Assessed by Cell Proliferation Assay

The CellTiter 96® AQueous One Solution Cell Proliferation Assay was employed as a cytotoxicity assay to assess the number of viable cells. This assay is based on the bioreduction of the MTS tetrazolium compound into a coloured formazan product, with the amount of formazan, measured by absorbance at 490 nm, being directly proportional to the number of viable cells. The protocol for evaluating cell viability and the detailed procedure for calculating cell cytotoxicity are provided in **Section 5.7.8.2**. The experiment was conducted during a secondment at The International Institute of Molecular Mechanisms and Machines (IMol) under the supervision of Dr. Carlo Vascotto.

For this experiment, 12,000 cells were seeded per well and cultured for 24 hours in 96-well culture plates. Following this incubation period, the scramble sequence, ON1, ON2, ON3, ON4, and ON5 were transfected into the cells for 6 hours using Lipofectamine™ 3000 in Gibco™ Opti-MEM™ cell medium. Each condition was performed in triplicate across three wells. After transfection, the cells were washed and incubated for an additional 24/48 hours in DMEM cell culture medium.

At the end of the incubation period, the CellTiter 96® AQueous One Solution Reagent was added to each well, and the cells were incubated with the reagent for an additional 4 hours. Subsequently, the plate was gently shaken to homogenize the compound released with the cell medium in each sample. Once a uniform colour was

achieved, the absorbance for each condition was measured at 490 nm using a plate reader. As previously mentioned, the absorbance is directly proportional to the number of viable cells.

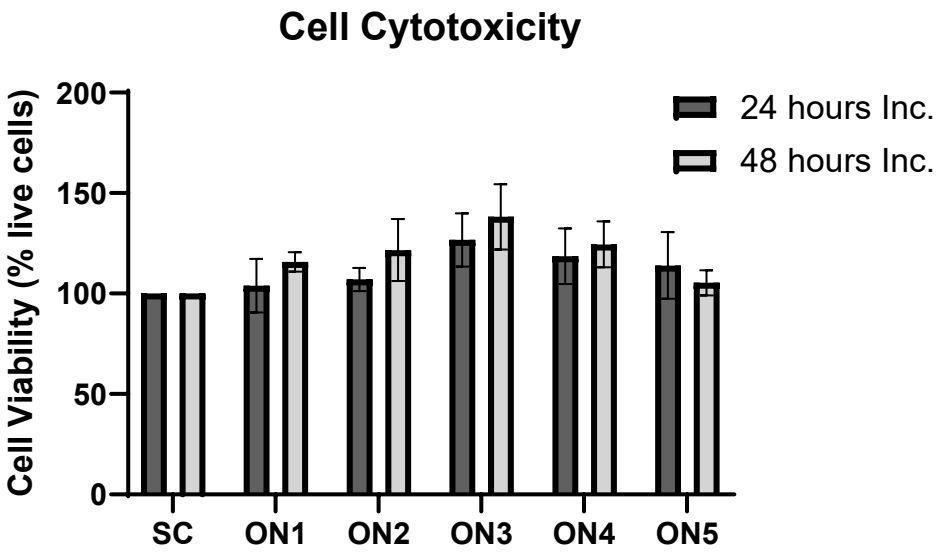


**Figure 3.17: Cell cytotoxicity analysis of HeLa cells transfected with scramble sequence (SC), ON1, ON2, ON3, ON4, ON5 using Lipofectamine™ 3000 Reagent in a 96 well plate for 24/48 hours transfection.** The assay was done in triplicate. Error bars are represented by ± SD.

The results indicate no significant cell mortality following transfection with any of the sequences after 24 and 48 hours of incubation (**Figure 3.17)**. Furthermore, sequences ON3, ON4, and ON5 exhibit higher percentages of cell viability compared to the Scramble sequence. This increase in cell viability is observed across all conditions after 48 hours, with the exception of ON5.

Based on the results obtained in the previous experiments, a decrease in cell viability was anticipated due to the reduction in c-Myc levels, particularly following incubation with sequences ON3, ON4, and ON5. c-Myc is a critical transcription factor that drives cellular proliferation by regulating genes involved in cell cycle progression, metabolism, and ribosome biogenesis. In most cases, its suppression has been associated with diminished cell growth, reduced colony formation, and impaired cell cycle progression, as demonstrated in various studies[205–208]. However, the reduction of c-Myc levels can, under specific conditions, decrease cytotoxicity in certain cancer

cells. This phenomenon is often associated with the metabolic state of the tumour microenvironment or the specific role of c-Myc in cellular processes.

Studies have demonstrated that reducing c-Myc levels under conditions of oxygen and glucose deprivation protects cancer cells from necrotic cell death by conserving energy and enabling adaptation to harsh microenvironments. Additionally, high c-Myc expression is linked to increased sensitivity to certain stressors, such as glucose deprivation or DNA damage. By downregulating c-Myc, cancer cells may adapt to metabolic stress, becoming less susceptible to these cytotoxic stresses and thereby increasing cell viability in such environments[209].

Moreover, in certain tumour cell lines, a reduction in c-Myc levels induces cell cycle arrest rather than apoptosis. This arrest decreases overall cellular activity and metabolic demands, potentially reducing susceptibility to cytotoxic agents and further enhancing cell viability[210].

In summary, while c-Myc is a key driver of proliferation and tumorigenesis, its reduction can sometimes provide a survival advantage to cancer cells under specific conditions by enabling metabolic adaptation or reducing sensitivity to cytotoxic stressors. Based on these findings, it can be concluded that the conditions under which transfection occurs—such as incubation with Gibco™ Opti-MEM™ medium (characterized by reduced glucose levels) or the cytotoxicity induced by Lipofectamine™ 3000 Reagent—may contribute to an increase in cell viability, particularly under conditions where c-Myc levels are reduced.

To validate these observations, the same assay was repeated using alternative techniques to confirm the results and effects observed in this experiment.

### 3.3.3.3 Sequence-Dependent Effects on HeLa Cell Survival Assessed by LDH Cytotoxicity Assay

Cellular cytotoxicity was also assessed using the Invitrogen™ CyQUANT™ LDH Cytotoxicity Assay Kit. This assay quantifies the concentration of lactate dehydrogenase (LDH) in the culture medium. LDH is a cytosolic enzyme that is released into the medium when the cell membrane is compromised, serving as an indicator of cell damage or death.

The assay is based on a coupled enzymatic reaction in which LDH catalyses the conversion of lactate to pyruvate, accompanied by the reduction of $NAD^+$ to NADH. The NADH produced subsequently reduces a tetrazolium salt to form a red formazan product, which can be measured spectrophotometrically at 490 nm. The amount of formazan generated is directly proportional to the amount of LDH released into the medium, which, in turn, reflects the level of cell death in the sample. The protocol for assessing cell viability and the detailed method for calculating cell cytotoxicity are described in **Section 5.7.8.1**.

The experimental setup for this assay was similar to that used for the CellTiter 96® AQueous One Solution Cell Proliferation Assay, with 12,000 cells seeded per well and cultured for 24 hours in 96-well culture plates. However, in this case, the assay evaluated the effects of the scramble sequence, ON1, ON2, ON3, ON4, and ON5 transfected into HeLa cells using either Lipofectamine™ 3000 or sequences biofunctionalized onto AuNPs@PEG@ssDNAs.

The transfection of sequences using AuNPs@PEG@ssDNAs followed the protocol outlined in **Section 5.7.1.3.2**. In this method, cells were incubated with the AuNPs@PEG@ssDNAs for 6 hours in Gibco™ Opti-MEM™ cell medium. After transfection, the cells were washed and incubated for an additional 24 or 48 hours in DMEM cell culture medium. In contrast, for transfection using Lipofectamine™ 3000, the cells were transfected directly in DMEM cell culture medium without any washes after the initial 6-hour incubation. This condition differs from the protocol used in the CellTiter 96® AQueous One Solution Cell Proliferation Assay described earlier.

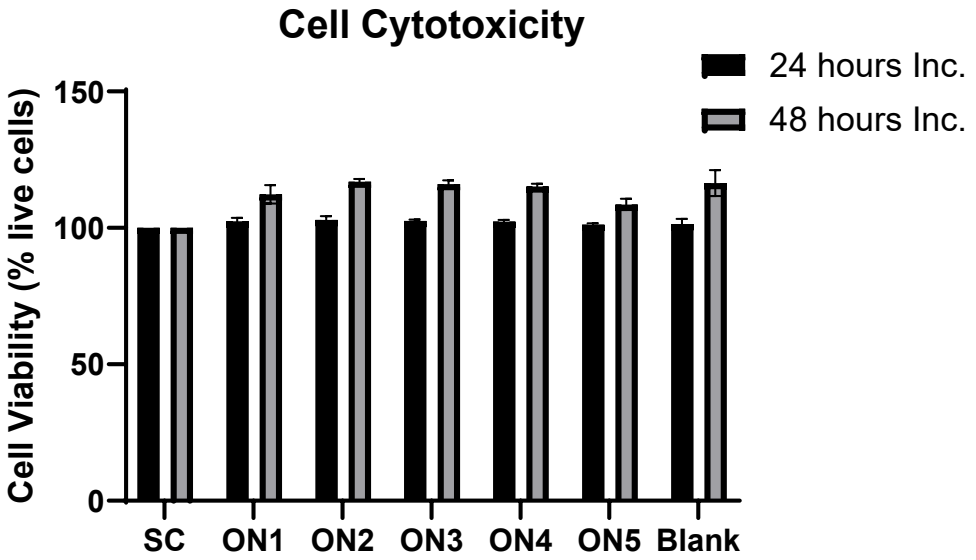


**Figure 3.18: Cell cytotoxicity analysis of HeLa cells transfected with scramble sequence (SC), ON1, ON2, ON3, ON4, ON5 using Lipofectamine™ 3000 Reagent in a 96 well plate for 24/48 hours transfection.** The "Blank" control represents cells exposed to the same volume of cell culture medium as the transfection samples, but without Lipofectamine™ 3000 or ONs. The assay was done in triplicate. Error bars are represented by ± SD.

The cell viability of HeLa cells following transfection with all sequences using Lipofectamine™ 3000 Reagent for 24 hours remains approximately 100% across all conditions (**Figure 3.18**). When examining the results after 48 hours, an increase in cell viability is observed in all cases compared to the values obtained at 24 hours, with ON5 exhibiting the smallest increase.

When comparing these results to those obtained in the CellTiter 96® AQueous One Solution Cell Proliferation Assay, it can be concluded that the modulation of c-Myc levels induced by the transfection of the sequences does not increase cell mortality in the samples.

Additionally, it appears that the glucose concentration in the cell culture medium plays a role in determining cell viability percentages. In this assay, where incubation was performed using DMEM cell medium, all viability percentages remained relatively consistent after 24 hours. However, in the CellTiter 96® AQueous One Solution Cell Proliferation Assay, where cells were incubated for the first 6 hours in Gibco™ Opti-

MEM™ medium with low glucose levels, cell viability percentages varied depending on the sequence transfected.

When comparing the results from both assays after 48 hours, a general trend of increasing cell viability percentages is observed. Notably, cells transfected with sequence ON5 consistently exhibit the smallest increase in viability across both assays.

Despite these findings, the reason why HeLa cells maintain high viability even with a significant reduction in c-Myc protein levels following the transfection of certain sequences remains unclear. In all cases, the cells demonstrate a high survival rate, which further increases after 48 hours. While it is true that transfection with ON5 results in slightly lower viability percentages compared to other sequences, this difference does not appear to be statistically significant, making it difficult to draw definitive conclusions about the impact of c-Myc downregulation on cell viability.

Additionally, the hypothesis that low glucose levels in the medium or increased cellular resistance to cytotoxicity induced by transfection could explain these results seems inaccurate. All cells transfected with different sequences exhibit similar behaviour in terms of viability, despite producing varying effects on c-Myc modulation.

Following the analysis of the results from experiments using Lipofectamine™ 3000, an assay was conducted to evaluate the transfection of the sequences biofunctionalized onto AuNPs@PEG@ssDNAs. This experiment aimed to determine whether an alternative delivery system would produce a distinct effect. Additionally, a control consisting of Au@PEG was included to assess whether the presence of AuNPs contributes to increased cell mortality.

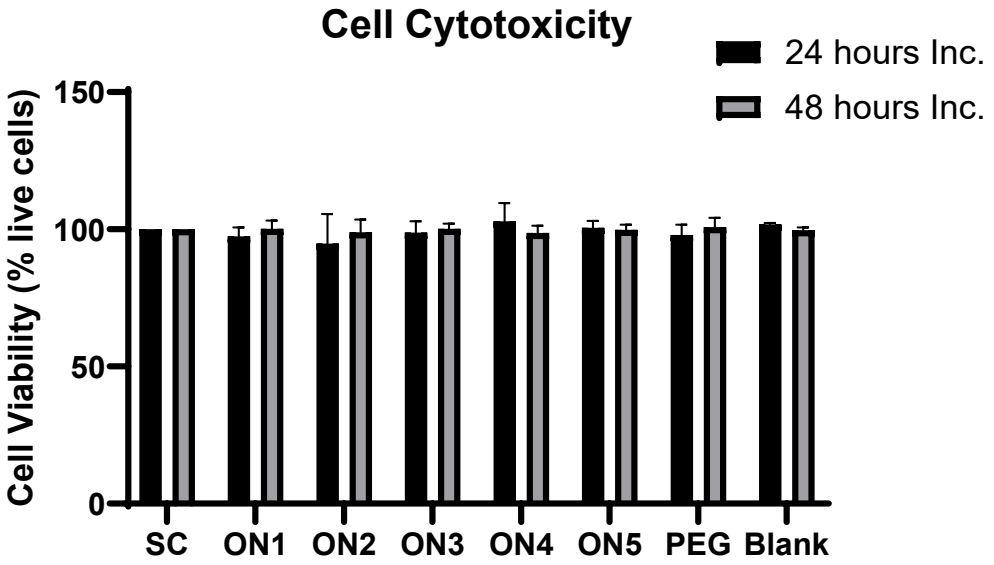


**Figure 3.19: Cell cytotoxicity analysis of of HeLa cells transfected using the biofunctionalized gold nanoparticles with a Scramble sequence (SC), ON1, ON2, ON3, ON4 and ON5 in a 96 well plate for 24/48 hour.** The "Blank" control represents cells exposed to the same volume of cell culture medium as the transfection samples, but without Lipofectamine™ 3000 or ONs. The assay was done in triplicate. Error bars are represented by ± SD.

The cell viability percentages remain similar to those of the Scramble control (**Figure 3.19**). Based on these results, it can be concluded that none of the sequences induce significant cell mortality in HeLa cells following transfection at either 24 or 48 hours, including sequence ON5, which was shown to downregulate c-Myc under these conditions. In this case, the viability percentages after 24 and 48 hours remain relatively consistent, aligning with the findings from the Western Blot and RT-qPCR assays, which suggest a lack of significant interaction between the sequences and the cells.

### 3.3.4 Comparative Cellular Uptake and Distribution of Oligonucleotides Delivered by Lipofectamine™ 3000 and AuNPs in HeLa Cells

Confocal microscopy was employed to investigate the delivery and internalization of various oligos into HeLa cells during transfection. This technique is a specialized form of standard fluorescence microscopy that utilizes specific optical components to produce high-resolution images of materials stained with fluorescent probes.

Sequences ON4 and ON5 were selected for the assay due to their significant impact on c-Myc modulation. ON4 demonstrated strong potential for upregulating mRNA levels in the RT-qPCR assays, while ON5 showed the most pronounced downregulation of c-Myc protein levels following transfection for 24 and 48 hours. A scrambled sequence was also included as a control to determine whether the internalization and localization of the oligonucleotides are sequence-dependent or influenced by the delivery system used. The sequences studied in this assay were modified to include a 6-Fluorescein (6-FAM) fluorophore attached to the 3' end of the oligonucleotide, enabling visualization of their delivery via microscopy. The sequences were synthesized and functionalized as described in **Chapter 5.2**. The primary difference in this process was the use of a CPG column containing a fluorescein phosphoramidite with a DMT group, which facilitates the coupling of subsequent phosphoramidites.

The initial experiment utilizing this technique involved analysing the delivery and internalization of different sequences by comparing their transfection via Lipofectamine™ 3000 with their transfection via biofunctionalized AuNPs@PEG@ssDNAs. For this purpose, 60,000 HeLa cells were seeded onto glass coverslips #1.5 or #1.5H in a 24-well plate. Following overnight incubation at 37°C in a cell culture incubator, the various transfections were performed according to the protocols outlined in **Sections 5.7.1.3.1** and **5.7.1.3.2.**

After a 6-hour transfection with AuNPs biofunctionalized with the different sequences, cells were fixed at 3, 6, 12, and 24 hours and stained with Wheat Germ Agglutinin (WGA) to visualize the plasma membrane and overall cell morphology, while also using

brightfield imaging. In parallel, the same procedure was conducted for cells transfected with Lipofectamine complexes of the sequences alone, to observe differences in delivery between the two methods. The fixation and immunofluorescence (IF) staining conducted after the transfection period followed the protocol described in **Section 5.7.10.1.**

The majority of cells exhibit the FAM fluorescent signal, indicating successful delivery of the sequences (**Figures 3.20-3-22**). When comparing the two delivery systems, Lipofectamine produces larger aggregates of the FAM signal, whereas the AuNPs result in smaller, discrete puncta distributed throughout the cells. This difference can be attributed to the delivery mechanisms: Lipofectamine encapsulates the sequences within particles, which are more prone to forming aggregates, while sequences biofunctionalized onto AuNPs remain individually linked to the nanoparticle surface, preventing aggregation. The fluorescent signal within cells begins to decrease between 12 and 24 hours; however, a substantial amount of signal is still observed at 12 hours.

Examining the localization of the sequences, it is evident that after transfection they are primarily located in both the nucleus and cytoplasm. Additionally, a notable accumulation of signal is observed around the outer layer of the nucleus, particularly for sequences ON4 and ON5. This may be explained by their interaction with mRNA targeting sequences as they are released from the nucleus, as well as their proximity to the endoplasmic reticulum (ER), where some mRNAs are translated on ribosomes attached to its membrane.

Finally, when comparing the three sequences used in this experiment (Scramble, ON4, and ON5), all appear to exhibit similar behaviour in terms of delivery under all tested conditions. This suggests that the delivery of sequences into cells is determined solely by the delivery system employed and is independent of the specific sequence being transfected.

## Scramble Sequence

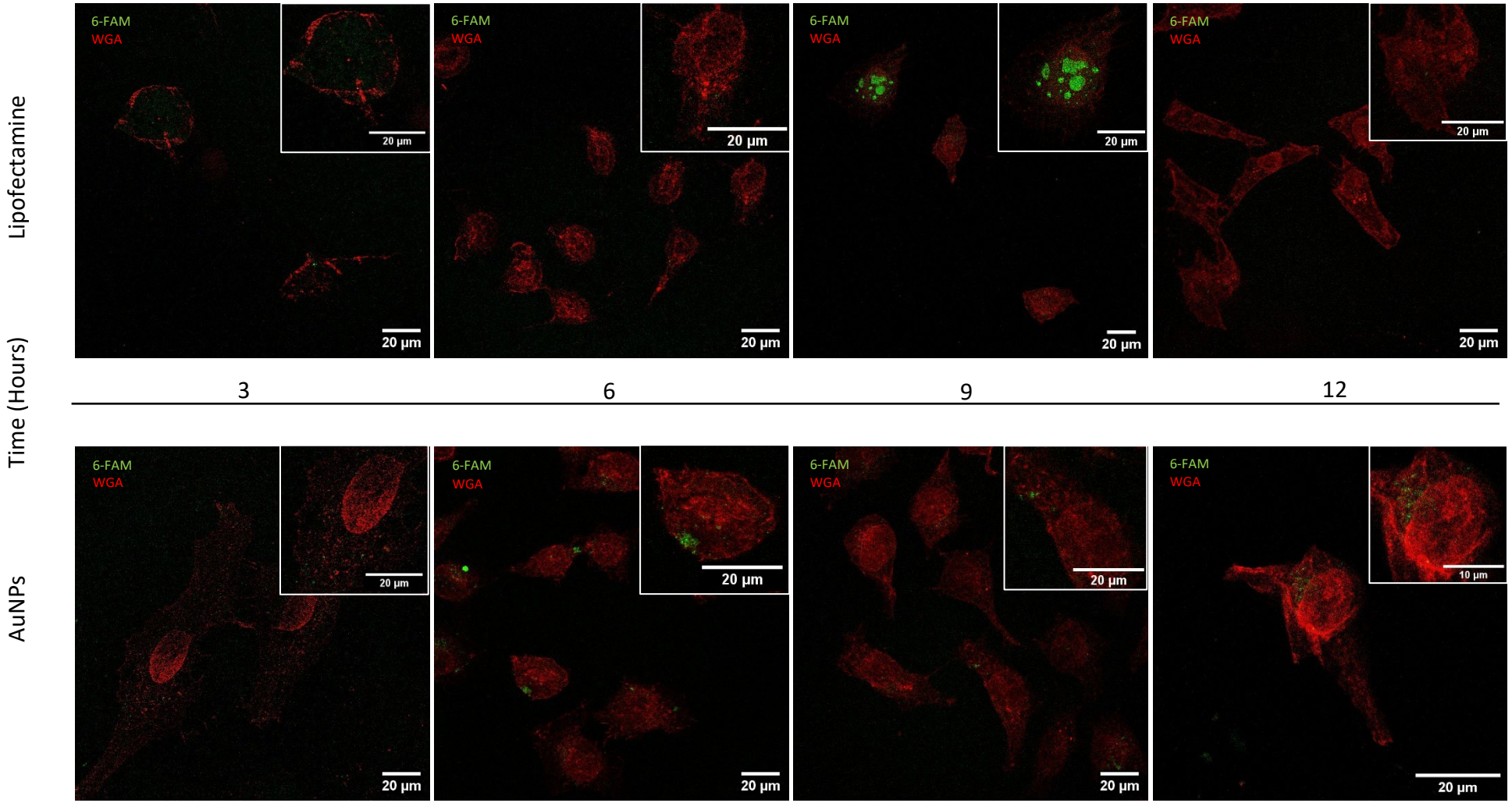


**Figure 3.20: Visualization of fixed cells transfected with fluorescent scramble sequence using confocal microscopy:** The left column displays cells transfected with Lipofectamine-ON complexes, while the right column shows cells incubated with AuNP-ONs, fixed at 3, 6, 12, and 24 hours (from top to bottom). The green fluorescent signal represents the localization of the ONs, while the cell membrane is labelled with Wheat Germ Agglutinin (WGA) in red.

**ON4 Sequence**

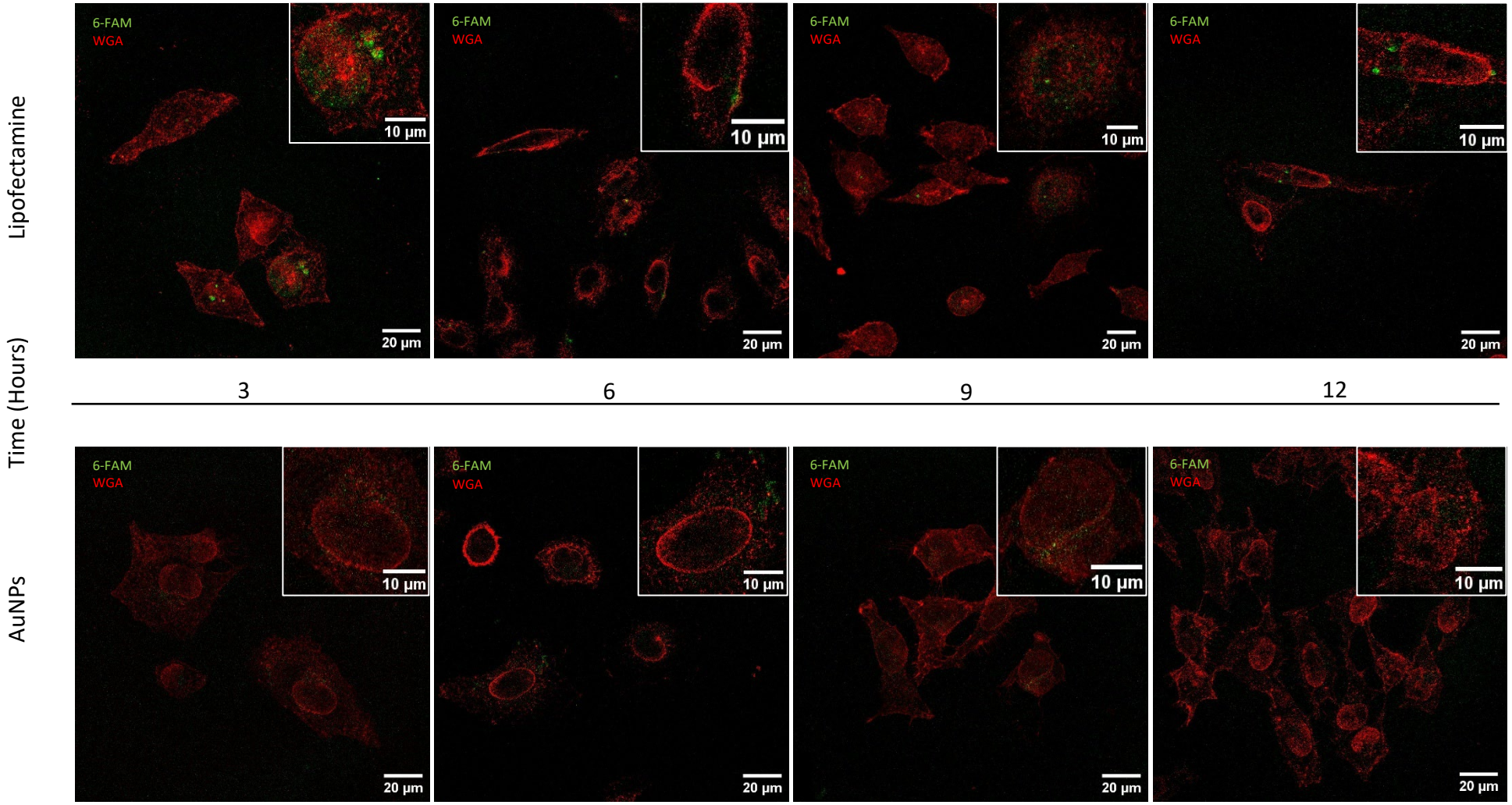


**Figure 3.21: Visualization of fixed cells transfected with fluorescent ON4 using confocal microscopy:** The left column displays cells transfected with Lipofectamine-ON complexes, while the right column shows cells incubated with AuNP-ONs, fixed at 3, 6, 12, and 24 hours (from top to bottom). The green fluorescent signal represents the localization of the ONs, while the cell membrane is labelled with Wheat Germ Agglutinin (WGA) in red.

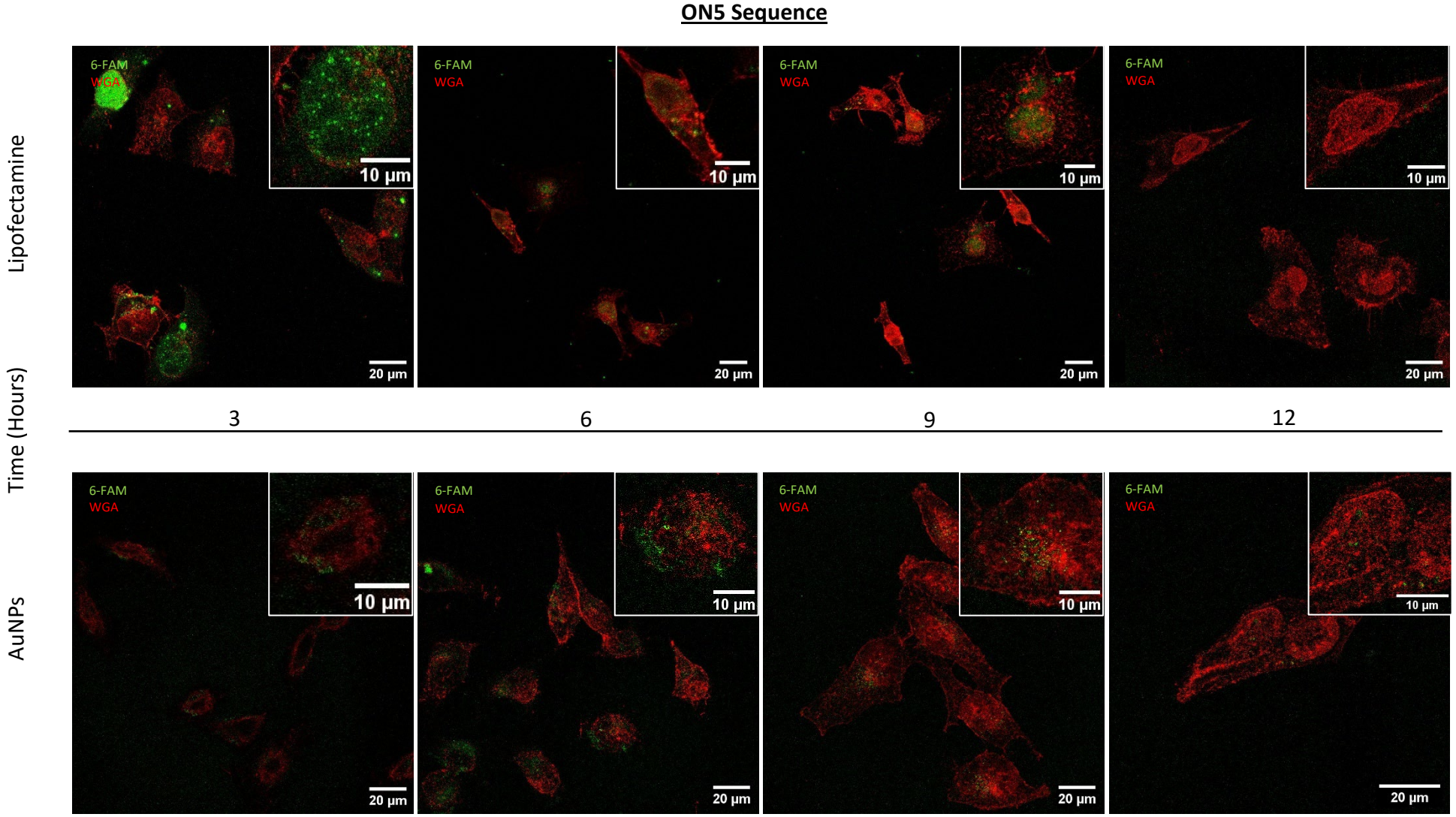


**Figure 3.22: Visualization of fixed cells transfected with fluorescent ON5 using confocal microscopy:** The left column displays cells transfected with Lipofectamine-ON complexes, while the right column shows cells incubated with AuNP-ONs, fixed at 3, 6, 12, and 24 hours (from top to bottom). The green fluorescent signal represents the localization of the ONs, while the cell membrane is labelled with Wheat Germ Agglutinin (WGA) in red.

Based on these results, a time-course experiment spanning 6 hours was conducted to monitor the internalization of AuNPs conjugated with 6-FAM-labeled oligonucleotides. For this assay, 60,000 HeLa cells were directly seeded onto 35 $mm^2$ glass-bottomed cell culture dishes. The experiment was performed using a Zeiss Spinning Disk microscope within an incubation chamber maintained at 37°C and 7% $CO_2$.

Fifteen different positions within the dish were selected, and the biofunctionalized AuNPs were carefully added dropwise. Images were captured every 15 minutes over a total duration of 6 hours. The complete protocol is detailed in **Section 5.7.10.2.** The different replicates for these experiments can be found in **Appendix H.**

Different images from the same field were taken at different time points for each oligos transfection process (**Figure 3.23**). For each time point, the left images display the isolated fluorescence signal of the scrambled sequence, indicating the localization of AuNPs in green. This signal is overlaid with Hoechst dye to visualize the nuclei in blue, while the cell outline is delineated by the DIC signal. Within each field, images are shown from immediately after AuNP addition (top left), followed by images taken at 2 hours (top right), 4 hours (bottom left), and 6 hours (bottom right), at which point the experiment concluded according to standard incubation procedures.

In the different conditions, some green signal is present immediately after AuNP addition; however, the overlay indicates that this signal does not originate from within the cells but likely from along the coverslip. In all conditions, the intensity of the signal increases over the incubation period. This is also true for the background, which gradually intensifies in the green channel over time. Additionally, at later time points, the AuNP signal remains in small discrete localizations, suggesting a lack of aggregation.

Despite the increase in background signal over time, there is also a noticeable rise in the fluorescent signal within the 6-hour time frame. Almost immediately after the addition of the FAM-tagged AuNPs, their presence becomes apparent, likely due to their density causing them to rapidly settle through the medium to the plane of the cells. In the initial frames following their addition, comparison with DIC images reveals

that the fluorescent signal is not yet located inside any cells; instead, the AuNPs appear to either interact with the plasma membrane or rest on the coverslip.

By 4 hours, however, the fluorescent signal continues to intensify, and more of it is observed genuinely inside the cells. At this stage, since the nucleus is visible at its widest point and the DIC images show clearly defined dark edges, it can be concluded that the green fluorescent signal is localized within the cytoplasm. Additional enlarged fields of view and time-lapse videos of the three sequences transfected are provided in Annex III.

As observed in the immunofluorescence assay, the signal also tends to localize in the perinuclear regions. This pattern is evident for both the scrambled sequence and the c-Myc active sequences, making it unclear whether this localization is related to the activity of the NPs or the oligonucleotides.

In conclusion, efficient delivery of the sequences into HeLa cells was achieved within 6 hours using both Lipofectamine™ 3000 and sequences biofunctionalized onto AuNPs. This demonstrates that AuNPs are an effective delivery system for oligonucleotide therapeutics in HeLa cells. Additionally, the uptake appears to be independent of the sequence, as both delivery systems successfully introduced the scrambled and active sequences into the cells, exhibiting similar behaviours.

## Scramble Sequence

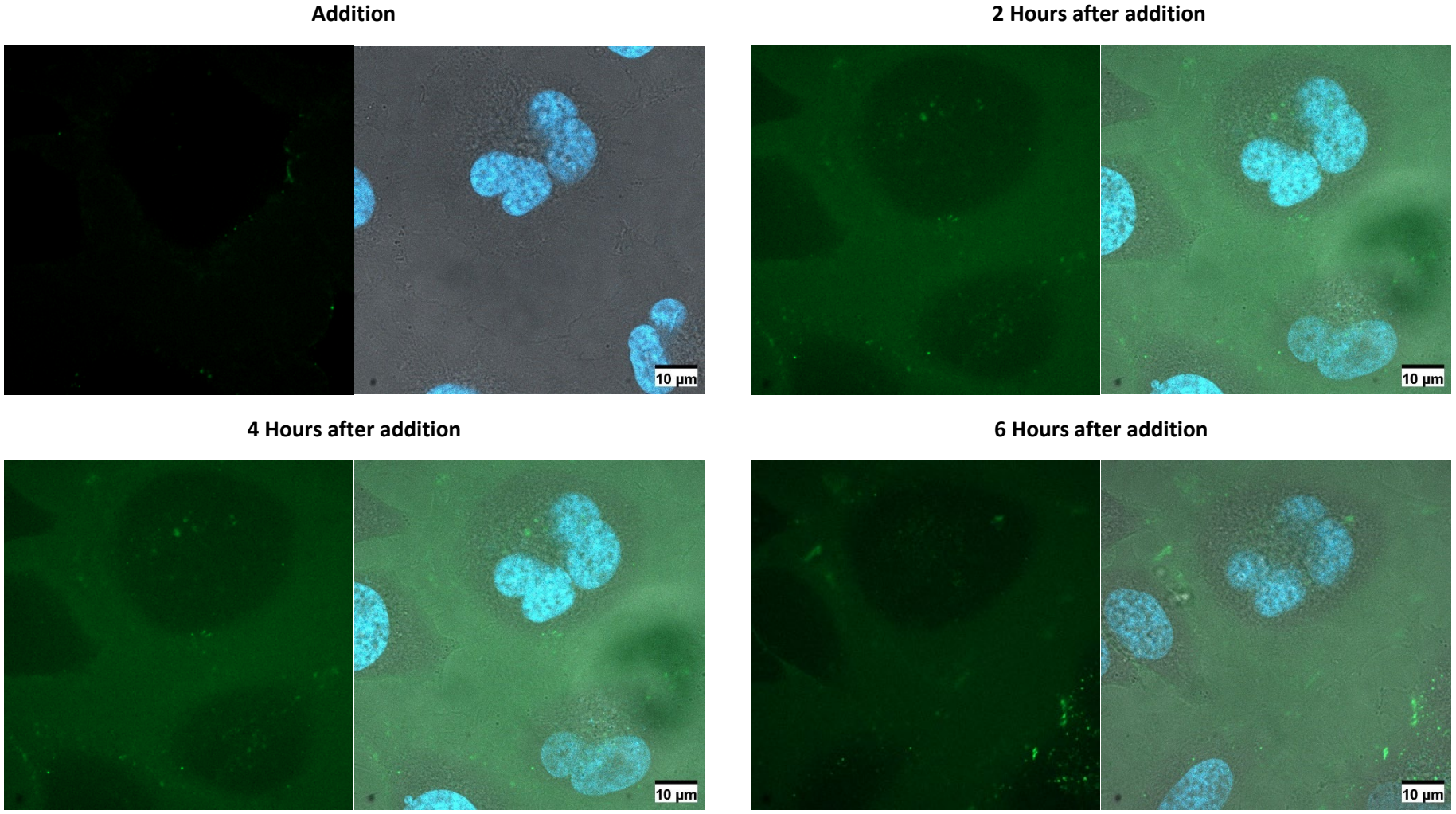


**Figure 3.23**: **Visualization of HeLa cell uptake of AuNP-delivered oligonucleotides (Scramble) using live imaging confocal microscopy:** One field from a time-series of live cells incubated with AuNPs functionalized with the scrambled sequence are presented. Images were captured at four time points: immediately after addition, and subsequently at 2, 4, and 6 hours. For each time point, the left panel displays only the AuNPs (green), while the right panel shows an overlay of the AuNPs (green), the nuclei stained with Hoechst dye (blue), and the cell outline visualized using DIC imaging.

## ON4 Sequence

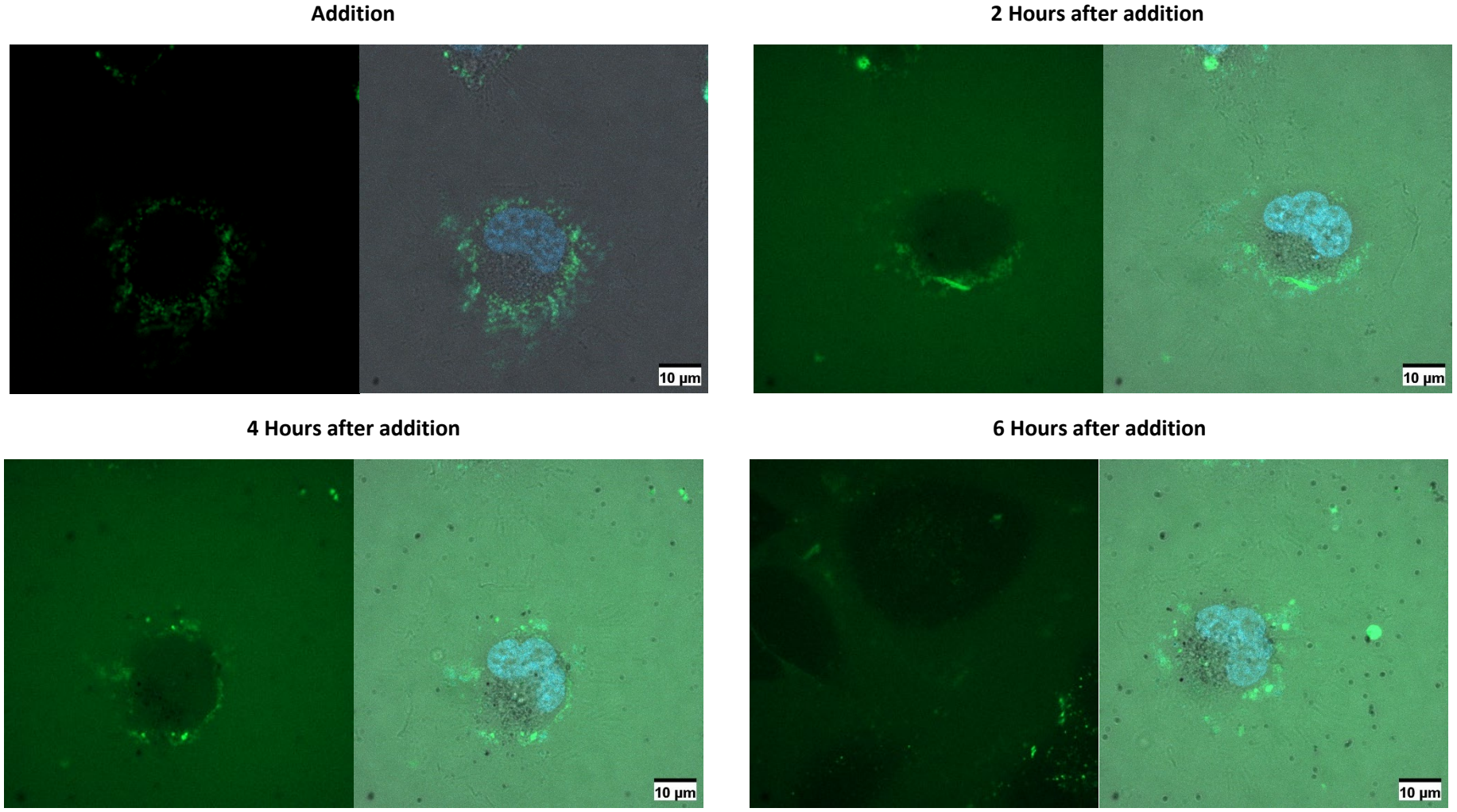


**Figure 3.24**: **Visualization of HeLa cell uptake of AuNP-delivered oligonucleotides (ON4) using live imaging confocal microscopy:** One field from a time-series of live cells incubated with AuNPs functionalized with ON4 are presented. Images were captured at four time points: immediately after addition, and subsequently at 2, 4, and 6 hours. For each time point, the left panel displays only the AuNPs (green), while the right panel shows an overlay of the AuNPs (green), the nuclei stained with Hoechst dye (blue), and the cell outline visualized using DIC imaging.

## ON5 Sequence

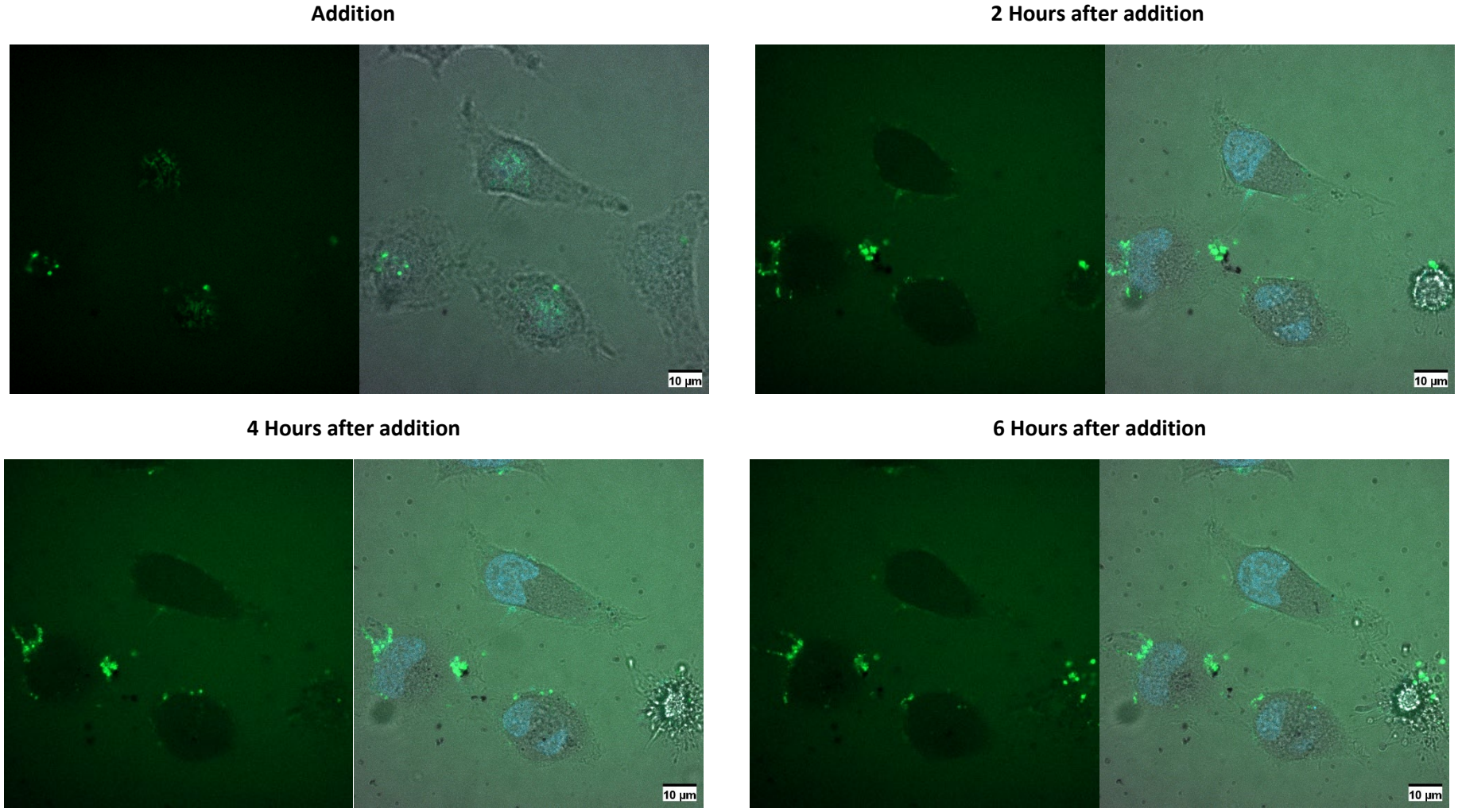


**Figure 3.25**: **Visualization of HeLa cell uptake of AuNP-delivered oligonucleotides (ON5) using live imaging confocal microscopy:** One field from a time-series of live cells incubated with AuNPs functionalized with ON5 are presented. Images were captured at four time points: immediately after addition, and subsequently at 2, 4, and 6 hours. For each time point, the left panel displays only the AuNPs (green), while the right panel shows an overlay of the AuNPs (green), the nuclei stained with Hoechst dye (blue), and the cell outline visualized using DIC imaging.

## 3.4 Conclusion

This chapter comprehensively evaluated the in vitro delivery and efficacy of ASOs targeting the *c-myc* IRES in HeLa cells, comparing conventional Lipofectamine™ 3000 transfection and a nano-delivery system using AuNPs@PEG@ssDNA. Lipofectamine™ 3000 was established as the optimal transfection reagent, with 3.75 µL per well in a 6-well plate providing the best balance between transfection efficiency and minimal cytotoxicity. Higher volumes increased cytotoxicity without improving efficacy, and the P3000™ supplement did not enhance delivery for these cytosolic ONs.

Among all sequences tested, ON5 consistently produced the strongest and most reproducible downregulation of *c-myc* mRNA and protein, both at 24- and 48-hours post-transfection. ON3 also showed significant protein downregulation at 24 hours, though this effect diminished by 48 hours. ON4 unexpectedly upregulated *c-myc* mRNA and protein at 24 hours, likely due to mRNA stabilization or disruption of inhibitory 5' UTR structures, but this effect was not sustained. ON1 and ON2 had minimal or no impact, likely due to poor hybridization efficiency related to their high GC content.

The AuNP-based delivery system achieved efficient cellular uptake and distribution, with confocal microscopy confirming localization in both the nucleus and cytoplasm. However, ONs delivered via AuNPs generally had less pronounced effects on *c-myc* mRNA and protein compared to Lipofectamine™ 3000, possibly due to steric hindrance or reduced hybridization efficiency when conjugated to nanoparticles. ON5 was the exception, maintaining significant protein downregulation at 48 hours post-transfection with AuNPs.

Across all delivery methods and ON sequences, cell viability remained high, with no significant cytotoxicity detected by flow cytometry, MTS, or LDH assays. Even sequences that strongly downregulated *c-myc* (e.g., ON5) did not induce significant cell death, suggesting that *c-myc* suppression alone is insufficient to trigger cytotoxicity in HeLa cells under these conditions, possibly due to compensatory survival pathways or metabolic adaptation. Both delivery systems-Lipofectamine™ 3000 and AuNPs-achieved rapid and efficient ON internalization, with no apparent sequence specificity

in uptake. AuNPs provided a more dispersed intracellular distribution, while Lipofectamine™ complexes tended to aggregate.

Taken together, ON5 is the most promising antisense sequence, demonstrating robust and reproducible downregulation of both *c-myc* mRNA and protein with both delivery systems, and maintaining its effect over time. ON3 may also be considered for short-term applications due to its initial protein suppression, though its effect wanes at later time points. ON1, ON2, and ON4 are less suitable for further development due to lack of efficacy or undesired upregulation effects.

# Chapter 4: Final Discussion, Conclusions and Future Work

This project focused on developing a technique to target the IRES structure of mRNA as a therapeutic approach. The primary objective was to utilize synthesized ssDNA sequences to modulate c-Myc expression levels as a potential cancer therapy.

Based on the results, it can be concluded that various modified sequences were successfully synthesized and demonstrated the ability to hybridize with the molecular target, producing measurable effects. The assays in this study targeted Domain 1 of the *c-myc* IRES structure. To achieve this, five different sequences were designed to comprehensively cover the region where ribosomal interaction was hypothesized to occur. These sequences were tested in cell-based assays to evaluate their impact on c-Myc levels. The synthesis process proved successful, as post-purification yields and purity levels were sufficient for subsequent experiments. Notably, the sequences incorporated modifications such as PS linkages, 5'-amino groups, LNAs, and, in some cases, 6'-FAM groups at the 3' end. However, further optimization is recommended for improving the coupling efficiency of the amino group modification.

Following synthesis, the 5'-amino group attached to the oligonucleotide sequences was conjugated to a PEG molecule containing an NHS group. While purification revealed areas for improvement—such as achieving clearer separation between conjugated and unconjugated sequences—the yields and purity obtained were adequate for proceeding with subsequent assays. Enhanced coupling efficiency could simplify purification by ensuring a higher proportion of sequences are conjugated with PEG.

The delivery system proposed in this project utilized AuNPs. These nanoparticles served not only as carriers for introducing the sequences into cells but also as tools to explore their unique properties, such as hyperthermia. Specifically, it was hypothesized that heating could alter the secondary structure of the IRES upon nanoparticle

hybridization, potentially modulating c-Myc levels. However, further experiments are needed to validate this hypothesis.

Characterization techniques confirmed that the nanoparticle system was successfully constructed. During functionalization, the nanoparticles remained stable and exhibited no aggregation. This robust protocol can serve as a versatile platform for attaching complementary sequences targeting various molecular structures.

Once characterized and quantified the sequence attachment per nanoparticle, the AuNPs@PEG@ssDNAs were tested in HeLa cells. A challenge encountered during this step was variability in sequence-to-nanoparticle ratios across different batches of biofunctionalized NPs. To address this, normalization was performed based on nanogram amounts of transfected material per cell. However, in cases where biofunctionalization efficiency was lower, higher nanoparticle quantities were required to achieve equivalent transfection levels. This variability was evident in live imaging videos, where some samples displayed increased nanoparticle deposition over time. Despite these challenges, the assays successfully identified sequence-specific effects on *c-myc* modulation.

In addition to employing AuNPs for conjugating and transfecting the sequences into cells, the primary objective of this project was to determine whether c-Myc levels could be modulated by targeting the IRES structure. The key focus was to evaluate whether the synthesized sequences effectively hybridize with the target and produce a measurable impact. To ensure reliable results, a commercial transfection agent, Lipofectamine 3000 Reagent, was used as a benchmark.

Initial assays using Lipofectamine demonstrated significant potential for downregulation of c-Myc expression, particularly evident in the Western blot results for sequences ON3, ON4, and ON5. These sequences showed a pronounced effect after 24 and 48 hours of incubation. It is noteworthy that two sequences, initially excluded due to their higher GC content, did not exhibit any impact on c-Myc levels. Testing these sequences was important for two reasons: first, to conduct a comprehensive screening of Domain 1 of the IRES structure; and second, to inform future designs of complementary sequences targeting this region.

The RT-qPCR results revealed an unexpected alteration in *c-myc* mRNA levels following hybridization with the target mRNA. After 24 hours, most sequences appeared to upregulate mRNA levels, with the exception of sequence ON5. This upregulation may be attributed to ASOs targeting the 5' UTR, which can stabilize mRNA transcripts and consequently increase mRNA levels. Additionally, ASOs may disrupt secondary structures such as G-quadruplexes and hairpins, which are known to inhibit translation.

After 48 hours, most sequences exhibited a tendency to downregulate *c-myc* mRNA levels. As previously described, this downregulation could result from mechanisms such as the NGD pathway, RNAse H1 recruitment, or interference with the binding of ribosomal subunits or other essential factors required for translation initiation.

Interestingly, sequences ON1 and ON2, which showed no interaction according to Western blot results, appeared to alter the molecular target in this assay. Further experiments are required to clarify these discrepancies and better understand the observed effects.

Based on these results, sequence ON5 demonstrated the highest efficiency in downregulating the molecular target, as evidenced by both RT-qPCR and Western blot assays. In contrast, sequence ON4 appeared to be the most active in upregulating *c-myc* levels, particularly in the RT-qPCR analysis. Although ON4 also exhibited some downregulation of the molecular target in Western blot assays, it maintained higher *c-myc* levels compared to the other active sequences. Sequence ON3 showed a moderate downregulation effect but was less effective than ON5.

When comparing these results to those obtained from sequences transfected while conjugated to nanoparticles, it was observed that the effects could not be fully replicated. However, some activity was detected with sequence ON5, which remained the most effective sequence. Further assays are required to clarify whether the diminished effect is due to interference caused by the presence of nanoparticles during hybridization or differences in delivery mechanisms. For instance, Lipofectamine encapsulates the sequences, whereas the AuNPs@PEG@ssDNAs have sequences attached to their surface. This difference may impact the concentration of

sequences delivered into cells, potentially explaining why only the most active sequence (ON5) produced a measurable effect.

Cytotoxicity assays indicated that none of the sequences increased cell mortality. However, c-Myc is a critical transcription factor involved in cellular proliferation by regulating genes associated with cell cycle progression, metabolism, and ribosome biogenesis. Its suppression is often linked to reduced cell growth, impaired colony formation, and disrupted cell cycle progression. The observed maintenance of cell viability despite reduced c-Myc levels may be attributed to transfection conditions—such as incubation with Gibco™ Opti-MEM™ medium (characterized by reduced glucose levels) or stress induced by Lipofectamine™ 3000 Reagent—which could promote cell survival. Additionally, it is possible that feedback mechanisms lead to increased expression of other proliferation-related genes compensating for reduced c-Myc levels. A broader gene screening would help identify such compensatory effects.

Confocal microscopy confirmed that both delivery systems (Lipofectamine 3000 Reagent and gold nanoparticles) effectively transfected cells with the sequences in less than 6 hours, as demonstrated by fluorescence signals within cells. However, transfection efficiency did not appear to be sequence-dependent since signals were also detected with scramble sequences.

In the immunofluorescence assay and live imaging analysis, the fluorescence signal predominantly localized in the perinuclear regions. However, additional assays are necessary to confirm this trend and to establish a potential correlation between signal localization and the impact of the sequences on modulating the molecular target.

In conclusion, while further optimization is warranted for certain steps—such as purification and coupling efficiency—the results demonstrate that this system is a promising tool for modulating gene expression via IRES targeting. This approach could pave the way for personalized cancer therapies by enabling precise control over gene expression using a unified methodology adaptable to various targets.

## 4.1 Future approaches

This project focused on targeting Domain 1 of the IRES structure within the *c-myc* mRNA, demonstrating varying impacts depending on the specific region targeted. However, the IRES structure also comprises a second domain, which presents a potential target for further investigation using a similar approach. Targeting this second domain would provide valuable insights into the functional roles of the IRES structure and its interactions with the ribosome.

With respect to the effects observed in this study, further analysis is warranted to determine whether the upregulation detected in RT-qPCR assays results from mRNA transcript stabilization or disruption of secondary structures such as G-quadruplexes and hairpins, which are known to inhibit translation. For sequences causing downregulation, further assays are needed to discern whether this effect results from steric hindrance caused by hybridization at ribosome-interacting regions or from RNase H-mediated degradation of the target RNA. Such assays could include treating cells with RNase H-specific inhibitors[211] to assess whether ASO-induced knockdown is blocked. If knockdown persists despite RNase H inhibition, it would suggest an alternative mechanism, such as steric blocking. Another approach could involve incubating synthetic RNA with ASOs in the presence of purified RNase H; cleavage in this context would confirm RNase H dependency.

This project also included a screening phase to evaluate *c-myc* modulation through incubation with various sequences. However, these assays were performed using only a single concentration. Future studies should explore the effects of varying concentrations and incubation times to determine whether the observed effects are consistent across different conditions and to identify the minimum effective concentration.

Regarding transfection using NPs, future work should aim to replicate the effects achieved with Lipofectamine-mediated delivery. If similar outcomes are not obtained due to potential steric hindrance caused by NPs, introducing a cleavable linker between the NPs and oligonucleotides may be beneficial. For example, a pH-dependent cleavable linker could enable sequence release upon interaction with acidic

endosomes within cells. Additionally, varying NP sizes and PEG chain lengths should be investigated to assess their impact on delivery efficiency. If successful transfection is achieved, it would be worthwhile to explore the multifunctional properties of AuNPs, such as their SLPR, and evaluate their potential for enhancing cancer treatment or for use in other sensing applications.

Finally, alternative delivery systems should be evaluated to identify more efficient methods for sequence delivery. These systems may include lipid NPs[212], exosomes[213], polymeric NPs[214], peptide-based NPs[215], cationic NPs[216] and GalNAc conjugates[217].

# Chapter 5: Experimental

## 5.1 Suppliers

The NPs utilized in this protocol were synthesized and characterized according to the methods described in **Chapter 5.2.** Sodium citrate tribasic dihydrate ($Na_3C_6H_5O_7 \cdot 2H_2O$), sodium borohydride ($NaBH_4$), gold (III) chloride hydrate ($HAuCl_4 \cdot xH_2O$), and poly(ethylene glycol) methyl ether thiol (were purchased from Sigma–Aldrich (Gillingham SP8 4XT, United Kingdom) and used as received. Silver nitrate ($AgNO_3$) (99.995% metal basis) was obtained from Alfa Aesar (Heysham LA3 2XY, United Kingdom). SH-PEG-NHS (0.8 kDa) was obtained from Abbexa (Cambridge CB4 0GJ, United Kingdom), while sodium bicarbonate ($NaHCO_3$) was sourced from Fluka Analytical (Gillingham SP8 4XT, United Kingdom). Dimethyl sulfoxide (DMSO) and ethanol were supplied by Fisher Scientific, United Kingdom

The DNA strands used in this process were synthesized following the procedures detailed in **Chapter 5.3**. The phosphoramidites, LNAs, 5'MMT-Amino C6 Modifier, 5'-TFA-Amino C6 Modifier, and all other reagents used in strand synthesis (including acetonitrile, deblocking reagent (3% Trichloroacetic acid (TCA) in DCM (dichloromethane)), DCM, activator (ETT (5-Ethylthio-1H-tetrazole) in acetonitrile), capping A (acetic anhydride in acetonitrile) & B (N-methylimidazole in acetonitrile), and oxidizer) as well as the triethanolamine (TEEA) (2.0 M) used in purification were purchased from LGC Biosearch Technologies, United Kingdom. Ammonium hydroxide ($NH_4OH$) and sodium chloride (NaCl) were supplied by Fisher Scientific, United Kingdom. Acetonitrile for purification was obtained from VWR Chemicals, United States. Methanol and diethylamine were sourced from Sigma-Aldrich, United Kingdom. Trifluoroacetic acid (TFA) was purchased from Acros Organics B.V.B.A., Belgium. Additionally, 1,1,1,3,3,3-Hexafluoropropan-2-ol (HFIP) was supplied by Apollo Scientific Ltd., United Kingdom. All other reagents used were of analytical grade.

## 5.2 Synthesis of Nanoparticles

### 5.2.1 Glassware cleaning

All glassware and Teflon-coated magnetic stir bars were cleaned using an aqua regia solution, a critical step in the synthesis of metallic NPs to ensure both the purity and reproducibility of the process. Aqua regia is highly effective in removing residual metallic particles, organic contaminants, and other impurities from the surfaces of glassware. Failure to eliminate these residues can interfere with the chemical reactions involved in nanoparticle synthesis, potentially resulting in inconsistent particle sizes, aggregation, or undesirable side reactions[218]. The aqua regia solution was prepared by mixing four parts of 35% hydrochloric acid (HCl) with one part of 65% nitric acid ($HNO_3$), typically using 48 mL of HCl and 12 mL of $HNO_3$, added sequentially in that order.

The prepared solution was allowed to react for 5 minutes in a vial before transferring to the next. This process was applied to all glassware.

After removing the Aqua Regia from each vial, it was rinsed with distilled water for a minimum of ten times and the water from the washes was collected. Once the aqua regia was removed from the last vial, the solution was added to the previous washes to dilute. Before disposal, the whole mixture was neutralized with a concentrated NaOH solution.

All cleaned glassware was left to dry overnight in the fume hood.

### 5.2.2 Synthesis of Gold nanoparticles

AuNPs were synthesized using the Turkevich method[171]. Initially, a cleaned round-bottom flask equipped with a condenser and a magnetic stirrer was prepared and filled with 150 mL of a 1 mM $HAuCl_4$ solution, measured using a volumetric flask. The solution was brought to the boil under vigorous stirring at 250 rpm. Simultaneously, 30 mL of a 38.8 mM sodium citrate solution were prepared and filtered. Once the 1 mM $HAuCl_4$ solution reached boiling, 15 mL of the 38.8 mM sodium citrate solution were rapidly added, resulting in a colour change from pale yellow to burgundy. Boiling was

maintained for an additional 10 minutes, after which the heat source was removed, and stirring continued for another 15 minutes. Once the solution cooled to room temperature, it was filtered through a 125 mm membrane filter[171] **(Figure 5.1)**

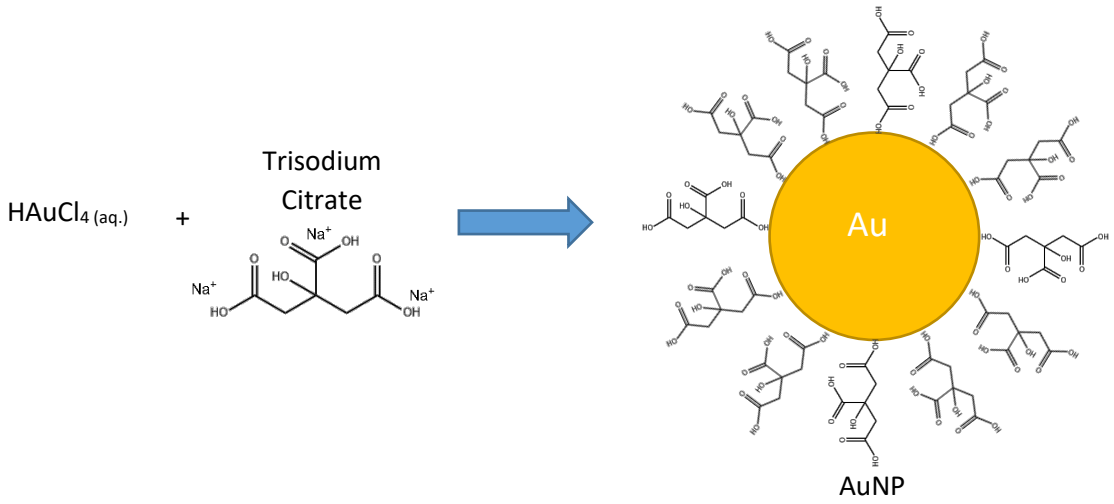


**Figure 5.1**: **Schematic representation of the synthesis of gold nanoparticles (AuNPs) using the Turkevich method.** This process involves the reduction of gold salt ($HAuCl_4$) with citrate, which acts both as a reducing agent and as a stabilizer on the nanoparticle surface.

## 5.2.3 Synthesis of Silver nanoparticles

Silver colloids were prepared using a modified version of the Lee-Meisel method[177,178]**(Figure 2.2)**. A cleaned vial equipped with a magnetic stirrer was filled with 100 mL of Milli-Q water using a volumetric flask. Subsequently, two aqueous solutions—250 µL of 100 mM $AgNO_3$ and 250 µL of 100 mM $Na_3Cit$—were added directly to the 100 mL of Milli-Q water under continuous stirring. After 5 minutes, 6 mL of freshly prepared 8 mM $NaBH_4$ were added dropwise to the solution under vigorous stirring. Using a fresh reducing agent solution was essential to maintain the stoichiometric reactivity of $NaBH_4$. The solution turned dark yellow and was stirred for a further 30 minutes, before it was left overnight in darkness at 4ºC.

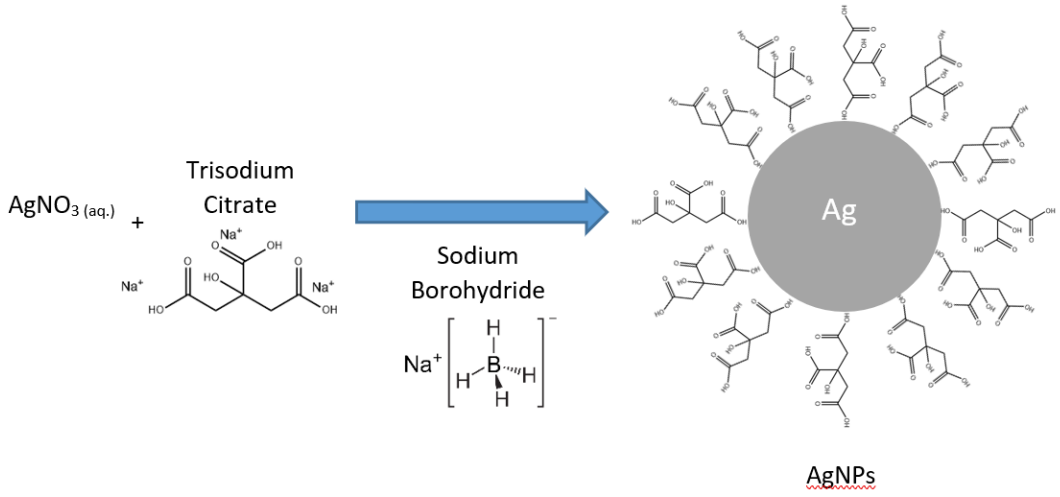


**Figure 5.2: Schematic representation of the synthesis of silver nanoparticles (AgNPs) using the Lee-Meisel method.** Size-controlled AgNPs are synthesized using a co-reduction approach, where $Na_3Cit$ and $NaBH_4$ serve as reducing agents.

## 5.2.4 PEGylation of Silver and Gold nanoparticles

To enhance colloidal stability and biocompatibility, both AuNPs and AgNPs were functionalized with PEG using a standardized protocol (**Figure 5.3**). For the PEGylation process, a mixture was prepared by combining 0.8 mL of 1.25 mM SH-PEG-methyl and 0.8 mL of 1.25 mM SH-PEG-NHS, both dissolved in ethanol. To this mixture, 0.66 mL of 25 mM $NaHCO_3$ in water was added to activate the thiol groups on the PEG molecules and maintain a slightly basic pH, which facilitates efficient conjugation to the nanoparticle surfaces.

For the functionalization of AuNPs, 5.74 mL of the colloidal gold solution was introduced into the reaction mixture in a round-bottom flask. The flask was sealed to prevent solvent evaporation, and the mixture was stirred overnight at room temperature to allow for complete PEGylation of the nanoparticles. Following the reaction, the PEGylated AuNPs were purified by centrifugation at 5,000 rpm for 30 minutes, a process that was repeated three times using Amicon® Ultra-Centrifugal Filters (100 kDa MWCO). The purified nanoparticles were then redispersed in Milli-Q water, yielding a final concentration of 6.57 nM AuNPs. The final reaction mixture contained 0.125 mM SH-PEG-methyl, 0.125 mM SH-PEG-NHS, and 20% (v/v) ethanol.

The same functionalization procedure was applied to AgNPs, with minor adjustments to accommodate differences in nanoparticle concentrations. For AgNPs, the final concentration in the reaction mixture was adjusted to 2.95 µM, while the concentrations of SH-PEG-methyl and SH-PEG-NHS remained at 0.125 mM each, and the ethanol content was maintained at 20% (v/v). The purification steps, including three cycles of centrifugation and redispersion in Milli-Q water, were identical to those used for AuNPs.

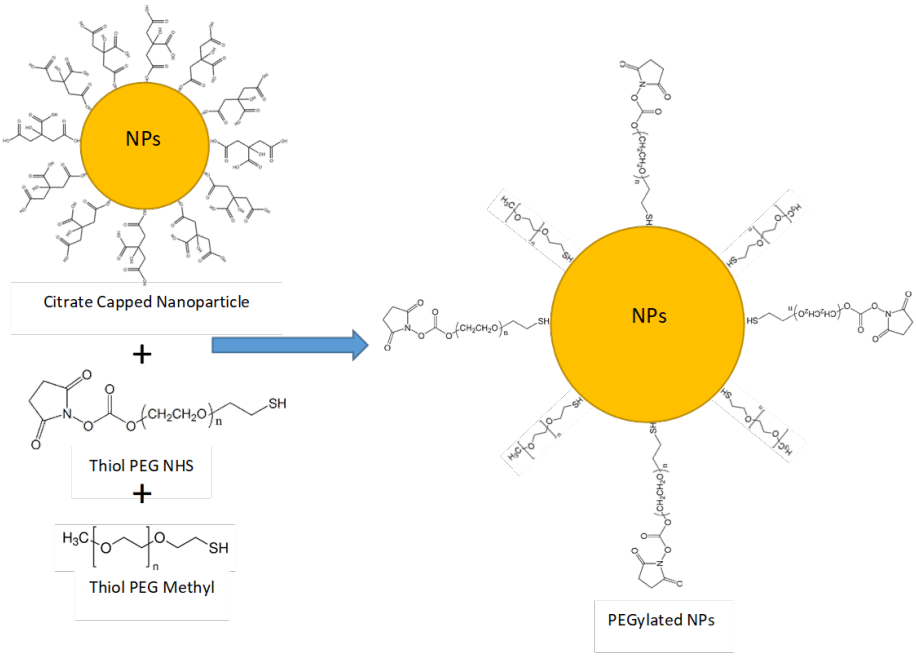


**Figure 5.3: Schematic representation of the PEGylation process of nanoparticles (NPs).** PEG molecules are attached to the surface of the nanoparticles through the displacement of citrate by the thiol group.

## 5.3 Synthesis of the ssDNA

### 5.3.1 Solid-phase synthesis

Solid-phase synthesis is a method for producing chemical compounds in which the reactant molecule is covalently bound to a solid support material, while reagents are added in the solution phase. This approach was employed in this project to synthesize the DNA strands required to form heteroduplexes with specific *c-myc* IRES sequences.

The DNA single strands were synthesized using the phosphoramidite method, originally developed by Robert Letsinger and Marvin Caruthers in the 1980s[219,220,221] and later adapted by Hubert Köster and colleagues in 1984[222]. This process, further

enhanced by solid-phase technology and automation, has become the standard method for DNA oligonucleotide manufacturing.

Phosphoramidite oligonucleotide synthesis proceeds in the 3’-to-5’ direction and is performed on a solid support enclosed within columns equipped with filters that permit the flow of reagents and solvents. The initial nucleotide is covalently attached to a solid-phase substrate, such as controlled pore glass (CPG) or polystyrene. This immobilization facilitates efficient washing and separation of reagents throughout the synthesis process, ensuring precise and controlled oligonucleotide assembly.

The phosphoramidite DNA synthesis process consists of a four-step cycle, as outlined in **Figure 5.4**:

- Deblocking (Detritylation): The nucleoside attached to the solid support is initially protected at the 5’-hydroxyl group with a 4,4’-dimethoxytrityl (DMT) group. This protective group ensures that only a single reactive site is available during the phosphoramidite coupling step, thereby preventing undesired side reactions or self-polymerization. Prior to the addition of the next nucleotide in the sequence, the DMT group must be removed to expose the 5’-hydroxyl group, enabling further elongation of the oligonucleotide chain. Detritylation is typically carried out using acidic solutions such as trichloroacetic acid (TCA) or dichloroacetic acid (DCA) dissolved in an organic solvent like dichloromethane. The cleavage of the DMT group generates an orange-coloured byproduct, which can be quantified to assess coupling efficiency by measuring the trityl yield.

- Coupling: After the deblocking step, the nucleoside phosphoramidite is combined with a weak acid activator, such as 5-(ethylthio)-1H-tetrazole (ETT). The activator protonates the diisopropylamino group of the phosphoramidite monomer, generating a highly reactive intermediate. The exposed 5’-hydroxyl group on the solid-support-bound nucleoside then acts as a nucleophile, attacking the phosphorus atom of the activated phosphoramidite. This reaction displaces the diisopropylamino group and forms a covalent phosphite triester bond between the two nucleosides, enabling chain elongation.

- Oxidation: The unstable phosphite triester intermediate is converted into a stable phosphate triester through an oxidation reaction using iodine in a mixture of pyridine, water, and tetrahydrofuran (THF). The resulting DNA backbone features a 2-cyanoethyl protecting group on the non-bridging oxygen atom, which safeguards against unwanted side reactions during subsequent synthesis cycles.

- Capping: Since it is not possible to achieve 100% reaction efficiency during coupling, unreacted 5’-hydroxyl groups may react with phosphoramidites in subsequent cycles, leading to the formation of oligonucleotides with missing bases (deletion mutations). These errors accumulate over multiple synthesis cycles, resulting in a heterogeneous mixture of oligonucleotides that are challenging to purify and unsuitable for most applications. To address this issue, a capping step is introduced following the coupling reaction. During this step, acetic anhydride reacts with the unreacted 5’-hydroxyl groups, forming chemically inert acetyl esters. This modification prevents these hydroxyl groups from participating in subsequent coupling reactions, thereby minimizing the occurrence of deletion mutations.

This cycle is repeated for each base to synthesize the desired oligonucleotide sequence.

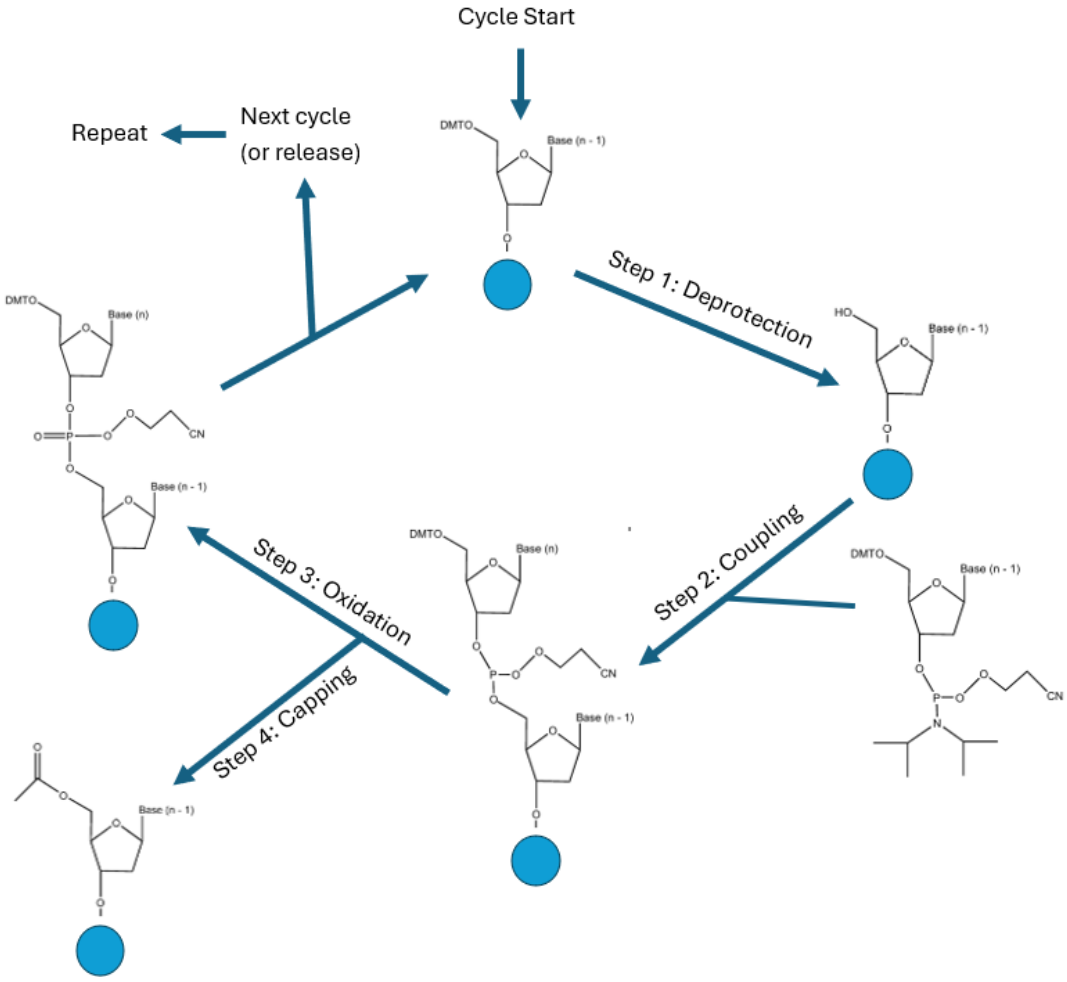


**Figure 5.4: Overview of the Phosphoramidite Method.** Synthesis cycle for the preparation of oligonucleotides using the phosphoramidite method. The diagram illustrates the phosphoramidite method of solid-phase oligonucleotide synthesis. The process begins with a nucleoside attached to a controlled pore glass (CPG) solid support (depicted as blue circles). Each synthesis cycle consists of four main steps: (1) deprotection (detritylation) to remove the 5'-DMT protecting group and expose a reactive hydroxyl group; (2) coupling, where an activated nucleotide is added to the growing chain; (3) oxidation, converting the unstable phosphite linkage to a stable phosphate; and (4) capping, which blocks any unreacted chains to prevent errors. These steps are repeated until the desired oligonucleotide sequence is assembled, after which the product is released from the CPG support.

The Expedite 8909 system was used to synthesize ssDNA at a 1 µmol scale in dual-column mode, enabling the simultaneous production of two sequences without compromising speed. Each synthesis cycle included detritylation (30 seconds for standard DNA), coupling (2 minutes), capping (18 seconds per reagent A and B), and oxidation (30 seconds), with all steps optimized for high-yield synthesis.

In this project, various modifications were introduced into the oligonucleotide sequences to provide distinct properties, including LNAs, phosphorothioates, and an amino moiety at the 5' end. LNA phosphoramidites typically require extended coupling times compared to standard DNA synthesis due to the steric hindrance associated with LNA monomers. For instance, coupling times ranging from 180 to 250 seconds are commonly recommended, depending on the specific synthesis protocol.

For the synthesis of phosphorothioates, sulfurization times generally range from 60 to 240 seconds, depending on the sulfurizing reagent employed. These times are notably longer than the 20–60 seconds required for standard iodine-based oxidation under typical conditions.

Additionally, a 5'-TFA-Amino Modifier C6 CE-Phosphoramidite was utilized to introduce an amino moiety at the 5' terminus of the sequence. In this case, a coupling time of 10 minutes is recommended to achieve high coupling efficiency. This extended duration, considerably longer than the typical 1–2 minutes required for standard phosphoramidites, is necessary to achieve optimal yield due to the lower reactivity characteristic of standard modifiers.

### 5.3.2 Deprotection and purification of the ssDNA sequences

Once the oligonucleotide synthesis is complete, it must be cleaved from the column resin, before deprotection, desalting and purification. For this procedure to be successful, the oligonucleotide must include a terminal base that has a DMT protecting group, or another hydrophobic modifier.

First, the synthesis column was washed back and forth with 1 mL of diethylamine (15% acetonitrile (ACN)) using two syringes held vertically for 1 minute. This step was repeated, leaving the syringes attached for approximately 20 minutes with 5-minute intervals to ensure the ACN thoroughly reached all controlled pore glass (CPG) supports within the column. Next, a new syringe was used to rinse the column with 1 mL of ACN, followed by another rinse with 1 mL of water.

Subsequently, 1.5 mL of 35% ammonium hydroxide ($NH_4OH$) was applied back and forth through the column for 1 minute. Ammonium hydroxide was utilized to cleave the oligonucleotide from the solid support of the column. This process was repeated three additional times over 1 hour. The oligonucleotide sequences were then collected from the column. To ensure complete recovery of all the oligonucleotide, the column was rinsed with an additional 0.5 mL of $NH_4OH$ (total volume: 2 mL). The solution was subsequently incubated overnight at 50°C (or at 65°C for 1 hour).

Following incubation, purification of the DNA strands with DMT or MMT protecting groups was performed using a Glen-Pak™ DNA purification cartridge, following the guidelines provided by Glen Research. The cartridges are comprised of a stationary phase which has a high affinity for the large aromatic DMT group, and anything that contains one is retained on the column. Any failure sequences that do not include a DMT group are washed away before cleaving the DMT group with 2% TFA, neutralizing the column and eluting to retrieve the desired product.

The previously incubated oligonucleotide sequences were cooled on ice and mixed with 1 mL solution (100 mg/mL NaCl), so that the salt concentration of the sample was approximately 50 mg/mL after loading the oligo. Once the oligo/salt mixture was then loaded onto the cartridge, the column was washed with 1 mL of a salt solution (5% MeCN in 100 mg/mL NaCl solution) to remove any remaining failure sequences from the cartridge. Subsequently, 2 x 1 mL of 4% TFA was used to remove the DMT group from the oligonucleotide, potentially visible as an orange band during cleavage. The cartridge was then washed with 2 x 1 mL of deionized water to remove TFA and excess salts. Finally, 1 mL of a 50:50 MeCN:$H_2O$ solution with 0.5% $NH_4OH$ was added to elute the purified oligonucleotide. The diluted ammonium hydroxide (0.5%) neutralizes any residual TFA. The eluent was collected after each wash and saved in case of loading failure or error.

Illustra™ NAP™-10 Columns were employed for purifying and desalting DNA strands. These disposable columns are pre-packed with Sephadex™ G-25 DNA-grade resin, allowing purification through gel filtration by gravity. Molecules larger than the matrix pores are excluded and elute first, while smaller molecules penetrate the matrix,

slowing their progress through the column and resulting in later elution. Following purification, all samples were dried under vacuum and stored at 4°C in a freezer.

## 5.4 ON-PEG Conjugation Assay

The conditions for the oligonucleotide-PEG conjugation assay were standardized in collaboration with the University of Ghent. During the optimization phase, reactions were performed using 300 µL of 50 µM ssDNA in bicarbonate buffer and 200 µL of 3,000 µM SH-PEG-NHS dissolved in DMSO or DMF, resulting in a 40-fold molar excess of PEG relative to the DNA.

Based on the results, a standardized protocol was established for subsequent experiments. The optimized reaction was carried out at pH 9.0, using 300 mM $NaHCO_3$ as the buffer for the ONs. SH-PEG-NHS (0.8 kDa) was again used in a 40-fold molar excess, this time relative to a 400 µM ON solution. For optimal solubility, SH-PEG-NHS was dissolved in DMSO and diluted to a final concentration of 24,000 µM.

To initiate the conjugation, 300 µL of the 400 µM ON solution was combined with 200 µL of the 24,000 µM SH-PEG-NHS solution in an Eppendorf tube. The mixture was incubated overnight at 25°C with continuous mixing at 600 rpm to promote efficient coupling.

The following day, the efficiency of the conjugation reaction was evaluated. Purification of the resulting ON-PEG conjugates was then performed using HPLC to separate the desired product from unreacted components and byproducts.

## 5.5 Surface Functionalization of AuNPs with Thiol-PEG-ASO Self-Assembled Monolayers

Citrate-coated AuNPs were functionalized by forming a self-assembled monolayer on their surface using a mixture of Thiol-PEG-ASOs and Thiol-PEG-methyl. To prepare the functionalization mixture, 0.2 mL of Thiol-PEG-ASO solution (0.35 mM) was added to 1.4 mL of Thiol-PEG-methyl solution (2.5 mM) under gentle stirring. After two minutes, the pH of the mixture was adjusted to 8.0 by adding 0.7 mL of 300 mM $NaHCO_3$ solution, which facilitates the deprotonation of thiol groups and promotes their

covalent binding to the gold nanoparticle surface. Subsequently, 4.7 mL of the AuNP colloidal solution was introduced into the reaction mixture. The system was sealed to prevent ethanol evaporation and stirred overnight at room temperature to ensure complete surface modification.

Following incubation, the functionalized AuNPs were purified by centrifugation at 7,000 rpm for 10 minutes, a process that was repeated three times to remove excess reagents and unbound ligands. The purified nanoparticles were then redispersed in Milli-Q water to obtain a stock solution (0.5 mL). The final concentration of the functionalized AuNPs was determined after purification and may vary depending on the efficiency of the process.

## 5.6 Physicochemical Characterization and Purification methods

### 5.6.1 High Performance Liquid Chromatography (HPLC)

#### 5.6.1.1 Analysis of the synthesized ssDNA sequences

The previously synthesized and purified single-stranded DNA sequences were analysed using a Varian 920-LC HPLC system equipped with UV detectors. The primary objective of this analysis was to assess the purity of the oligonucleotide sequences.

The mobile phase consisted of a TEA-HFIP buffer solution (Solution A), prepared by mixing 1.2 mL of 1 M TEA with 998.4 µL of 101 mM HFIP to produce a solution containing 8.6 mM TEA and 100 mM HFIP at pH 8.3. Methanol (Solution B) was used as the eluent. The stationary phase employed was an XBridge OST C18 column (4.6 x 50 mm, 2.5 µm particle size) from Waters.

For sample analysis, 20 µL of each oligonucleotide solution was injected into the HPLC system. Separation of the oligonucleotide sequences was achieved using gradient elution with methanol at 60 °C, increasing linearly from 5% to 100% methanol over 40 minutes at a flow rate of 0.6 mL/min (**Table 5.1**). Elution was monitored by a UV detector set at 260 nm, enabling identification of the peaks corresponding to different sequences during the separation process.

**Table 5.1: HPLC 60˚C gradient method conditions.** Solution A: TEA-HFIP buffer containing 8.6 mM triethylamine (TEA) and 100 mM hexafluoroisopropanol (HFIP) at pH 8.3. Solution B: Methanol.

| Time (min) | Flow (ml/min) | % Solution A | % Solution B |
|---|---|---|---|
| **Pre-run** | 0.6 | 95 | 5 |
| **0.1** | 0.6 | 95 | 5 |
| **5** | 0.6 | 95 | 5 |
| **30** | 0.6 | 40 | 60 |
| **35** | 0.6 | 0 | 100 |
| **40** | 0.6 | 0 | 100 |
| **50** | 0.6 | 95 | 5 |

### 5.6.1.2 Purification of the SH-PEG-ASOs after the bioconjugation

The objective of the bioconjugation process was to conjugate the ASOs with PEG, which would subsequently be utilized to coat the surface of the NPs. The SH-PEG-NHS molecules were reacted with ssDNA containing $NH_2$ through overnight incubation under specific conditions, including a pH of 9 and a molar ratio of 40 equivalents of SH-PEG-NHS (0.8 kDa) to 400 µM DNA. DMSO was employed as the solvent for PEG, while a 300 mM $NaHCO_3$ solution was used as the buffer for the oligonucleotides.

Following the incubation of SH-PEG-NHS with ssDNA-$NH_2$, the product of the NHS-amino coupling reaction was purified using a Varian 920-LC HPLC system equipped with UV detectors and a Varian 440-LC Fraction Collector. The primary objective of this process was to isolate the DNA conjugated with PEG from unreacted oligonucleotides and excess PEG.

The buffers used for this purification were the same as those employed in the physicochemical characterization of ssDNA. The mobile phase consisted of a TEA-HFIP buffer solution (Solution A), while methanol (Solution B) served as the eluent. The stationary phase utilized was an XBridge™ BEH300 Prep C18 column (10 x 250 mm, 10 µm particle size) from Waters.

The entire reaction volume (500 µL) was purified through multiple injections of 50 µL each, which is the maximum injection volume for this HPLC system. The desired

product was separated from unreacted oligonucleotides and excess PEG using gradient elution with methanol, increasing linearly from 5% to 100% over 25 minutes at a flow rate of 2.5 mL/min (**Table 5.2**). Elution was monitored by a UV detector set at 260 nm, enabling identification of peaks corresponding to different sequences during the separation process (**Figure 5.1**).

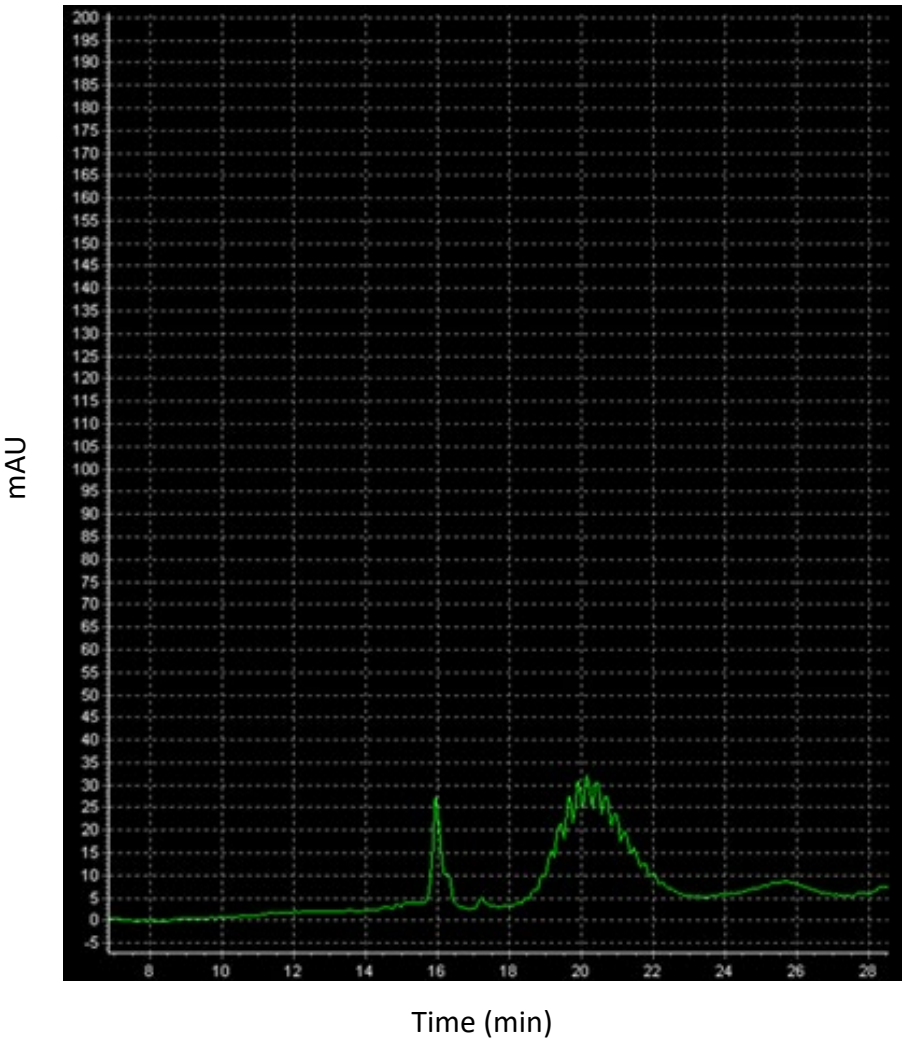


**Figure 5.5: HPLC chromatogram representing the UV-Vis monitorization at 260 nm during the separation process by gradient.**

It is important to note that several control experiments were conducted to accurately identify the peak corresponding to the DNA sequences that had been successfully conjugated. The product peak consistently appeared at higher elution times compared to the unmodified DNA sequence, attributed to the longer retention time of the PEG-conjugated DNA. Finally, the Varian 440-LC Fraction Collector was employed to isolate and purify the desired product from the entire sample.

**Table 5.2: HPLC gradient method conditions for purification.** Solution A: TEA-HFIP buffer containing 8.6 mM triethylamine (TEA) and 100 mM hexafluoroisopropanol (HFIP) at pH 8.3. Solution B: Methanol.

| Time (min) | Flow (ml/min) | % Solution A | % Solution B |
|---|---|---|---|
| **Pre-run** | 2.5 | 95 | 5 |
| **0.1** | 2.5 | 95 | 5 |
| **2** | 2.5 | 45 | 55 |
| **17.5** | 2.5 | 5 | 95 |
| **19** | 2.5 | 0 | 100 |
| **20** | 2.5 | 0 | 100 |
| **25** | 2.5 | 95 | 5 |

## 5.6.2 UV-Vis Spectrophotometer

### 5.6.2.1 NanoDrop 2000 UV-Vis Spectrophotometer

To determine the concentration of the DNA strands, a NanoDrop 2000 UV-Vis spectrophotometer (Thermo Scientific) was utilized. DNA absorbance was measured at a wavelength of 260 nm, and the concentration was calculated using an extinction coefficient of 33 ng•cm/µL. The results were used to calculate the oligonucleotide concentration at various stages of the project by applying the Beer-Lambert law:

$$\boldsymbol{A = \varepsilon\, l\, c}$$

where $\boldsymbol{A}$ is the absorbance, $\boldsymbol{\varepsilon}$ is the molar absorptivity (extinction coefficient), $\boldsymbol{l}$ is the optical path length (1 cm for this assay), and $\boldsymbol{c}$ is the concentration of the solution.

In the NanoDrop 2000 UV-Vis spectrophotometer, the actual optical path length automatically adjusts between 1 mm (0.1 cm) and 0.05 mm (0.005 cm) based on the sample's absorbance. However, the software normalizes all absorbance readings to the standard 10 mm (1 cm) path length used in conventional cuvettes. As a result, the reported absorbance value (A260) is already standardized and can be directly used in calculations as if it were measured with a 1 cm path length.

Using the calculated concentrations, it was possible to determine the amount of moles present in each sample and, consequently, evaluate the synthesis yield, as shown in **Table 2.2**. Additionally, the number of moles remaining in the supernatant after

functionalization with SH-PEG-ASO was calculated to estimate the percentage of total ssDNA moles coupled to NPs. This analysis provided insights into both synthesis efficiency and coupling performance

#### 5.6.2.2 AvaSpec-2048 Fiber Optic Spectrometer

The status of the NPs was verified by detecting the surface plasmon resonance (SPR) bands using UV-Vis spectroscopy. The spectra were obtained with a 1-cm path length quartz cuvette, using an AvaSpec-2048 Fiber Optic Spectrometer. The absorbance of the colloidal solutions was measured over a wavelength range of 350–800 nm. For sample preparation, 1 mL of the stock solution was collected and diluted 1:1 in a quartz cuvette. After each measurement, the cuvette was cleaned thoroughly using aqua regia to ensure accuracy and prevent contamination.

#### 5.6.2.3 Cary 100 Uv-Visible Spectrophotometer

The presence of DNA attached to the NPs after the functionalization process was confirmed using a Cary 100 UV-Vis spectrophotometer. By comparing the surface plasmon resonance (SPR) bands of the nanoparticle solutions with the DNA absorption peak at 260 nm, it was possible to quantify the amount of DNA coupled to the NPs.

The spectra were recorded using a 10-mm path length quartz cuvette with a Cary 100 UV-Visible Spectrophotometer, measuring absorbance in the wavelength range of 350–800 nm. Samples were prepared by collecting 200 µL of the stock solution and diluting it appropriately in a quartz cuvette. After each measurement, the cuvette was thoroughly cleaned with aqua regia to ensure accuracy and prevent contamination.

### 5.6.3 Mass Spectrometry

Mass spectrometry analysis was performed using a MicrOTOF mass spectrometer (Bruker Daltonics, Bremen, Germany) equipped with a time-of-flight (TOF) analyser. Samples of 30 µL at a concentration of 30 µM were analysed. The deconvolution of DNA strand fragments was employed to determine the mass of the sequences. Additionally, the analysis verified whether any bases were missing, indicating potential deletions in the desired oligonucleotide, and confirmed whether the oligonucleotide was synthesized correctly.

The purity of the sequences was also assessed by comparing the peaks observed in the UV-Vis analysis with their corresponding deconvoluted masses. This approach allowed for the evaluation of reaction efficiency. All data were acquired in negative ion mode.

### 5.6.4 Dynamic Light Scattering (DLS)

The hydrodynamic diameter of citrate-capped NPs and functionalized NPs was measured using dynamic light scattering (DLS) at 25 °C with a Zetasizer Nano ZS90. The size distribution was evaluated based on the polydispersity index (PdI), which ranges from 0.0 for a completely monodisperse sample to 1.0 for a highly polydisperse sample. Data interpretation was conducted by analysing the size distribution according to the intensity of scattered light.

For each condition, three independent measurements were performed. Each measurement consisted of 10 sub-measurements, each lasting 10 seconds.

### 5.6.5 Transmission Electron Microscopy (TEM)

The morphology, shape, and size of the NPs were examined using transmission electron microscopy (TEM) with a Hitachi HT7700, operated at an accelerating voltage of 100 kV. A drop of the nanoparticle solution was deposited onto a carbon-coated copper grid for imaging.

The mean particle size was determined by analysing size distribution graphs, which were generated by measuring approximately 150 particles from each sample. Image analysis was conducted using the software ImageJ.

## 5.7 Molecular Biology

### 5.7.1 Cell Assays

All the cell experiments were performed in HeLa Cells that were maintained in gamma-sterilised, tissue culture-treated 75 cm2 flasks, in a 37°C incubator (5% CO2).

#### 5.7.1.1 Cell Maintenance

Cells were maintained by passaging every 2–3 days, depending on their growth rate, using Dulbecco's Modified Eagle Medium with GlutaMAX™ (DMEM) (Gibco® by Life Technologies™) supplemented with 10% heat-inactivated fetal bovine serum (FBS) (Sigma-Aldrich). Passaging was performed when the cell coverage reached 100%, as confirmed under a microscope.

To passage the cells, the culture medium was first removed, and 1 mL of $Mg^{2+}$ and $Ca^{2+}$-free PBS (Sigma-Aldrich) was added to the plate to wash the cells and remove residual proteins and cellular debris. Subsequently, 1 mL of TrypLE™ Express (Gibco® by Life Technologies™) was added to cover the entire surface. This enzyme acts similarly to trypsin, detaching the cells from the plate surface. The plate was then incubated for 5 minutes at 37 °C, the optimal temperature for enzymatic activity.

To stop cell detachment and collect the cells, 2 mL of supplemented medium was added. For routine cell maintenance, 1 mL of the detached cell suspension was retained in the plate. Cells were transferred to a new plate once a week to ensure proper growth conditions.

#### 5.7.1.2 Cell Counting

Cells were counted the day prior to transfection. As previously described, the old growth medium was removed, and the cells were washed with 1 mL of PBS. Subsequently, 2 mL of TrypLE™ Express was added, and the cells were incubated at 37 °C until fully detached. The entire volume of the plate was collected and transferred into a 15 mL Falcon tube, followed by centrifugation at 3000 rpm for 5 minutes.

The cell count was performed using the TC20 Automated Cell Counter (Bio-Rad). The resulting cell pellet was resuspended in 10 mL of PBS, ensuring thorough resuspension.

For the assay, a 96-well plate was used. In a new well, 10 µL of the cell suspension was mixed with 10 µL of trypan blue. The mixture was then pipetted into one of the chambers of the Cell Counting Slides designed for the TC10™/TC20™ Cell Counter (Bio-Rad) and inserted into the equipment.

The system provided both the cell concentration (cells/mL) and the percentage of viable cells. These data were used to calculate the required volume of cell suspension needed to seed each well with the desired number of cells for subsequent growth.

#### 5.7.1.3 Cell Transfection

##### 5.7.1.3.1 Lipofectamine Transfection

Cells were seeded in 6-well plates at a concentration of $3x10^5$ cells per well to achieve 70–90% confluency at the time of transfection.

Transfection was performed using Lipofectamine™ 3000 Reagent (Invitrogen) following the manufacturer's protocol. Briefly, Lipofectamine™ 3000 was diluted in Opti-MEM™ Medium and mixed thoroughly. In a separate tube, a master mix of single-stranded DNA (ssDNA) was prepared by diluting the ssDNA in Opti-MEM™ Medium.

The diluted DNA solution was then combined with the diluted Lipofectamine™ 3000 Reagent in a 1:1 ratio. The resulting mixture was incubated at room temperature for 10–15 minutes to allow the formation of DNA-lipid complexes.

After incubation, the DNA-lipid complex was added to the cells and incubated for 6 hours. Following this, the media was removed, and the cells were washed twice with PBS. Finally, fresh growth media containing serum was added, and the cells were allowed to express the delivered cargo for 24–48 hours.

**Table 5.3: Lipofectamine™ 3000 Reagent component per well in a 6-welll plate.**

| Component (per well)<br>6-well plate | |
|---|---|
| **DNA-lipid complex** | 250 µL |
| **DNA amount** | 2500 ng |
| **P3000™ Reagent** | 5 µL |
| **Lipofectamine™ 3000 Reagent used** | 3.75 and 7.5 µL |

**Table 5.4: Lipofectamine™ 3000 Reagent transfection procedure details.**

| Procedure details | |
|---|---|
| **Component** | 6-well plate |
| **Adherent Cells** | 0.25-1x$10^6$ |
| **Opti-MEM™ Medium** | 125 µL × 2 |
| **Lipofectamine™ 3000 Reagent** | 3.75 and 7.5 µL |
| **Opti-MEM™ Medium** | 250 µL |
| **DNA (0.5–5 µg/µL)** | 5 µg |
| **P3000™ Reagent (2 µL/µg DNA)** | 10 µL |
| **Diluted DNA (with P3000™ Reagent)** | 125 µL |
| **Diluted Lipofectamine™ 3000 Reagent** | 125 µL |

#### 5.7.1.3.2 AuNPs@PEG@ssDNA Transfection

AuNPs biofunctionalized with ASOs were transfected independently. Similar to the lipofectamine-mediated transfection protocol, 3 × $10^5$ cells were seeded per well in 6-well plates containing 2 mL of growth medium. At this cell density, confluency levels reached approximately 60%–80% at the time of transfection.

Prior to transfection, the growth medium in each well was removed and replaced with 2 mL of fresh Opti-MEM™ Reduced Serum Medium. The volume of AuNPs@PEG@ssDNA solution administered to each well was adjusted according to the specific AuNPs@PEG@ASO stock solution, due to batch-dependent variations in

biofunctionalized ssDNA content. To achieve precise delivery of 2500 ng of ASOs into the cell culture, quantitative analysis of ssDNA concentration in each AuNPs@PEG@ASO solution was performed to calculate the required transfection volume. The calculated volumes of AuNPs@PEG@ssDNA solutions corresponding to 2500 ng of ASOs were then introduced into each well at standardized final concentrations: 0.12 µM for Scramble, ON1, ON2, ON3, and ON5 formulations, and 0.12 µM for the ON4 formulation.

After 6 hours, the cell culture medium was replaced with DMEM supplemented with 10% FBS. The cells were then incubated with the AuNPs@PEG@ssDNAs at 37 °C for either 24 or 48 hours. Following the incubation period, the cells were harvested for further analysis.

## 5.7.2 Protein Extraction and Purification

### 5.7.2.1 Protein Extraction

For lysing and extracting proteins from HeLa cells, Radioimmunoprecipitation Assay (RIPA) buffer was used. A 10X RIPA Lysis Buffer (Sigma–Aldrich) was diluted with sterile distilled water at a ratio of 1:9. The solution was stirred and refrigerated for at least two hours prior to use. Immediately before use, the buffer was supplemented with the required volume of Halt™ Protease and Phosphatase Inhibitor Cocktail (100X stock, Sigma–Aldrich) to achieve a final 1X concentration.

Six hours after transfection, the Opti-MEM™ cell medium (Gibco® by Life Technologies™) was removed, and the cells were washed twice with PBS. Fresh cell medium supplemented with FBS was then added. Twenty-four hours after transfection, the growth medium was removed from the plates, and the cell culture dishes were placed on ice. The culture medium was carefully aspirated, and ice-cold PBS was added to wash the cells. The PBS was then aspirated, and ice-cold RIPA lysis buffer (300 µL per well for a 6-well plate) was added to the dishes. The plates were gently swirled or shaken on ice for 5 minutes to ensure complete lysis.

The cell lysate was subsequently collected and transferred to a microcentrifuge tube. The samples were centrifuged at approximately 13,000 rpm for 15 minutes. After

centrifugation, the supernatant containing the proteins was carefully collected and transferred to a new microcentrifuge tube, while the pellet was discarded.

#### 5.7.2.2 Protein Quantification

A Bradford assay was employed to determine the protein concentration in the samples. This assay is based on the formation of a complex between the dye Brilliant Blue G and proteins in solution. The binding of the dye to proteins causes a shift in the dye's absorption maximum from 465 nm to 595 nm, with the absorbance at 595 nm being proportional to the protein concentration in the sample[223].

The Bradford reagent (Sigma-Aldrich) used in this experiment contains Brilliant Blue G dissolved in phosphoric acid and methanol. The assay was conducted using a 96-well plate, with each condition measured in triplicate.

First, the Bradford reagent was thoroughly mixed and brought to room temperature. A standard curve was prepared using bovine serum albumin (BSA) stock solutions at concentrations of 0, 0.25, 0.5, 0.75, 1, and 1.4 mg/mL. For the assay, 5 µL of each protein standard was added to separate wells of the 96-well plate. In blank wells, 5 µL of buffer was added, while 5 µL of each unknown sample was pipetted into designated wells. Subsequently, 250 µL of Bradford reagent was added to each well.

The plate was gently mixed on a shaker for at least 30 seconds and incubated at room temperature for a minimum of 5 minutes but no longer than 1 hour, as prolonged incubation can lead to degradation of the protein-dye complex.

Absorbance measurements were taken using a spectrophotometer set to 595 nm. The absorbance values from the standard curve were used to generate a formula that allowed calculation of the protein concentration in each sample

### 5.7.3 Western Blot

The expression of c-Myc in cells treated with oligonucleotides was detected by western blot using NuPAGE™ 4–12% Bis-Tris Mini Protein Gels (1.0–1.5 mm) from Thermo Fisher Scientific.

Based on the known protein concentration in each sample, the required volume of lysate to load 20 µg of protein per well was calculated. A 2X sample buffer containing β-mercaptoethanol (BME) was prepared by mixing 950 µL of 2X Laemmli sample buffer (Bio-Rad) with 50 µL of BME. Protein samples were then diluted 1:1 in the prepared sample buffer (e.g., 100 µL protein sample + 100 µL 2X sample buffer containing BME). The mixture was heated at 95 °C for 5 minutes.

During the heating step, the gel was assembled into the electrophoresis tank with the wells facing the central chamber, which was filled with 1X Running Buffer (Sigma-Aldrich). After heating, the appropriate volume of each sample was loaded onto the SDS-PAGE gel to ensure 20 µg of protein per well. The gel was run at 150 V until the dye front reached the bottom.

Proteins were transferred from the gel to a 0.45 µm PVDF membrane (Bio-Rad) using a semi-dry transfer method with the Trans-Blot® Turbo™ Transfer System (Bio-Rad). The membrane was first immersed in 100% methanol (Fisher Scientific) for a few seconds until translucent, then equilibrated in transfer buffer for 2–3 minutes. Once equilibrated, the membrane was ready for protein binding.

Fourteen pieces of 0.34 mm filter paper were soaked in 1X Tris-Glycine Buffer (Invitrogen). In the tray of the Trans-Blot® Turbo™ transfer system, seven layers of wet filter paper were placed, followed by the equilibrated membrane, the gel, and another seven layers of wet filter paper. The tray was closed and locked, and the standard mini-dry transfer protocol was executed.

After transfer, the efficiency of protein transfer was verified using Ponceau S reagent. The membrane was then blocked in TBS-Tween (TBS-T) containing 5% (w/v) non-fat dry skimmed milk for 60 minutes at room temperature.

Following blocking, the membrane was incubated overnight at 4 °C with primary antibodies diluted in TBS-T containing 5% BSA. For c-Myc detection, a c-Myc Monoclonal Antibody (9E10) (Invitrogen) was used at a concentration of 0.5 µg/µL (30 µL in 10 mL of TBS-T with 5% BSA). For GAPDH detection as a housekeeping control, GAPDH Loading Control Monoclonal Antibody (GA1R) (Invitrogen) was used at a dilution of 0.05:10,000 under the same conditions.

The next morning, the membrane was washed three times with TBS-T for 10 minutes each. It was then incubated with secondary antibodies protected from light for one hour at room temperature on a rocker. For GAPDH detection, Goat anti-Mouse IgG (H+L) Secondary Antibody conjugated to HRP (Invitrogen) was used at a dilution of 1:10,000. For c-Myc detection, the same secondary antibody was used at a dilution of 1:15,000 in a total volume of 10 mL. After incubation, the membrane was washed twice with TBS-T for 10 minutes each.

Finally, detection was performed using Novex® ECL Substrate reagents (Invitrogen), a chemiluminescent substrate for HRP-based immunodetection on western blot membranes. The substrate consists of two components: Reagent A (luminol) and Reagent B (an enhancer), mixed in equal volumes to produce an intense light emission. For this assay, 3 mL of each reagent were used to develop the blots. The signal was detected using the ChemiDoc MP Imaging System (Bio-Rad) under chemiluminescent High Sensitivity Mode.

### 5.7.4 RNA Extraction and Quantification

Total RNA extraction from cells was performed using a phenol-chloroform protocol. After the incubation period, the cells were harvested using cell scrapers, and the resulting suspension was transferred into 1.5 mL microcentrifuge tubes. The samples were centrifuged at 3000 rpm at room temperature for 5 minutes.

Following centrifugation, the supernatants were collected and stored if required for future use. The remaining pellets were resuspended in 500 µL of TRIzol reagent (Sigma-Aldrich), mixed thoroughly by vortexing, and incubated at room temperature for 5 minutes. If immediate processing was not possible, the extracts were stored at -80°C.

To induce phase separation, 20% of the total volume of chloroform ($CHCl_3$) (Sigma-Aldrich) was added to each sample. This step separates proteins into the organic phase, DNA into the interphase, and RNA into the aqueous phase. The samples were vortexed vigorously for 15 seconds and incubated at room temperature for 5 minutes. Subsequently, the samples were centrifuged at 10,000 rpm at 4°C for 30 minutes.

After centrifugation, the aqueous phase (top layer) containing RNA was carefully transferred to a new tube (approximately 200 µL). To precipitate RNA, isopropanol (i-PrOH) (Sigma-Aldrich) equivalent to half the volume of the aqueous phase and 1 µL of Glycogen Blue (Invitrogen) were added. The mixture was vortexed for 15 seconds and stored at -80°C for at least 30 minutes.

Following incubation, the samples were thawed on ice and centrifuged at 13,000 rpm at 4°C for 30 minutes. The supernatants containing isopropanol were carefully removed without disturbing the RNA pellet and discarded. The pellets were then washed with 500 µL of 75% ethanol, followed by centrifugation at 13,000 rpm at 4°C for 10 minutes. After centrifugation, the ethanol was carefully removed, and the pellets were air-dried at room temperature for no longer than 15 minutes.

Finally, each RNA pellet was resuspended in 20 µL of RNase-free water (Qiagen). The RNA concentration was measured by absorbance at a wavelength of 260 nm (A260) using a spectrophotometer (NanoDrop; Thermo Scientific). The RNA concentration in each sample was calculated based on absorbance data using the Beer-Lambert law.

### 5.7.5 Reverse Transcription

The previously extracted and quantified RNA was used as a template to synthesize cDNA through a reverse transcription (RT) reaction. Unless otherwise specified, all procedures were performed on ice to ensure RNA integrity.

For the reverse transcription, 100 ng of RNA from each sample was used. The reaction mixture was prepared using the reagents provided in the High-Capacity cDNA Reverse Transcription Kit (Applied Biosystems, 4368814) and combined according to the proportions outlined in **Table 5.5**. The final reaction volume for each sample was 10 µL.

The prepared samples were then loaded into a Bio-Rad Thermal Cycler Tetrad 2, and the reverse transcription reaction was carried out according to the thermal cycling conditions (**Table 5.6**).

**Table 5.5: Content of Reverse Transcription Master Mix.**

| Reagent | Volume (µL) | Concentration |
|---|---|---|
| **RT Buffer (10X)** | 1 | 1x |
| **Random Primers (10X)** | 1 | 1x |
| **dNTP (100 mM)** | 0.4 | 4 mM |
| **RNAse inhibitor (40 U/µl, Promega)** | 0.5 | 2 U/µL |
| **MS Reverse Transcriptase (50 U/µl)** | 0.5 | 2.5 U/µL |
| **RNA+H2O** | 6.6 | 100 ng of RNA |

**Table 5.6: Thermocycler set-up for cDNA synthesis.**

| | Primer annealing | cDNA synthesis | Enzyme Deactivation | Hold |
|---|---|---|---|---|
| **Temperature (°C)** | 25 | 37 | 85 | 4 |
| **Time (min)** | 10 | 120 | 5 | ∞ |

## 5.7.6 Quantitative PCR (qPCR)

Quantitative Polymerase Chain Reaction (qPCR) was performed to measure the RNA levels of *c-myc* in each sample. TaqMan® technology, based on 5' nuclease chemistry, was employed to quantify transcript expression. This method utilizes a fluorescent probe along with primers to enable the detection of specific PCR products. The probe is labelled with two fluorescent moieties: a FAM™ or VIC™ dye label at the 5' end and a nonfluorescent quencher (NFQ) at the 3' end. The NFQ quenches the fluorescence of the dye by overlapping its excitation spectrum while both are present on the same probe.

At the start of qPCR, the reaction temperature is raised to denature the double-stranded cDNA. The temperature is then lowered to allow the primers and probe to hybridize with their specific DNA target. Subsequently, Taq polymerase, a DNA polymerase enzyme, binds to the 3' end of the primers and begins synthesizing new DNA strands. In addition to its polymerase activity, Taq polymerase exhibits

exonuclease activity, which cleaves the TaqMan probe upon encountering it, separating the dye from the quencher.

With each PCR cycle, more dye molecules are released, resulting in an increase in fluorescence intensity that is proportional to the number of amplifications. The accumulated fluorescence was detected using the Analytik Jena qTower³ 84 G Real-Time PCR System.

In this experiment, cDNA obtained from reverse transcription was diluted at a 1:10 ratio using RNase- and DNase-free distilled water (dd$H_2O$, Gibco). A commercial primer for *c-myc* (Hs00153408_m1, Invitrogen) was used to detect the canonical *c-myc* transcript (NP_002458.2). *GAPDH* (Hs02786624_g1, Invitrogen) served as the housekeeping gene and internal control. By comparing *c-myc* expression levels to *GAPDH* mRNA levels, it was ensured that any observed changes in *c-myc* levels were due to translational effects.

The qPCR master mix was prepared as described in **Table 5.7** for a total reaction volume of 5 µL per well.

**Table 5.7: qPCR master mix composition.**

| Reagent | Volume (µl) |
|---|---|
| **TaqMan Universal Master Mix II (Applied Biosystems)** | 2,5 |
| **RNAse and DNAse-free distilled H2O (ddH2O, Gibco)** | 0,25 |
| **Primer *c-myc* (Hs00153408_m1, Invitrogen) or primer *GAPDH* (Hs02786624_g1, Invitrogen)** | 1,25 |
| **cDNA obtained from the reverse transcription** | 1 |

The PCR program utilized for the experiment is outlined in **Table 5.8**.

**Table 5.8: Thermocycler setup for qPCR.**

| | Initial Steps | | PCR- 40 cycles | |
|---|---|---|---|---|
| | **UNG Activation** | **Polymerase Activation** | **Denaturation** | **Annealing/ Extension** |
| **Temperature** | 50 °C | 95 °C | 95 °C | 60 °C |
| **Time** | 2 min | 10 min | 15 s | 1 min |

To analyse the *c-myc* mRNA levels in the samples, the data were normalized to the mRNA levels of *GAPDH*, which served as the endogenous control. The calculations used in the analysis were as follows:

$$\Delta Ct = avgCt\ (c\text{-}myc) - avgCt(GAPDH)$$

$$RQ = 2^{-\Delta Ct}$$

The relative quantification (RQ) values obtained for the different samples were then compared to evaluate the effects of the various treatments on *c-myc* mRNA levels.

## 5.7.7 Flow Cytometer

To assess cell cytotoxicity following incubation with the different treatments, the cells were washed with PBS and harvested using 1X TrypLE Express (Gibco). The harvested cells were then centrifuged at 1500 rpm at 4 °C for 5 minutes, and the resulting pellet was resuspended in PBS. A control for dead cells was prepared by incubating cells at 60 °C for 20 minutes. After incubation, PBS was removed by centrifugation at 1500 rpm at 4 °C for 5 minutes.

The cells were stained using the Zombie Violet™ Fixable Viability Kit (BioLegend) at a dilution of 1:100 and incubated for 30 minutes at 4 °C in the dark. Following staining, 3 mL of PBS containing 0.5% Bovine Serum Albumin (BSA, Sigma) was added, and the cells were centrifuged again at 1500 rpm at 4 °C for 5 minutes. The washing step was repeated with another 3 mL of PBS containing 0.5% BSA.

Finally, the cells were resuspended in PBS containing 0.5% BSA and analysed using a BD FACSAria II flow cytometer (BD Biosciences).

## 5.7.8 Cell Cytotoxicity

### 5.7.8.1 Invitrogen™ CyQUANT™ LDH Cytotoxicity Assay

Cellular cytotoxicity was quantified using the Invitrogen™ CyQUANT™ LDH Cytotoxicity Assay Kit, which measures lactate dehydrogenase (LDH) levels in the culture medium. LDH is a cytosolic enzyme released into the medium when the cell membrane is compromised, serving as an indicator of cellular cytotoxicity. The assay quantifies LDH

through a coupled enzymatic reaction: LDH catalyses the conversion of lactate to pyruvate, reducing $NAD^+$ to NADH. The NADH then reduces tetrazolium salt to a red formazan product, which can be measured spectrophotometrically at 490 nm. The amount of formazan produced is directly proportional to the LDH released into the medium, reflecting the degree of cytotoxicity.

The kit is composed of the following compounds and reagents essentials for measuring LDH activity:

- LDH Substrate Mix: Contains lactate (substrate) and $NAD^+$ (cofactor) required for the LDH-catalysed reaction, producing NADH.
- Tetrazolium Salt: Reduced by NADH to form a coloured formazan product measurable at 490 nm.
- Lysis Buffer: Used to lyse cells, providing a total cell death control for 100% cytotoxicity.
- Stop Solution: Stops the enzymatic reaction to prevent overexposure of the substrate to LDH.
- Assay Buffer: Ensures optimal pH and ionic conditions for the LDH reaction.

The optimal number of cells was plated in 100 µL of medium per well in triplicate wells of a 96-well tissue culture plate. After overnight incubation at 37°C in a cell culture incubator, 10 µL of sterile ultrapure water was added to one set of triplicate wells to measure spontaneous LDH activity. Another set of triplicate wells was left untreated to serve as a control for calculating maximum LDH activity. Finally, 10 µL of the respective treatment solutions were added to the remaining wells, and the cells were incubated overnight at 37°C with appropriate $CO_2$ levels.

For the triplicate wells designated for maximum LDH activity, 10 µL of 10X Lysis Buffer was added and mixed thoroughly. The plates were then incubated at 37°C with appropriate $CO_2$ levels for 45 minutes. After incubation, 50 µL of medium from each well was transferred to a new 96-well flat-bottom plate in triplicate wells and incubated at room temperature for 30 minutes, protected from light.

Finally, 50 µL of Stop Solution was added to each sample well and mixed gently by tapping.

Absorbance was measured at 490 nm and 680 nm. To determine LDH activity, the absorbance value at 680 nm (background) was subtracted from the absorbance value at 490 nm.

The percentage of cell cytotoxicity was then calculated using the following formula:

$$\%\ \mathbf{Cytotoxicity} = \left(\frac{\mathbf{Compound\ treated\ LDH\ activity} - \mathbf{Spontaneous\ LDH\ activity}}{\mathbf{Maximum\ LDH\ activity} - \mathbf{Spontaneous\ LDH\ activity}}\right)\mathbf{x100}$$

### 5.7.8.2 CellTiter 96® AQueous One Solution Cell Proliferation Assay

The CellTiter 96® AQueous One Solution Cell Proliferation Assay was employed as a cytotoxicity assay to quantify the number of viable cells. This assay is based on a tetrazolium compound, [3-(4,5-dimethylthiazol-2-yl)-5-(3-carboxymethoxyphenyl)-2-(4-sulfophenyl)-2H-tetrazolium, inner salt; MTS], and an electron coupling reagent, phenazine ethosulfate (PES). PES is chemically stable, allowing it to be combined with MTS to form a stable reagent solution.

The MTS compound is bioreduced by metabolically active cells into a coloured formazan product that is soluble in the culture medium. This reduction process is mediated by NADPH or NADH, which are produced by dehydrogenase enzymes present in viable cells.

The assay procedure involves adding 20 µL of the CellTiter 96® AQueous One Solution Reagent to each well of a 96-well plate containing 100 µL of culture medium and samples. The plate is then incubated at 37°C in a humidified atmosphere with 5% $CO_2$ for 1–4 hours. Following incubation, the absorbance is measured at 490 nm using a microplate reader. The amount of formazan product, as indicated by absorbance at 490 nm, is directly proportional to the number of viable cells in the sample.

The percentage of cell cytotoxicity was then calculated using the following formula:

$$\%\ \mathbf{Cytotoxicity} = \left(\frac{\mathbf{Live\ Control\ Absorbance\ } - \mathbf{Compound\ Absorbance}}{\mathbf{Live\ Control\ Absorbance\ } - \mathbf{Death\ Control\ Absorbance}}\right)\mathbf{x100}$$

In this formula, "Live Control Absorbance" represents the absorbance of untreated cells (indicating 100% viability), "Death Control Absorbance" represents the absorbance of cells treated to induce complete cell death (indicating 0% viability), and "Compound Absorbance" is the absorbance of cells treated with the compound being tested. This calculation provides the percentage of cytotoxicity induced by the test compound, normalized to the range between fully viable and fully non-viable cells.

## 5.7.9 Microscopy

Brightfield microscopy was utilized to visually assess nanoparticle deposition and internalization in HeLa cells. The analysis was conducted using a Nikon Diaphot Inverted Phase Contrast Photomicroscope equipped with a 40x (LWD) phase objective and an electronic 3-axis micromanipulator system. Images were captured using a Nikon D3300 DSLR camera.

For the assay, HeLa cells were seeded in 6-well plates and incubated under specific conditions (AuNPs@PEG@ssDNA, AuNPs@PEG, ssDNA, and water) for 24 hours. Following the incubation period, the 6-well plates were directly imaged using the microscope. The captured images were subsequently analysed using the Fiji image processing software package.

## 5.7.10 Confocal Microscopy

### 5.7.10.1 Immunofluorescence (IF)

HeLa cells (60,000 per well) were seeded onto #1.5 or #1.5H glass coverslips in a 24-well plate. After overnight incubation at 37°C in a cell culture incubator, the appropriate treatment was added to the cells, which were further incubated under the same conditions for a specified duration. Following incubation, the cells were fixed with 4% (w/v) paraformaldehyde (PFA) for 15 minutes at room temperature and permeabilized with 0.25% Triton X-100 in 1X PBS for 5 minutes. To block nonspecific binding, the cells were incubated with 10% goat serum (Sigma-Aldrich) in PBS for 1 hour.

Subsequently, the cells were incubated overnight at 4°C in a humidity chamber with the relevant primary antibodies (mouse or rabbit). The coverslips were then washed three times for 5 minutes each with Solution A (Duolink) and incubated with the corresponding goat anti-mouse or goat anti-rabbit secondary antibody for 2 hours at room temperature in a humidity chamber, protected from light. Optionally, cells were treated with Hoechst 33342 for nuclear staining or proceeded directly to the washing steps.

The cells were washed sequentially: once with Solution A, once with Solution B (Duolink), and finally with a 1:100 dilution of Solution B. The coverslips were mounted onto glass slides using Fluoromount (Sigma) and allowed to dry for 30 minutes at room temperature, protected from light. The slides were then sealed with clear nail polish and stored at 4°C. Before imaging, slides were thawed and wiped to remove condensation.

Confocal images were acquired using a Leica SP8 inverted confocal microscope (Leica Microsystems) with a 12-bit depth and a resolution of 1024x1024 pixels. The emission wavelength was set to match the specific maxima of the fluorophore, and the detector was adjusted to begin 10 nm beyond this maximum to ensure full coverage of the emission spectrum. Imaging was performed using a 63x oil immersion objective.

#### 5.7.10.2 Live Imaging Microscopy

In this experimental procedure, 60,000 HeLa cells were seeded directly onto 35 $mm^2$ glass-bottom cell culture dishes one day prior to the assay. After overnight incubation at 37°C in a cell culture incubator, the culture medium was removed, and the cells were washed with PBS. The medium was then replaced with Opti-MEM + GlutaMAX. The dish was subsequently placed in a Spinning Disk microscope (Zeiss) equipped with an incubation chamber maintained at 37°C with 7% $CO_2$.

Fifteen positions within the dish were selected, and the middle plane of the cells was identified to ensure that the signal from the sequence originated from within the cells. Functionalized AuNPs were carefully added dropwise to the dish to avoid disturbing the cells and to maintain focus on the preselected positions. Images were captured

every 15 minutes over a total duration of 6 hours using a 40x water immersion objective.

### 5.7.11 Software

Microscopy images and the characterization of biofunctionalized AuNPs were analysed using **FiJi ImageJ** software (version 2.14).

Flow cytometry data were analysed using **FlowJo™ v10** software, while western blot analysis was conducted with Image Lab software (version 6.1).

Statistical analyses were performed using **GraphPad Prism 10.**

The **GGGenome Ultrafast Sequence Search** tool was utilized to confirm that the synthesized sequences were complementary to the molecular target. Additionally, the software was used to verify that the scramble sequence did not correspond to any sequence present in the human genome, ensuring it would not hybridize with any region or produce unintended effects.

# Appendix A: **Modelling analysis of the ASOs secondary structures**

The DNA mfold server was used to study the secondary structures of the ASOs previously selected from the IRES structure of the *c-myc*. The software was utilized to check which sequences could be an impediment to form a heteroduplex with the mRNA target.

- **Scramble**

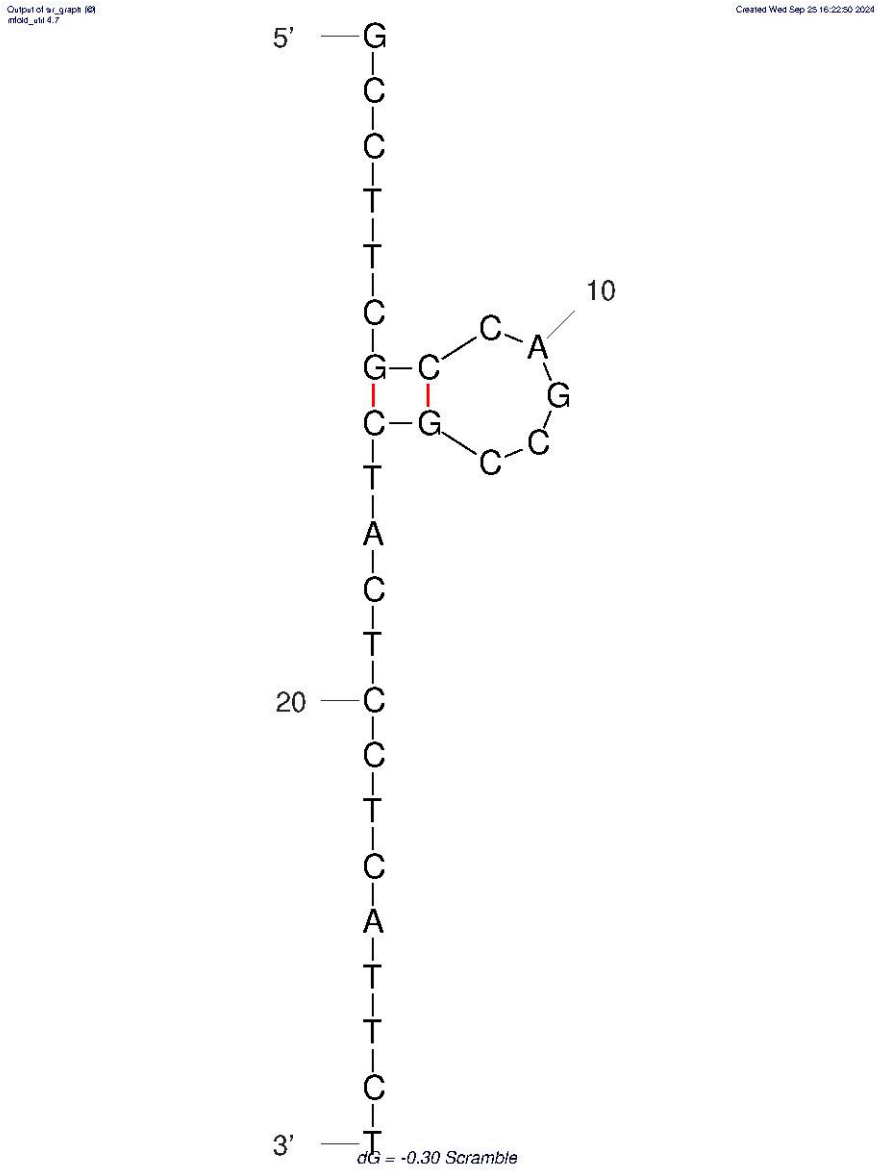


**Figure A.1: Predicted secondary structure of Scramble sequence using mfold.**

- **ON1**

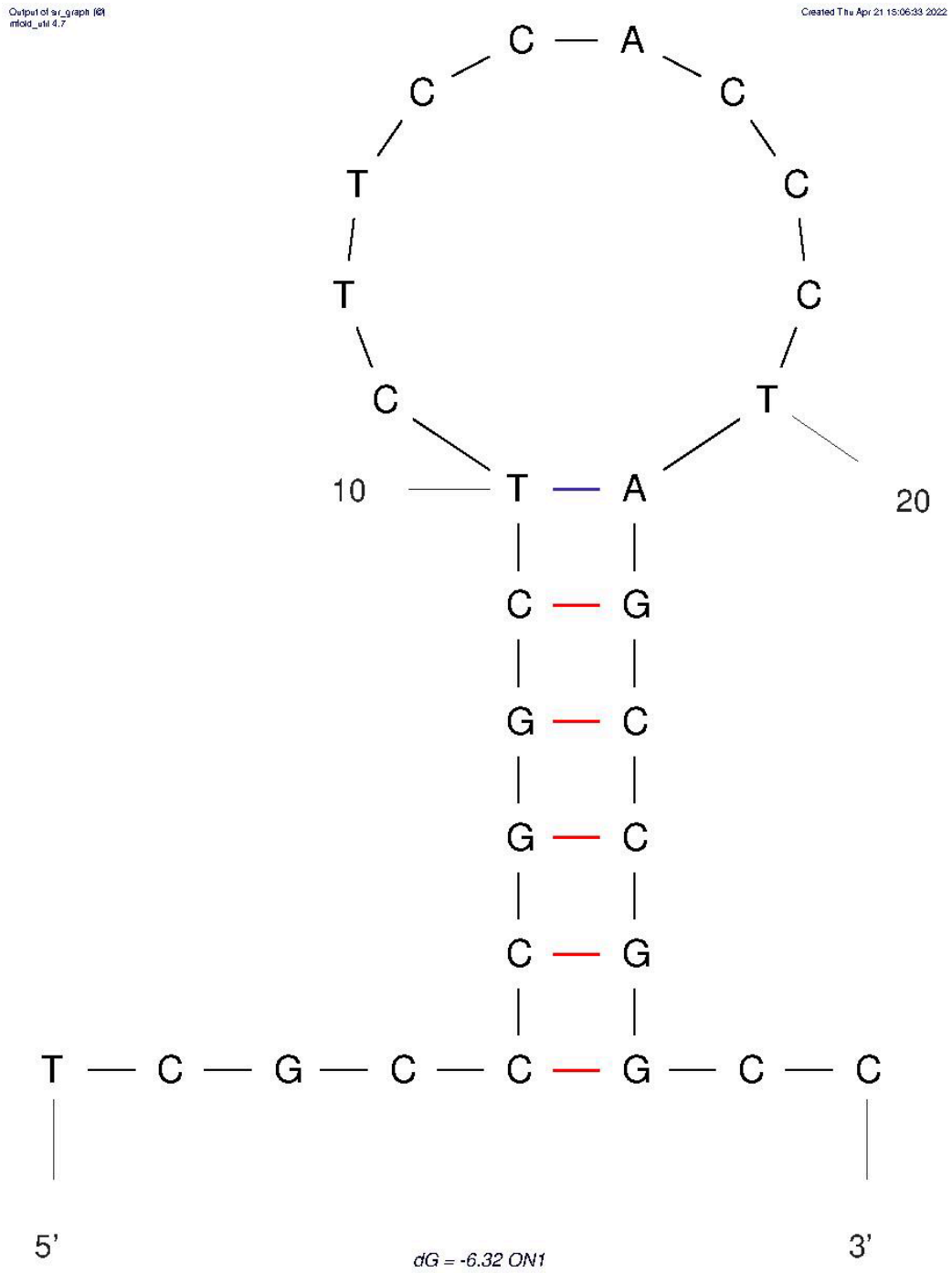


**Figure A.2: Predicted secondary structure of ON1 using mfold.**

- **ON2**

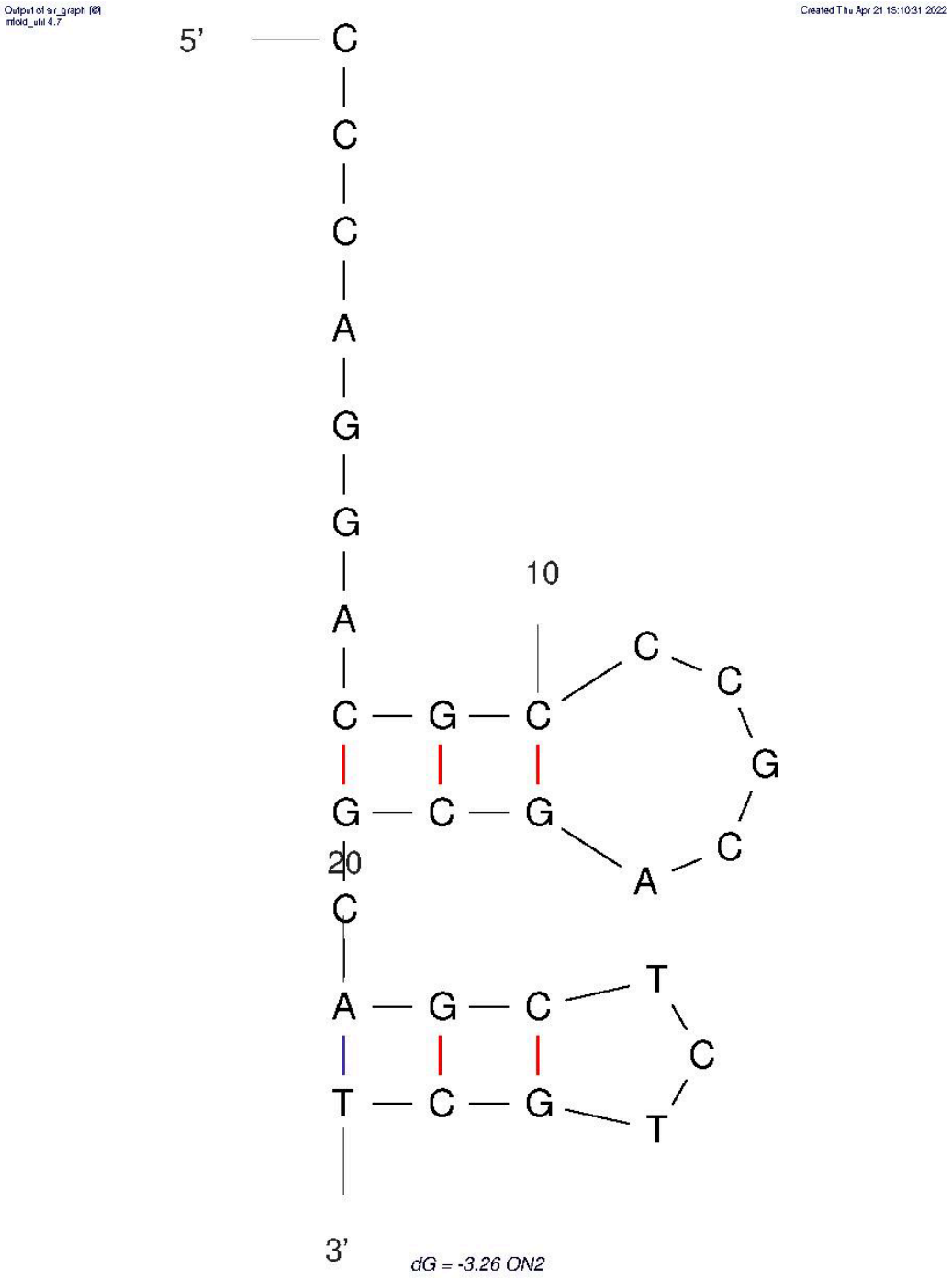


**Figure A.3: Predicted secondary structure of ON2 using mfold.**

- **ON3**

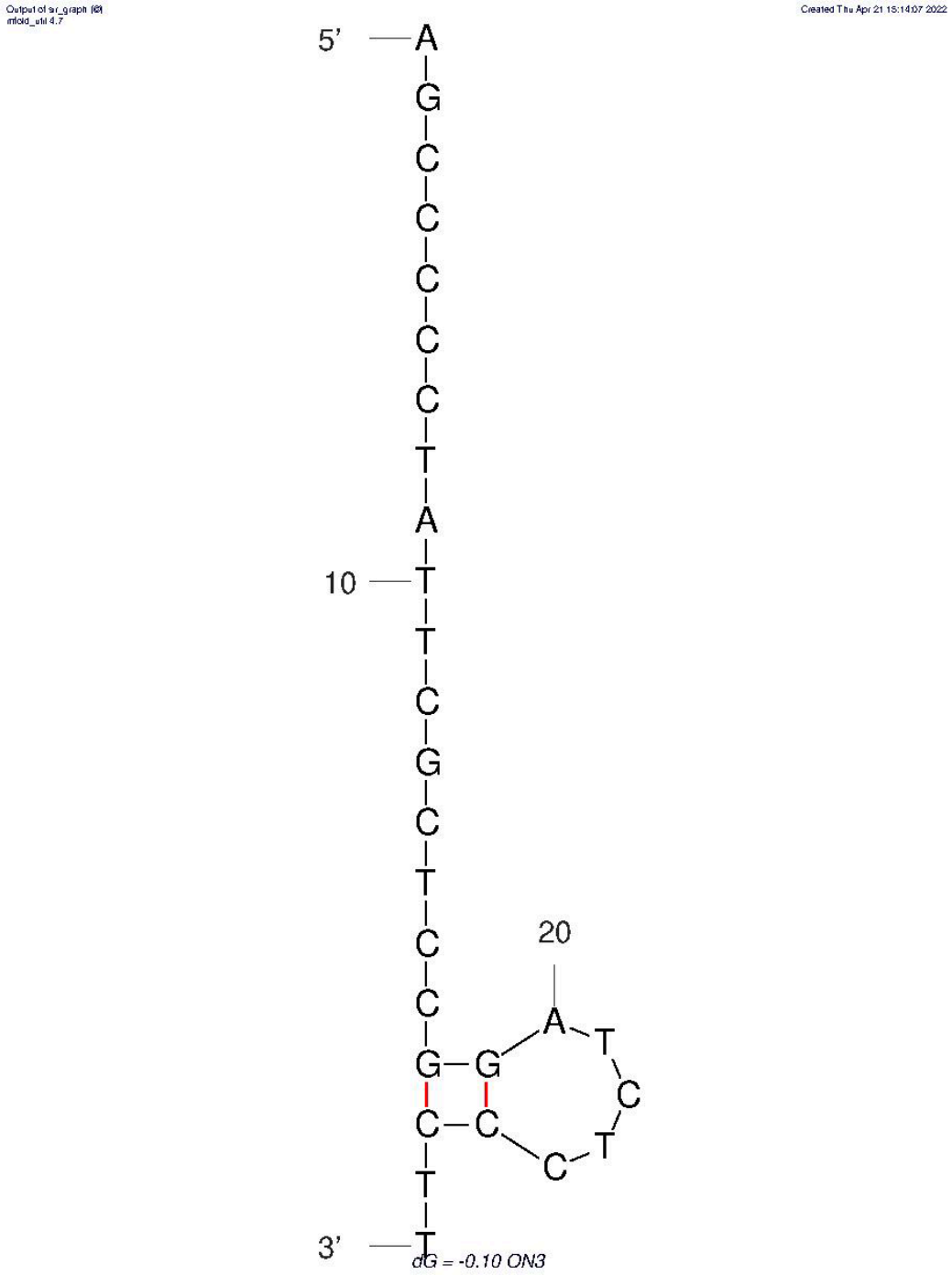


**Figure A.4: Predicted secondary structure of ON3 using mfold.**

- **ON4**

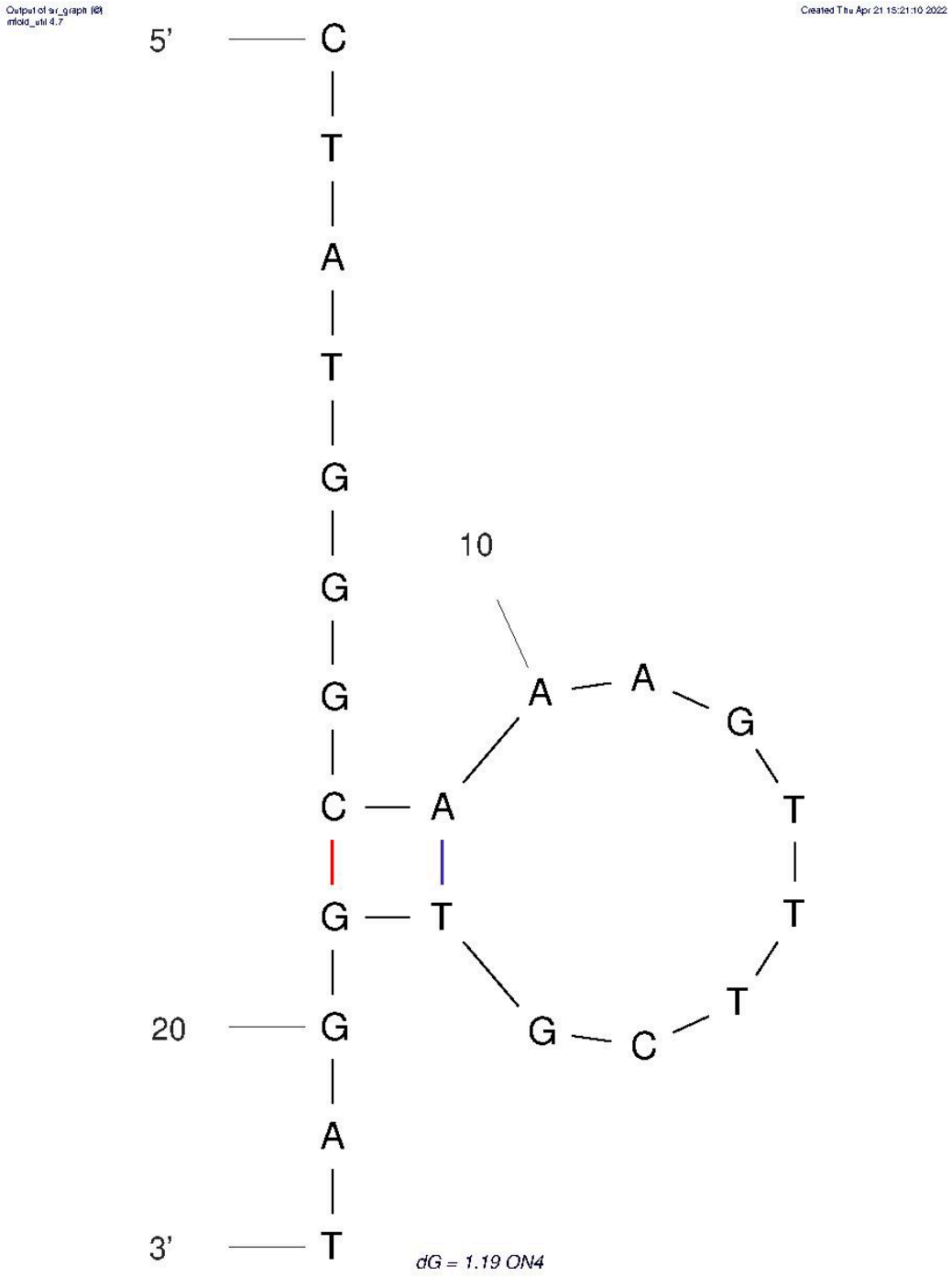


**Figure A.5: Predicted secondary structure of ON4 using mfold.**

- **ON5**

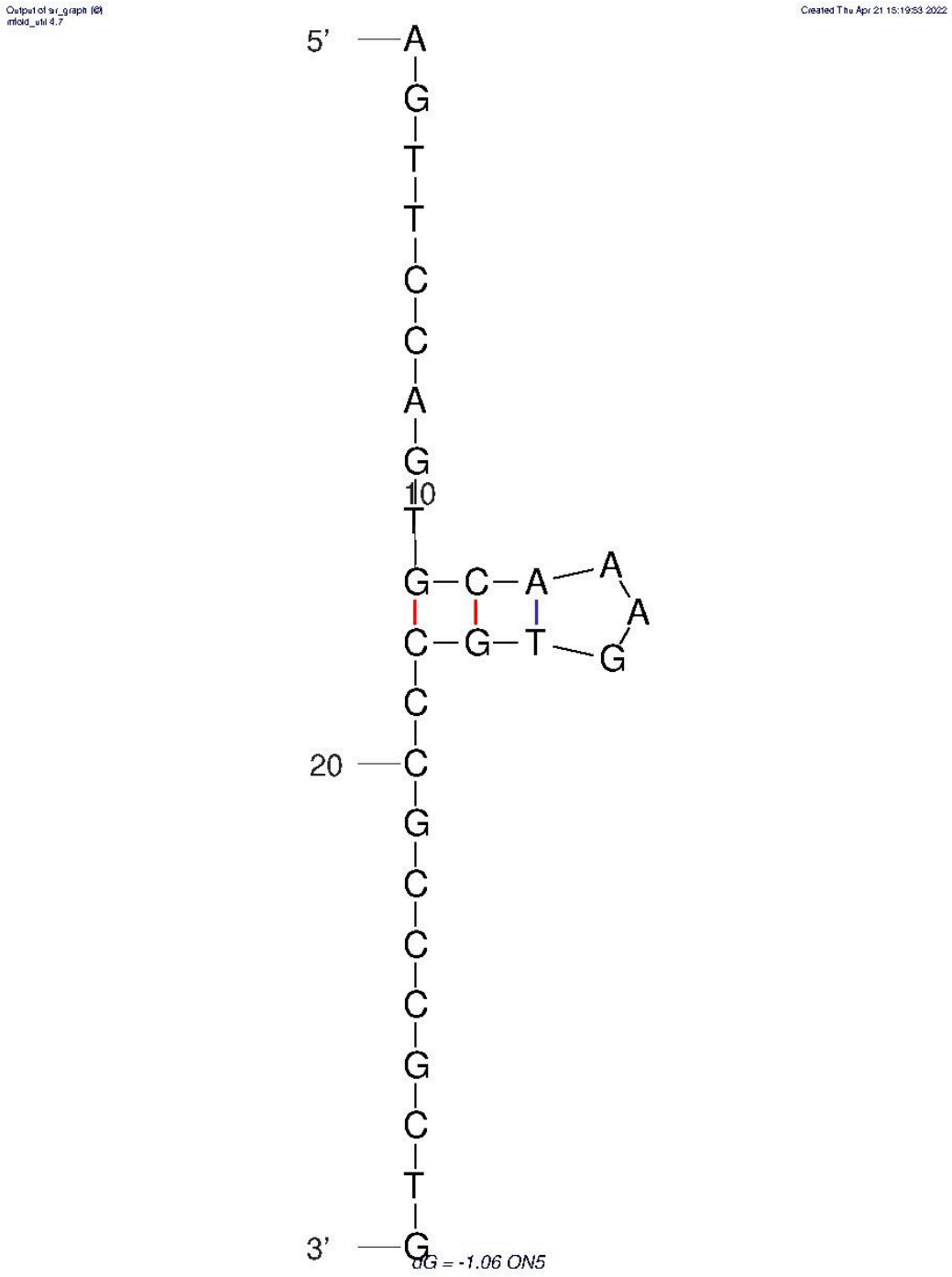


**Figure A.6: Predicted secondary structure of ON5 using mfold.**

# Appendix B: **Mass Spectrometry analysis of the synthesized sequences**

Mass spectrometry analysis checks if the sequences are lacking some bases corresponding to a deletion in the desired oligo and if the purity of the sequences comparing the peaks present in the UV-Vis analysis with their deconvoluted mass.

- **ON1**

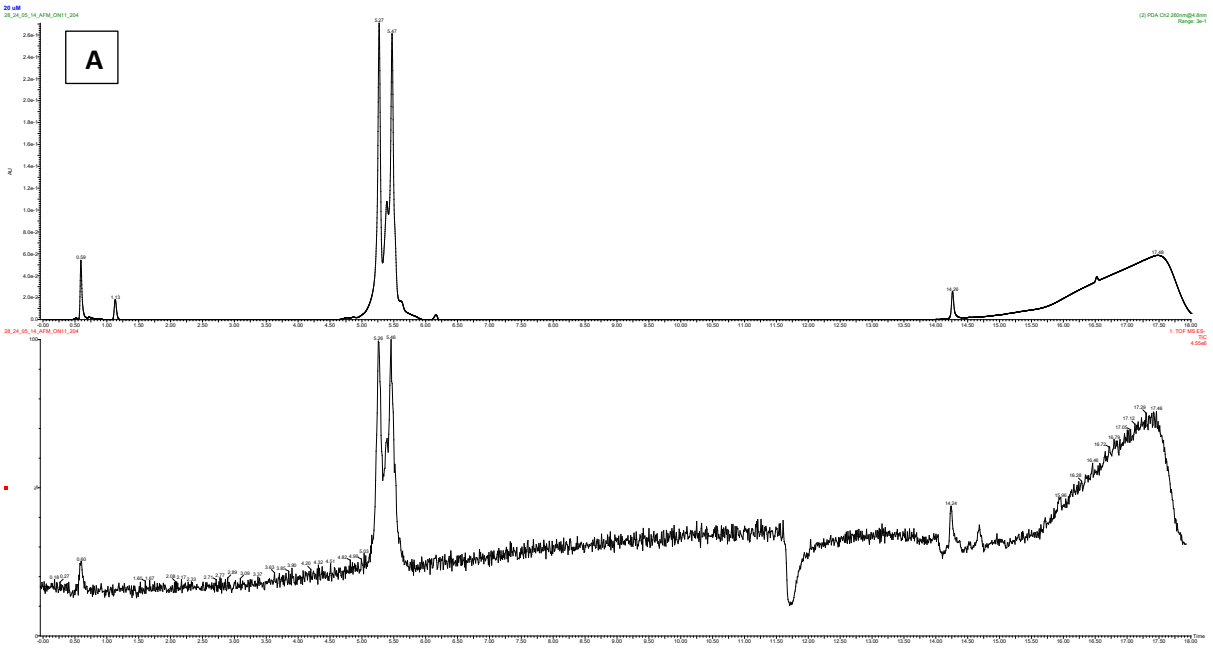

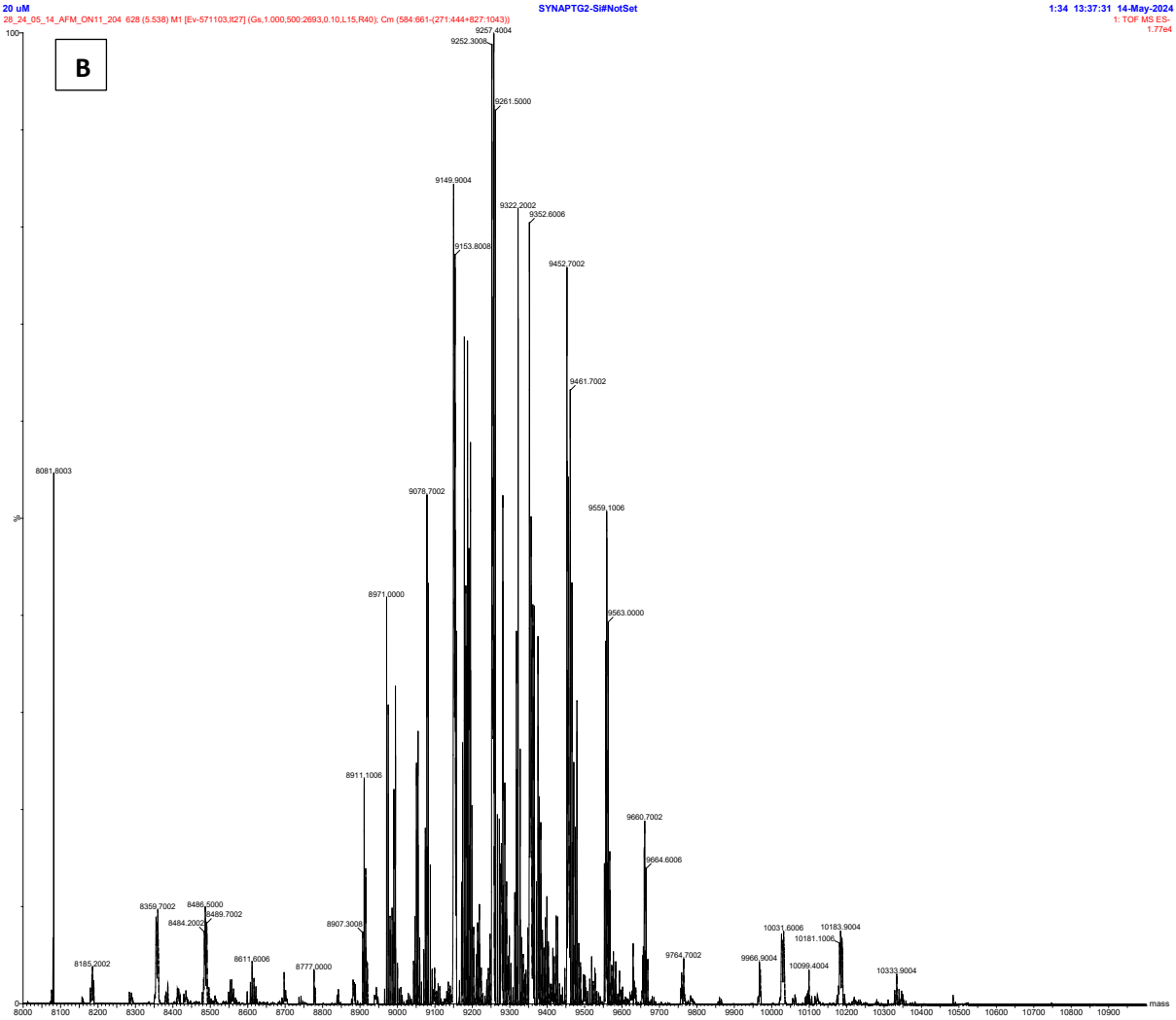


**Figure B.1: LC-ESI-MS analysis of ON1.** (A) Uv-Vis chromatogram at 260 nm (B) Mass spectrum deconvolution of the main peak at 5.47 min.

- **ON2**

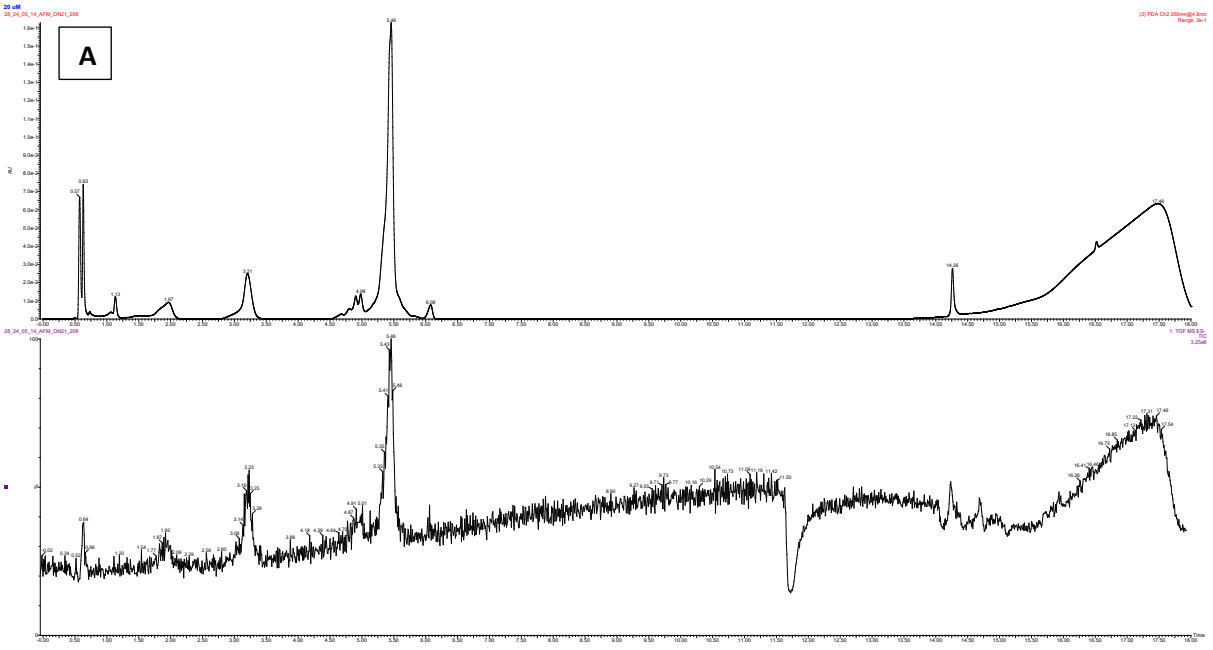


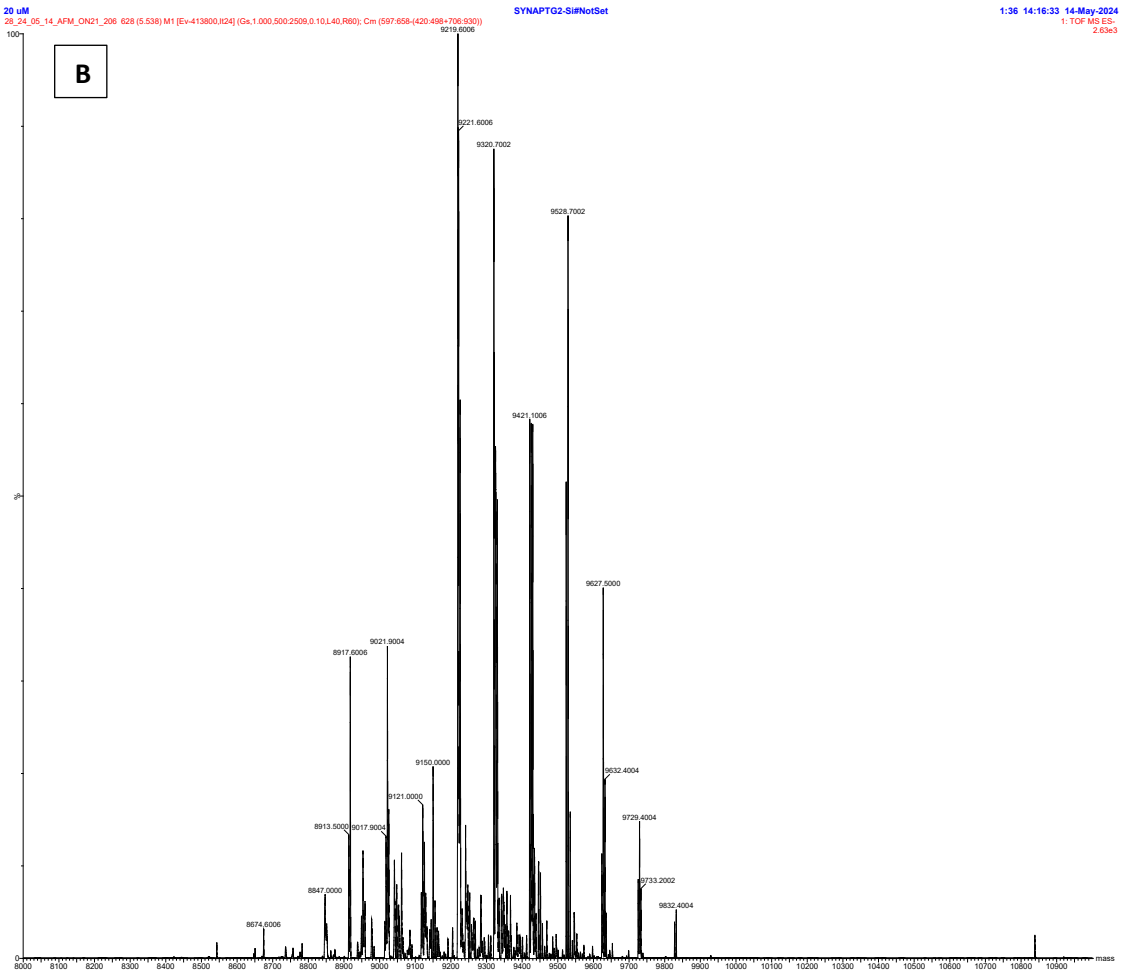


**Figure B.2: LC-ESI-MS analysis of the ON2** (A) Uv-Vis chromatogram at 260 nm (B) Mass spectrum deconvolution of the main peak at 5.46 min.

- **ON3**

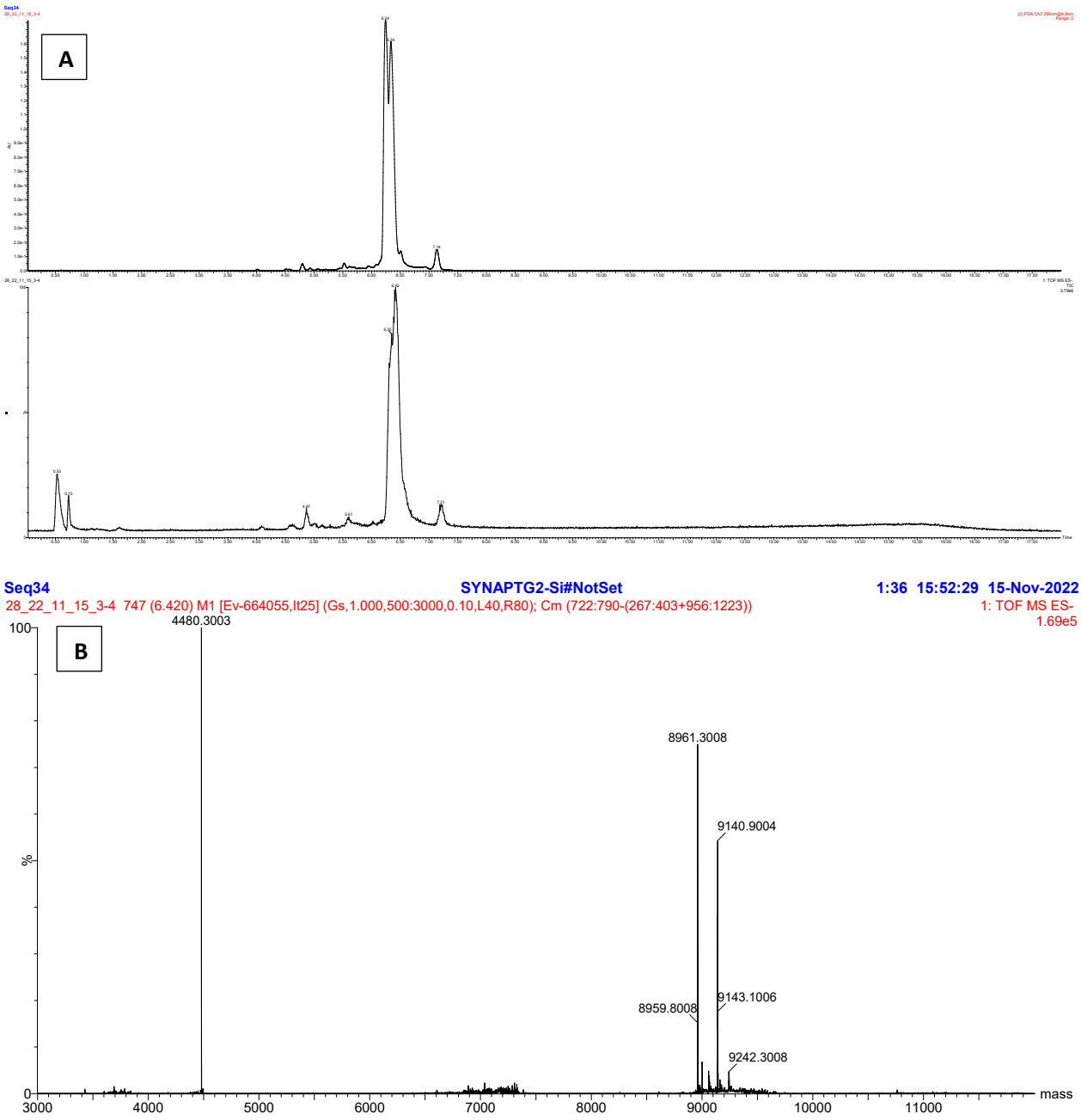


**Figure B.3: LC-ESI-MS analysis of the ON3** (A) Uv-Vis chromatogram at 260 nm (B) Mass spectrum deconvolution of the main peak at 6.24 min.

- **ON4**

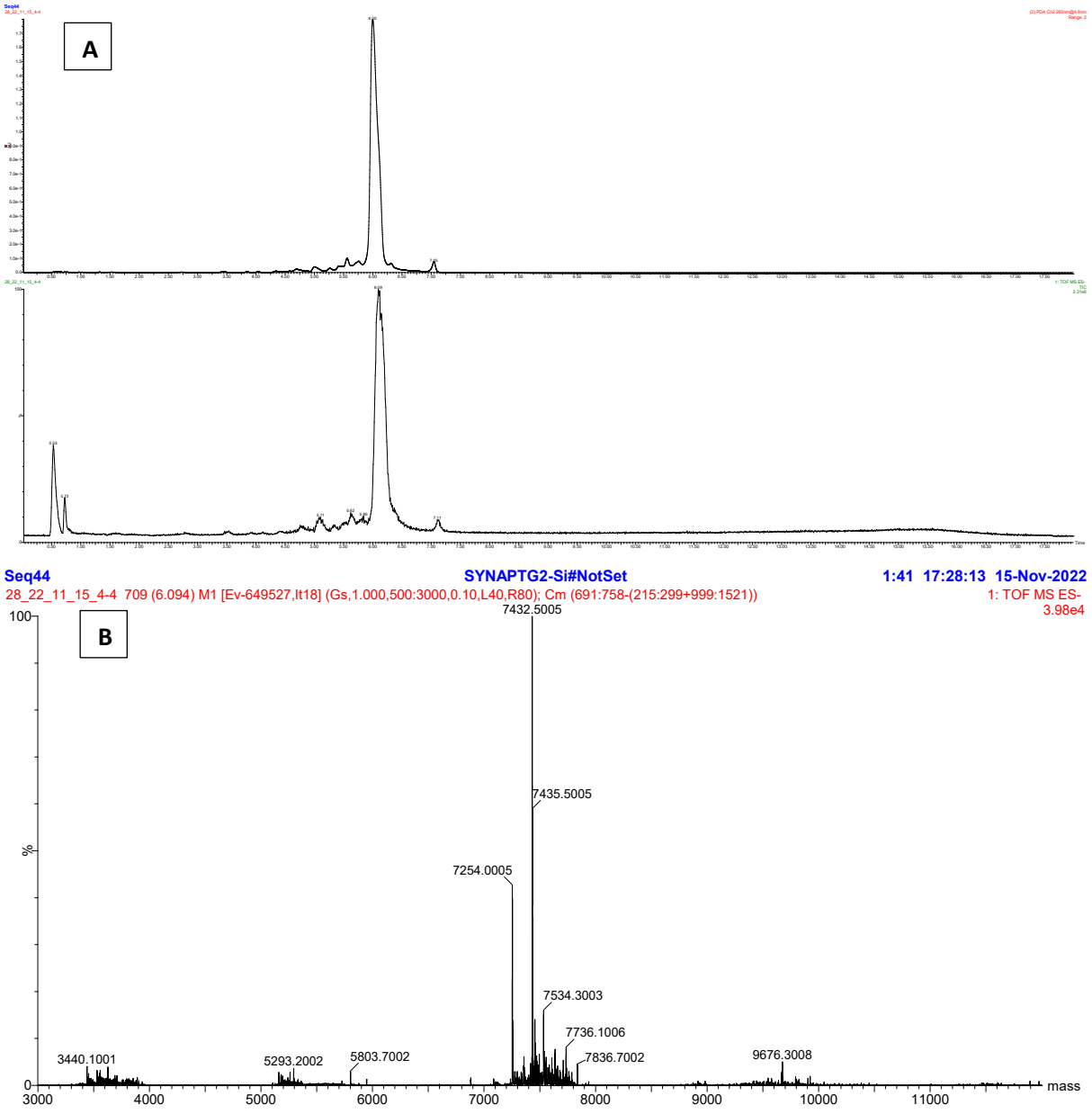


**Figure B.4: LC-ESI-MS analysis of the ON4** (A) Uv-Vis chromatogram at 260 nm (B) Mass spectrum deconvolution of the main peak at 6.00 min.

- **ON5**

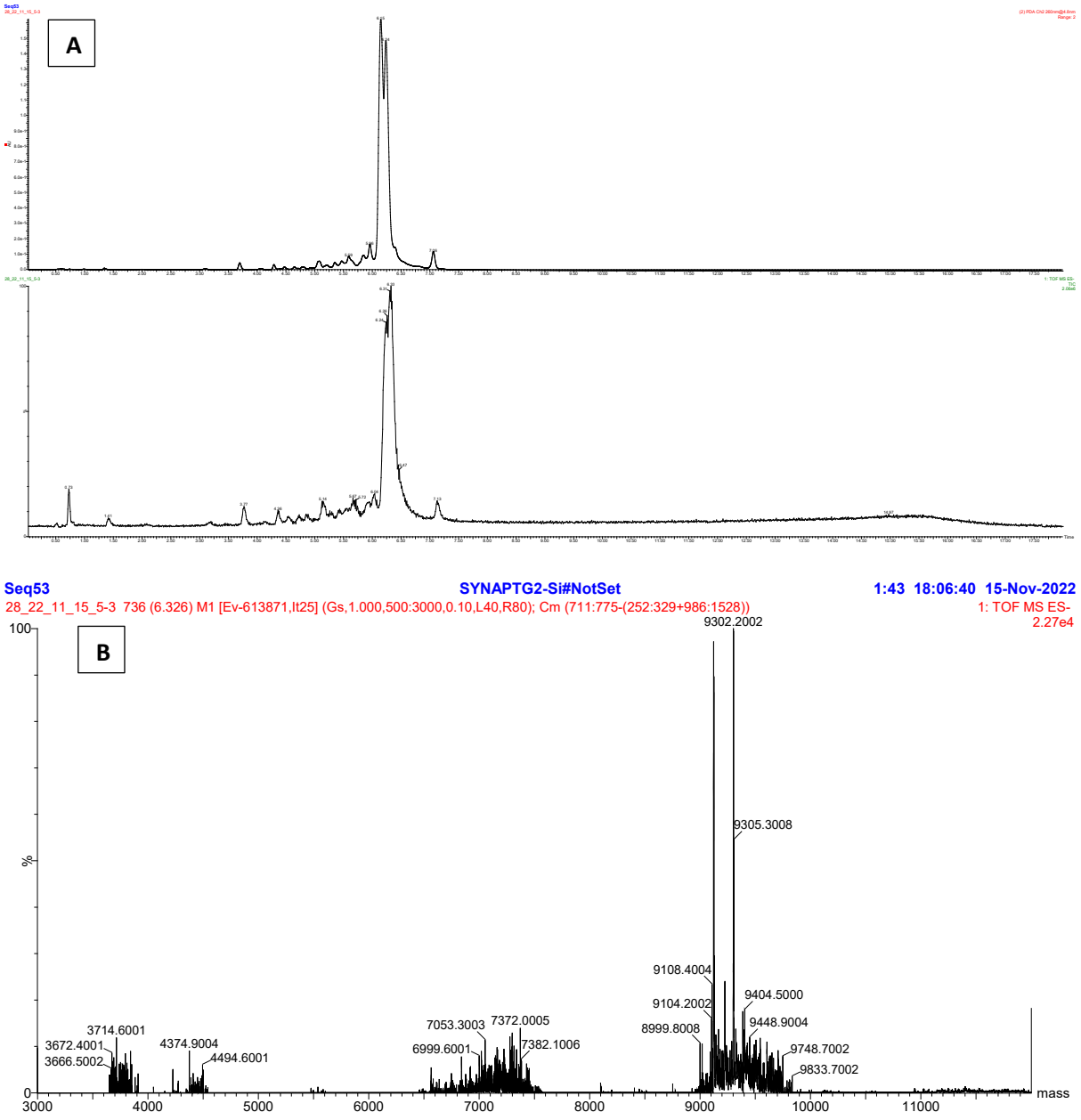


**Figure B.5: LC-ESI-MS analysis of the ON5** (A) Uv-Vis chromatogram at 260 nm (B) Mass spectrum deconvolution of the main peak at 6.15 min.

# Appendix C: **HPLC analysis of the synthesized sequences**

The purity of the oligonucleotides was confirmed using HPLC. In the different chromatograms the peaks correspond to the DNA sequences synthesized and their replicates.

- **ON1**

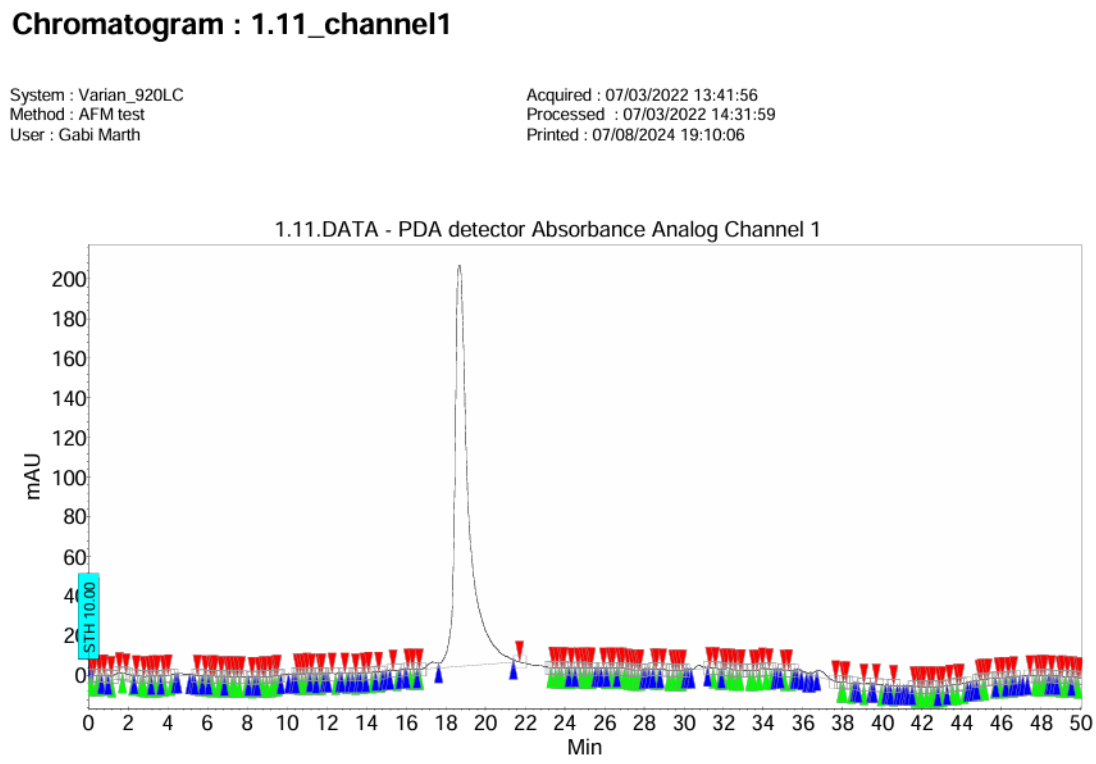


**Figure C.1: HPLC chromatogram of the synthesized ON1 sequence**.

- **ON2**

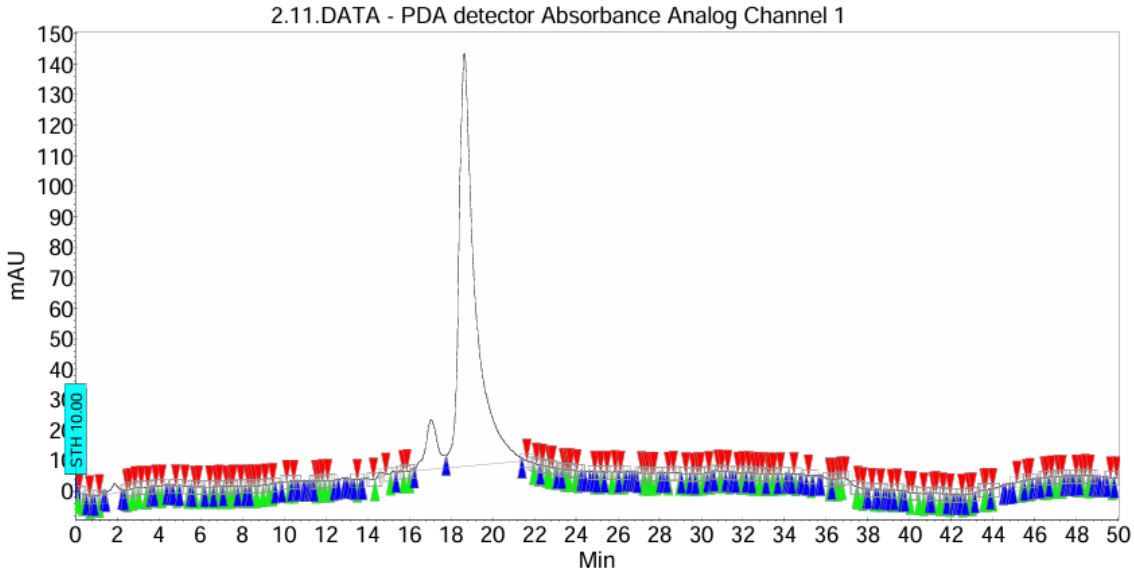


**Figure C.2: HPLC chromatogram of the synthesized ON2 sequence.**

- **ON3**

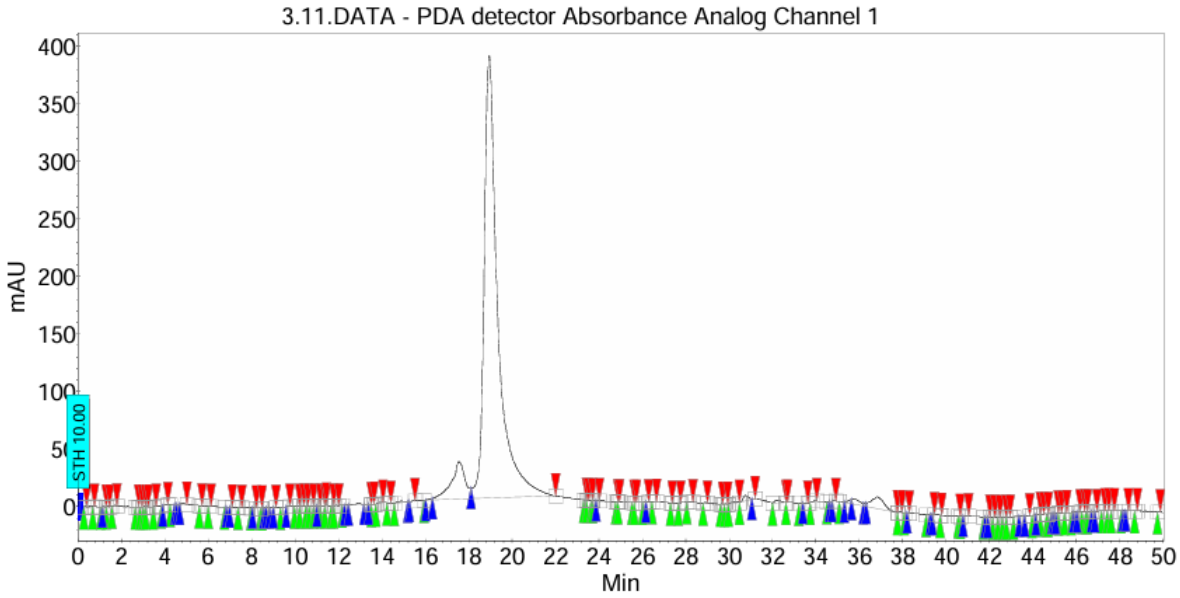


**Figure C.3: HPLC chromatogram of the synthesized ON3 sequence.**

- **ON4**

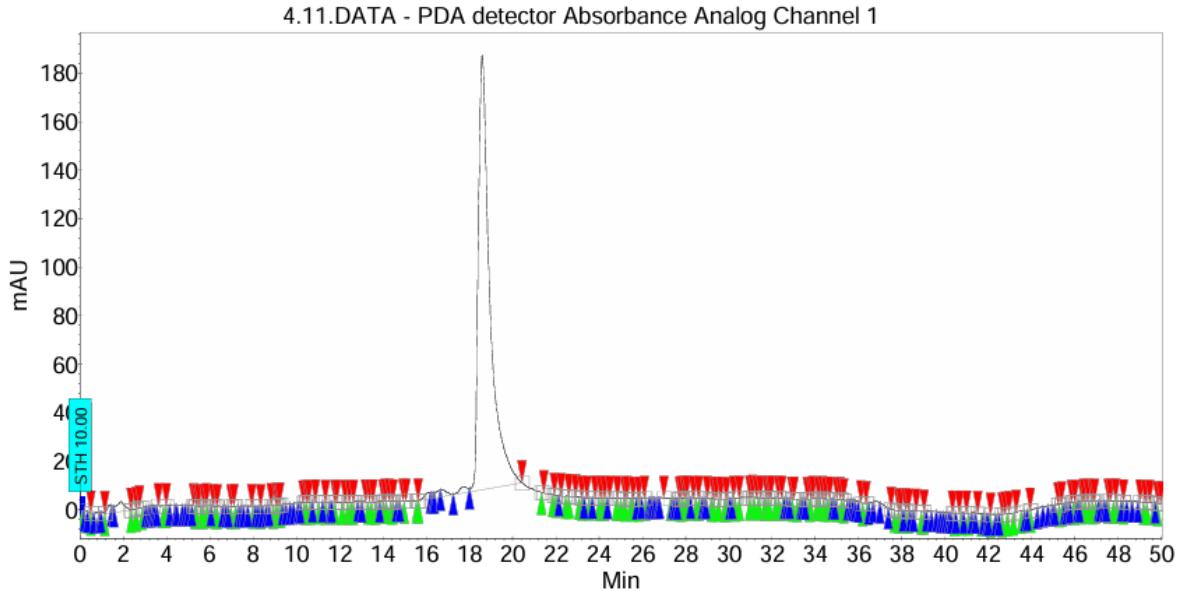


**Figure C.4: HPLC chromatogram of the synthesized ON4 sequence.**

- **ON5**

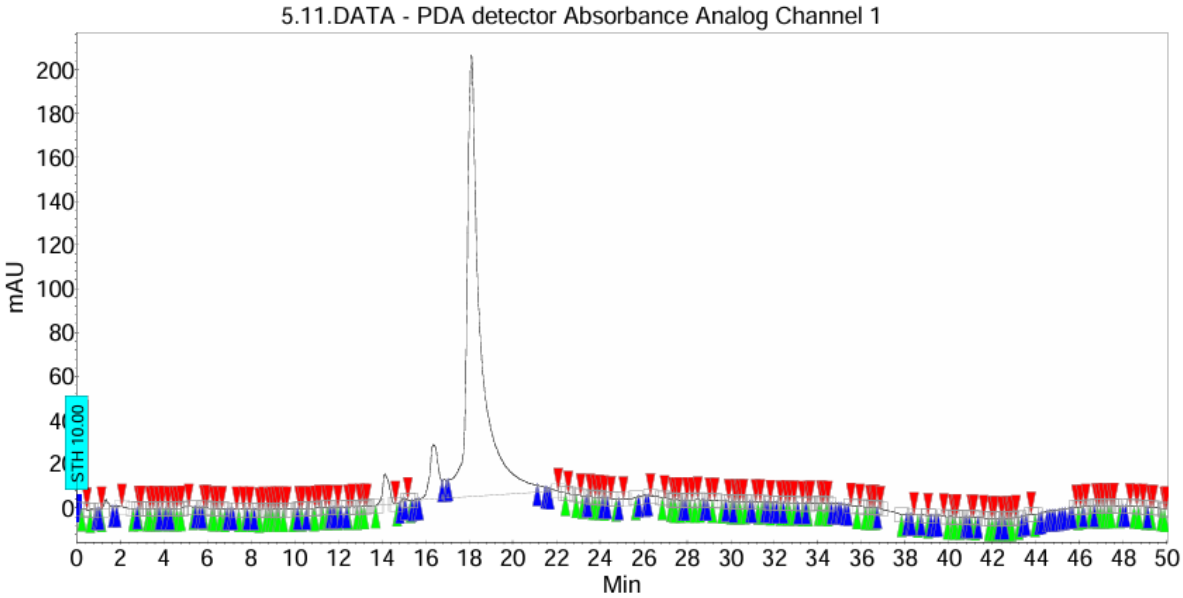


**Figure C.5: HPLC chromatogram of the synthesized ON5 sequence.**

# Appendix D: **LC-MS-ESI analysis of the purified PEG-bioconjugated sequences**

The purification of SH-PEG-ASO was performed using HPLC. In the chromatograms different sections were collected in order to separate the peak of the DNA sequences that have been coupled to the SH-PEG-NHS from the unconjugated sequences. The analysis of the purified fractions was performed by LC-ESI-MS.

- **Scramble**

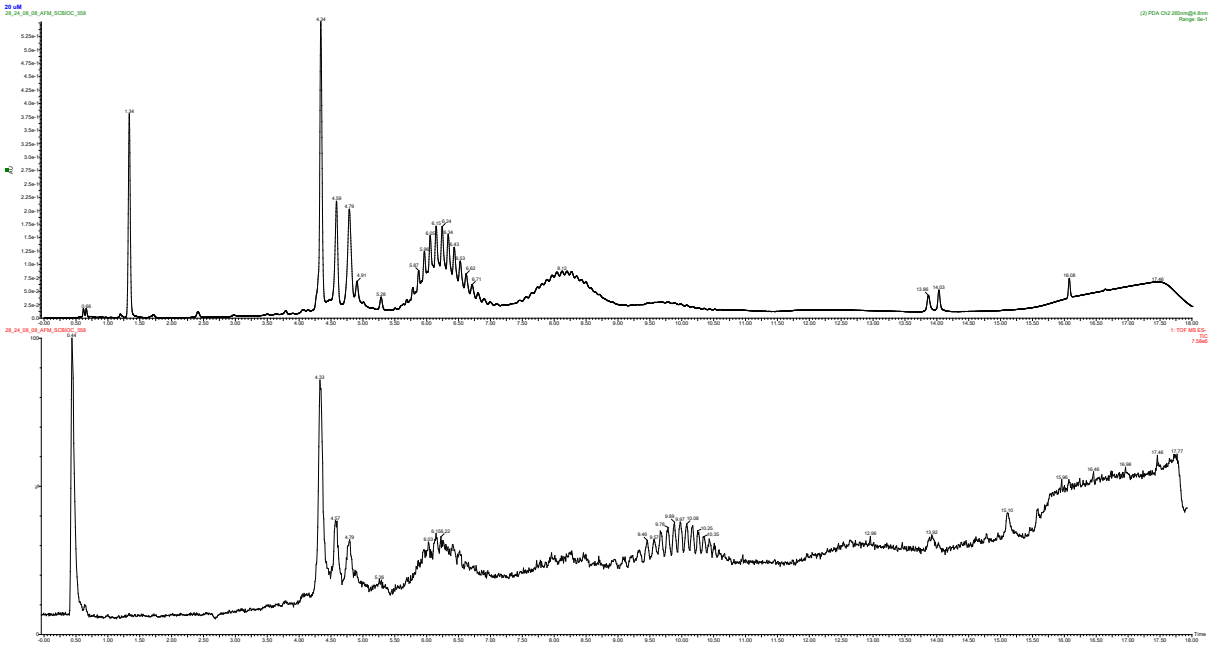

**Figure D.1: HPLC chromatogram representing the purified product from bioconjugation of scramble sequence.**

- **ON1**

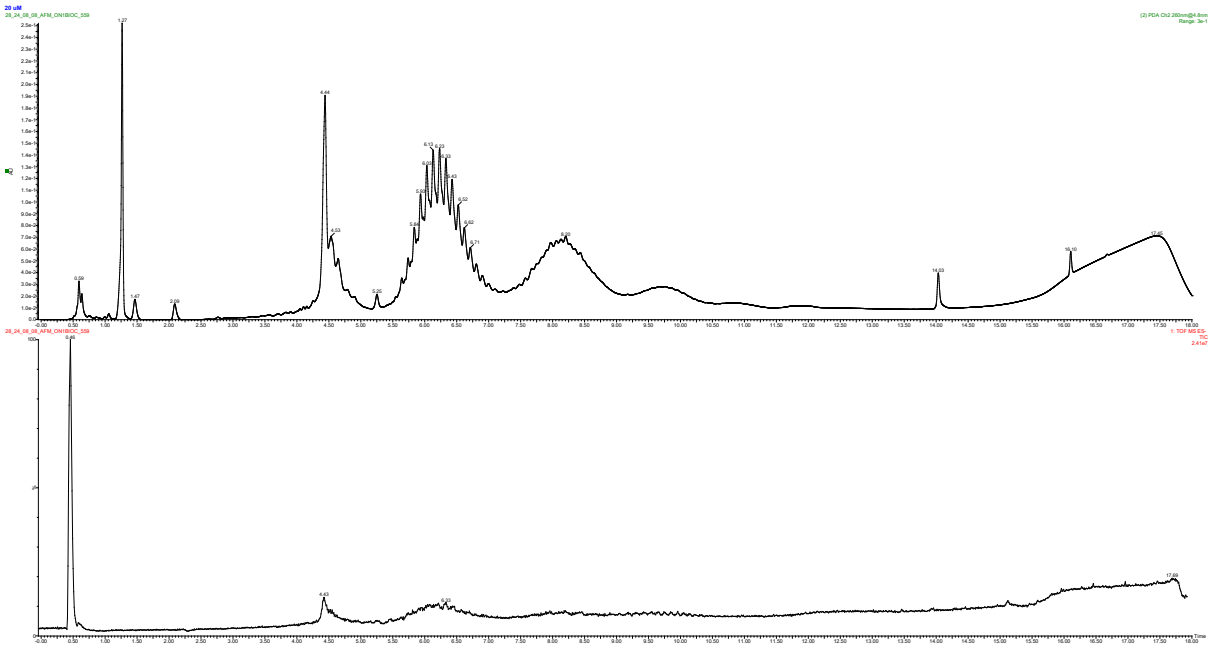

**Figure D.2: HPLC chromatogram representing the purified product from bioconjugation of sequence ON1.**

- **ON2**

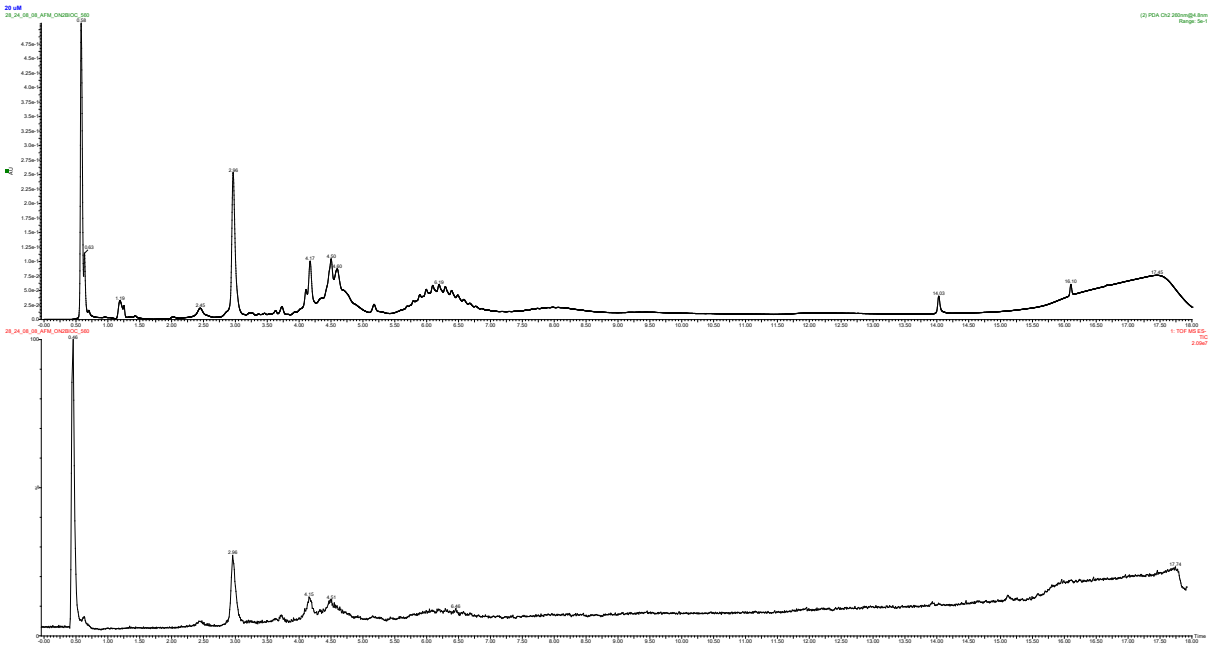

**Figure D.3: HPLC chromatogram representing the purified product from bioconjugation of sequence ON2.**

- **ON3**

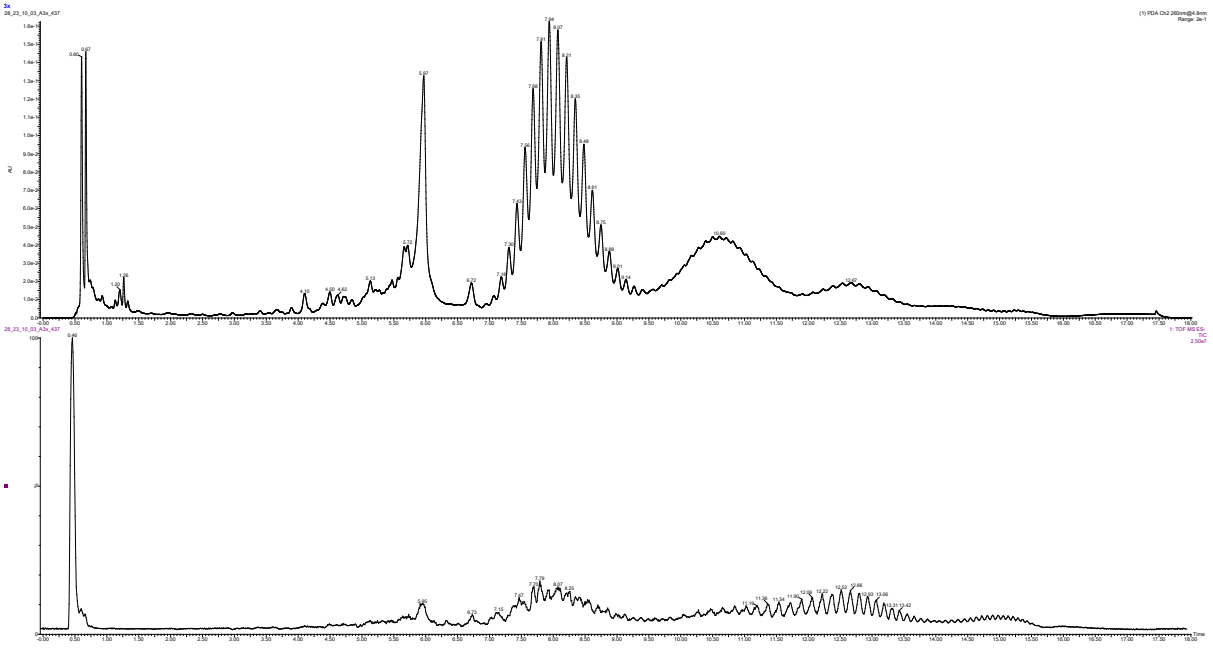

**Figure D.4: HPLC chromatogram representing the purified product from bioconjugation of sequence ON3.**

- **ON4**

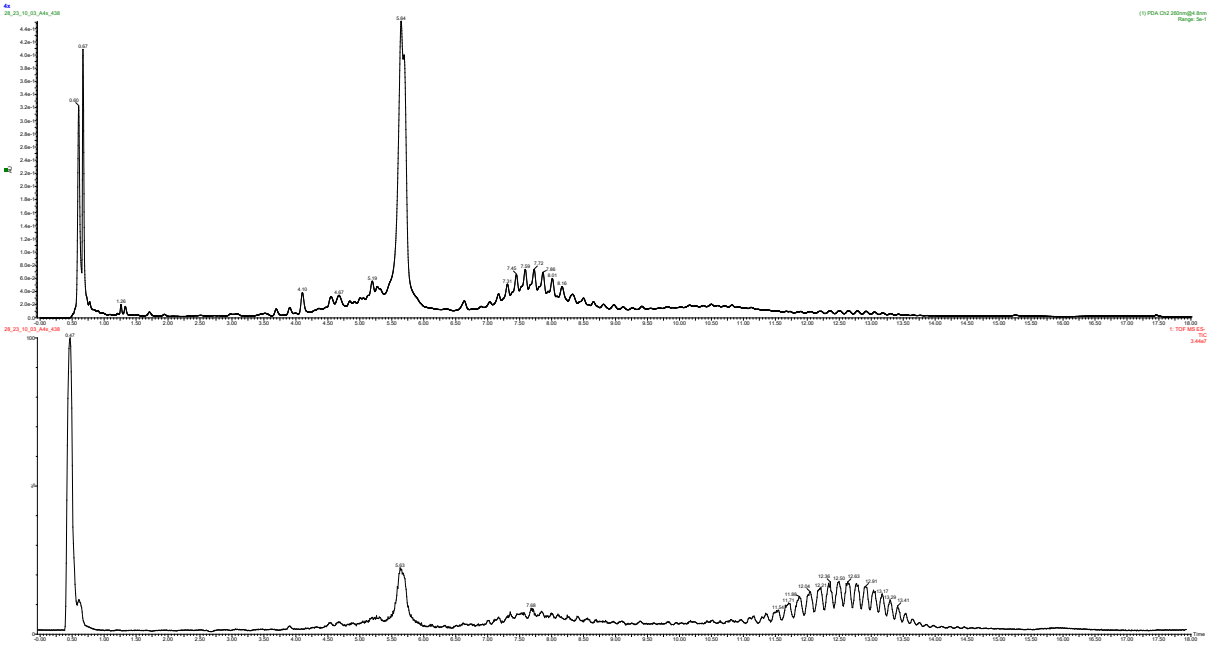

**Figure D.5: HPLC chromatogram representing the purified product from bioconjugation of sequence ON4.**

- **ON5**

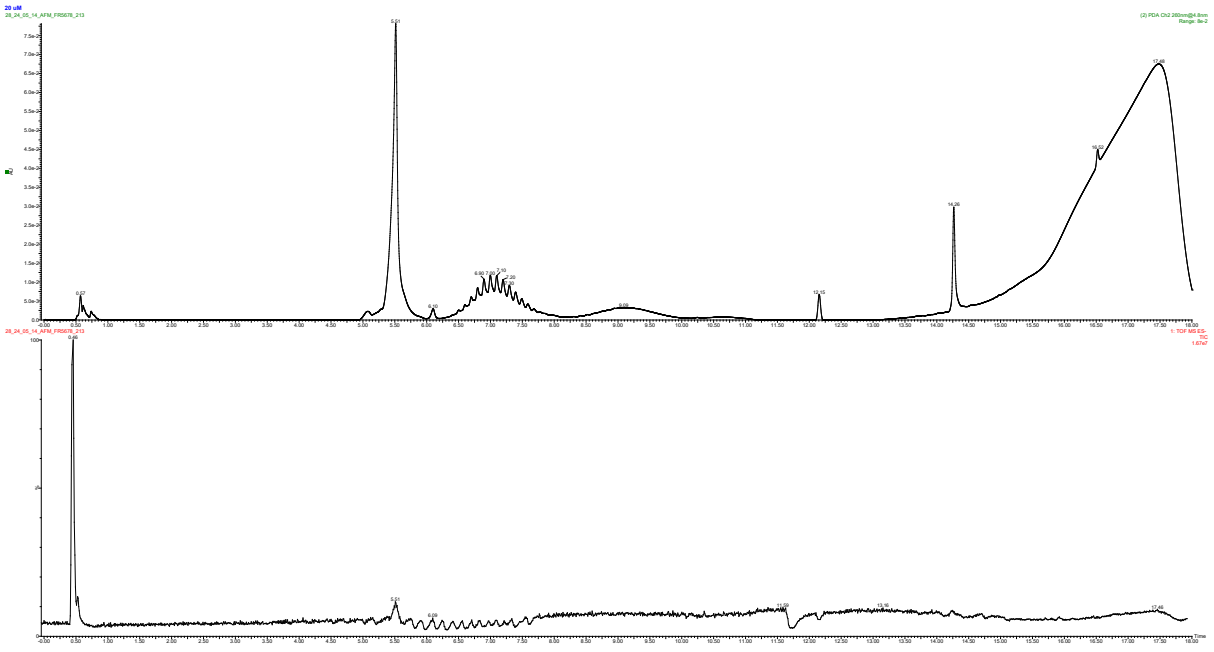

**Figure D.6: HPLC chromatogram representing the purified product from bioconjugation of sequence ON5.**

# Appendix E: **Western Blot Replicates**

The modulation of c-Myc protein levels was analysed using Western blotting to assess the impact of different sequences on endogenous c-Myc protein levels following the transfection of each sequence.

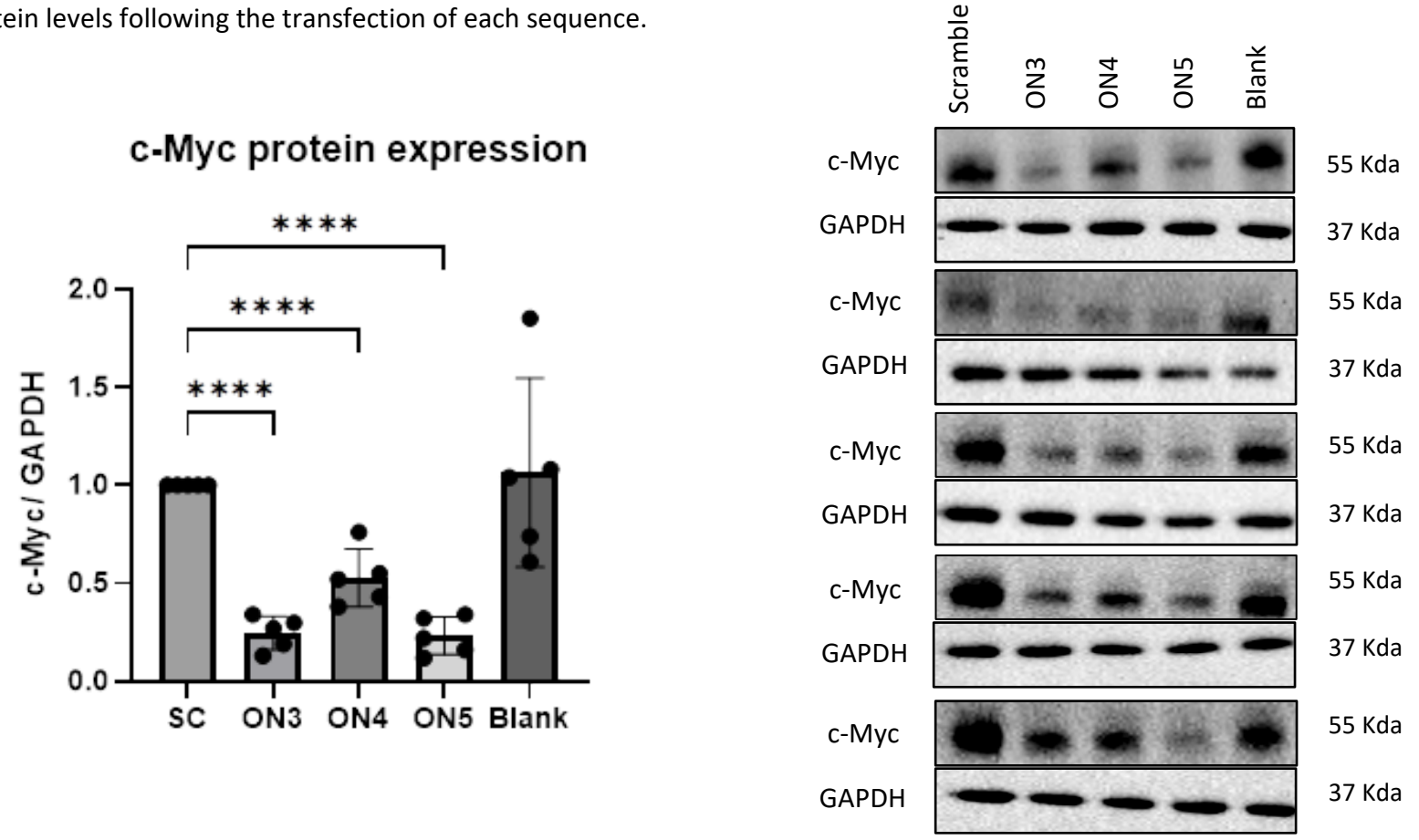


**Figure E.1: Western Blot results of HeLa cells transfected, using Lipofectamine 3000™ Reagent with a Scramble sequence, ON3, ON4 and ON5 for 24 hours.** The "Blank" control represents cells exposed to the same volume of cell culture medium as the transfection samples, but without Lipofectamine™ 3000 or ONs. The error bars represent variability within the samples. Statistical analysis was done using a one-way ANOVA with a Dunnett's multiple comparison test. Asterisks indicate the level of significance between groups: *P ≤ 0.05, **P ≤ 0.01, ***P ≤ 0.001, ****P ≤ 0.0001.

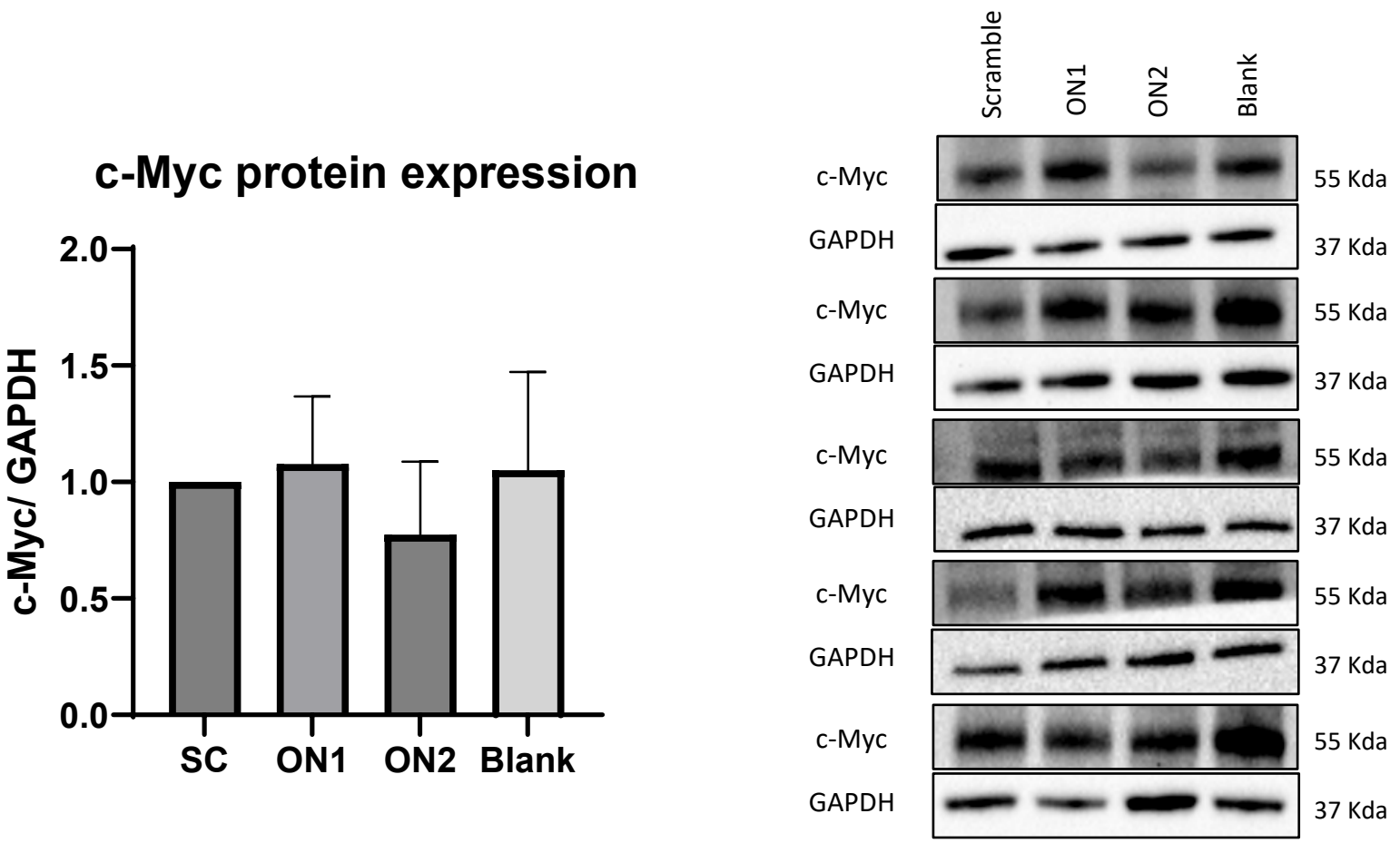


**Figure E.2: Western Blot results of HeLa cells transfected, using Lipofectamine 3000™ Reagent with a Scramble sequence, ON1, ON2 for 24 hours.** The "Blank" control represents cells exposed to the same volume of cell culture medium as the transfection samples, but without Lipofectamine™ 3000 or ONs**.** The error bars represent variability within the samples. Statistical analysis was done using a one-way ANOVA with a Dunnett's multiple comparison test. Asterisks indicate the level of significance between groups: *P ≤ 0.05, **P ≤ 0.01, ***P ≤ 0.001, ****P ≤ 0.0001.

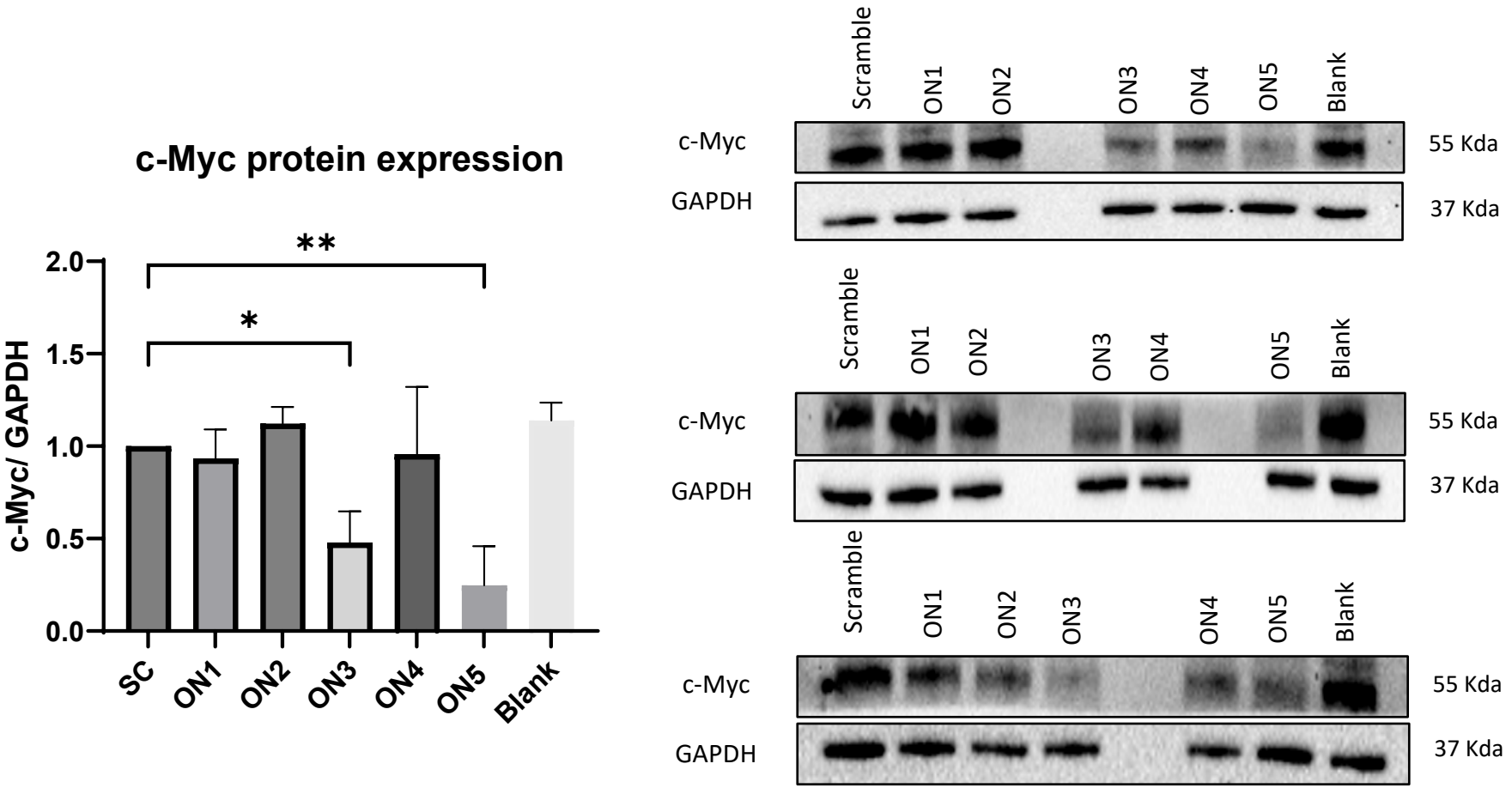


**Figure E.3: Western Blot results of HeLa cells transfected, using Lipofectamine 3000™ Reagent with a Scramble sequence, ON1, ON2, ON3, ON4 and ON5 for 48 hours.** The "Blank" control represents cells exposed to the same volume of cell culture medium as the transfection samples, but without Lipofectamine™ 3000 or ONs**.** The error bars represent variability within the samples. Statistical analysis was done using a one-way ANOVA with a Dunnett's multiple comparison test. Asterisks indicate the level of significance between groups: *P ≤ 0.05, **P ≤ 0.01, ***P ≤ 0.001, ****P ≤ 0.0001.

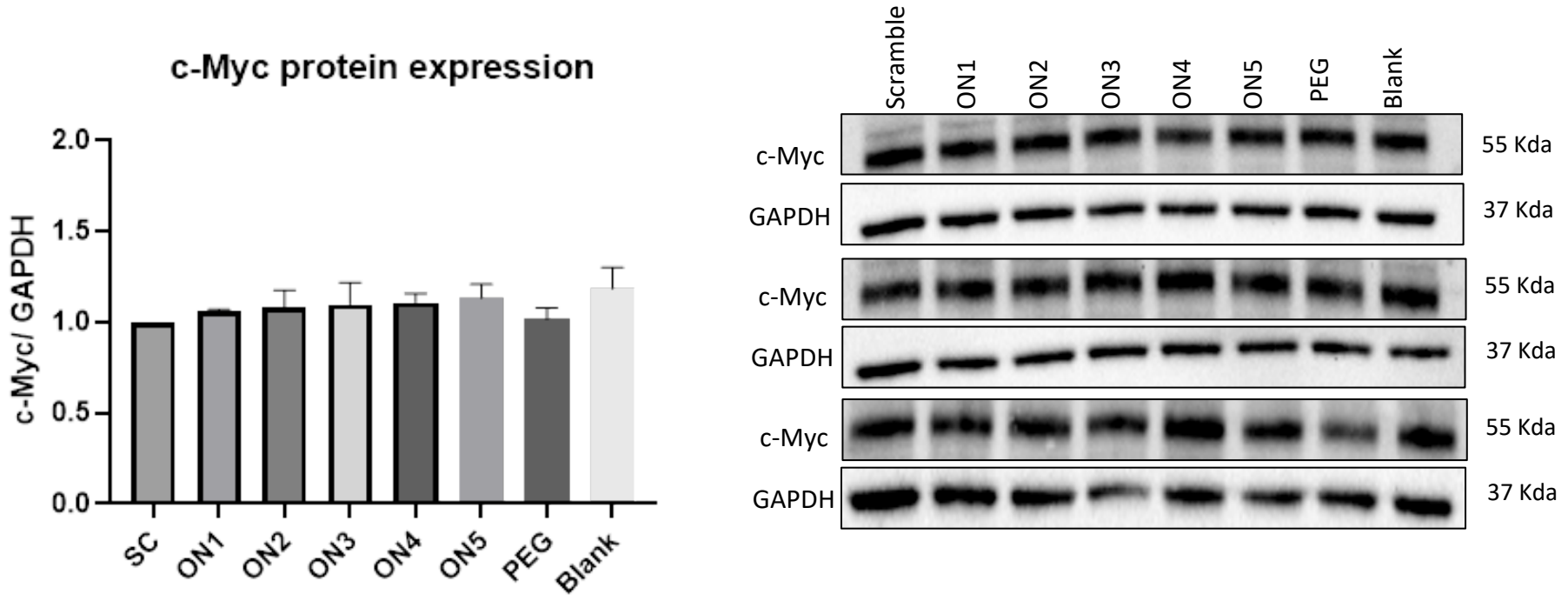


**Figure E.4: Western Blot results of HeLa cells transfected using the biofunctionalized gold nanoparticles with a Scramble sequence, ON1, ON2, ON3, ON4 and ON5 for 24 hours**. The "Blank" control represents cells exposed to the same volume of cell culture medium as the transfection samples, but without Lipofectamine™ 3000 or ONs. The error bars represent variability within the samples. Statistical analysis was done using a one-way ANOVA with a Dunnett's multiple comparison test. Asterisks indicate the level of significance between groups: *P ≤ 0.05, **P ≤ 0.01, ***P ≤ 0.001, ****P ≤ 0.0001.

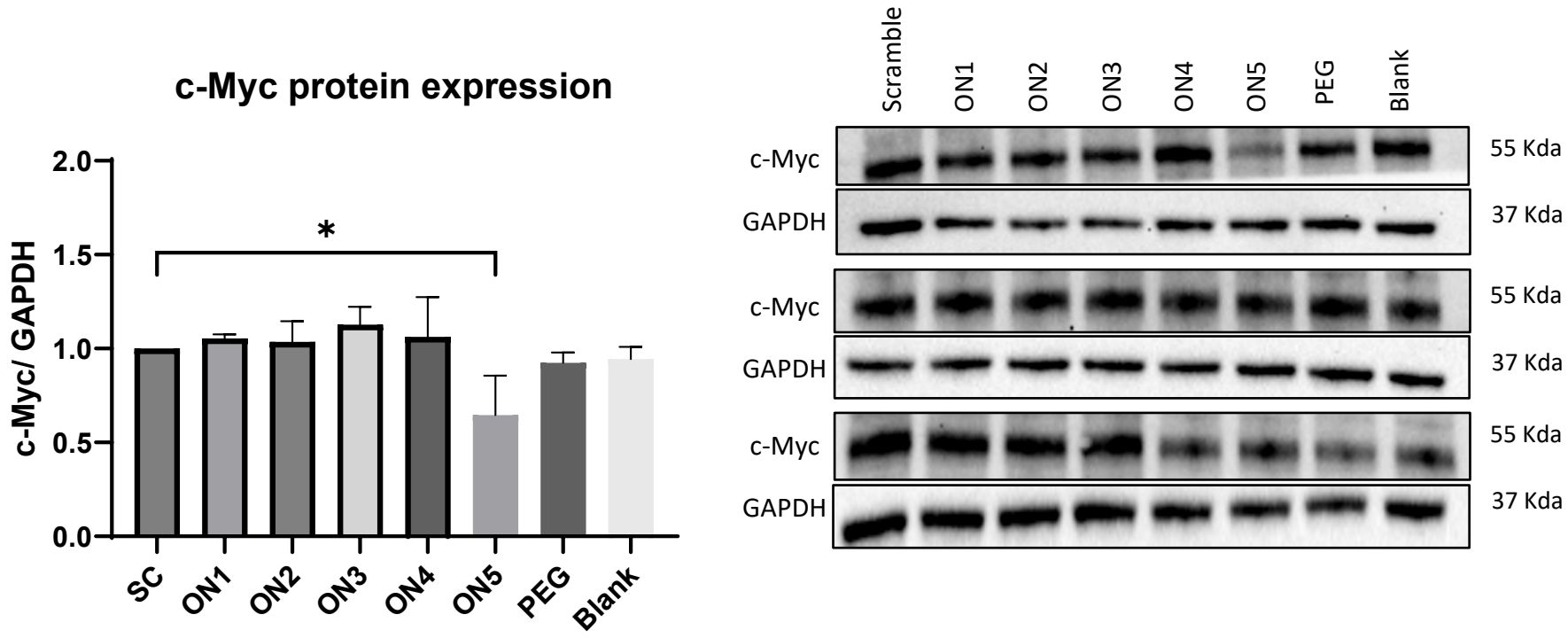


**Figure E.5: Western Blot results of HeLa cells transfected using the biofunctionalized gold nanoparticles with a Scramble sequence, ON1, ON2, ON3, ON4 and ON5 for 48 hours.** The "Blank" control represents cells exposed to the same volume of cell culture medium as the transfection samples, but without Lipofectamine™ 3000 or ONs. The error bars represent variability within the samples. Statistical analysis was done using a one-way ANOVA with a Dunnett's multiple comparison test. Asterisks indicate the level of significance between groups: *P ≤ 0.05, **P ≤ 0.01, ***P ≤ 0.001, ****P ≤ 0.0001.

# Appendix F: **RT-qPCR Replicates**

The endogenous *c-myc* mRNA levels in HeLa cells transfected with modified synthesized oligonucleotides were analysed using RT-qPCR.

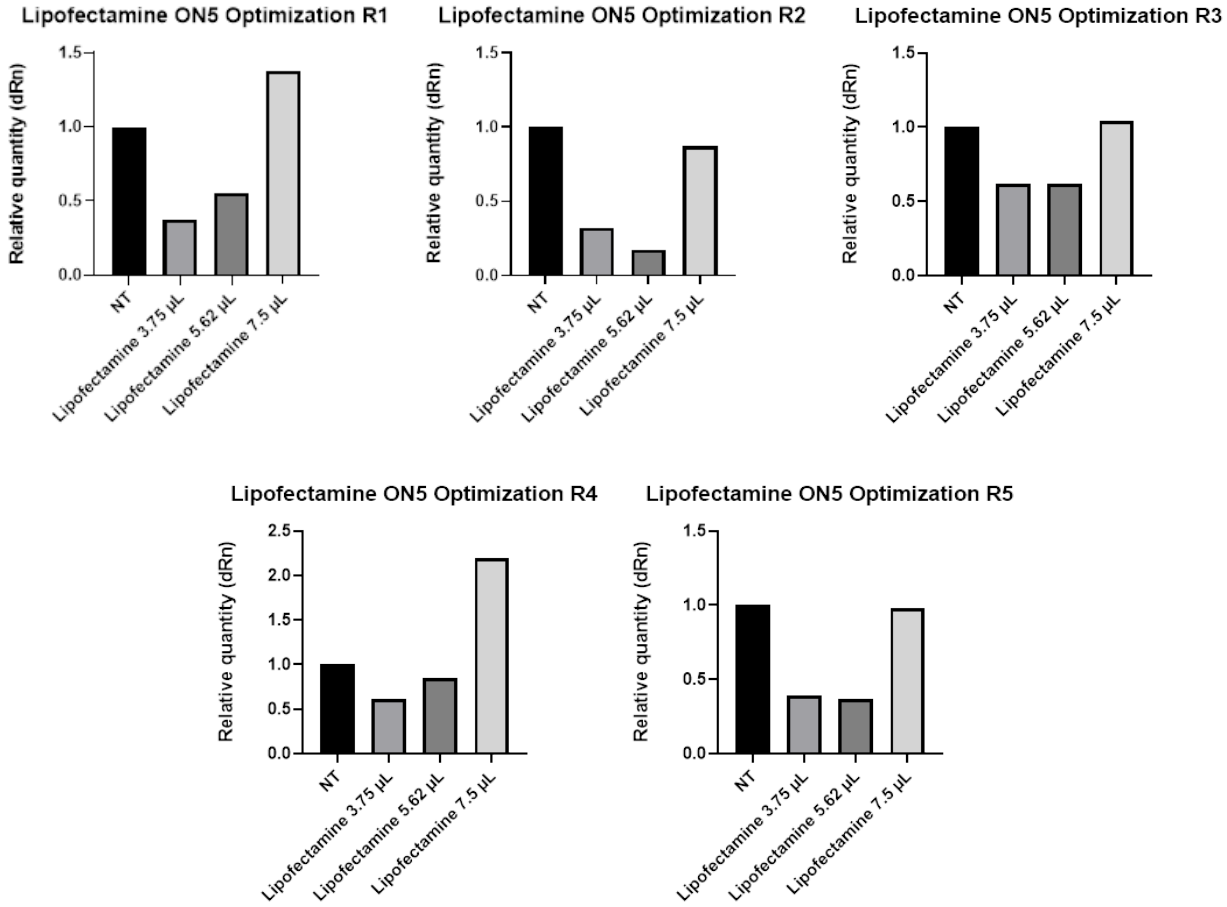


**Figure F.1: Analysis of RT-qPCR of HeLa cells transfected with ON5 using 3.75, 5.62 and 7.5 µL of Lipofectamine™ 3000 Reagent for 24 hours transfection.**

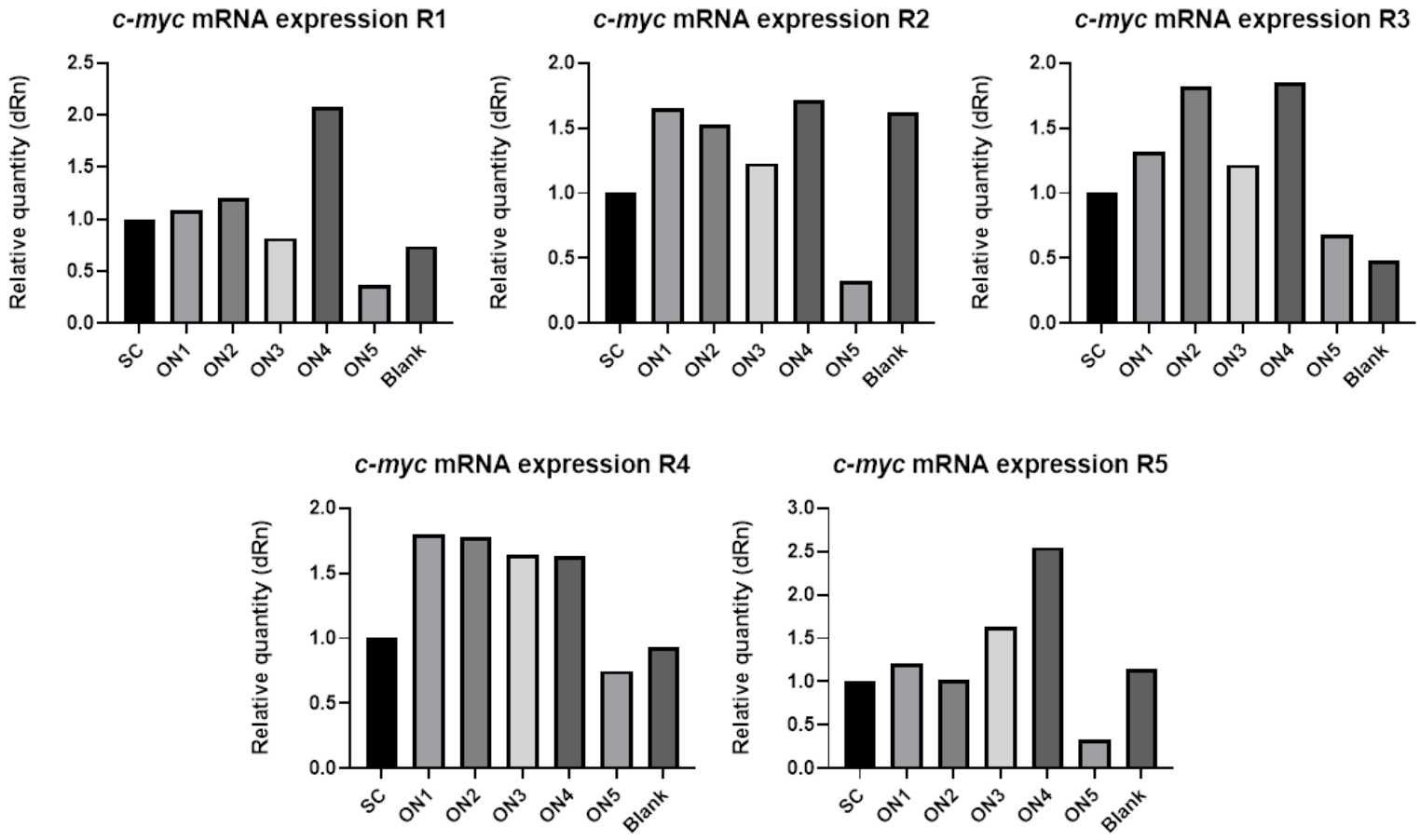


**Figure F.2: RT-qPCR results of HeLa cells transfected with Lipofectamine 3000™ Reagent using a Scramble sequence (SC), ON1, ON2, ON3, ON4, and ON5 for 24 hours.** The "Blank" control represents cells exposed to the same volume of cell culture medium as the transfection samples, but without Lipofectamine™ 3000 or ONs.

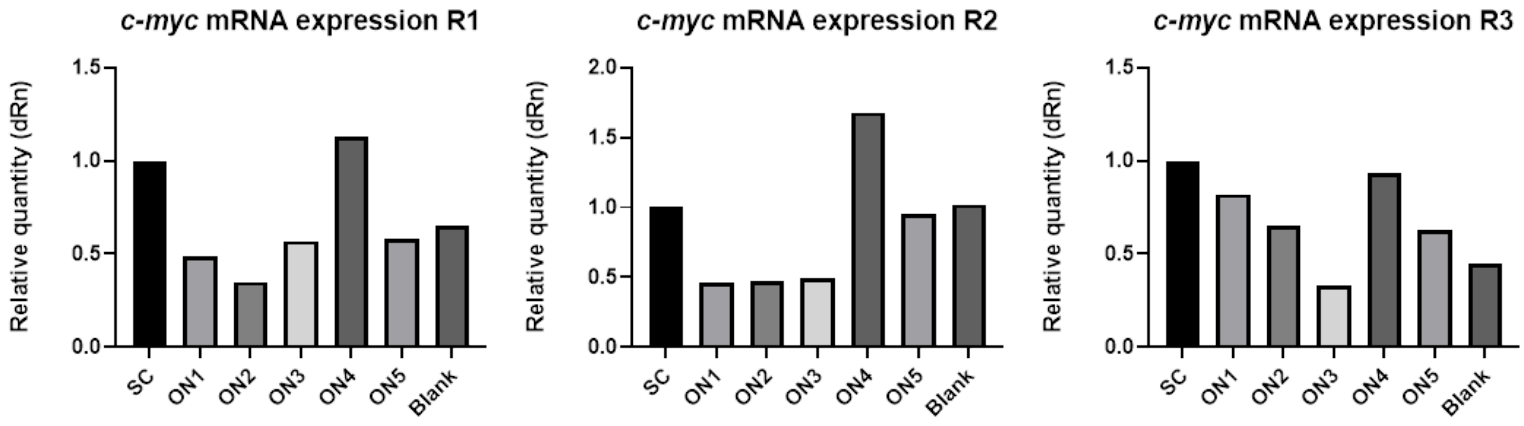


**Figure F.3: RT-qPCR results of HeLa cells transfected with Lipofectamine 3000™ Reagent using a Scramble sequence (SC), ON1, ON2, ON3, ON4, and ON5 for 48 hours.** The "Blank" control represents cells exposed to the same volume of cell culture medium as the transfection samples, but without Lipofectamine™ 3000 or ONs.

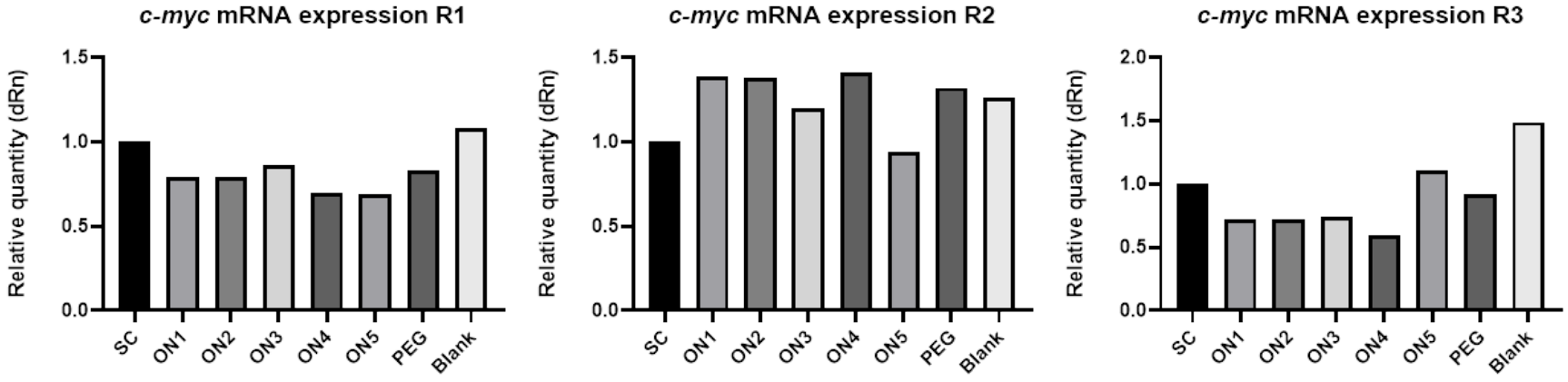


**Figure F.4: RT-qPCR results of HeLa cells transfected with Scramble sequence (SC), ON1, ON2, ON3, ON4, and ON5 biofunctionalized onto AuNP, for 24 hours.** The "Blank" control represents cells exposed to the same volume of cell culture medium as the transfection samples, but without Lipofectamine™ 3000 or ONs.

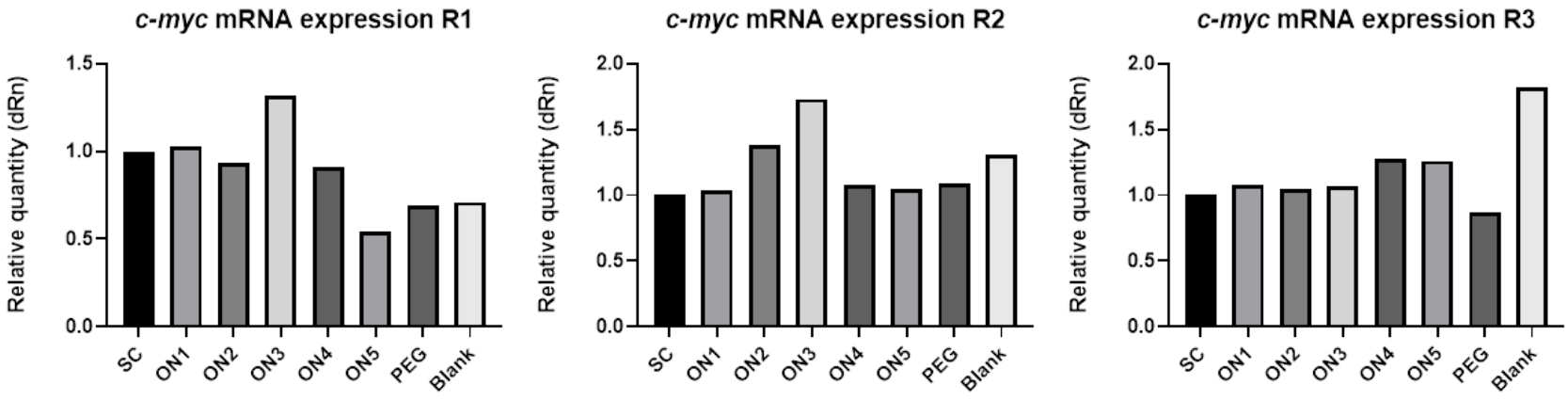


**Figure F.5: RT-qPCR results of HeLa cells transfected with Scramble sequence (SC), ON1, ON2, ON3, ON4, and ON5 biofunctionalized onto AuNP, for 48 hours.** The "Blank" control represents cells exposed to the same volume of cell culture medium as the transfection samples, but without Lipofectamine™ 3000 or ONs.

# Appendix G: **Cell Cytotoxicity Replicates**

The evaluation of the cell cytotoxicity induced by the transfection of the different sequences translated was assessed by Flow Cytometry, CyQUANT™ LDH Cytotoxicity Assay and the CellTiter 96® AQueous One Solution Cell Proliferation Assay.

**Live Control**

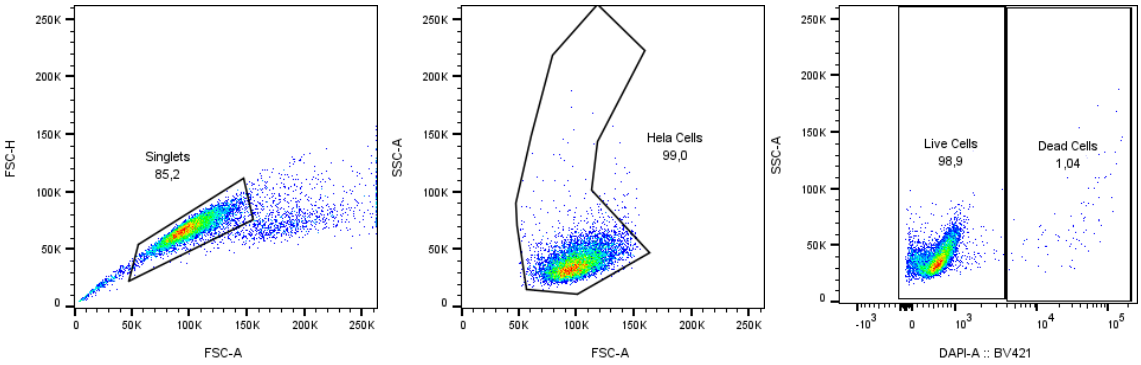


**Dead Control**

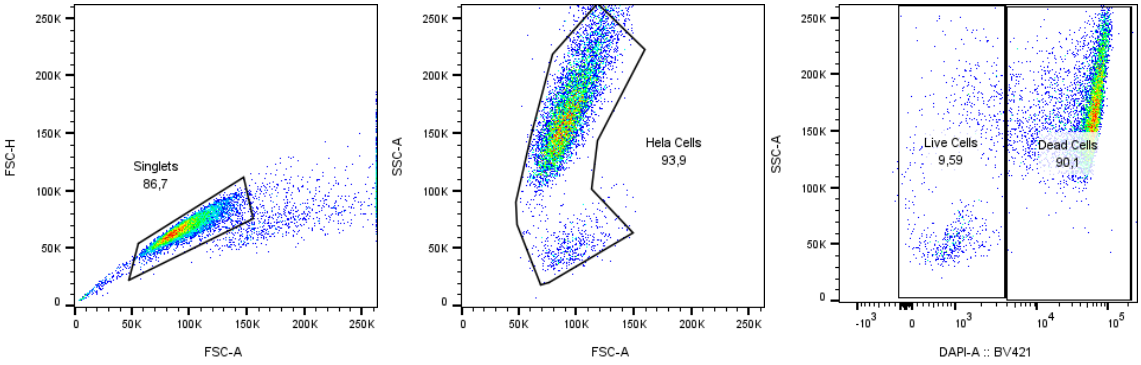


**Scramble**

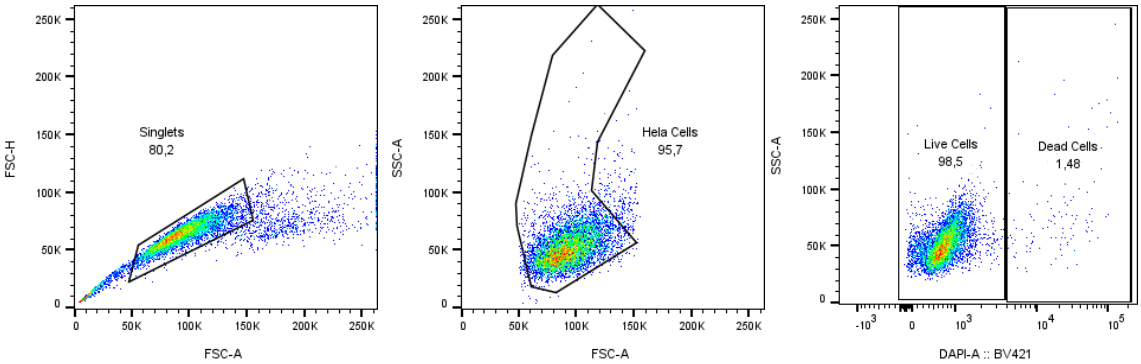

## ON1

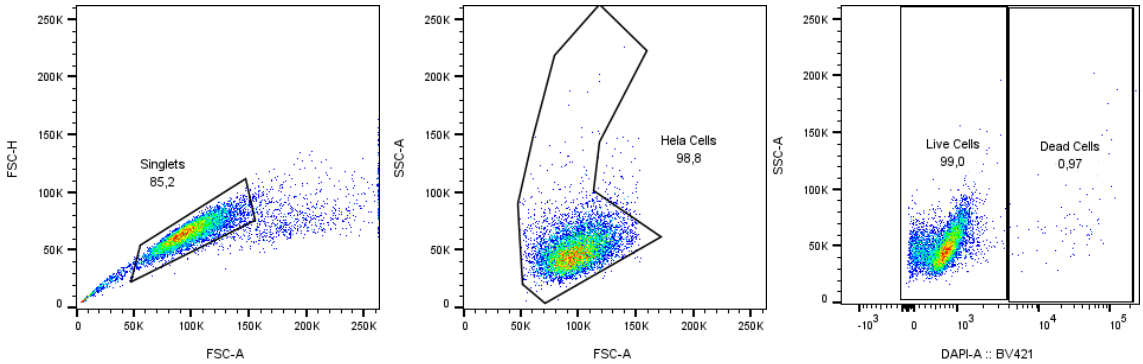


## ON2

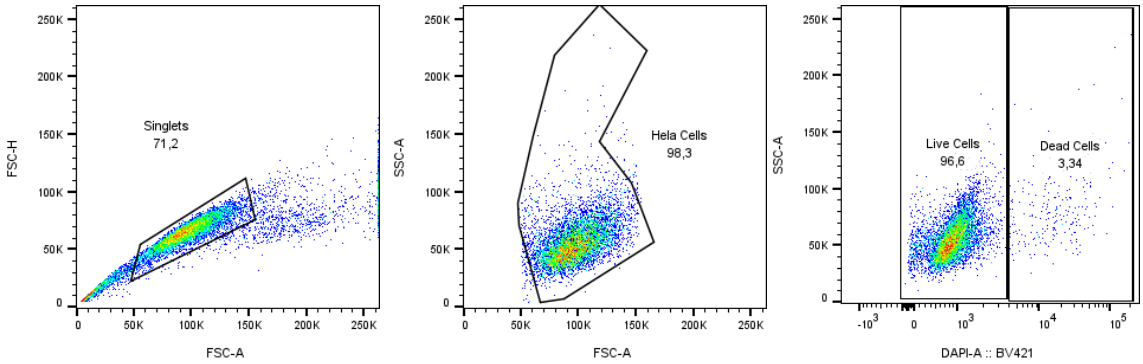


## ON3

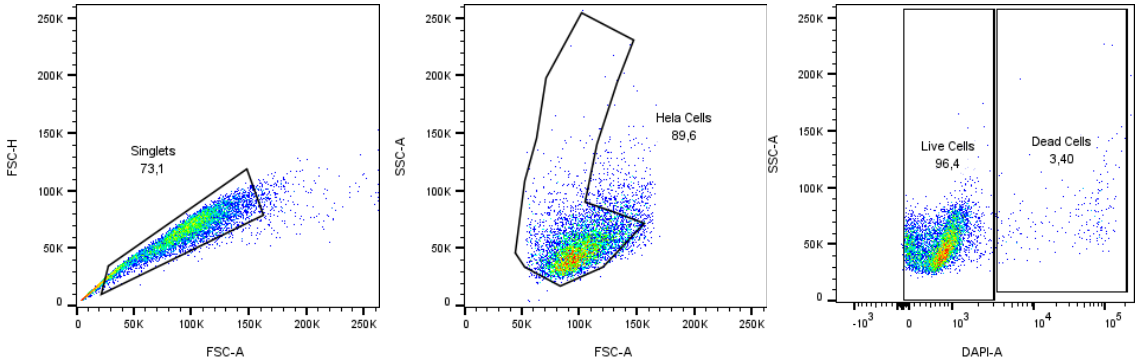


## ON4

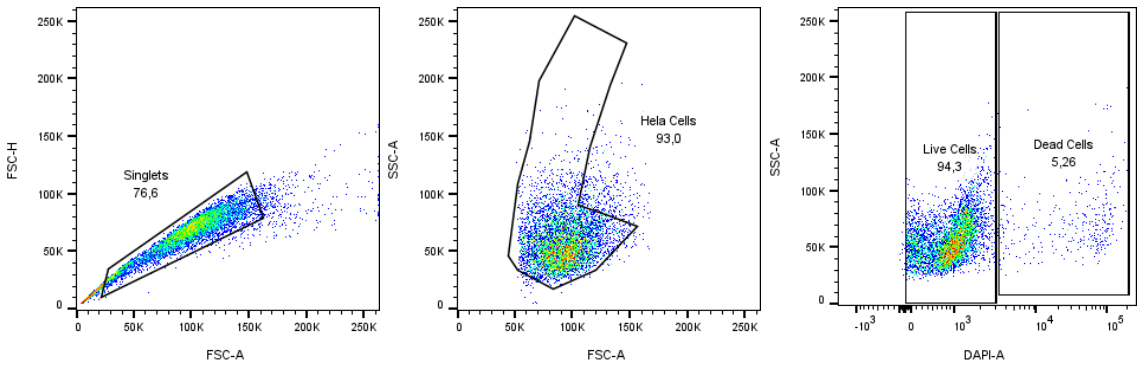

**ON5**

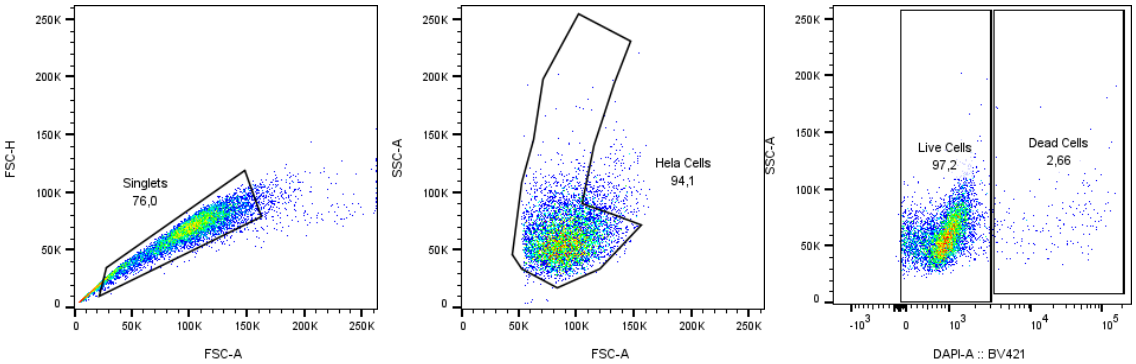


**Figure G.1: Cell cytotoxicity analysis by Flow Cytometry of HeLa cells transfected with scramble sequence, ON1, ON2, ON3, ON4, ON5 using Lipofectamine™ 3000 Reagent in a 6 well plate for 24 hours transfection.**

## Live Control

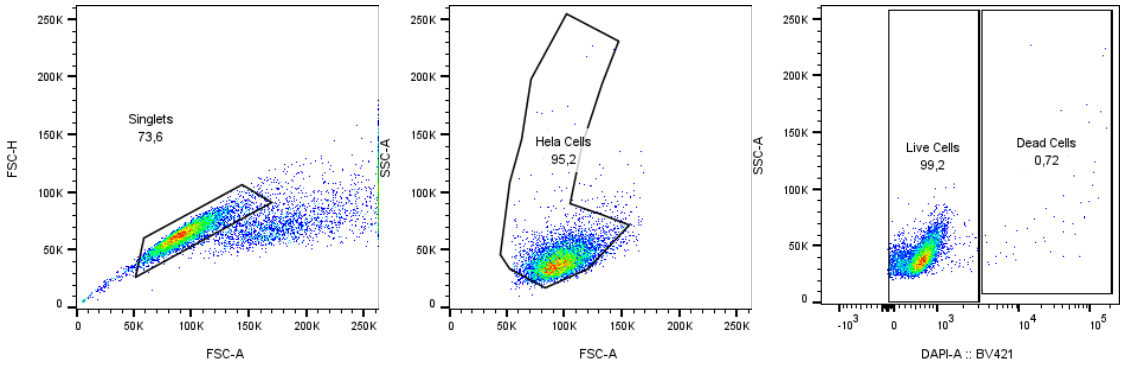


## Dead Control

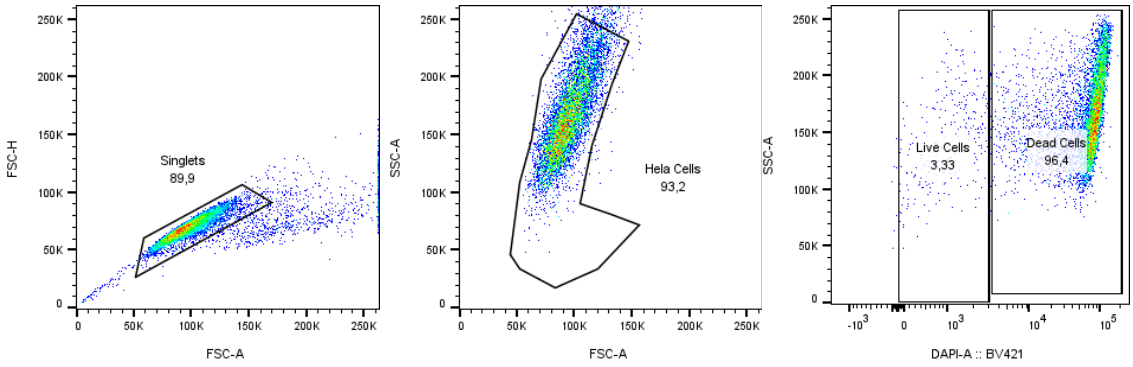


## Scramble

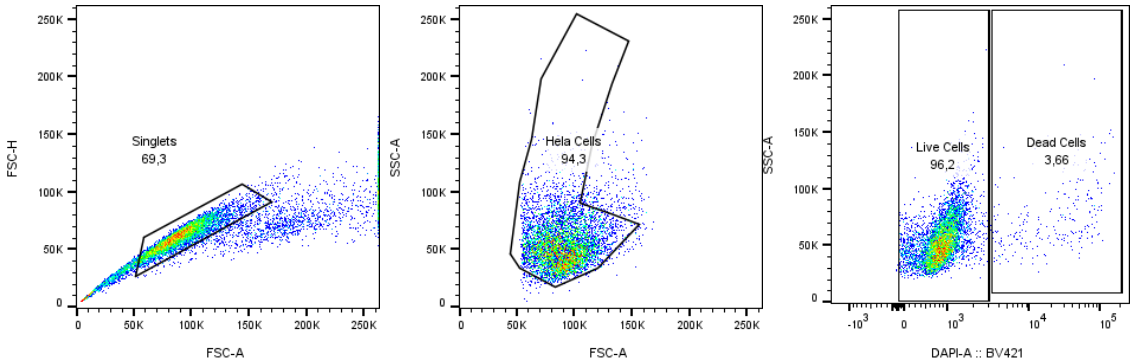


## ON1

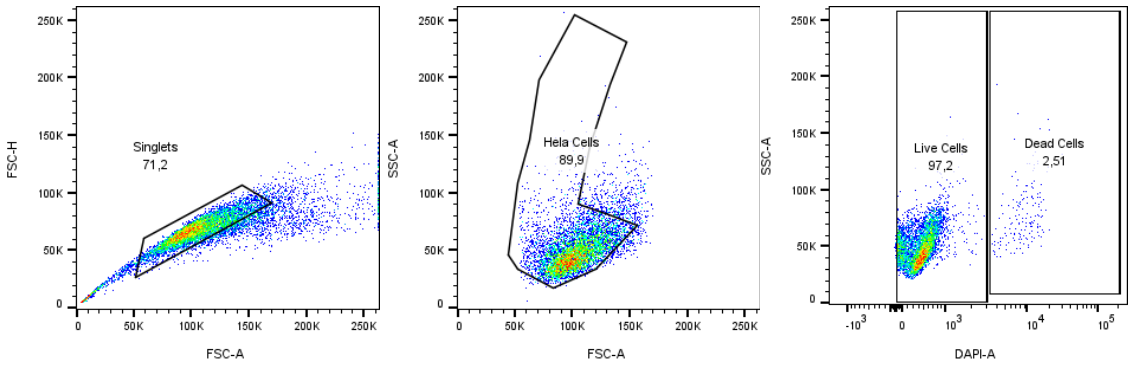

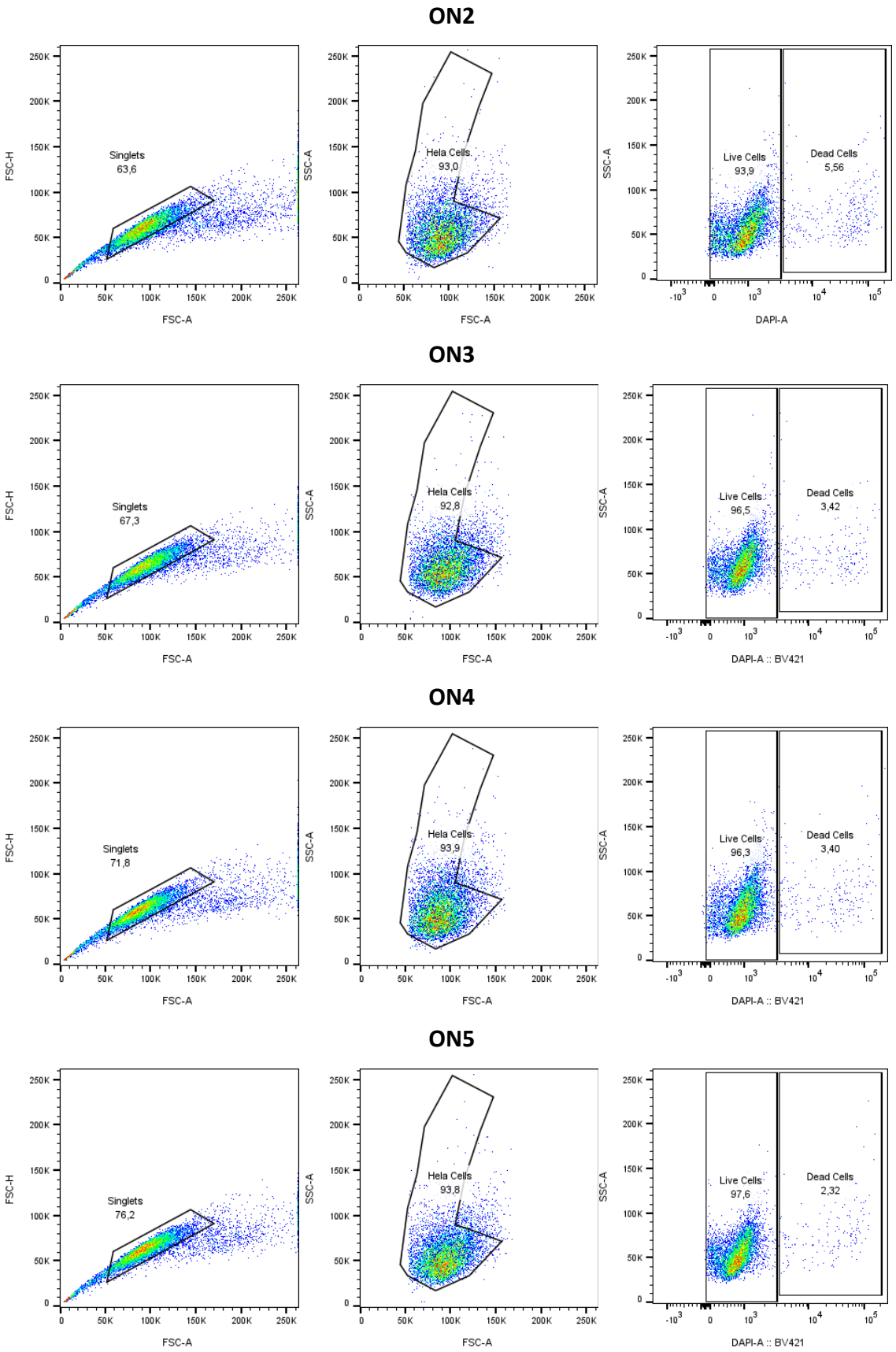


**Figure G.2: Cell cytotoxicity analysis by Flow Cytometry of HeLa cells transfected with scramble sequence, ON1, ON2, ON3, ON4, ON5 using Lipofectamine™ 3000 Reagent in a 6 well plate for 48 hours transfection.**

# Appendix H: **Confocal Microscopy Live Imaging Videos**

The cellular internalization of sequences biofunctionalized with AuNPs was analysed using confocal microscopy. Images were acquired at 15-minute intervals over a total observation period of 6 hours.

**Scramble Sequence**

6h timelapse Scr #03

6h timelapse Scr #04

6h timelapse Scr #06

6h timelapse Scr #08

**Sequence ON4**

6h timelapse ON4 #05

6h timelapse ON4 #09

6h timelapse ON4 #14

6h timelapse ON4 #15

**Sequence ON5**

6h timelapse ON5 #02

6h timelapse ON5 #03

6h timelapse ON5 #08

# Bibliography


1 F. Crick, Nature, 1970, **227**, 561–563.

2 R. Dahm, *Dev. Biol.*, 2005, **278**, 274–288.

3 G. D. Khedkar, B. Prakash, C. D. Khedkar and B. A. Chopade, *Nucleic Acids*, Elsevier, 1st edn., 2015.

4 Y. Motorin, S. Muller, I. Behm-Ansmant and C. Branlant, *Methods Enzymol.*, 2007, **425**, 21–53.

5 P. Shing Ho and M. Carter, in *DNA Replication*, 2011, pp. 1–30.

6 A. Gutierrez Aguirregabiria, PhD thesis, University of Southampton, 2019.

7 F. Crick and J. Watson, *Nature*, 1953, **171**, 737–741.

8 U. Heinemann and Y. Roske, *Symmetry*, 2020, **12**, 737.

9 M. A. Hoy, R. C. King and W. D. Stansfield, *A Dictionary of Genetics*, Oxford University Press, 1997, vol. 80.

10 H. M. Wu, N. Dattagupta and D. M. Crothers, *Proc. Natl. Acad. Sci. U.S.A.*, 1981, **78**, 6808–6811.

11 A. H. Wang, J. Quigley, G. Kolpak, F. Marel, G. Boom and J. Rich, *Cell*, 1981, **24**, 211–221.

12 E. Chargaff, R. Lipshitz and C. Green, *J. Biol. Chem*., 1952, **195**, 155–160.

13 A. B. Pradhan, L. Haque, S. Bhuiya and S. Das, *RSC Adv*., 2015 ,5

14 H. Lodish, A. Berk, C. A. Kaiser and M. Krieger, *Molecular Cell Biology*, W. H. Freeman, 8th edn., 2016.

15 B. Alberts, A. Johnson, J. Lewis, M. Raff, K. Roberts and P. Walter, *Molecular Biology of the Cell*, Garland Science, New York, 4th edn., 2002.

16 J. M. Berg, J. L. Tymoczko and L. Stryer, *Biochemistry*, W.H. Freeman, 2015.

17 G. M. Blackburn, M. Egli, M. J. Gait and J. K. Watts, (ed.), *Nucleic Acids in Chemistry and Biology*, Royal Society of Chemistry, 4th edn., 2022.

18 N. J. Proudfoot, *Genes Dev.*, 2011, **25**, 1770–1782.

19 M. C. Wahl, C. L. Will and R. Lührmann, *Cell*, 2009, **136**, 701–718.

20 C. L. Will and R. Lührmann, *Cold Spring Harb. Perspect. Biol.*, 2011, **3**, 1–2.

21 R. Alexander and D. Davies, *J. Am. Chem. Soc.*, 1956, **907**, 3548–3549.

22 A. Rich, *Proc. Natl. Acad. Sci. U. S. A.*, 1960, 1044–1053.

23 X. Xu and S.-J. Chen, *Methods Mol. Biol.*, 2015, **1316**, 1–11.

24 G. M. Blackburn, M. J. Gait, D. Loakes and D. M. Williams, *Nucleic Acids in Chemistry and Biology, 3rd edn.*, 2006.

25 M. Parisien and M. François, *J. Struct. Biol.*, 2012, **179**, 252–260.
26 F. Mignone, C. Gissi, S. Liuni and G. Pesole, *Genome Biol.*, 2002, **3**, 1–10.
27 K. Leppek, R. Das and M. Barna, *Nat. Rev. Mol. Cell Biol*. 2018, **19**, 158–174.
28 S. Xue and M. Barna, *RNA Biol.*, 2015, **12**, 1083–1087.
29 P. F. Renz, F. Valdivia Francia and A. Sendoel, *Exp. Cell Res.*, 2020, **396**, 112229.
30 Y. Chu, R. Kalantari, D. W. Dodd and D. R. Corey, *Nucleic Acid Ther.*, 2012, **22**, 147–151.
31 H. Domíniguez Moreno, G. Schotta and S. N. Richter, Nat. Commun., 2021, **12**, 3885.
32 M. K. Herndon, C. C. Quirk and J. H. Nilson, *Control of Hormone Gene Expression*, Elsevier, 7th edn., 2015, vol. 1–2.
33 E. Matoulkova, E. Michalova, B. Vojtesek and R. Hrstka, *RNA Biol.*, 2012**, 9**, 563–576.
34 A. M. Zubiaga, J. G. Belasco and M. E. Greenberg, *Mol. Cell Biol.*, 1995, **15**, 2219–2230.
35 A. S. Halees, E. Hitti, M. Al-Saif, L. Mahmoud, I. A. Vlasova-St. Louis, D. J. Beisang, P. R. Bohjanen and K. S. A. Khabar, *RNA Biol*., 2011, **8**, 681–691.
36 J. Hui, G. Reither and A. Bindereif, *RNA*, 2003, **9**, 931–936.
37 E. C. Theil and R. S. Eisenstein, *J. Biol. Chem.*, 2000, **275**, 40659–40662.
38 L. Latrèche, O. Jean-Jean, D. M. Driscoll and L. Chavatte, *Nucleic Acids Res.*, 2009, **37**, 5868–5880.
39 Y. B. Zhao and J. Krishnan, *BMC Syst. Biol.*, 2014, **8**, 25.
40 F. Buttgereit and M. D. Brand, *Biochem. J.*, 1995, **312**, 163–167.
41 N. E. Shirokikh, S. K. Archer, T. H. Beilharz, D. Powell and T. Preiss, *Nat. Protoc.*, 2017, **12**, 697–731.
42 A. A. Komar and M. Hatzoglou, *Front. Oncol.*, 2015, **5**, 1–10.
43 T. A. Karginov, D. Parviz, H. Pastor, B. L. Semler and M. Christopher, *Trends Genet.*, 2018, **33**, 129–142.
44 A. A. Komar and M. Hatzoglou, *Front. Oncol.*, 2015, **5**, 1–10.
45 A. A. Komar and M. Hatzoglou, *Cell Cycle*, 2011, **10**, 229–240.
46 R. J. Jackson, C. U.T. Hellen and T. V. Pestova, *Nat. Rev. Mol. Cell. Biol.*, 2015, **11**, 113–127.
47 M. Holcik, *Curr. Cancer Drug Targets*, 2014, **4**, 299–311.
48 M. Kozak, *Nucleic Acids Res.*, 1987, **15**, 8125–8148.
49 M. Kozak, *EMBO J.*, 1997, **16**, 2482–2492.
50 A. Unbehaun, S. I. Borukhov, C. U. T. Hellen and T. V. Pestova, *Genes Dev.*, 2004, **18**, 3078–3093.
51 T. E. Dever, J. D. Dinman and R. Green, *Cold Spring Harb. Perspect. Biol.*, 2018, **10**, 1–19.

52 R. J. Jackson, C. U. T. Hellen and T. V. Pestova, *Termination and post-termination events in eukaryotic translation*, Elsevier, 1st edn., 2012, vol. 86.

53 M. Holcik, *Curr. Cancer Drug Targets*, 2005, **4**, 299–311.

54 A. A. Komar and M. Hatzoglou, *Cell Cycle*, 2011, **10**, 229–240.

55 J. Pelletier and N. Sonenberg, *Nature*, 1988, **334**, 320–325.

56 S. Vagner, B. Galy and S. Pyronnet, *EMBO Rep.*, 2001, **2**, 893–898.

57 C. U. T. Hellen, *Biochim. Biophys. Acta Gene Regul. Mech.*, 2009, **1789**, 558–570.

58 Y. Yang and Z. Wang, *J. Mol. Cell. Biol.*, 2019, **11**, 911–919.

59 A. A. Komar, B. Mazumder and W. C. Merrick, *Gene*, 2012, **502**, 75–86.

60 A. A. Komar and M. Hatzoglou, *J. Biol. Chem.*, 2005, **280**, 23425–23428.

61 A.C. Godet, F. David, F. Hantelys, F. Tatin, E. Lacazette, B. Garmy-Susini and A.-C. Prats, Int. J. Mol. Sci., 2019, **20**, 924-

62 R. M. Young, S. J. Wang, J. D. Gordan, X. Ji, S. A. Liebhaber and M. C. Simon, *J. Biol. Chem.*, 2008, **283**, 16309–16319.

63 H. Oppermann, A. D. Levinson, H. E. Varmus, L. Levintow and J. M. Bishop, *Cell Biol.*, 1979, **76**, 1804–1808.

64 S. K. Madden, A. D. de Araujo, M. Gerhardt, D. P. Fairlie and J. M. Mason, *Mol. Cancer*, 2021, **20**, 1–18.

65 H. S. Sekhon, C. A. London, M. Sekhon, P. L. Iversen and G. R. Devi, *Lung Cancer*, 2008, **60**, 347–354.

66 L. Soucek, J. Whitfield, C. P. Martins, A. J. Finch, D. J. Murphy, N. M. Sodir, A. N. Karnezis, L. B. Swigart, S. Nasi and G. I. Evan, *Nature*, 2008, 455, 679–683.

67 C. M. Koh, A. Sabò and E. Guccione, *Bioessays*, 2016, **38**, 266–275.

68 M. Kalkat, J. De Melo, K. A. Hickman, C. Lourenco, C. Redel, D. Resetca, A. Tamachi, W. B. Tu and L. Z. Penn, *Genes (Basel)*, 2017, **8**, 2–30.

69 C. V. Dang, *Cell*, 2012, **149**, 22–35.

70 S. R. Hann and R. N. Eisenman, *Proteins Encoded by the Human c-myc Oncogene: Differential Expression in Neoplastic Cells*, 1984, vol. 4.

71 J. Stone, T. De Lange, G. Ramsay, E. Jakobovits, J. Michael Bishop, H. Varmus and W. Lee, *Definition of Regions in Human c-myc That Are Involved in Transformation and Nuclear Localization*, 1987, vol. 7.

72 C. Benassayag, L. Montero, N. Colombié, P. Gallant, D. Cribbs and D. Morello, *Mol. Cell. Biol.*, 2005, **25**, 9897–9909.

73 A. Kubickova, J. B. De Sanctis and M. Hajduch, *Int. J. Mol. Sci.*, 2023, **24**.

74 D. M. Miller, S. D. Thomas, A. Islam, D. Muench and K. Sedoris, *Clin. Cancer Res.*, 2012, **18**, 5546–5553.

75 M. Stoneley, T. Subkhankulova, J. P. C. Le Quesne, M. J. Coldwell, C. L. Jopling, G. J. Belsham and A. E. Willis, Nucleic Acids Res., 2000, **28**, 687–694.

76 C. Nanbru, I. Lafon, S. Audigier, M. C. Gensac, S. Vagner, G. Huez and A. C. Prats, *J. Biol. Chem.*, 1997, 272, 32061–32066.

77 J. P. C. Le Quesne, M. Stoneley, G. A. Fraser and A. E. Willis, *J. Mol. Biol.*, 2001, **310**, 111–126.

78 M. Stoneley and A. E. Willis, *Oncogene*, 2004, **23**, 3200–3207.

79 K. S. Frazier, *Toxicol. Pathol.*, 2015, **43**, 78–89.

80 C. Wang, J. Zhang, J. Yin, Y. Gan, S. Xu, Y. Gu and W. Huang, *Signal Transduct. Target. Ther.*, 2021, **6**, 117.

81 A. Wiegering, F. W. Uthe, T. Jamieson, Y. Ruoss, M. Huttenrauch, M. Kuspert, C. Pfann, C. Nixon, S. Herold, S. Walz, L. Taranets, C. T. Germer, A. Rosenwald, O. J. Sansom and M. Eilers, *Cancer Discov.*, 2015, **5**, 768–881.

82 S. T. Crooke, B. F. Baker, R. M. Crooke and X.-h. Liang, *Nat. Rev. Drug Discov.,* 2021, **20**, 427–453.

83 R. Kole, A. R. Krainer and S. Altman, *Nat. Rev. Drug Discov*., 2012

84 M. A. Havens and M. L. Hastings, *Nucleic Acids Res.,* 2016, **44**, 6549–6563.

85 X. Shen and D. R. Corey, *Nucleic. Acids. Res.*, 2018, **46**, 1584–1600.

86 F. Eckstein, *Nucleic. Acid. Ther.*, 2014, **24**, 374–387.

87 S. T. Crooke, T. A. Vickers and X. H. Liang, *Nucleic Acids Res.*, 2021, **48**, 5235–5253.

88 T. Chen, S. Tang, Y. Fu, J. G. Napolitano and K. Zhang, *J. Chromatogr. A.*, 2022, **1678**.

89 H. Jahns, N. Taneja, J. L. S. Willoughby, M. Akabane-Nakata, C. R. Brown, T. Nguyen, A. Bisbe, S. Matsuda, M. Hettinger, R. M. Manoharan, K. G. Rajeev, M. A. Maier, I. Zlatev, K. Charisse, M. Egli and M. Manoharan, *Nucleic Acids Res.*, 2022, **50**, 1221–1240.

90 M. E. Gleave and B. P. Monia, *Nat. Rev. Cancer.*, 2005, **5**, 468–479.

91 A. M. Quemener, L. Bachelot, A. Forestier, E. Donnou-Fournet, D. Gilot and M. D. Galibert, *Wiley Interdiscip. Rev. RNA*, 2020, **11**, 1–22.

92 M. Koziolkiewicz, E. Gendaszewska, M. Maszewska, C. A. Stein and W. J. Stec, *Blood*, 2001, **98**, 995–1002.

93 D. Venkateswarlu, K. E. Lind, V. Mohan, M. Manoharan and D. M. Ferguson, *Nucleic Acids Res.*, 1999, **27**, 2189–2195.

94 T. P. Prakash, *Chem. Biodivers.*, 2011, 8, 1616–1641.

95 A. Ray and B. Nordén, *FASEB J.*, 2000, **14**, 1041–1060.

96 A. Gupta, A. Mishra and N. Puri, *J. Biotechnol.*, 2017, **259**, 148–159.

97 F. Pellestor and P. Paulasova, *Eur. J. Hum. Genet.*, 2004, **12**, 694–700.

98 L. B. Griffin, K. E. January, K. W. Ho, K. A. Cotter and G. V. Callard, *Endocrinology*, 2013, **154**, 4158–4169.

99 A. R. Timme-Laragy, S. I. Karchner and M. E. Hahn, *Methods Mol. Biol.*, 2012, **889**, 51–71.

100 P. M. McTigue, R. J. Peterson and J. D. Kahn, *Biochemistry*, 2004, **43**, 5388–5405.

101 J. H. P. Chan, S. Lim and W. S. F. Wong, *Clin. Exp. Pharmacol. Physiol.*, 2006, **33**, 533–540.

102 D. Latorra, K. Arar and J. M. Hurley, *Mol. Cell. Probes.*, 2003, **17**, 253–259.

103 M. Christou, J. Wengel, K. Sokratous, K. Kyriacou, G. Nikolaou, L. A. Phylactou and N. P. Mastroyiannopoulos, *Nucleic. Acid. Ther.*, 2020, **30**, 80–93.

104 K. Rowel, Q. Lim, R. Maruyama, Y. Echigoya, Q. Nguyen, A. Zhang, H. Khawaja, S. Chandra, T. Jones, P. Jones, Y.-W. Chen and T. Yokota, *PNAS*, 2020, **117**, 16509–16515.

105 S. Kauppinen, B. Vester and J. Wengel, *Drug Discov. Today Technol.*, 2005, **2**, 287–290.

106 J. Elmén, M. Lindow, S. Schütz, M. Lawrence, A. Petri, S. Obad, M. Lindholm, M. Hedtjärn, H. F. Hansen, U. Berger, S. Gullans, P. Kearney, P. Sarnow, E. M. Straarup and S. Kauppinen, *Nature*, 2008, **452**, 896–899.

107 M. Alló, V. Buggiano, J. P. Fededa, E. Petrillo, I. Schor, M. De La Mata, E. Agirre, M. Plass, E. Eyras, S. A. Elela, R. Klinck, B. Chabot and A. R. Kornblihtt, *Nat. Struct. Mol. Biol.*, 2009, **16**, 717–724.

108 M. Sherman and L. Contreras, *Computational approaches in design of nucleic acid-based therapeutics*, 2017.

109 M. Rehmsmeier, P. Steffen, M. Höchsmann and R. Giegerich, *RNA*, 2004, 10, 1507–1517.

110 S. T. Crooke, *Biotechnol Genet. Eng. Rev.*, 1998, **15**, 121–158.

111 B. P. Monia, E. A. Lesnik, C. Gonzalez, W. F. Lima, D. McGee, C. J. Guinosso, A. M. Kawasaki, P. Dan Cook and S. M. Freier, *J. Biol. Chem.,* 1993, **268**, 14514–14522.

112 A. A. Koshkin, S. K. Singh, P. Nielsen, V. K. Rajwanshi, R. Kumar, M. Meldgaard, C. E. Olsen and J. Wengel, *LNA (Locked Nucleic Acids): Synthesis of the Adenine, Cytosine, Guanine, 5-Methylcytosine, Thymine and Uracil Bicyclonucleoside Monomers, Oligomerisation, and Unprecedented Nucleic Acid Recognition*, 1998, vol. 54.

113 C. F. Bennett and E. E. Swayze, *Annu. Rev. Pharmacol. Toxicol.*, 2010, **50**, 259–293.

114 J. H. Kim, J. H. Yeom, J. J. Ko, M. S. Han, K. Lee, S. Y. Na and J. Bae, *J. Biotechnol.*, 2011, **155**, 287–292.

115 J. Torrecilla, A. Rodríguez-Gascón, M. Á. Solinís and A. del Pozo-Rodríguez, BioMed. Res. Int., 2014, **2014**, 161794.

116 U. S. Haque and T. Yokota, *Cells*, 2023, **12**.

117 A. D. Springer and S. F. Dowdy, *Nucleic Acid Ther.*, 2018, **28**, 109–118.

118 T. Iannitti, J. C. Morales-Medina and B. Palmieri, *Curr. Drug Targets*, 2014, **15**, 1–11.

119 S. McDowall, M. Aung-Htut, S. Wilton and D. Li, *Front. Neurosci.*, 2024.

120 A. Dieckmann, P. H. Hagedorn, Y. Burki, C. Brügmann, M. Berrera, M. Ebeling, T. Singer and F. Schuler, *Mol. Ther. Nucleic Acids*, 2018, **10**, 45–54.

121 S. Michel, K. Schirduan, Y. Shen, R. Klar, J. Tost and F. Jaschinski, *Mol. Diagn. Ther.*, 2021, **25**, 77–85.

122 L. V Varga, S. Tó, I. Novák and A. Falus, *Antisense strategies: functions and applications in immunology*, 1999, vol. 69.

123 S. P. Henry, M. A. Jagels, T. E. Hugli, S. Manalili, R. S. Geary, P. C. Giclas and A. A. Levin, *Nucleic Acid Ther.*, 2014, **24**, 326–335.

124 K. S. Frazier, *Toxicol. Pathol.*, 2015, **43**, 78–89.

125 H. Wu, A. Wahane, F. Alhamadani, K. Zhang, R. Parikh, S. W. Lee, E. M. McCabe, T. P. Rasmussen, R. Bahal, X. B. Zhong and J. E. Manautou, *Curr. Opin. Toxicol.*, 2022, **32**.

126 A. Zaslavsky, M. Adams, X. Cao, A. Yamaguchi, J. Henderson, P. Busch-Østergren, A. Udager, S. Pitchiaya, B. Tourdot, T. Kasputis, S. J. Church, S. K. Lee, S. Ohl, S. Patel, T. M. Morgan, A. Alva, T. W. Wakefield, Z. Reichert, M. Holinstat and G. S. Palapattu, *Thromb. Res.*, 2021, **200**, 64–71.

127 K. S. Frazier, *Toxicol. Pathol.*, 2015, **43**, 78–89.

128 H. Lightfoot, A. Schneider and J. Hall, in *Oligonucleotide-Based Drugs and Therapeutics*, Wiley, 2018, pp. 107–136.

129 J. M. Migliorati, S. Liu, A. Liu, A. Gogate, S. Nair, R. Bahal, T. P. Rasmussen, J. E. Manautou and X. B. Zhong, *Drug Metab. Dispos.*, 2022, 50, 888–897.

130 B. R. Leavitt, P. R. Cullis and R. van der Meel, *Nat. Nanotechnol.*, 2021, **16**, 630–643.

131 C. A. Stein and D. Castanotto, *Mol. Ther.*, 2017, **25**, 1069–1075.

132 K. P. Anderson, M. C. Fox, V. Brown-Driver, M. J. Martin and R. F. Azad, *Inhibition of Human Cytomegalovirus Immediate-Early Gene Expression by an Antisense Oligonucleotide Complementary to Immediate-Early RNA*, 1996, vol. 40.

133 F. Fogacci, N. Ferri, P. P. Toth, M. Ruscica, A. Corsini and A. F. G. Cicero, *Drugs*, 2019, **79**, 751–766.

134 O. Sheikh and T. Yokota, *Arch. Toxicol.*, 2022, **96**.

135 V. Maharshi and S. Hasan, *Clin. Drug. Investig.*, 2017, **37**, 807–817.

136 L. Gales, *Pharmaceuticals*, 2019, **12**.

137 G. Eser and H. Topaloğlu, *Genes (Basel)*, 2022, **13**.

138 P. R. Clemens, V. K. Rao, A. M. Connolly, A. D. Harper, J. K. Mah, E. C. Smith, C. M. McDonald, C. M. Zaidman, L. P. Morgenroth, H. Osaki, Y. Satou, T. Yamashita and E. P. Hoffman, *JAMA Neurol.*, 2020, **77**, 982–991.

139 S. Takeda, P. R. Clemens and E. P. Hoffman, *J. Neuromuscul. Dis.*, 2021, **8**, S343–S358.

140 L. J. Scott, *Drugs*, 2020, **80**, 335–339.

141 Y. Y. Syed, *Drugs*, 2021, **81**, 841–848.

142 P. Cochat and G. Rumsby, *N. Engl. J. Med.*, 2013, **369**, 649–658.

143 I. Khan, K. Saeed and I. Khan, *Arab. J. Chem.*, 2019, **12**, 908–931.

144 P. Sabourian, G. Yazdani, S. S. Ashraf, M. Frounchi, S. Mashayekhan, S. Kiani and A. Kakkar, *Int. J. Mol. Sci.*, 2020, **21**, 1–20.

145 A. M. Ealias and M. P. Saravanakumar, *IOP Conf. Ser. Mater. Sci. Eng.*, 2017, **263**, 0–15.

146 J. Jeevanandam, A. Barhoum, Y. S. Chan, A. Dufresne and M. K. Danquah, *Beilstein J. Nanotechnol.*, 2018, **9**, 1050–1074.

147 Y.-H. Luo, L. W. Chang and P. Lin, *BioMed. Res. Int.,* 2015, **2015**, 143720.

148 D. Singh, S. Singh, J. Sahu, S. Srivastava and M. R. Singh, *Artif. Cells Nanomed. Biotechnol.*, 2016, **44**, 401–409.

149 M. Kumar, I*nt. J. Appl. Eng. Res.*, 2019, **14**, 491–494.

150 A. Zielińska, F. Carreiró, A. M. Oliveira, A. Neves, B. Pires, D. N. Venkatesh, A. Durazzo, M. Lucarini, P. Eder, A. M. Silva, A. Santini and E. B. Souto, *Molecules*, 2020, *25*, 3731,

151 X. Hou, T. Zaks, R. Langer and Y. Dong, *Nat. Rev. Mater.*, 2021, **6,** 1078–1094.

152 J. Krishna, A. S. Perumal, I. Khan, R. Chelliah, S. Wei, C. M. A. Swamidoss and B. Bharathiraja, *Synthesis of nanomaterials for biofuel and bioenergy applications*, INC, 2021.

153 F. Ahmad, M. M. Salem-bekhit, F. Khan, S. Alshehri and A. Khan, *Nanomaterials*, 2022, **12**, 1333.

154 L. Thangavelu, A. H. Adil, S. Arshad, E. Devaraj, S. K. Mallineni, R. Sajja, A. Chakradhar and M. I. Karobari, *J. Nanomater.,* 2021, **2021**, 1–15.

155 K. M. Mayer and J. H. Hafner, *Chem. Rev.*, 2011, **111**, 3828–3857.

156 K. A. Willets and R. P. Van Duyne, *Annu. Rev. Phys. Chem.*, 2007, **58**, 267–297.

157 V. A. G. Rivera, F. A. Ferri and E. Marega, in *Plasmonics - Principles and Applications*, 2012.

158 K. T. Yong, Y. Sahoo, M. T. Swihart and P. N. Prasad, *Colloids Surf. A. Physicochem. Eng. Asp.*, 2006, **290**, 89–105.

159 J. A. Zamora-Justo, P. Abrica-González, G. R. Vázquez-Martínez, A. Muñoz-Diosdado, J. A. Balderas-López and M. Ibáñez-Hernández, J. Nanomater., 2019, **2019**, 1–12.

160 M. J. Mitchell, M. M. Billingsley, R. M. Haley, M. E. Wechsler, N. A. Peppas and R. Langer, *Nat. Rev. Drug. Discov.*, 2021, **20**, 101–124.

161 E. C. Dreaden, L. A. Austin, M. A. MacKey and M. A. El-Sayed, *Ther. Deliv.*, 2012, **3**, 457–478.

162 I. A. Mohammed and F. J. Al-Gawhari, *Syst. Rev. Pharm.,* 2020, **11**, 888–910.

163 E. C. Dreaden, L. A. Austin, M. A. Mackey and M. A. El-Sayed, *Ther. Deliv.*, 2012, **3**, 457–478.

164 S. B. Yaqoob, R. Adnan, R. M. Rameez Khan and M. Rashid, *Front. Chem.*, 2020, **8**, 1–15.

165 W. Weecharangsan, P. Opanasopit, T. Ngawhirunpat, T. Rojanarata and A. Apirakaramwong, *AAPS PharmSciTech.*, 2006, **7**, 8–13.

166 A. Reznickova, P. Slepicka, N. Slavikova, M. Staszek and V. Svorcik, *Colloids Surf. A. Physicochem. Eng. Asp.*, 2017, **523**, 91–97.

167 Y. Hatakeyama, J. I. Kato, T. Mukai, K. Judai and K. Nishikawa, *Bull. Chem. Soc. Jpn.*, 2014, **87**, 773–779.

168 L. E. Van Vlerken, T. K. Vyas and M. M. Amiji, *Pharm. Res.*, 2007, **24**, 1405–1414.

169 K. E. Sapsford, W. R. Algar, L. Berti, K. B. Gemmill, B. J. Casey, E. Oh, M. H. Stewart and I. L. Medintz, *Chem. Rev.*, 2013, **113**, 1904–2074.

170 A. Hoeben, E. A. J. Joosten and M. H. J. van den Beuken-Van Everdingen, *Cancers (Basel)*, 2021, **13**, 1–3.

171 D. Jiaqi, C. Paul L., P. Georgios, D. Phillip and M. Brij M., *Physiol. Behav.*, 2016, **176**, 100–106.

172 A. Soni, Y. Gautam, I. Kumar, C. Kumari, M. Devi and Y. Yamini, *Int. J. Pharm. Sci. Rev. Res.*, 2023, **79**(2), 227–243

173 P. Mathur, S. Jha, S. Ramteke and N. K. Jain, *Artif. Cells Nanomed. Biotechnol.,* 2018, **46**, 115–126.

174 S. Simon, N. R. S. Sibuyi, A. O. Fadaka, S. Meyer, J. Josephs, M. O. Onani, M. Meyer and A. M. Madiehe, *Biomedicines*, 2022, **10**, 2792.

175 M. Todorova, M. Milusheva, L. Kaynarova, D. Georgieva, V. Delchev, S. Simeonova, B. Pilicheva and S. Nikolova, *Biomedicines*, 2023, 11, 1593.

176 G. Sanità, B. Carrese and A. Lamberti, Front. Mol. Biosci., 2020, **7**, 587012.

177 S. Wojtysiak and A. Kudelski, *Colloids Surf. A. Physicochem. Eng. Asp.*, 2012, **410**, 45–51.

178 P. C. Lee and D. Meisel, J. Phys. Chem., 1982, **86**, 3391–3395.

179 J. Groll and M. Moeller, in *Encyclopedia of Biophysics*, ed. G. C. K. Roberts, Springer, Berlin, Heidelberg, 2013, pp. 2531–2536.

180 V. Maggi, F. Bianchini, E. Portioli, S. Peppicelli, M. Lulli, D. Bani, R. Del Sole, F. Zanardi, A. Sartori and R. Fiammengo, *Chem. Eur. J.*, 2018, **24**, 12093–12100.

181 G. Mohamad Sadeghi, *Int. J. Nanomater. Nanotechnol. Nanomed.*, 2017, **2**, 001–006.

182 J. S. Suk, Q. Xu, N. Kim, J. Hanes and L. M. Ensign, *Adv. Drug. Deliv. Rev.*, 2016, **99**, 28–51.

183 G. Zhang, Z. Yang, W. Lu, R. Zhang, Q. Huang, M. Tian, L. Li, D. Liang and C. Li, *Biomaterials*, 2009, **30**, 1928–1936.

184 Y. Wang, J. E. Q. Quinsaat, T. Ono, M. Maeki, M. Tokeshi, T. Isono, K. Tajima, T. Satoh, S. ichiro Sato, Y. Miura and T. Yamamoto, *Nat. Commun.*

185 K. Kozics, M. Sramkova, K. Kopecka, P. Begerova, A. Manova, Z. Krivosikova, Z. Sevcikova, A. Liskova, E. Rollerova, T. Dubaj, V. Puntes, L. Wsolova, P. Simon, J. Tulinska and A. Gabelova, *Nanomaterials*, 2021, **11**, 1–17.

186 P. Talarska, M. Boruczkowski and J. Żurawski, *Nanomaterials*, 2021, **11**, 2454.

187 N. Desai, AAPS J., 2012, **14**, 282–295.

188 K. Alaqad and T. A. Saleh, J. Environ. Anal. Toxicol., 2016, **6**, 384.

189 O. V Matveeva, D. H. Mathews, A. D. Tsodikov, S. A. Shabalina, R. F. Gesteland, J. F. Atkins and S. M. Freier, *Nucleic Acids Res.*, 2003, **31**, 4989–4994.

190 T. Andrian, S. Pujals and L. Albertazzi, *Nanoscale Adv.*, 2021, **3**, 6876–6881.

191 M. Vita and M. Henriksson, *Semin. Cancer Biol.*, 2006, **16**, 318–330.

192 J. Conde, J. Rosa, J. M. de la Fuente and P. V. Baptista, *Biomaterials*, 2013, **34**, 2516–2523.

193 E. C. Dreaden, A. M. Alkilany, X. Huang, C. J. Murphy and M. A. El-Sayed, *Chem. Soc. Rev.*, 2012, **41**, 2740–2779.

194 N. L. Rosi, D. A. Giljohann, C. S. Thaxton, A. K. R. Lytton-Jean, M. S. Han and C. A. Mirkin, *Science*, 2006, **312**, 1027–1030.

195 M. Stoneley, F. E. Paulin, J. Pc, L. Quesne, S. A. Chappell and A. E. Willis, *Oncogene*, 1998, **16**, 423–428.

196 J. C. C. Hsu, J. B. Pawlak, M. Laurent-Rolle and P. Cresswell, *STAR Protoc.*, 2022, **3**.

197 J. Schindelin, I. Arganda-Carreras, E. Frise, V. Kaynig, M. Longair, T. Pietzsch, S. Preibisch, C. Rueden, S. Saalfeld, B. Schmid, J.-Y. Tinevez, D. J. White, V. Hartenstein, K. Eliceiri, P. Tomancak and A. Cardona, *Nat. Methods*, 2012, **9**, 676–682.

198 K. Zagorovsky, L. Y. T. Chou and W. C. W. Chan, *PNAS*, 2016, **113**, 13600–13605.

199 A. M. Winkelsas, C. Grunseich, G. G. Harmison, K. Chwalenia, C. Rinaldi, S. M. Hammond, K. Johnson, M. Bowerman, S. Arya, K. Talbot, M. J. Wood and K. H. Fischbeck, *Mol. Ther. Nucleic Acids*, 2021, **23**, 731–742.

200 X. H. Liang, H. Sun, W. Shen, S. Wang, J. Yao, M. T. Migawa, H. H. Bui, S. S. Damle, S. Riney, M. J. Graham, R. M. Crooke and S. T. Crooke, *Nucleic Acids Res.*, 2017, **45**, 9528–9546.

201 X. H. Liang, J. G. Nichols, C. W. Hsu, T. A. Vickers and S. T. Crooke, *Nucleic Acids Res.*, 2019, **47**, 6900–6916.

202 X. H. Liang, J. G. Nichols, C. L. de Hoyos and S. T. Crooke, *Nucleic Acids Res.*, 2020, **48**, 9840–9858.

203 T. A. Vickers and S. T. Crooke, *PLoS One*, 2014, **9**.

204 A. J. Ward, M. Norrbom, S. Chun, C. F. Bennett and F. Rigo, *Nucleic Acids Res.*, 2014, **42**, 5871–5879.

205 X. Ren, Z. Zhang, J. Tian, H. Wang, G. Song, Q. Guo, J. Tian, Y. Han, Q. Liao, G. Liu, H. Ding and G. Jiang, *Oncol. Lett.*, 2017, **14**, 6833–6840.

206 M. F. Zacarías-Fluck, L. Soucek and J. R. Whitfield, *Front. Cell Dev. Biol.*, 2024, **12**.

207 Z. Niu, H. Liu, M. Zhou, H. Wang, Y. Liu, X. Li, W. Xiong, J. Ma, X. Li and G. Li, *Acta. Biochim. Biophys. Sin. (Shanghai)*, 2015, **47**, 183–191.

208 C. V Dang, *c-Myc Target Genes Involved in Cell Growth*, 1999, vol. 19.

209 H. Okuyama, H. Endo, T. Akashika, K. Kato and M. Inoue, *Cancer Res.*, 2010, **70**, 10213–10223.

210 H. Wang, S. Mannava, V. Grachtchouk, D. Zhuang, M. S. Soengas, A. V. Gudkov, E. V. Prochownik and M. A. Nikiforov, *Oncogene*, 2008, **27**, 1905–1915.

211 P. L. Boyer, S. J. Smith, X. Z. Zhao, K. Das, K. Gruber, E. Arnold, T. R. Burke, Jr. and S. H. Hughes, *J. Virol*., 2018, **92**

212 X. Hou, T. Zaks, R. Langer and Y. Dong, *Nat. Rev. Mater*., 2021, **6**, 1078–1094.

213 Mendonça, M. C. P., Kont, A., Rodriguez Aburto, M., Cryan, J. F., and O'Driscoll, C. M, *Mol. Pharmaceutics*, 2021, **18**, 1491–1506.

214 Sristi, W. H. Almalki, R. Karwasra, G. Gupta, S. Singh, A. Sharma, A. Sahebkar and P. Kesharwani, in *Progress in Molecular Biology and Translational Science*, Elsevier, 2024, vol. 204, 219–248.

215 T. Lehto, K. Ezzat and Ü. Langel, in *Progress in Molecular Biology and Translational Science*, Elsevier B.V., 2011, vol. 104, 397–426.

216 Leber, N., Nuhn, L., Zentel, R., *Macromol. Biosci*., 2017, **17**, 1-15.

217 J. Scharner, S. Qi, F. Rigo, C. F. Bennett and A. R. Krainer*, Mol. Ther. Nucleic Acids*, 2019, **16**, 313–325

218 L. Scarabelli, A. Sánchez-Iglesias, J. Pérez-Juste and L. M. Liz-Marzán, *J. Phys. Chem. Lett*., 2015, **6**, 4270–4279.

219 M. D. Matteucci and M. H. Caruthers, *J. Am. Chem. Soc.*, 1981, **98**, 3185–3191.

220 S. L. Beaucage and M. H. Caruthers, *Tetrahedron. Lett.*, 1981, **22**, 1859–1862.

221 M. H. Caruthers, *Science (1979)*, 1985, **230**, 281–285.

222 H. K. N. D. Sinha, J. Biernat, J. McManus, *Nucleic Acids Res.*, 1984, **12**, 4539–4557.

223 M. M. Bradford, *Anal. Biochem.*, 1976, **72**, 248–254.